







Université du Québec  
à Rimouski

**Chronostratigraphie des processus sédimentaires associés à la transition postglaciaire dans le détroit d’Hudson et sur la marge continentale du Labrador**

Thèse présentée

dans le cadre du programme de doctorat en océanographie  
en vue de l’obtention du grade de Philosophiae doctor (Ph.D)

PAR

© **Quentin Duboc**

**Mai 2024**





**Composition du jury :**

**Gwenaëlle Chaillou, présidente du jury, Université du Québec à Rimouski**

**Guillaume St-Onge, directeur de recherche, Université du Québec à Rimouski**

**Patrick Lajeunesse, codirecteur de recherche, Université Laval**

**Matthias Moros, codirecteur de recherche, Leibniz-Institut für Ostseeforschung**

**Warnemünde**

**Etienne Brouard, examinateur externe, Commission géologique du Canada**

Dépôt initial le 28 avril 2023

Dépôt final le 10 mai 2024



UNIVERSITÉ DU QUÉBEC À RIMOUSKI  
Service de la bibliothèque

Avertissement

La diffusion de ce mémoire ou de cette thèse se fait dans le respect des droits de son auteur, qui a signé le formulaire « *Autorisation de reproduire et de diffuser un rapport, un mémoire ou une thèse* ». En signant ce formulaire, l'auteur concède à l'Université du Québec à Rimouski une licence non exclusive d'utilisation et de publication de la totalité ou d'une partie importante de son travail de recherche pour des fins pédagogiques et non commerciales. Plus précisément, l'auteur autorise l'Université du Québec à Rimouski à reproduire, diffuser, prêter, distribuer ou vendre des copies de son travail de recherche à des fins non commerciales sur quelque support que ce soit, y compris Internet. Cette licence et cette autorisation n'entraînent pas une renonciation de la part de l'auteur à ses droits moraux ni à ses droits de propriété intellectuelle. Sauf entente contraire, l'auteur conserve la liberté de diffuser et de commercialiser ou non ce travail dont il possède un exemplaire.



« Ceux qui vivent, ce sont ceux qui luttent ; ce sont  
Ceux dont un dessein ferme emplit l'âme et le front,  
Ceux qui d'un haut destin gravissent l'âpre cime,  
Ceux qui marchent pensifs, épris d'un but sublime,  
Ayant devant les yeux sans cesse, nuit et jour,  
Ou quelque saint labeur ou quelque grand amour. »

*Victor Hugo, Les Châtiments, 1852*



## REMERCIEMENTS

Pour m’ avoir permis d’ œuvrer sur cette thèse, je tiens tout d’ abord à remercier mes directeurs de recherche, à commencer par mon directeur Guillaume St-Onge qui m’ a proposé le sujet, offert de superbes opportunités d’ aller en mer, et soutenu tout le loooong du doctorat à travers les moultés péripéties endurées. Merci pour ton écoute, ton empathie, et ton éternel optimisme ! Merci également à mon codirecteur Patrick Lajeunesse pour m’ avoir apporté de l’ aide sur les aspects du Quaternaire et de la géophysique : les discussions avec toi étaient toujours efficaces et enrichissantes, et mes visites à Québec ont été source de déblocage technique. Many thanks also to Matthias, whom I was able to visit a few times in Warnemünde before the pandemic, for our long “Holocenic” discussions and your help with the cores’ chronologies. Je tiens également à remercier André Rochon et Calvin Campbell pour leur présence sur mon comité de thèse, ainsi que Gwenaëlle Chaillou et Étienne Brouard pour avoir participé à l’ évaluation de la thèse : j’ ai beaucoup apprécié votre enthousiasme et vos commentaires!

Malgré les apparences, un doctorat n’ est pas le fruit du travail d’ une seule personne, et nombreux·ses sont celles et ceux qui ont contribué de près ou de loin à la concrétisation de ce projet, de cette thèse, dans l’ ombre des portes de laboratoires. Je tiens donc à remercier ce cher Quentin B., côtoyé depuis 10 ans, travailleur au caractère bien trempé et attachant, et à Maxence St-Onge pour les mesures en laboratoire. Merci aussi à Dominique Lavallée pour les centaines d’ échantillons de sédiments mesurés au granulomètre-laser, à Mathieu Babin, Jean-François Hélie et Agnieszka Adamowicz pour les mesures d’ IRMS, et à Julie Major et Jean-Grabiél Auger, mes « esclaves » pré-pandémiques au tamisage de sédiment. Merci également à Kerstin Perner pour sa contribution clé à ce travail à travers la récolte des foraminifères à Warnemünde, ainsi qu’ à Tilo von Dobenech et Thomas Frederichs qui m’ ont accueilli pendant 1 mois dans leur laboratoire à Bremen pour travailler sur les propriétés

magnétiques du sédiment. Enfin, merci aux membres du laboratoire de Patrick (Léo, Alexis et Pier-Olivier) pour leur aide pour les données géophysique. Pour finir, je tiens à envoyer plein de reconnaissance envers les 4 « mousequerétaires » de l'ISMER pour leur disponibilité et leur bienveillance : Brigitte, Marielle, Nancy et bien sûr l'inoubliable et chaleureuse « maman des étudiant·e·s » Martine Belzile.

L'expérience doctorale n'aurait par ailleurs pas été la même sans le regroupement **ArcTrain**, qui m'a permis d'échanger avec l'Allemagne et de partager des expériences avec des étudiant·e·s venant des 4 coins du monde. Lina, Mattia, Béa, Jens, Jeetendra, Rémi, Damien, Valentin, Dmitrii, Anouk... I miss you guys! D'ailleurs, l'organisation de l'école d'été et du meeting ArcTrain en 2019, avec Charles, Amélie, Pascal, Jade B. et Jade F. aura assurément été un moment phare de ma thèse.

Je tiens finalement à mentionner l'organisme **Thèsez-Vous**, dont les retraites d'écriture m'ont permis d'enclencher la vitesse supérieure pour terminer la thèse. J'envoie d'ailleurs des pensées, peut-être en rêve funky, qui sait, à Alexandra et Gabrielle, et les autres avec qui j'ai passé une bonne partie du marathon final de rédaction.

Tout au long de la thèse, de nombreuses personnes m'ont soutenu, parfois en vivant une expérience bien similaire! Et s'il y en a bien une qui sort du lot, c'est mon partner de PhD, Arthur... Soutien moral infaillible au cours de cette épreuve. Je prendrais bien une tite bière sur ta terrasse, avec un jeu de société! Tu me manques, mais je sais qu'on se reverra souvent. Dans la même veine, ma chère Mymy, qui dès le début me disait que je ne finirais pas ma thèse en 3, ni même 4 ans... Si j'avais su à quel point tu avais raison! On en a traversé des épreuves, et maintenant te voilà maman sur une ferme en Normandie...

Deuxième maison pendant des années, **La Grotte** a connu beaucoup de passage. Merci aux personnes qui y ont habité au cours des 7 dernières années, et celles gravitant autour dans le lab de géologie : Julie, Charles-Édouard, Marie, Édouard, Yann, Omnain, Adriana, Simon N., Simon F., Naïs, Sarah, Fatma, Jade B., Anne, Zélie, Ménil, Kelsey, Maria-Émilia, Florian,



Camille, Juliette, Élodie, Pauline, Raphaël, Stefano et Morgane... avec une pensée spéciale pour Pierre-Arnaud, qui fut longtemps le mentor du labo et source de sagesse.

Dans mes premières années de doctorat, plusieurs personnes ont partagé mon quotidien en colocation. Pour la qualité de la vie en société que j'ai eu à leur côté, leurs soutiens dans les moments difficiles, et leur patience quant à ma non-présence ou mes allées et venues compliquées, je remercie Antoine, Greg, Maude, Delphine, Mathilde, Hugues, Patricia et ce cher coloc de confinement Jonathan.

Après 5 ans bien immergé en milieu québécois, j'ai été dépaysé par ma propre nationalité avec mon arrivée à l'**ISMER** pour la maîtrise en 2012. Mais ces années doctorales m'ont permis d'apprécier la compagnie de nombreux·ses compatriotes expatrié·e·s, dont plusieurs sont retourné·e·s dans l'hexagone depuis : cette chère Sarah, qui m'a tenu compagnie dans plusieurs retraites d'écriture, ce fofou de Léo avec qui les discussions vont toujours bon train, cet inarrêtable Tinou, ce Guillaume Bridier toujours partant pour l'aventure, cette Camille Berthod toujours là pour ses ami·e·s, cet Efflam plus breton que la Bretagne... Et Julie, Baptiste, Élodie, Tony, Clémence et Thibault, Sophia, Hélène, Delphine, Thomas, Leila, Angy, Candice et Nathan, Lola, Greg BD... Et Kévin! Ce cher Kévin – pas français attention – dont les compétences et les capacités multitâches ne cessent de m'impressionner.

Beaucoup d'autres personnes ont mis de la couleur dans ma vie au cours des dernières années, parfois très sporadiquement, parfois sur de plus longues périodes, et je me dois de les mentionner. Je pense à Jeanjean, à Melany, à Guillaume Cochon, Jessie, Vincent et Marie Boirot (chartreuse!) avec Martin et la gang du théâtre, et Élodie et Gaël, à Étienne GG et Martin Laroche, à la gang du RÉVUS, à celle du Lèche-Babines avec Myriam, Caro et Alex notamment, à Cath BC, à Marine, à Marie Dixneuf et la bande de l'époque COVID – Augustin, Joris, Sarah, Marc, Joëlle N. et Pauline – à Myriam G., à Jean-Luc, à Alice, Caro et Joëlle G., à Valentin et Elsa, Jonathan P., Muriel, Estelle, Matt Plante, Julien et Sophia, Jennifer, et Sandrine.

Les personnes qui me connaissent bien savent que je n'oublierai jamais de mentionner... **le Crêpe-Chignon** ! Cet endroit où l'ambiance, l'équipe et les conditions de travail n'ont pas leur pareil en restauration, et dont je fais sans cesse la publicité. Plus qu'un lieu de travail, c'est un repère, un refuge dans la tempête, un foyer toujours allumé par la chaleur des employé·e·s, où on se sent si facilement chez soi. Un énorme merci aux incroyables Stéphanie et Jinny pour avoir donné naissance à cette institution rimouskoise et m'avoir inclus dans leur équipe en 2008. Merci aux nombreuses belles personnes avec qui j'ai partagé les rushs démentiels et refait le monde au comptoir. Je pense notamment à Raph, gourou de la décroissance et des jeux de sociétés, à ce grand cru de Janek, à ma partner de canot-Camping et accordéoniste Isa, à l'expressive et aimante Maki, à l'inspirante Améliane (et ses sœurs), à Marilyne qui continue de tricoter sa belle humeur... Et aussi à Gigi, Marie-Ange, Cath Duval, Sylvie, Philou (et ses frères), Marie, Joël, Julie et Zach, Rose, Ève, Béa, Lou, Lila, Noé, Thierry, Charlotte, Pascale, Leon... et les ancien·ne·s comme Mireille, Tony, Chantal, Alice, les frères Villeneuve... Sans oublier l'éternel chef-cuisinier David, et feu Marco parti trop vite, auquel Evan et Marjorie ont rendu hommage en nommant leur café « Chapeau-Moustache ». Merci aussi à eux d'exister, leur succulent café a beaucoup coulé dans mes veines pendant la rédaction !

Et finalement, je remercie la famille. Ma « cousine jumelle » Pauline, mon cousin Alex qui m'a rendu visite à Rimouski... Et tous les autres cousin·e·s, oncles et tante, que je ne vois bien sûr pas assez souvent... Ma grand-mère toujours très vive d'esprit pour ses presque 90 ans. Et, pour finir, je remercie du fond du cœur mes parents : ma petite maman, toujours là pour me conseiller, et mon sensible papa toujours là pour moi, avec sa compagne Chantal. Merci de m'avoir soutenu dans mes choix, et surtout merci pour les valeurs que vous m'avez transmises et qui ont grandement contribué à former la personne que je suis aujourd'hui.

## RÉSUMÉ

La reconstruction de l'évolution des anciens inlandsis offre l'opportunité de mieux appréhender les conséquences futures des fluctuations des marges glaciaires antarctiques et groenlandaises. Au dernier maximum glaciaire, l'Inlandsis laurentidien couvrait la majeure partie du Canada, puis s'est progressivement réduit jusqu'à la disparition complète du dôme du Labrador il y a environ 6000 ans. Ce recul s'est accompagné de perturbations océaniques et climatiques, telles que l'événement froid de 8,2 ka causé par la vidange du lac proglaciaire Agassiz-Ojibway (LAO) dans l'Atlantique nord qui a perturbé la circulation océanique. Le retrait des glaces s'est également soldé par une transformation drastique des environnements côtiers canadiens passant de paysages glaciaires à des conditions proches de l'actuel. De plus, les processus glaciaires et paraglaciaires ont causé une importante remobilisation de sédiments, souvent vers les lacs et les bassins des marges continentales. Dans ce contexte, cette thèse a pour objectif de préciser la chronostratigraphie du recul des marges de l'Inlandsis laurentidien et des processus sédimentaires associés à celle-ci et à la transition postglaciaire subséquente. Un accent est mis sur les événements reliés à la vidange du LAO, dont certains points chronologiques sont encore débattus. Pour ce faire, cinq longues carottes sédimentaires ont été prélevées dans différents bassins à fort taux de sédimentation dans l'ouest du détroit d'Hudson, les fjords Nachvak et Saglek au nord du Labrador, et le lac Melville au sud du Labrador. Une analyse multi-traceurs des carottes, combinée à de solides chronologies basées sur 69 âges  $^{14}\text{C}$  et à des profils acoustiques de sous-surface, a permis d'établir un portrait de la dynamique sédimentaire de chaque secteur suivant le retrait de la marge glaciaire.

Dans les fjords Nachvak et Saglek au nord du Labrador, les profils de sous-surface révèlent la présence d'importants dépôts de mouvements de masse suggérant l'occurrence possible de séismes associés au rebond glacio-isostatique postglaciaire, notamment au début de l'Holocène. Par ailleurs, la chronologie des séquences sédimentaires indique que le fjord Nachvak se serait déglacé avant le Dryas récent, environ 2000 ans avant le fjord Saglek. Cette déglaciation asynchrone s'explique par l'effet tampon de la baie de Saglek. De plus, la présence de couches sédimentaires à haut taux de carbonates détritiques déposées entre 9,2 et 8,1 cal ka BP révèle que les fjords ont enregistré les derniers événements de déglaciation de la baie d'Hudson, qui incluent notamment la vidange finale du LAO.

Par ailleurs, ces mêmes événements de déglaciation sont identifiés de façon plus précise dans deux carottes provenant des bassins Ouest et Sud-Ouest du détroit d'Hudson. La couche rouge, marqueur chronostratigraphique régional connu, est ici datée à  $8,67 \pm 0,15$  cal ka BP et associée à un drainage sous-glaciaire du LAO. Peu après, un recul important de la marge glaciaire s'est produit en baie d'Hudson, comme en témoigne un apport important

de débris transportés par les glaces (IRDs), suivi d'une période de stabilité de 300-400 ans. Une double couche d'IRDs et de carbonates détritiques est ensuite corrélée à une vidange finale du LAO en deux temps, combinée à la chute du barrage de glace qui le retenait. Cet événement aurait débuté vers 8,21 cal ka BP et aurait duré environ un siècle. Ces enregistrements mettent également en évidence une importante différence d'âge réservoir de  $^{14}\text{C}$  entre les deux bassins, causée par l'influence de la marge glaciaire proximale.

Dans le lac Melville, une carotte de 14 m a été échantillonnée dans un bassin moins profond que le chenal principal. Sa chronologie, complétée avec des corrélations paléomagnétiques de bonne qualité, indique que la marge glaciaire était proche du bassin pendant l'événement froid de 9,3 ka, et a ensuite rapidement reculé vers l'ouest jusqu'à la localisation de la moraine de Sebaskachu. Le taux de sédimentation est alors passé de 1 à 0,1 cm/an pendant la transition postglaciaire. Cette transition a été marquée par des changements de conditions redox entre 8,2 et 7,8 cal ka BP indiquant une diminution de l'apport de matière organique corrélée à l'événement froid de 8,2 ka.

Dans l'ensemble, cette thèse apporte plus de précisions sur l'évolution de la marge de l'Inlandsis laurentidien, en particulier dans les fjords Nachvak et Saglek et en baie d'Hudson. En effet, confirmer le drainage final du LAO vers 8,2 cal ka BP implique que le barrage de glace y a subsisté jusque-là. Par ailleurs, cette thèse met en valeur les importances relatives des processus glaciomarins, paraglaciaires et postglaciaires dans la dynamique sédimentaire des différentes zones. En outre, la fin de la transition postglaciaire est marquée par des changements de courants marins et des périodes de forte productivité primaire qu'il serait intéressant d'investiguer.

Mots clés : Inlandsis laurentidien ; marge glaciaire ; séquence sédimentaire ; transition postglaciaire ; Holocène ; lac Agassiz-Ojibway ; fjords du Labrador ; lac Melville ; détroit d'Hudson ; carbonates détritiques.



## ABSTRACT

The reconstruction of past ice sheet evolution offers the opportunity to better understand the future consequences of Antarctic and Greenland ice margin fluctuations and their impacts. During the Last Glacial Maximum, the Laurentide Ice Sheet covered most of Canada, then gradually shrank until the complete disappearance of the Labrador dome about 6000 years ago. This retreat was accompanied by oceanic and climatic disturbances, such as the 8.2 ka cold event attributed to the proglacial Lake Agassiz-Ojibway (LAO) drainage in the North Atlantic that disrupted ocean circulation. The ice retreat also resulted in a drastic transformation of Canadian coastal environments from glacial landscapes to near present-day conditions. In addition, glacial and paraglacial processes have caused significant sediment remobilization, often towards lakes and continental margin basins. In this context, this thesis aims to precise the chronostratigraphy of the sedimentary processes associated with the Laurentide Ice Sheet margin retreat and the subsequent postglacial transition. An emphasis is put on events related to the LAO drainage, for which some chronological points are still debated. To this end, five long sediment cores were collected from different basins with high sedimentation rates along the Labrador and northern Quebec continental margin. Core physical, chemical and magnetic properties, combined with robust chronologies based on 69  $^{14}\text{C}$  ages and subsurface acoustic profiles, provided a picture of the sedimentary dynamics of each area following the retreat of the ice margin.

In Nachvak and Saglek Fjords located in northern Labrador, subsurface profiles reveal the presence of significant mass movement deposits, suggesting the possible occurrence of earthquakes associated with isostatic readjustment, especially during the Early Holocene. Furthermore, the chronology of sedimentary sequences indicates that Nachvak Fjord was deglaciated before the Younger Dryas, and about 2000 years before Saglek Fjord. This asynchronous deglaciation is explained by the buffering effect of Saglek Bay. Furthermore, the presence of sedimentary layers with high detrital carbonate content deposited between 9.2 and 8.1 cal ka BP reveal that the fjords recorded the last deglaciation events of Hudson Bay.

These deglaciation events are more precisely identified in two cores from the western and southwestern Hudson Strait basins. The red layer, a known regional chronostratigraphic marker, is here dated at  $8.67 \pm 0.15$  cal ka BP and associated with a subglacial LAO drainage. Shortly after, a major ice margin retreat occurred in Hudson Bay, as evidenced by a high rate of ice-transported debris (IRDs), followed by a 300-400 years period of stability. A double layer of IRDs and detrital carbonates is then correlated with a two-stage final LAO drainage, combined with the collapse of the ice dam that was retaining it. This event would have started around 8.21 cal ka BP and would have lasted about a century. These records also highlight a

large difference in  $^{14}\text{C}$  reservoir age between the two basins, caused by the influence of the proximal ice margin.

In Lake Melville, a 14 m-long core was sampled from a basin shallower than the main channel. Its chronology, supplemented with good quality paleomagnetic correlations, indicates that the ice margin was close to the basin during the 9.3 ka cold event, and then rapidly retreated westward to the Sebaskachu moraine. The sedimentation rate then decreased from 1 to 0.1 cm/yr during the postglacial transition. This transition was marked by changes in redox conditions between 8.2 and 7.8 cal ka BP indicating a decrease in organic matter input correlated with the 8.2 ka cold event.

Overall, this thesis provides further insight into the evolution of the Laurentide Ice Sheet margin, particularly in Nachvak and Saglek Fjords and Hudson Bay. Indeed, confirming the final drainage of the LAO around 8.2 cal ka BP implies that the ice dam remained present until then. Furthermore, this thesis highlights the relative importance of glaciomarine, paraglacial and postglacial processes in the sedimentary dynamics of the different areas. In addition, the late postglacial transition is marked by changes in marine currents and periods of high primary productivity that would be interesting to investigate.

*Keywords:* Laurentide Ice Sheet; ice margin; sedimentary sequence; postglacial transition; Holocene; Lake Agassiz-Ojibway; Labrador fjords; Lake Melville; Hudson Strait; detrital carbonates.





## TABLE DES MATIÈRES

REMERCIEMENTS.....	ix
RÉSUMÉ.....	xiii
ABSTRACT.....	xvi
TABLE DES MATIÈRES.....	xix
LISTE DES TABLEAUX.....	xxiii
LISTE DES FIGURES.....	xxv
LISTE DES ABRÉVIATIONS, DES SIGLES ET DES ACRONYMES.....	xxxiii
LISTE DES SYMBOLES.....	xxxvi
INTRODUCTION GÉNÉRALE.....	1
1. INTRODUCTION A LA PROBLEMATIQUE.....	1
2. REGION D'ETUDE.....	5
2.1 La baie et le détroit d'Hudson.....	6
2.2 Le plateau continental et la côte du Labrador.....	7
3. CONTEXTE QUATERNAIRE ET SEDIMENTAIRE.....	12
3.1 Retrait de l'Inlandsis laurentidien.....	12
3.2 L'événement de 8.2 ka.....	15
3.3 Séquence sédimentaire quaternaire sous-marine.....	18
4. OBJECTIFS DE LA THESE.....	19
5. METHODOLOGIE.....	21
5.1 Profils sismiques et carottage.....	21
5.2 Analyses tomodynamométriques.....	23
5.3 Propriétés physiques et chimiques continues.....	24
5.4 Analyses d'isotopes stables.....	26
5.5 Analyses granulométriques.....	26
5.6 Magnétomètre à gradient alternatif.....	27
5.7 Magnétomètre cryogénique.....	28
5.8 Chronologie.....	29

6.	ORGANISATION DE LA THESE .....	31
Chapitre 1 Séquences sédimentaires holocènes des fjords Nachvak et Saglek (nord du Labrador) comme enregistrement de la déglaciation des monts Torngat et de la baie d'Hudson.....		
		33
1.1	RESUME EN FRANÇAIS DU PREMIER ARTICLE .....	33
1.2	HOLOCENE SEDIMENTARY SEQUENCES FROM NACHVAK AND SAGLEK FJORDS (NORTHERN LABRADOR) AS A RECORD OF DEGLACIATION OF THE TORNGAT MOUNTAINS AND HUDSON BAY .....	35
1.3	INTRODUCTION .....	36
1.4	STUDY AREA.....	38
	1.4.1 Physiographic setting .....	38
	1.4.2 Background .....	40
1.5	MATERIALS AND METHODS .....	44
	1.5.1 Geophysical data .....	44
	1.5.2 Sampling .....	44
	1.5.3 Physical properties analyses .....	45
	1.5.4 Grain-size analyses .....	46
	1.5.5 Magnetic properties analysis.....	46
	1.5.6 Organic geochemistry .....	46
	1.5.7 Radiocarbon chronology.....	47
1.6	RESULTS.....	49
	1.6.1 Fjord geomorphology.....	49
	1.6.2 Saglek Fjord general geomorphology.....	50
	1.6.3 Sub-bottom profiles .....	56
	1.6.4 Cores sedimentology.....	59
	1.6.5 Hysteresis parameters .....	63
	1.6.6 Organic matter geochemistry .....	64
	1.6.7 Core chronology.....	65
1.7	DISCUSSION.....	65
	1.7.1 Sedimentary sequences .....	65
	1.7.2 Mass-movement deposits.....	67
	1.7.3 Timing of deglaciation and deposition of massive MMDs.....	69
	1.7.4 Regional and local deglacial and postglacial events.....	71
	1.7.5 Deglacial to postglacial history and changes in sedimentary regimes.....	77

1.8	CONCLUSIONS .....	80
1.9	ACKNOWLEDGMENTS.....	81
1.10	REFERENCES .....	81
1.11	SUPPLEMENTARY MATERIAL (FIGURES).....	94
CHAPITRE 2 Trois vidanges du lac Agassiz-Ojibway identifiées dans de nouveaux enregistrements sédimentaires à haute résolution de l'ouest du détroit d'Hudson.....		96
2.1	RESUME EN FRANÇAIS DU DEUXIEME ARTICLE.....	96
2.2	THREE LAKE AGASSIZ-OJIBWAY DRAINAGES EVENTS CONSTRAINED IN NEW HIGH-RESOLUTION SEDIMENTARY RECORDS FROM THE WESTERN HUDSON STRAIT .....	97
2.3	INTRODUCTION .....	98
2.4	STUDY AREA .....	100
	2.4.1 Physiography and oceanography .....	100
	2.4.2 Deglaciation and Quaternary sequence .....	101
2.5	METHODS.....	102
	2.5.1 Sampling.....	102
	2.5.2 Sediment analyses .....	103
	2.5.3 Chronology .....	104
2.6	RESULTS .....	107
	2.6.1 Lithology .....	107
	2.6.2 Chronologies.....	110
2.7	DISCUSSION .....	112
	2.7.1 Detailed record of Hudson Bay deglacial events considering a consistent $\Delta R$ .....	113
	2.7.2 Implications of reservoir age variations .....	119
2.8	CONCLUSIONS .....	121
2.9	ACKNOWLEDGMENTS.....	122
2.10	REFERENCES .....	122
CHAPITRE 3 Évolution des processus sédimentaires et des conditions environnementale dans le lac Melville, Labrador, depuis 9200 ans .....		130

3.1	RESUME EN FRANÇAIS DU TROISIEME ARTICLE .....	130
3.2	EVOLUTION OF DEGLACIAL SEDIMENTARY PROCESSES AND ENVIRONMENTAL CONDITIONS IN LAKE MELVILLE, LABRADOR, SINCE THE LAST 9.2 KA .....	131
3.3	INTRODUCTION .....	131
3.4	STUDY AREA.....	133
3.5	MATERIALS AND METHODS .....	136
	3.5.1 Acoustic profiling and sampling .....	136
	3.5.2 Physical and chemical measurements .....	136
	3.5.3 Cryogenic magnetometer .....	137
	3.5.4 Discrete analyses.....	138
	3.5.5 Chronology .....	139
3.6	RESULTS.....	140
	3.6.1 Acoustic stratigraphy .....	140
	3.6.2 Core lithology .....	142
	3.6.3 Rock-magnetic analyses.....	145
	3.6.4 NRM and paleomagnetic directional data.....	147
3.7	DISCUSSION.....	149
	3.7.1 Deglacial sedimentary sequence .....	149
	3.7.2 Age-modelling .....	150
	3.7.3 Evolution of sedimentary and environmental conditions .....	154
3.8	CONCLUSION .....	156
3.9	ACKNOWLEDGMENTS .....	157
3.10	REFERENCES.....	158
	CONCLUSION GÉNÉRALE.....	167
	RÉFÉRENCES BIBLIOGRAPHIQUES .....	179

## LISTE DES TABLEAUX

<b><u>Tableau 1.</u></b> <u>Coordonnées, profondeur et longueur des carottes sédimentaires étudiées dans la présente thèse.</u> .....	23
<b><u>Table 2.</u></b> <u>List of AMS radiocarbon ages analyzed and calibrated in Calib8.2 (Stuiver et al., 2020) using the Marine20 dataset (Heaton et al., 2020).</u> .....	49
<b><u>Table 3.</u></b> <u>Acoustic units in the sedimentary sequences of Nachvak and Saglek Fjords</u> .....	52
<b><u>Table 4.</u></b> <u>List of AMS radiocarbon ages analyzed and calibrated in Calib8.2 (Stuiver et al., 2020) using the Marine20 dataset (Heaton et al., 2020) and the <math>\Delta R</math> value of <math>-73 \pm 64</math> yr proposed by Pieńkowski et al. (2022).</u> .....	106
<b><u>Table 5.</u></b> <u>List of AMS radiocarbon ages analyzed and calibrated in Calib8.2 (Stuiver et al., 2020) using the Marine20 dataset (Heaton et al., 2020) and a <math>\Delta R</math> value of <math>0 \pm 0</math> yr</u> .....	140
<b><u>Table 6.</u></b> <u>Paleomagnetic chronostratigraphic markers (tie-points) based on correlation between core 13-03-GC, the geomagnetic field model CALS10k.2 (Korte et al., 2011) calculated for the localisation of core 13-03-GC and three other paleomagnetic records: Greenland-Iceland PSV composite (Stoner et al., 2007), Site U1305 in Labrador Sea (Stoner et al., 2013) and the Eastern Canada Paleostack (Barletta et al., 2010b). Tie-points labelled with I and D correspond respectively to inclination and declination and are identified in Fig. 38.</u> .....	153



## LISTE DES FIGURES

- Figure 1.** Carte de la région d'étude avec un aperçu de la circulation océanique régionale, inspirée de Stewart & Howland (2009) et de Lochte et al. (2019b). Les flèches rouges indiquent les courants plus chauds. Les étoiles jaunes indiquent la localisation des carottes sédimentaires analysées dans cette thèse, dans les 3 secteurs correspondant aux chapitres (titres en jaune). LC : courant du Labrador. ....6
- Figure 2.** Carte topographique de la région des fjords Nachvak et Saglek. La zone en vert correspond au parc national des monts Torngats. ....9
- Figure 3.** Bathymétrie du bras de mer Hamilton incluant la baie Goose, le lac Melville et la baie Groswater. Tiré de Kamula et al. (2017). .... 11
- Figure 4.** Salinité en fonction de la profondeur du bras de mer Hamilton et du plateau du Labrador. Modifié de Vilks & Mudie (1983). .... 12
- Figure 5.** Carte de l'extension maximale des inlandsis en Amérique du Nord au LGM (18 ka, ou 21,7 cal ka BP), avec localisation des dômes de Keewatin, de Foxe-Baffin et du Labrador. La ligne en pointillés correspond à la limite du LIS proposée par Dyke et al., (2004). Tiré de Dalton et al (2020). .... 13
- Figure 6.** Évolution de l'extension du LIS dans la région du système de la baie d'Hudson entre 8,5 et 7,2 <sup>14</sup>C ka BP (9,6 et 8,1 cal ka BP). La ligne en pointillés correspond à la limite du LIS proposée par Dyke et al., (2004). Tiré de Dalton et al (2020). .... 15
- Figure 7.** **A)** Extension approximative de l'Inlandsis laurentidien avant le drainage final du LAO et la chute du barrage de glace de la baie d'Hudson. La zone rouge représente la zone couverte par les erratiques rouges d'où provient le sédiment de la couche rouge du détroit d'Hudson. **B)** Carte de la position de la marge glaciaire et de l'ouest du LAO au nord du Manitoba lors d'un éventuel drainage sous-glaciaire à environ 8,6 cal ka BP. Les flèches ondulées indiquent la position probable des chenaux de drainage. La position de dunes et de chenaux sous-marins associés au drainage sont également indiqués (Tiré de Gauthier et al., 2020). **C)** Cicatrices arquées laissées par des icebergs sur le fond de la baie d'Hudson lors de la vidange finale du LAO (Tiré de Lajeunesse & St-Onge, 2008). .... 17

<b>Figure 8.</b> Récupération de la carotte à gravité MSM46-28-04-GC dans le fjord Nachvak. ....	22
<b>Figure 9.</b> Images tomographiques de la carotte 28 (Fjord Nachvak) obtenue avec le MSCL-XCT de l'ISMER-UQAR. Les cercles indiquent les coquilles de bivalves identifiées à l'aide de l'image. Les débris laissés par les glaces (IRDs) sont également bien visibles, ainsi qu'une couche de sédiments probablement déposée rapidement entre 824 et 830 cm. ....	24
<b>Figure 10.</b> A) Magnétomètre à gradient alternatif MicroMag 2900. B) Schéma d'une boucle d'hystérésis avec l'identification des paramètres principaux. Inspiré de Maher (2007). ....	28
<b>Figure 11.</b> Map of the study area with the Northwest Atlantic Circulation (adapted from Lochte et al., 2019b), with the location of Nachvak and Saglek Fjords. Yellow stars and white circles are the location of cores from this study and other cores referred in this work, respectively. ....	40
<b>Figure 12.</b> Swath bathymetry map of Nachvak Fjord, with location of seismic lines AA', BB', CC', DD' and EE' (Fig. 14) and coring sites of core 28-04-GC (this study) and core AM09-PC-N602 (Richerol et al., 2015). GU = gullies; HS = headscarps; IP = icebergs pits; MR = morainic ridges. Yellow dotted lines show the limit of depositional lobes. ....	42
<b>Figure 13.</b> Swath bathymetry map of Saglek Fjord, with location of seismic lines FF', GG', HH' and JJ' (Fig. 15) and coring sites of core 14-05-GC. All the names of Saglek basins and sill are proposed in this study. GU = gullies; HS = headscarps; IP = icebergs pits; MR = morainic ridges. Yellow dotted lines show the limit of depositional lobe. Yellow plain lines are the limits of sediment fans. White dotted lines are the location of the Saglek Moraines as identified by Ives (1976). ....	43
<b>Figure 14.</b> Acoustic profiles from Nachvak Fjord. Location of the profiles are indicated on Fig. 12. The different acoustic units are indicated and delimited. Zone highlighted in light yellow represent the identified MMDs. Profiles AA', BB' and CC' were obtained during the MSM46 cruise, whereas profiles DD' and EE' are from the Amundsen Science Data Collection and was obtained during the ArcticNet campaign of November 2009. ....	54
<b>Figure 15.</b> Acoustic profiles from Saglek Fjord. Location of the profiles are indicated on Fig. 13. The different acoustic units are indicated and delimited. Light yellow patches represent the identified MMDs, while the orange ones represent the sidewall echoes interfering with the signal (SWE). Profile HH' and JJ' were obtained during the MSM46 cruise, whereas profiles FF'	



et GG' come from Amundsen Science Data Collection and were obtained during the leg4b of the ArcticNet campaign of November 2009.....55

**Figure 16.** Stratigraphic framework of Nachvak and Saglek Fjords made from acoustic data. The different units are represented, as well as their internal reflectors. Light grey represents where we do not have sufficient acoustic penetration.....59

**Figure 17.** A) and B) Physical, geochemical and sedimentological properties of cores 14-05-GC and 28-04-GC respectively along with their CT-scan images (for core 28-004-GC), pictures, logs and age-models. Note that the magnetic susceptibility has a logarithmic scale. Colors are associated with the different units described in section 4.3 plus the RDLs (in brown) and the pinkish layer in core 28-04-GC (in red). The age-models are made with AMS <sup>14</sup>C ages from foraminifera and mollusc shells. Also represented is the sedimentation rate calculated by interpolation between all of the ages (green plain line) and the same without including ages that generate aberrant variations in sedimentation rates (grey line). The dashed line at the top represents the theoretical sedimentation rate if there is no loss at the core top. C) and D) Diagram of  $k_{LF}$  versus Ca/Ti of cores 14-05-GC and 28-04-GC respectively, with logarithmic scales. ....62

**Figure 18.** A) and B) Magnetic susceptibility Ca/Ti and weighted percentage of two sieve sizes (>63  $\mu$ m and >150  $\mu$ m) for the lower parts – units L1, L2 and L3 – of cores 14-05-GC and 28-04-GC respectively, along with the core pictures. The  $a^*$  is also added for core 28-04-GC. Detrital carbonate (DC) layers of unit 2 are highlighted in blue, the pinkish layer in pink and the RDLs in grey. The median probability of <sup>14</sup>C ages obtained on these sections are also indicated. C) Zoom on the CT-scan of the pinkish layer.....63

**Figure 19.** Comparison of detrital carbonate record in core MD99-2236 (Jennings et al., 2015) and percentage of dinocyst *P. Dalei* (Richerol et al., 2016) against magnetic susceptibility, Ca/Ti and Hcr/Hc of cores 14-05-GC (in blue) and 28-04-GC (in red) and  $\delta^{13}C$  of core 14-05-GC. Gaps are left in core 14-05-GC for the record eroded by the turbidites. The blue and red bars correspond to the three DC peak identified in our cores.....74

**Figure 20.** Conceptual models representing the successive depositional environments in Nachvak and Saglek Fjords during and after the deglaciation. Arrows show different MMDs (plain arrows), hemipelagic or glacial (dotted brown arrows) and DC-rich (blue dotted arrows) sediment inputs. ....79

**Figure 21.** Day-diagrams made with AGM data from cores 14-05-GC and 28-04-GC, along with hysteresis curves of representative samples for each unit of the

core. Grey hysteresis curves correspond to raw hysteresis data, whereas the black ones are corrected for paramagnetic and diamagnetic components..... 94

**Figure 22.** Carbon and nitrogen properties for cores 14-05-GC and 13-03-GC along with their magnetic susceptibility. Also shown is a diagram of  $\delta^{13}\text{C}$  versus C/N for each core for comparison with the values of different sources of organic matter, based on Lamb et al. (2006). ..... 95

**Figure 23.** Map of the study area with extension of the Laurentide Ice Sheet before the drainage of Lake Agassiz-Ojibway. Yellow stars represent locations of the cores used in the study. The red patch is the principal area of red erratics dispersed by the ice-sheet from the Dubawnt Group at the northwest. .... 101

**Figure 24.** Sub-bottom profiles of the coring locations of A) Core 20 in the Western Basin and B) Core 24 in the Southwestern Basin. A sediment velocity of 1500 m/s is used to correlate the cores with the acoustic signal. .... 103

**Figure 25.** Physical and chemical properties of cores 20 and 24 with their age-models, their photography and the CT-scan images of their respective u-channels. The results of sediment sieving at 63 and 150  $\mu\text{m}$  is also shown, as well as core age-models obtained from AMS  $^{14}\text{C}$  ages. The red circles indicate ages that were not included in the BACON age-models. Pale blue, grey and red rectangles highlight respectively the double detrital carbonate peak (DDCP), the 20 cm-thick IRD-rich layer and the red layer that are recognized in both cores. .... 109

**Figure 26.** Zoomed comparison of the lower sections of both cores 20 and 24 with their  $a^*$ , Ca/Ti and sieving data. Black numbers correspond to calibrated  $^{14}\text{C}$  ages. Ages in red are those not considered in the age-model building with Bacon. .... 110

**Figure 27.** Separated interpolations between mollusc and foraminifera samples from cores 20 and 24. Blue and red bars indicate the temporal occurrence of the DDCP and the red layer respectively..... 112

**Figure 28.** Comparison of Hudson Bay deglacial event markers from different records on a same time-frame. a) and b) Ca/Ti and  $>150\mu\text{m}$  sieving data from cores 24 and 20 respectively according to the Bacon age-model; c) Same data from core 20 according to an interpolation between the  $^{14}\text{C}$  indicated by red dots; d) Diagram of the Lake Ojibway varve sequence from Godbout et al. (2019) matched with core 20 record by considering the pre-final LAO drainage at 8.21 cal ka BP; e) ages of the subglacial drainage spilling the red layer and the last LAO drainage according to Gauthier et al. (2020); f) Ca/Ti of core MSM46-28-04-GC from Nachvak Fjord (Duboc et al., 2023); g) Total carbonate content of core MS99-2236 (Jennings et al.,

2015); h) % of *Pachyderma Sinistral* of core MD99-2251 (Ellison et al, 2006). Sequences in red and blue correspond respectively to the red layer and the detrital-carbonate layer associated with the last LAO drainage in the different records. Vertical purple bars represent the timing of the LAO two-stage last drainage determined by Brouard et al. (2021)..... 115

**Figure 29.** Schematic representation of red sediment dispersal with a freshwater plume formed by a subglacial drainage of Lake Agassiz-Ojibway (blue arrow) under the Hudson Bay Ice Saddle. Red dotted arrows represent particle fallout from the plume containing high concentration of fine red sediment. .... 117

**Figure 30.** Schematic view of the last deglacial events in Hudson Bay. A) Early opening of the Tyrrell Sea. B) First, subglacial LAO drainage eroding and carrying red sediment downstream. C) Ice ablation caused by the LIS retreat, following the first drainage. 4) Collapse of the HBIS and catastrophic, final LAO drainage triggering the 8.2 ka event. .... 119

**Figure 31.** Map of the Lake Melville area. A) Extension of the Laurentide Ice Sheet over North America at the Last Glacial Maximum, from Stokes (2017). B) Zoom on Southeastern Labrador with *yellow scattered* lines representing moraines systems. C) Map of Lake Melville with multibeam data from the ArcticNet Basemaps Database, the localisation of core MSM46-13-03-GC and of the Sebaskachu Moraine system. The red line shows the location of the acoustic profile of Figure 32. .... 135

**Figure 32.** Acoustic profile obtained during the MDM46 cruise. A) Complete profile with location indicated in figure 31. B) Zoom on the shallow basin with position of core 13-03-GC. Sediment thicknesses have been estimated with a sediment velocity of 1500 m/s, as in other fjord-like environments (Hjelstuen et al., 2009; Bellwald et al., 2016). C) Same as B) but with colors highlighting the different units described in section 3.1: A1 in brown with an uncertain base at the basin bottom; A2 in purple, A3 in yellow and A4 in blue at the top. .... 141

**Figure 33.** A) Physical, chemical, sedimentological and magnetic properties of core 13-03-GC versus depth, along with its photography and the CT-scan image from the u-channels. Colors are associated to the different units described in section 4.2. B) Diagram of  $k_{ARM}$  VS  $k_{LF}$  with lines representing different magnetic grain-size threshold proposed by King et al. (1983). C) Diagram of  $\delta^{13}C$  versus C/N for comparison with the values of different sources of organic matter, based on Lamb et al. (2006)..... 144

**Figure 34.** Zoom on specific sections of core 13-03-GC with their photographs, some chemical, physical or magnetic properties and the location of calibrated

AMS  $^{14}\text{C}$  ages from foraminifera (in red) and mollusc shells (in blue). **A)** Unit 1, also with the CT-scan from u-channels. **B)** Section covering the transition of units 3 and 4a, also with an image with the thick carbonated IRD found in the core. .... 145

**Figure 35.** Data obtained from AGM measurements. A) Specific hysteresis curves from samples representing the different units of core 13-03-GC. Grey hysteresis curves correspond to raw hysteresis data, whereas the black ones are corrected for paramagnetic and diamagnetic components. B) Day diagram with all measured sampled. C) Combination of all normalized and corrected hysteresis curves showed above. .... 147

**Figure 36.** Natural remanent magnetization measurements of core 13-03-GC along with its magnetic susceptibility. The MAD of NRM and ChRM are plotted, as well as the inclination of the geocentric axial dipole model ( $I_{\text{GAD}}$ ). .... 148

**Figure 37.** Paleomagnetic comparison of **(A)** inclination and **(B)** declination between core 13-03-GC from Lake Melville, the geomagnetic field model from Korte et al. (2011) and other regional records: the Greenland-Iceland PSV composite (GreenIce; Stoner et al., 2007), Site U1305 in Labrador Sea (Stoner et al., 2013) and the Eastern Canada Paleostack (Barletta et al., 2010b). .... 152

**Figure 38.** Final age model of core 13-03-GC based on AMS  $^{14}\text{C}$  ages from foraminifera and mollusc shells, and on tie-points from paleomagnetic correlations of inclination and declination. Variations of sedimentation rates are also plotted in red with a logarithmic scale. On the top right, the dark and the light blue bar represents respectively the 8.2 ka event and the long-term cooling starting around 8.6 ka cal BP (Rohling and Pälike, 2005). The white pentagon corresponds to the age of the thick carbonate IRD found in core 13-03-GC, while the brown square represents the age of the Sebaskachu moraine (Couette et al., 2023). Colours in the background correspond to the five units of core 13-03-GC as in Figure 33. .... 154

**Figure 39.** Schematic representation of deglaciation steps in the Lake Melville area. Locations of core 13-03-GC and the Sebaskachu moraine are indicated. The blue arrows represent fluvio-glacial runoff from the LIS. .... 155

**Figure 40.** Figure synthèse comparant les résultats des différents secteurs entre eux et avec d'autres études, en fonction du temps. Les événements froids de 8,2, 9,3 et 10,3 ka y sont indiqués par les rectangles turquoises, de même que le refroidissement général de 8,6 ka en bleu pâle (rectangle bleu pâle ; Rohling & Pälike, 2005). Les événements de drainage final du LAO sont également indiqués (losanges bleus ; Gauthier et al., 2020 ; Brouard et al., 2021) de même que l'épisode de transgression marine du LAO (losange vert ;

Gauthier et al., 2020) et l'évolution du pourcentage total de carbonates de la carotte MD99-2236, avec les pics de carbonates détritiques (DCP ; Jennings et al., 2015). Les barres colorées en dégradés représentent les séquences sédimentaires des cinq bassins, réparties selon les trois zones (vert = postglaciaire ; jaune = transition ; bleu = glaciomarin ; blanc = zone englacée). Les barres noires verticales indiquent la base de la carotte de chaque bassin, avec son numéro. Les petites courbes bleues et brunes représentent les pics de carbonates détritiques et d'IRDs, respectivement, tandis que le losange rouge représente le dépôt de la couche rouge. L'avancée de Cochrane et l'exposition de la moraine de Sebaskachu sont également indiquées (losanges orange) de même que l'IRD carbonaté de la carotte 13. Finalement, les barres grises et blanches représentent des épisodes de forte et faible productivité primaire, respectivement, causant des changements de propriétés magnétiques dans les carottes respectives.....175



## LISTE DES ABRÉVIATIONS, DES SIGLES ET DES ACRONYMES

<b>ARM</b>	<i>Anhysteretic Remanent Magnetization</i> – Aimantation rémanente anhystérétique
<b>Cal BP</b>	<i>Calendar age Before Present</i> – Âge calendaire avant le présent (avant 1950)
<b>ChRM</b>	<i>Characteristic Remanent Magnetization</i> – Aimantation rémanente caractéristique
<b>DC</b>	<i>Detrital Carbonates</i> – Carbonates détritiques
<b>DDCP</b>	<i>Double Detrital Carbonate Peak</i> – Double pic de carbonates détritiques
<b>GAD</b>	<i>Geocentric Axial Dipole</i> – Dipole axial géocentrique
<b>HBIS</b>	<i>Hudson Bay Ice Saddle</i> – Barrage de glace de la baie d’Hudson
<b>Hc</b>	<i>Coercive force</i> – Coercivité
<b>Hcr</b>	<i>Remanent coercive force</i> – Coercivité rémanente
<b>IRDs</b>	<i>Ice-Rafted Debris</i> – Débris délesté(s) par les glaces
<b>IRM</b>	<i>Isothermal Remanent Magnetization</i> – Aimantation rémanente isothermale
<b>k<sub>ARM</sub></b>	<i>Susceptibility of the Anhysteretic Remanent Magnetization</i> – Susceptibilité de l’aimantation rémanente anhystérétique
<b>k<sub>LF</sub></b>	<i>Low-field magnetic susceptibility</i> – Susceptibilité magnétique à faible champ
<b>LAO</b>	Lac Agassiz-Ojibway
<b>LC</b>	<i>Labrador Current</i> – Courant du Labrador

<b>LGM</b>	<i>Last Glacial Maximum</i> – Dernier maximum glaciaire
<b>LIS</b>	<i>Laurentide Ice Sheet</i> – Inlandsis Laurentidien
<b>MAD</b>	<i>Maximum Angular Deviation</i> – Déviation angulaire maximale
<b>MDF</b>	<i>Medium Destructive Field</i> – Champ destructif moyen
<b>MMD</b>	<i>Mass-Movement Deposit</i> – Dépôt de mouvement de masse
<b>Mrs</b>	<i>Saturation remanence</i> - Rémanence à saturation
<b>Ms</b>	<i>Magnetic moment at saturation</i> – Moment magnétique à saturation
<b>MSCL</b>	<i>Multi Sensor Core Logger</i> – Banc de mesure à multi-senseurs
<b>NRM</b>	<i>Natural Remanent Magnetization</i> – Aimantation rémanente naturelle
<b>RDL</b>	<i>Rapidly Deposited Layer</i> – Couche déposée rapidement
<b>YD</b>	<i>Younger Dryas</i> – Dryas récent





## LISTE DES SYMBOLES

$\delta^{13}\text{C}$  Delta-C-13 – Mesure du ratio des isotopes stable du carbone-13 ( $^{13}\text{C}$ ) et carbone-12 ( $^{12}\text{C}$ ) (utilisé comme traceur de provenance de la matière organique)

$\delta^{18}\text{O}$  Delta-O-18 – Mesure du ratio des isotopes stable de l'oxygène-18 ( $^{18}\text{O}$ ) et oxygène-16 ( $^{16}\text{O}$ ) (utilisé comme traceur de température)

$\Delta\text{R}$  Delta-R – Correction d'âge réservoir localisée

$^{14}\text{C}$  Carbone-14 – isotope radiogénique du carbone utilisé pour la datation radiocarbone)





## INTRODUCTION GÉNÉRALE

### 1. INTRODUCTION A LA PROBLEMATIQUE

La tendance actuelle à la réduction du volume des inlandsis de l'Antarctique et du Groenland ainsi que des glaciers de montagne soulève des questions sur les impacts de ce phénomène à court, moyen et long terme sur le niveau marin global (e.g., Alley et al., 2005 ; Rignot et al., 2011 ; Zemp et al., 2019), la circulation océanique et le climat, et par conséquent sur les écosystèmes et les populations humaines. Dans ce contexte de changement environnemental, l'étude d'épisodes de déglaciation majeure dans l'histoire géologique représente une source d'information permettant de mieux comprendre les interactions complexes entre climat, océan, cryosphère, lithosphère et biosphère, et de pouvoir anticiper les changements à venir. Lors du dernier maximum glaciaire (LGM), le plus grand inlandsis alors présent sur Terre était l'Inlandsis laurentidien. Il couvrait la majeure partie du Canada et une partie du nord des États-Unis lors de son extension maximale à environ 24 cal ka BP (Dyke et al., 2004 ; Stokes, 2017 ; Dalton et al., 2020). À la suite du LGM, à la faveur de l'augmentation de l'insolation estivale de l'hémisphère nord, la taille de l'inlandsis s'est progressivement réduite jusqu'à sa complète disparition entre 6,7 et 5,7 cal ka BP (e.g., Ullman et al., 2016 ; Dalton et al., 2020). Cette période de déglaciation ne fut cependant pas linéaire : elle fut caractérisée par d'importantes variations climatiques faisant fluctuer le taux de recul des marges de l'inlandsis, en particulier pendant les périodes froides telles que le Dryas récent ou les événements de 9,3 et 8,2 ka (e.g., Rinterknecht et al., 2014 ; Porinchi et al., 2019 ; Young et al., 2020). À la suite de leur déglaciation, les régions en périphérie de la marge transitèrent progressivement vers des conditions environnementales proches de l'actuel (e.g., de Vernal et al., 2013). Cette transition postglaciaire fut cependant accompagnée d'une transformation du paysage associée à d'importantes arrivées d'eaux de

fontes, au réajustement isostatique de la lithosphère subséquent au retrait de la glace, ou encore à la remobilisation massive de sédiments qui découle de ces processus (e.g., Lambeck et al., 2014 ; Dietrich et al., 2017 ; Rémillard et al., 2017 ; Vacchi et al., 2018 ; Bellwald et al., 2019). Ainsi, l'étude des processus sédimentaires associés à la déglaciation et à la transition postglaciaire permet d'évaluer l'impact des variations climatiques passées sur l'environnement dans un contexte de déglaciation aboutie.

Les fluctuations glaciaires passées peuvent être étudiées à l'aide des dépôts sédimentaires terrestres ou aquatiques générés par l'érosion et l'apport massif de sédiments par les glaciers. Ainsi, par exemple, les moraines sont formées par des stabilisations ou des réavancées de la marge glaciaire et sont utilisées, lorsque bien datées, pour reconstituer les positions successives de la marge et son taux de recul (e.g., Occhietti et al., 2011 ; Ullman et al., 2016 ; Margreth et al., 2017 ; Couette et al., sous presse). Par ailleurs, au cours d'une déglaciation, les lacs et les bassins sédimentaires des fjords et des marges continentales sont les réceptacles de quantités importantes de sédiments charriés par les glaciers et les eaux de fonte et pouvant former des séquences de plusieurs centaines de mètres d'épaisseur (e.g., Duchesne et al., 2007 ; St-Onge et al., 2008 ; Hjelstuen et al., 2009 ; MacLean et al., 2001 ; Poiré et al., 2018). Les variations chimiques et physiques des sédiments nous renseignent non seulement sur la dynamique de recul de la marge glaciaire (e.g., Hall et al., 1999; Lévesque et al., 2020), mais également sur les changements environnementaux tels que les variations de température ou de salinité des eaux (e.g., Moros et al., 2004 ; Caron et al., 2019a; Allan et al., 2021), les courants marins (e.g., McCave et al., 2017; Deschamps et al., 2019; Hoffmann et al., 2019), ou les conditions régionales de températures et de précipitations (e.g., Quillman et al., 2010; Richerol et al., 2016). En outre, les bassins sédimentaires peuvent contenir d'épais dépôts formés par des processus paraglaciers : des processus non glaciaires mais conditionnés par la présence passée de glace, qui jouent un rôle majeur dans la dynamique sédimentaire au cours de la transition postglaciaire (e.g., Syvitski & Praeg, 1989 ; Stoker et al., 2010 ; Dietrich et al., 2017). Ces dépôts peuvent prendre plusieurs formes, tels que des mouvements de masse (MMD), des turbidites ou des hyperpycnites qui peuvent témoigner de mouvements gravitaires, d'aléas sismiques, ou

encore de crues ou de vidanges de lacs d'origine glaciaire (e.g., St-Onge et al., 2004, 2012 ; Mulder et Chapron, 2010 ; Broom et al., 2017 ; Duboc et al., 2017 ; Bellwald et al., 2019). Ainsi, l'étude des variations chimiques et physiques des sédiments permet d'établir un cadre chronologique et stratigraphique qui forme la base pour reconstruire l'histoire environnementale régionale et locale pendant la transition postglaciaire jusqu'à des conditions modernes.

Dans le cas de la marge continentale du détroit d'Hudson et du Labrador, dans l'est du Canada, la transition postglaciaire s'effectue surtout après « l'événement de 8,2 ka », le plus important événement climatique de l'Holocène (11,7 cal ka BP – aujourd'hui). Cet événement froid d'une durée d'environ 160 ans et très marqué dans les enregistrements paléoclimatiques de l'hémisphère nord aurait été causé par l'arrivée massive d'eau douce dans l'Atlantique Nord, perturbant la circulation de retournement méridionale de l'Atlantique (AMOC) (Alley et al., 1997 ; von Grafenstein et al., 1998 ; Barber et al., 1999 ; Thomas et al., 2007). L'eau douce en question proviendrait de la vidange catastrophique du lac proglaciaire Agassiz-Ojibway (LAO) et de la chute du barrage de glace de la baie d'Hudson qui le séparait des eaux de la baie (Barber et al., 1999 ; Lajeunesse et St-Onge, 2008 ; Roy et al., 2011 ; Matero et al., 2017 ; Lochte et al., 2019a ; Brouard et al., 2021). Cependant, les études ne s'accordent pas toutes sur les différentes étapes menant à cet événement ainsi que sur leur chronologie (e.g., Jennings et al., 2015 ; Lochte et al., 2019a ; Brouard et al., 2021). En effet, seulement quelques siècles se sont écoulés entre l'ouverture de la mer de Tyrrell (ancêtre de la baie d'Hudson) et le drainage du LAO, ce qui peut générer un amalgame d'interprétations des indicateurs des différents événements dans les enregistrements de faible résolution (Jennings et al., 2015). En outre, cet amalgame peut être favorisé par la difficulté d'estimer l'âge réservoir du  $^{14}\text{C}$ , sur lequel sont majoritairement basées les chronologies. En effet, les variations du couvert de glace et des apports d'eau de fonte appauvrie en  $^{14}\text{C}$  peuvent faire varier l'âge réservoir local de plusieurs centaines d'années entre la période de déglaciation et l'actuel (e.g., Vickers et al., 2010 ; Lewis et al., 2012 ; Lochte et al., 2019a). L'analyse de nouveaux enregistrements sédimentaires à haute résolution provenant de la région du système de la baie d'Hudson serait donc bénéfique pour apporter de nouvelles

précisions chronostratigraphiques sur l'événement majeur qu'est la fin du LAO. De plus, la reconnaissance de marqueurs sédimentaires identiques d'un secteur à l'autre pourrait permettre de quantifier les différences d'âge réservoir entre lesdits secteurs à un même moment.

Une étude chronologiquement détaillée de séquences sédimentaires à haute résolution peut donc aider à mieux comprendre la dynamique sédimentaire résultant de la déglaciation et de la transition postglaciaire qui suit. Dans le cas de la présente thèse, la marge continentale du détroit d'Hudson et du Labrador est investiguée au travers de secteurs clés diversifiés autant par leurs localisations que par leurs contextes physiographiques : l'ouest du détroit d'Hudson, les fjords Nachvak et Saglek au nord du Labrador, et enfin le lac estuarien Melville au sud du Labrador (Fig. 1). De façon générale, ces zones ont été choisies pour leurs bassins contenant d'épaisses séquences sédimentaires qui ont le potentiel de couvrir l'Holocène avec une haute résolution temporelle. Tout d'abord, les fjords Nachvak et Saglek ont la particularité d'avoir été influencés à la fois par le recul de la marge glaciaire locale et par les eaux de la marge continentale (Bell & Josenhans, 1996 ; Brown et al., 2012 ; Richerol et al., 2016). Par ailleurs, bien que les formations glaciaires terrestres du secteur du fjord Saglek ont fait l'objet de plusieurs investigations (Ives, 1957, 1976 ; Clark, 1988 ; Clark et al., 2003), aucune étude ne s'est intéressée à la séquence quaternaire des bassins de ce fjord. Pourtant, la grande taille du fjord Saglek et de son bassin de drainage, de même que sa localisation septentrionale, en font un candidat de choix pour une étude holocène à haute résolution. Quant au Lac Melville, sa localisation à l'intérieur des terres fait de lui un secteur clé pour mieux préciser la dynamique de recul de la marge glaciaire dans le sud du Labrador (e.g., Vilks & Mudie, 1983 ; Syvitski & Lee, 1997 ; Couette et al., sous presse). En outre, bien que de longues carottes sédimentaires aient déjà été prélevées dans ces différents secteurs (outre le fjord Saglek), leurs chronologies holocènes étaient souvent imprécises ou incomplètes, soit par le manque de dates, soit par la quasi-absence de séquence postglaciaire (e.g., Vilks & Mudie, 1983 ; MacLean et al., 2001 ; Haberzettl et al., 2010). Ainsi, de nouvelles données seraient bénéfiques pour améliorer les connaissances sur les chronostratigraphies locales. De plus, les bassins du détroit d'Hudson ont le potentiel d'avoir enregistré plus précisément les



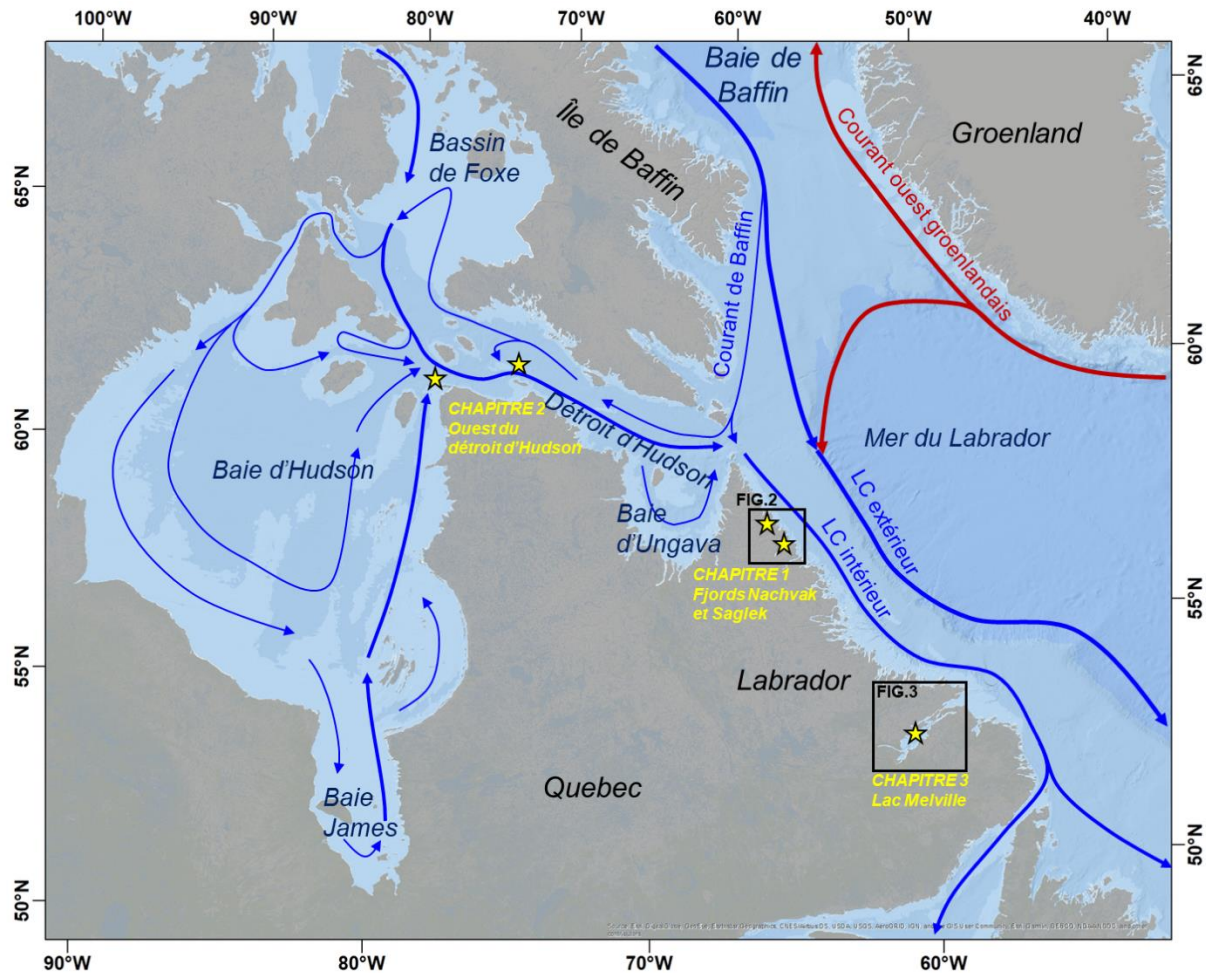
événements de la déglaciation de la baie d'Hudson. En outre, une couche de sédiments fins rouges riches en hématite et associée à la vidange du LAO a déjà été observée dans des carottes provenant de ces bassins (Kerwin, 1996 ; St-Onge & Lajeunesse, 2007 ; Haberzettl et al., 2010) de même que sur la marge continentale du Labrador (Jennings et al., 2015 ; Lochte et al., 2019a).

Le but de cette thèse est donc de contribuer à la compréhension des processus sédimentaires affectant différents environnements de la marge continentale allant du détroit d'Hudson au sud du Labrador dans un contexte de déglaciation. Cette recherche se base notamment sur une analyse multi-traceurs de longues carottes sédimentaires couvrant la majeure partie de l'Holocène, combinée à des profils acoustiques de sous-surface et, pour certains sites, des données multifaisceaux. Précisément, la période temporelle d'intérêt s'étale approximativement de 9,5 à 6,0 ka cal BP, et englobe la fin du retrait de l'Inlandis laurentidien ponctuée par les événements froids de 9,3 et 8,2 ka, ainsi que la transition postglaciaire dans cette région.

Dans les sections ci-dessous sont présentés la région d'étude incluant les différents secteurs, ainsi que le contexte quaternaire et sédimentaire de la région. S'ensuivent une description détaillée des objectifs de la thèse et le détail de la méthodologie employée, avant de terminer avec la présentation de l'organisation de la thèse.

## **2. REGION D'ETUDE**

Les sites d'intérêt pour la présente étude sont dispersés de la baie d'Hudson au plateau continental du Labrador (Fig. 1). Ils se retrouvent dans trois secteurs aux contextes physiographiques et océanographiques distincts, soit celui de la baie et du détroit d'Hudson, celui des fjords Nachvak et Saglek, et enfin celui du lac Melville, les deux derniers secteurs étant directement connectés au plateau continental du Labrador.



**Figure 1.** Carte de la région d'étude avec un aperçu de la circulation océanique régionale, inspirée de Stewart & Howland (2009) et de Lochte et al. (2019b). Les flèches rouges indiquent les courants plus chauds. Les étoiles jaunes indiquent la localisation des carottes sédimentaires analysées dans cette thèse, dans les 3 secteurs correspondant aux chapitres (titres en jaune). LC : courant du Labrador.

## 2.1 La baie et le détroit d'Hudson

La baie et le détroit d'Hudson font partie du « système de la baie d'Hudson » qui inclut également la baie James, le bassin de Foxe et la baie d'Ungava (Straneo & Saucier, 2008b). Ce système peut se comparer à une mer intérieure et est uniquement connecté à l'archipel

Arctique au nord-ouest par les détroits de Fury et de Hecla au nord du bassin de Foxe, et à la mer du Labrador à l'est par le détroit d'Hudson (Prinsenbergh, 1986 ; Saucier et al., 2004). Malgré sa notable superficie de 841 000 km<sup>2</sup>, la baie d'Hudson a une profondeur moyenne de seulement 150 m et une bathymétrie relativement plane (Saucier et al., 2004 ; Kuzyk et al., 2009). Elle débouche au nord-est sur le détroit d'Hudson, de 800 km de longueur dans l'axe est-ouest et 90 km de large et dont la bathymétrie en forme de U varie généralement entre 200 et 400 m (Drinkwater, 1986 ; Andrews & MacLean, 2003). Le détroit d'Hudson comprend trois bassins profonds formés par des structures en demi-graben parallèles à son axe principal : deux bassins à l'ouest (nommés informellement bassins Sud-Ouest et Ouest) d'une profondeur d'environ 400-500 m, et un bassin à l'est (le bassin Est) atteignant 900 m de profondeur et dont la limite orientale est un seuil de 400 m de profondeur marquant la limite avec la mer du Labrador (MacLean, 2001 ; Andrews & MacLean, 2003).

En baie d'Hudson, les eaux provenant du bassin de Foxe au nord se mélangent aux eaux fluviales en une circulation antihoraire qui s'évacue vers le détroit d'Hudson (Prinsenbergh, 1986). Dans celui-ci, des eaux profondes salées atlantiques entrent par la mer du Labrador à l'est et se mélangent avec les eaux plus douces provenant du bassin de Foxe et des baies d'Hudson et d'Ungava. Le tout résulte en une circulation majoritairement ouest-est, malgré une plus faible circulation est-ouest le long de la côte nord alimentée par le courant de Baffin. Dans le détroit d'Hudson, les marées sont importantes avec une amplitude moyenne de 3 à 6 mètres et des courants variant de 0,20 à 1 m/s, et favorisent une bonne homogénéisation de la colonne d'eau (Drinkwater, 1988 ; Hill et al., 2011).

## **2.2 Le plateau continental et la côte du Labrador**

Le plateau continental du Labrador s'étend sur 200 km au large du Labrador et est creusé sur toute sa longueur par un chenal de 500-800 m de profondeur (la cuvette marginale du Labrador) qui le divise en un plateau intérieur et un plateau extérieur. Le plateau intérieur, constitué de roches cristallines précambriennes, a une profondeur inférieure à 200 m, tandis

que le plateau extérieur est composé de roches sédimentaires phanérozoïques incisées par de nombreux chenaux et ravins nommés « *saddle* » (Josenhans et al, 1986 ; Vilks et al., 1987 ; Shaw et al., 2014). La côte du Labrador se caractérise par la présence de nombreux fjords excavés par les glaciers dans les roches précambriennes du bouclier canadien lors des successions de périodes glaciaires. Dans les montagnes Torngat au nord, où sont situés les fjords Nachvak et Saglek, le dénivelé est particulièrement élevé entre des bassins de 300 m de profondeur et des flancs de montagnes atteignant 1000 m de hauteur, tandis que la côte centrale et sud est dominée par des bras de mer qualifiés de « fjards » à la topographie plus irrégulière avec des bassins moins profonds et une large zone intertidale (Engstrom & Hansen, 1985 ; Brown et al., 2012). C'est là qu'est situé le bras de mer Hamilton qui mène au lac Melville.

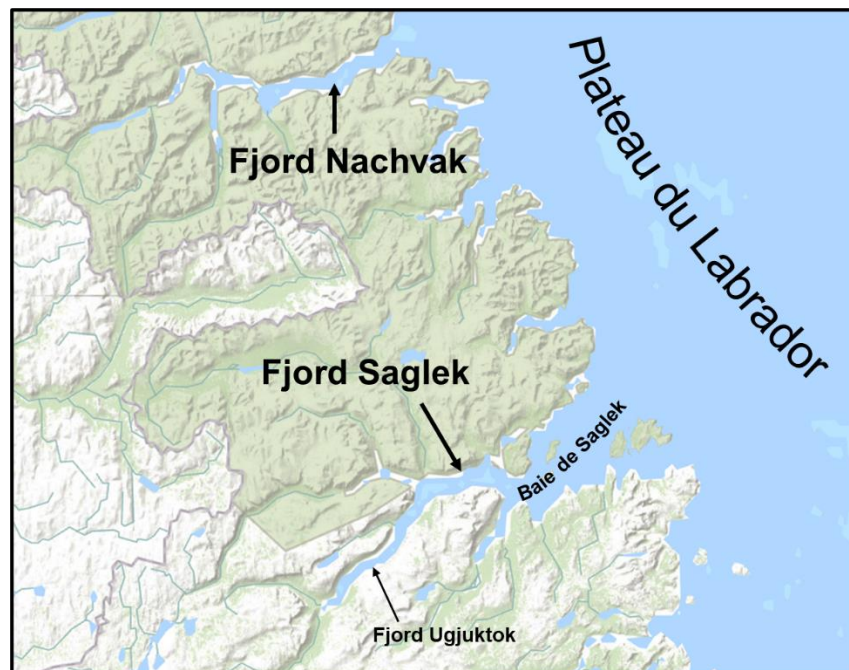
Le long du Labrador, le courant du Labrador (LC) s'écoule en direction sud-est et se divise en deux branches. La branche interne, peu profonde, et centrée sur le plateau continental, est surtout formée des eaux plus douces et plus froides provenant de la baie de Baffin et du détroit d'Hudson. Plus à l'est, le long du talus continental, la branche externe du LC charrie les eaux atlantiques plus chaudes et plus salées venant d'une partie du courant ouest groenlandais (Straneo & Saucier, 2008a ; Lochte et al., 2019b).

### 2.2.1 Les fjords Nachvak et Saglek

Les fjords Nachvak et Saglek sont deux fjords échancrés dans les roches gneissiques précambriennes des monts Torngat au nord du Labrador (Fig. 2). Ils ont la morphologie typique des longs fjords efflanqués de hautes montagnes et sont divisés en profonds bassins creusés par les anciens glaciers et séparés par des seuils (Bell & Josenhans, 1997; Brown et al., 2012). Le fjord Nachvak, long d'environ 45 km et large de 2 à 4 km, est composé de quatre bassins allant de 90 à 210 m de profondeur séparés par des seuils profonds de 10 à 180 m. Son bassin extérieur, le plus profond, est directement relié à la mer du Labrador dont il est séparé par un seuil d'environ 50 m. Un peu plus large, le fjord Saglek est long de 65

km et son bassin extérieur atteint plus de 300 m de profondeur (Bastick, 2009; Bentley & Kahlmeyer, 2012). Il est poursuivi au sud-ouest dans les terres par le fjord Ugjuktok, plus étroit, et ouvre à l'est sur la baie de Saglek qui le sépare de la mer du Labrador.

Dans les fjords, les marées ont une amplitude atteignant 2 m et montrent d'importantes vitesses tidales, favorisant un bon échange d'eau entre leurs bassins et la marge continentale du Labrador. La colonne d'eau s'en retrouve bien mélangée et le fond des bassins ne montre pas de déficit d'oxygène (Bentley & Kahlmeyer, 2012; Brown et al., 2012).

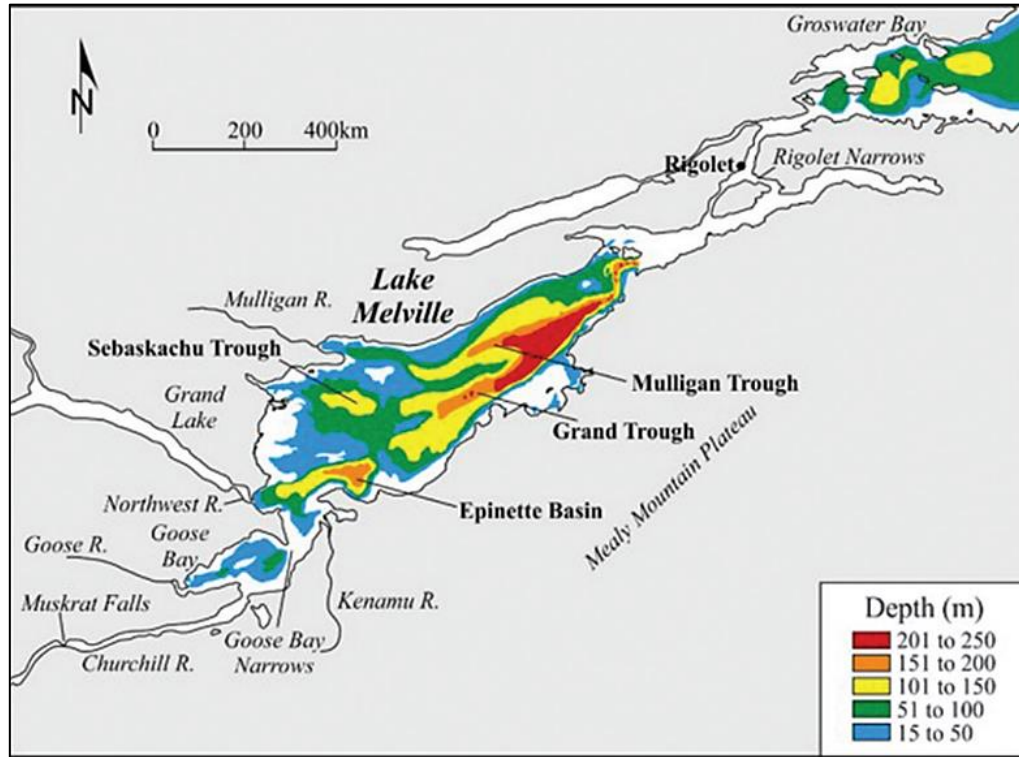


**Figure 2.** Carte topographique de la région des fjords Nachvak et Saglek. La zone en vert correspond au parc national des monts Torngats.

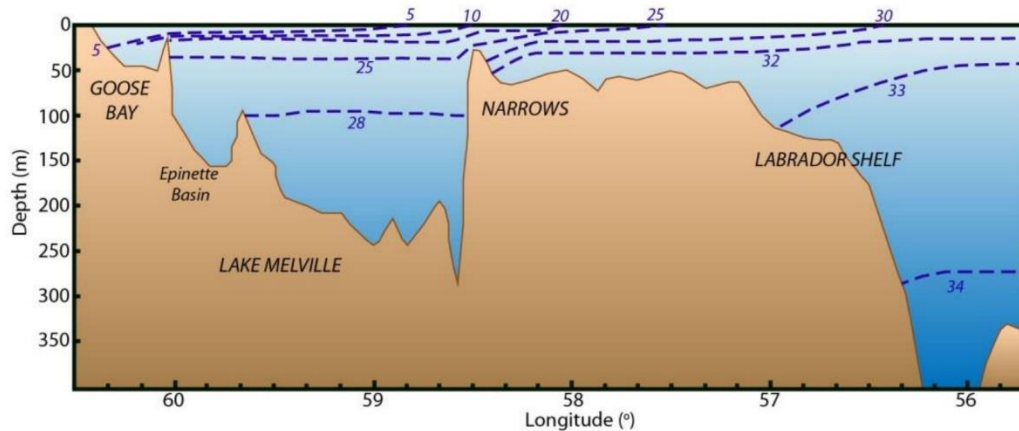
### 2.2.2 Le lac Melville

Le lac Melville est un lac estuarien pouvant être qualifié de fjord et situé dans le système du bras de mer Hamilton qui s'étend sur 250 km dans les terres, creusé dans des roches intrusives et métamorphiques de la province géologique du Grenville (Vilks & Mudie,

1983 ; Vilks et al., 1987 ; Brown et al., 2012). La topographie régionale est plutôt basse, à l'exception de la rive sud surplombée par les monts Mealy. La bathymétrie du lac Melville est en général inférieure à 100 m, mais est caractérisée par la présence de quatre chenaux profonds dont les deux plus grands coalescent vers l'est pour former un bassin de 250 m de profondeur (Fig. 3). La limite orientale du lac est marquée par un seuil de seulement 28 m de profondeur, au-delà duquel un long passage étroit nommé littéralement les Narrows et profond de 50 m, mène à la baie Groswater et au plateau continental. Le lac Melville reçoit environ 94 km<sup>3</sup> d'eau douce par année en provenance de cinq rivières, notamment les rivières Churchill et Goose qui donnent sur la baie Goose au sud-ouest du lac (Syvitski & Lee, 1997; Kamula et al., 2017). Cet intrant majeur d'eau douce engendre une forte stratification du lac avec une couche de surface peu salée s'écoulant vers l'est (~10 psu), et des eaux de fond plus salées venant de la mer du Labrador. Cependant, le seuil peu profond empêche les eaux de plus de 30 psu d'entrer dans le lac (Fig. 4), évitant ainsi une stagnation des eaux de fond (Vilks & Mudie, 1983).



**Figure 3.** Bathymétrie du bras de mer Hamilton incluant la baie Goose, le lac Melville et la baie Groswater. Tiré de Kamula et al. (2017).



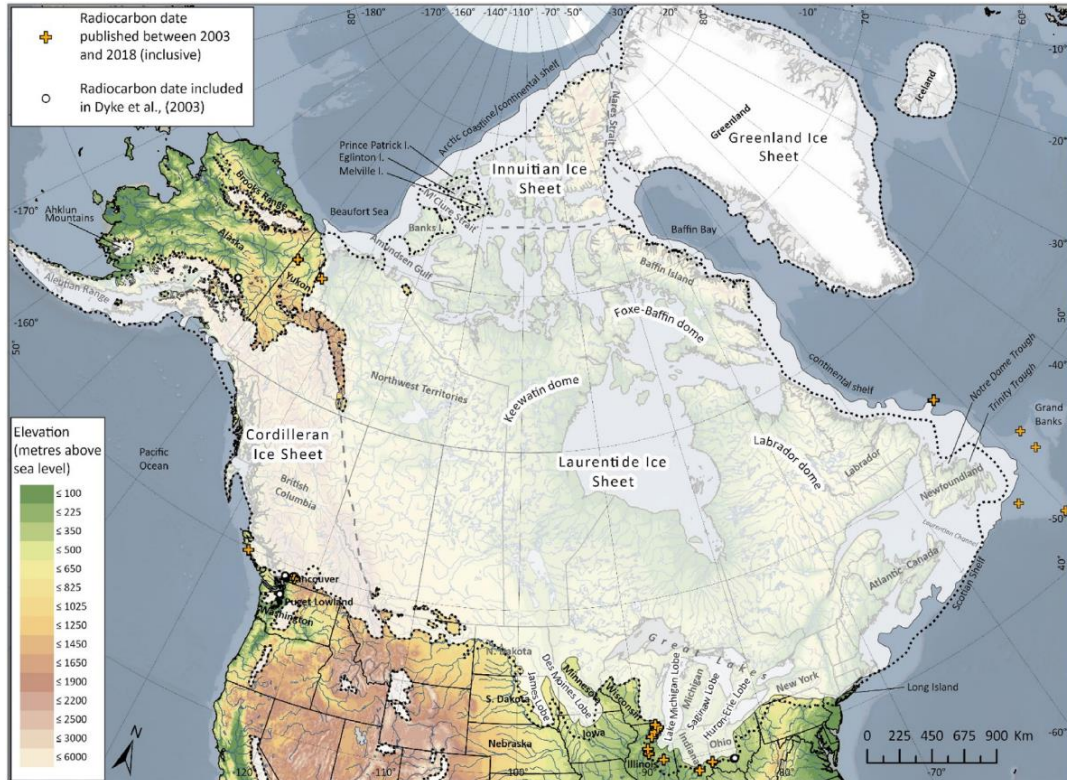
**Figure 4.** Salinité en fonction de la profondeur du bras de mer Hamilton et du plateau du Labrador. Modifié de Vilks & Mudie (1983)

### 3. CONTEXTE QUATERNAIRE ET SEDIMENTAIRE

#### 3.1 Retrait de l’Inlandsis laurentidien

L’Inlandsis laurentidien aurait atteint son extension maximale vers 25-24 ka cal BP, et était alors fusionné avec l’Inlandsis de la Cordillère à l’ouest et l’Inlandsis Inuit au nord, lui-même relié à l’Inlandsis du Groenland par le détroit de Nares (Fig. 5 ; Dyke, 2004 ; Stokes, 2017 ; Dalton et al., 2020). L’Inlandsis laurentidien avait alors une épaisseur de glace allant jusqu’à 3,5 km, et était constitué de trois dômes principaux : le dôme de Keewatin à l’ouest, celui de Foxe-Baffin au nord et celui du Labrador à l’est. Au milieu de ces dômes se situait l’actuelle baie d’Hudson, et le détroit d’Hudson était occupé par le plus important et le plus rapide des courants glaciaires de l’inlandsis (Tarasov et al., 2012 ; Margold et al., 2018). Les études ont longtemps débattu de l’extension orientale de l’inlandsis au LGM, mais un consensus affirme que la glace atteignait la rupture de pente du plateau continental autant en baie de Baffin qu’en mer du Labrador (e.g. Margold et al., 2018 ; Dalton et al., 2020 ; Lévesque et al., 2020).





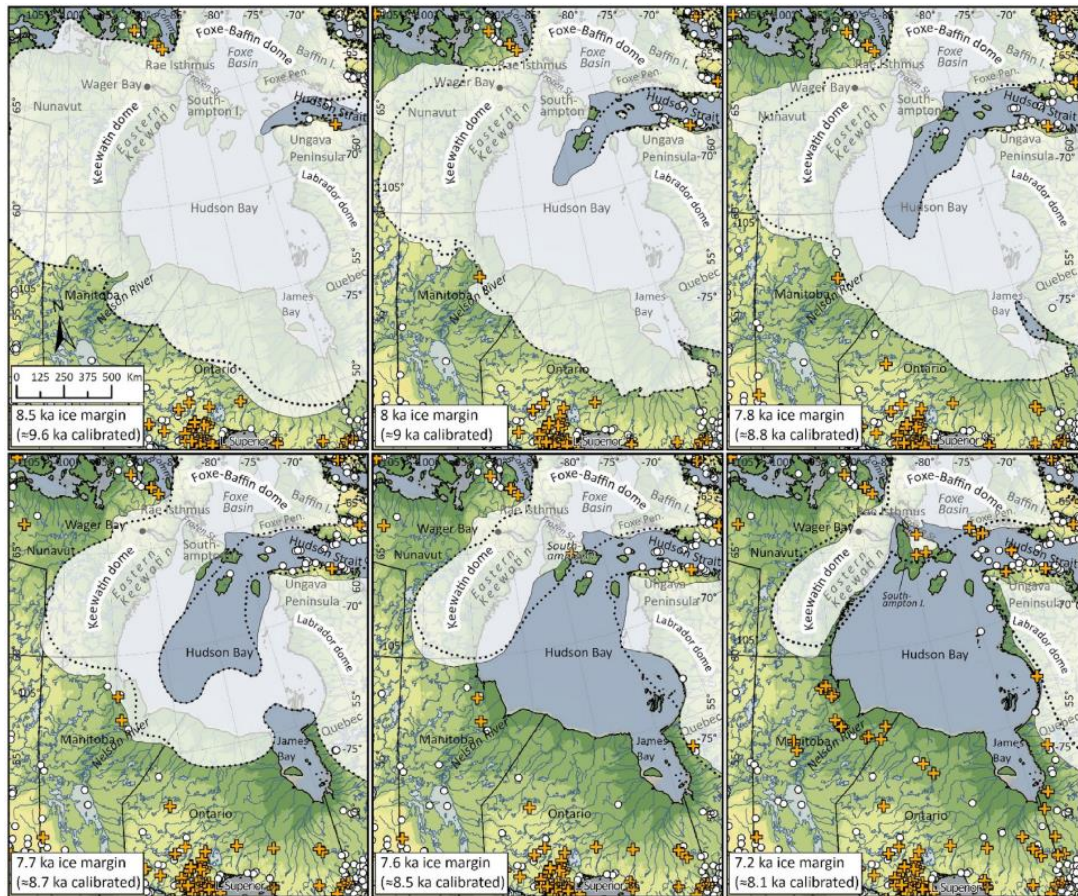
**Figure 5.** Carte de l’extension maximale des inlandsis en Amérique du Nord au LGM (18 ka, ou 21,7 cal ka BP), avec localisation des dômes de Keewatin, de Foxe-Baffin et du Labrador. La ligne en pointillés correspond à la limite du LIS proposée par Dyke et al., (2004). Tiré de Dalton et al (2020).

Le LIS a ensuite commencé son retrait progressif vers 21,5 cal ka, tout d’abord dans les secteurs méridionaux. À l’est, il y a peu d’évidences de recul des marges glaciaires avant 17.0 cal ka BP, à l’exception du golfe du Saint-Laurent qui a commencé à s’ouvrir dès 20,0 cal ka BP (Rémillard et al., 2016). La déglaciation s’est accélérée au cours de la période chaude du Bølling-Allerød (14,7-12,9 cal ka BP) au cours de laquelle le golfe et l’estuaire maritime du Saint-Laurent se sont très vite retrouvés entièrement libres de glace (Shaw et al., 2006 ; Occhietti et al., 2011 ; Rémillard et al., 2016). À l’ouest et au sud, l’importante fonte du LIS a entraîné la formation de grands lacs proglaciaires dont les lacs Agassiz et Ojibway vers 14 et 11-10 cal ka BP respectivement. Le brusque drainage d’une partie du lac Agassiz,

possiblement vers l'Arctique canadien par la vallée du Mackenzie au nord-ouest, aurait alors contribué à déclencher la période froide du Dryas récent (12,8-11,7 cal ka BP ; Murton et al., 2010 ; Deschamps et al., 2018 ; Norris et al., 2021). Pendant cette période, les marges glaciaires ont généralement stagné, voir avancé, ralentissant la perte de volume du LIS (Shaw et al., 2006 ; St-Onge et al., 2008 ; Dietrich et al., 2017).

Par la suite, le réchauffement du début de l'Holocène accéléra le retrait de la marge glaciaire dans les fjords de l'est du Canada et dans le détroit d'Hudson. Ce recul a été interrompu à plusieurs reprises lors des événements froids de 10,3, 9,3 et 8,2 ka (Ullman et al., 2016 ; Young et al., 2020 ; Couette et al., 2023). Au Labrador, la marge continentale était a priori libre de glace dès 12,0 cal ka BP (Hall et al., 1999) et le fjord Nachvak dès 10,3 cal ka BP (Gallagher, 1989). Dans le lac Melville, une baie de vélage s'est formée vers 11,0 cal ka BP et a persisté jusqu'à environ 8,2-8,4 ka cal BP quand une stagnation de la marge glaciaire a formé la moraine de Sebaskachu à l'ouest du lac (King, 1985 ; Syvitski & Lee, 1997 ; Couette et al., sous presse). Plus au nord, la marge glaciaire du dôme du Labrador a retraversé deux fois le détroit d'Hudson jusqu'à l'île de Baffin : lors des épisodes de Gold Cove et de Noble Inlet au cours des événements de 10,3 et 9,3 ka respectivement (Kaufman et al., 1993 ; Jennings et al., 1998, 2015). L'influence des eaux chaudes de l'Atlantique a ensuite accéléré le retrait du courant glaciaire du détroit d'Hudson qui a laissé place à une baie de vélage dans la baie d'Hudson, formant la mer de Tyrrell (Fig. 6 ; Hillaire-Marcel, 1977 ; Jennings et al., 2015 ; Lochte et al., 2019a). Le LAO, combinaison des lacs Agassiz et Ojibway, s'est alors retrouvé séparé de cette mer par le mince barrage de glace de la baie d'Hudson qui formait le dernier lien entre les dômes du Keewatin et du Labrador (Roy et al., 2011 ; Lochte et al., 2019a). S'en est suivie la vidange du LAO en plusieurs étapes successives, impliquant également la désintégration du barrage de glace, qui ont mené à l'événement froid de 8,2 ka (Barber et al., 1999 ; Lochte et al. 2019a ; Gauthier et al., 2020). Après cela, le dôme du Labrador a rapidement perdu en superficie et a disparu quelque part entre 6,7 et 5,7 cal ka BP (e.g. Dyke et al., 2004 ; Ullman et al., 2016 ; Dalton et al., 2020). La fin de la fonte du LIS a cependant favorisé la présence d'une lentille d'eau douce très tard dans la mer du Labrador (Weiser et al., 2021). Ceci aurait retardé le début du maximum

thermal de l'Holocène (HTM) dans la région allant de l'est de la baie d'Hudson au sud du Groenland : il aurait débuté entre 7,0 et 6,4 cal ka BP, comparativement à avant 8,0 cal ka BP dans le reste de l'Arctique (Kaufman et al., 2004 ; McCave et al., 2019).



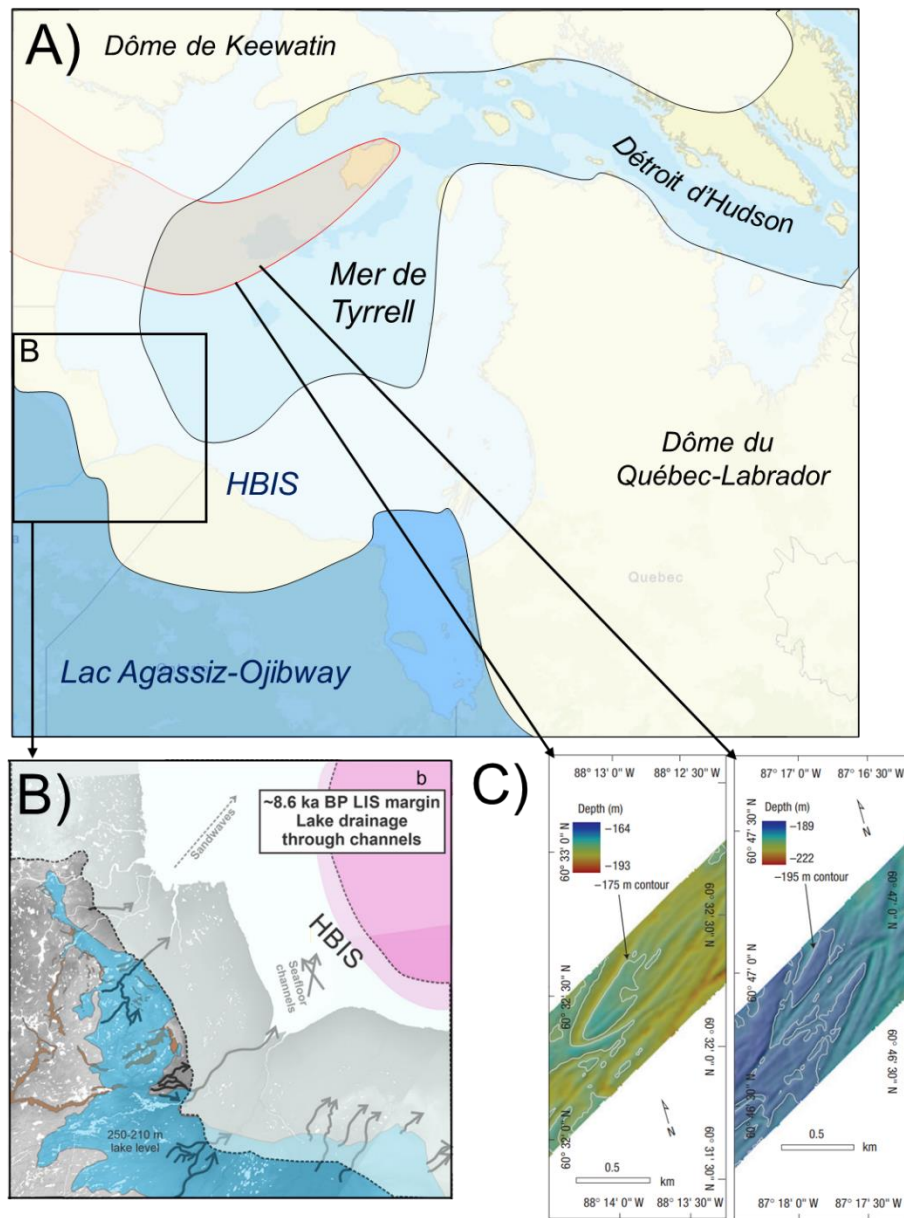
**Figure 6.** Évolution de l'extension du LIS dans la région du système de la baie d'Hudson entre 8,5 et 7,2  $^{14}\text{C}$  ka BP (9,6 et 8,1 cal ka BP). La ligne en pointillés correspond à la limite du LIS proposée par Dyke et al., (2004). Tiré de Dalton et al (2020).

### 3.2 L'événement de 8.2 ka

Dans les années 1980 et 1990, des carottes de glace du Groenland ont révélé la présence d'une période froide particulièrement marquée aux alentours de 8,2 ka (Alley et al., 1997),

qui fut ensuite corrélée à d'autres indicateurs de changement climatiques à travers l'hémisphère nord (e.g. Baldini et al., 2002 ; Weninger et al., 2006 ; Lutz et al., 2007 ; Hormes et al., 2009). Cette anomalie a été associée à un ralentissement de l'AMOC, causé par un important apport d'eau douce dans l'Atlantique Nord lors de la vidange du LAO (Barber et al., 1999 ; Clark et al., 2001). Cet événement a été relié à la présence d'une couche de silt argileux rouge trouvée dans des carottes prélevées dans le détroit d'Hudson et datée à  $8,47 \pm 0,30$  cal ka BP (Kerwin, 1996). Ce sédiment fin rouge riche en hématite proviendrait d'erratiques d'origine glaciaire localisés dans le nord-ouest de la baie d'Hudson (Fig. 7A ; Shilts, 1980) et qui auraient été dispersés lors la dernière vidange du LAO jusqu'en mer du Labrador (Barber et al., 1999 ; St-Onge et al., 2007 ; Jennings et al., 2015). Des indicateurs, tels que des dunes de sable dans le sud de la baie d'Hudson ou des chenaux sous-marins, ont ensuite permis de suggérer que le LAO a subi un ou plusieurs drainages sous-glaciaires avant l'événement final, théorie ensuite appuyée par des modèles (Fig. 7B ; Hillaire-Marcel et al., 2007 ; St-Onge & Lajeunesse, 2007 ; Lajeunesse & St-Onge, 2008). Certains modèles suggèrent que la fonte du barrage de glace de la baie d'Hudson aurait largement contribué à la perturbation de l'AMOC en générant des armadas d'icebergs (Matero et al., 2017 ; Lochte et al., 2019a), qui ont d'ailleurs laissé des traces sur le fond de la baie (Fig. 7C ; Lajeunesse & St-Onge, 2008). Malgré cela, les études ne s'accordent toujours pas sur la chronologie des différents indicateurs et événements. En effet, certaines études prônent un drainage final aux alentours de 8,45-8,55 cal ka BP (Barber et al., 1999 ; Lochte et al., 2019a). Dalton et al. (2020) eux-mêmes ont conservé les isochrones de Dyke et al. (2004) impliquant la fin du LAO avant 8,5 cal ka BP. D'autres études favorisent plutôt la théorie d'un événement final proche de 8,2 cal ka BP, avec une dispersion du sédiment rouge lors de l'ouverture de la mer de Tyrrell (Jennings et al., 2015 ; Brouard et al., 2021) ou lors d'un événement de drainage sous-glaciaire suivant celle-ci (Gauthier et al., 2020). En effet, la couche a été plus récemment datée à  $8,55 \pm 0,06$  cal ka BP (Jennings et al., 2015). Finalement, Brouard et al., (2021) ont compilé et recalibré des centaines d'âges  $^{14}\text{C}$  qui, combinés aux séquences de varves du lac Ojibway (Godbout et al., 2019, 2020), suggèrent deux drainages à quelques décennies d'intervalles entre 8,22 et 8,15 cal ka BP.





**Figure 7.** A) Extension approximative de l’Inlandsis laurentidien avant le drainage final du LAO et la chute du barrage de glace de la baie d’Hudson. La zone rouge représente la zone couverte par les erratiques rouges d’où provient le sédiment de la couche rouge du détroit d’Hudson. B) Carte de la position de la marge glaciaire et de l’ouest du LAO au nord du Manitoba lors d’un éventuel drainage sous-glaciaire à environ 8,6 cal ka BP. Les flèches ondulées indiquent la position probable des chenaux de drainage. La position de dunes et de chenaux sous-marins associés au drainage sont également indiqués (Tiré de Gauthier et al., 2020). C) Cicatrices arquées laissées par des icebergs sur le fond de la baie d’Hudson lors de la vidange finale du LAO (Tiré de Lajeunesse & St-Onge, 2008).

### 3.3 Séquence sédimentaire quaternaire sous-marine

Les séquences sédimentaires formées pendant et après le retrait de la marge glaciaire comprennent généralement des sédiments de contact glaciaire, glaciomarins (proximaux et distaux), paraglaciaires et postglaciaires (Syvitski, 1991). Les sédiments de contact glaciaire sont déposés directement en contact avec le glacier et constituent souvent la plus grande partie des séquences quaternaires (Syvitski & Praeg, 1989 ; MacLean et al., 2001). Lorsque la marge glaciaire commence à s'éloigner, les sédiments délivrés par la glace sont mieux triés : les particules plus grossières s'accumulent à proximité de la glace tandis que les plus fines sont transportés par suspension (Syvitski, 1991). Ces processus forment des dépôts glaciomarins proximaux et distaux pouvant être différenciés et qui informent sur l'évolution du recul de la marge glaciaire. Lorsque la marge glaciaire se retrouve sur terre, les eaux de fonte perpétuent cette dynamique sédimentaire par l'action fluvioglaciaire. En outre, plusieurs processus paraglaciaires peuvent être responsables de l'apport de grandes quantités de sédiments. Le terme paraglaciaire englobe tous les phénomènes non-glaciaires qui sont cependant conditionnés par la présence passée de glace (Syvitski & Praeg, 1989 ; Mercier, 2007). Il peut s'agir de mouvements de masse générés par des processus gravitaires ou des aléas sismiques associés au rebond isostatique, ou encore la remobilisation de sédiments glaciaires par des eaux fluviales (e.g., Stoker et al., 2010 ; Dietrich et al., 2017 ; Bellwald et al., 2019). D'un point de vue sédimentaire, la transition postglaciaire correspond donc à l'évolution de l'environnement glaciomarin vers des conditions postglaciaires, et s'accompagne souvent de processus paraglaciaires causés par l'ajustement de l'environnement suivant le retrait de la glace. Cette transition se termine quand les conditions environnementales et la dynamique sédimentaire sont proches de l'actuel.

Sur la marge continentale allant de la baie d'Hudson au sud du Labrador, la stratigraphie quaternaire se résume souvent à une épaisse séquence de sédiments de contact glaciaire recouverte d'une beaucoup plus fine épaisseur de sédiments postglaciaires (e.g., Syvitski & Praeg, 1989 ; MacLean et al., 2001 ; St-Onge et al., 2008 ; Shaw et al., 2014). En baie d'Hudson, par exemple, la plus grande partie du plancher est couverte de till, et les

séquences sédimentaires complètes sont surtout localisées près des côtes où la dynamique sédimentaire postglaciaire est contrôlée par les apports fluviaux (Stewart and Lockhart, 2005 ; Haberzettl et al., 2010). Dans le détroit d’Hudson et sur la marge du Labrador, les forts courants postglaciaires ont lessivé les sédiments glaciomarins, et la séquence postglaciaire type consiste souvent en un pavage de sédiments grossiers de quelques dizaines de centimètres d’épaisseur (MacLean et al., 2001 ; Shaw et al., 2014). Les bassins, en revanche, contiennent des séquences complètes dont l’épaisseur atteint des dizaines voire des centaines de mètres. C’est le cas des trois principaux bassins du détroit d’Hudson et des *saddles* de la marge externe du Labrador où ont déjà été récoltées plusieurs carottes sédimentaires couvrant une partie de l’Holocène (e.g. MacLean et al., 2001 ; Haberzettl et al., 2010 ; Shaw et al., 2014 ; Jennings et al., 2015 ; Rashid et al., 2017 ; Lochte et al., 2019a, 2019b). Les fjords du Labrador et le lac Melville sont aussi d’importants réceptacles de sédiments et en contiennent plusieurs centaines de mètres déposés par et après le retrait des marges glaciaires locales (e.g., Bell & Josenhans, 1997 ; Syvitski & Lee, 1997). Ces milieux sont cependant propices aux processus paraglaciers, en particulier les mouvements de masse, pouvant acheminer d’importants volumes de sédiments en peu de temps dans les bassins des fjords (e.g. Bellwald et al., 2019 ; Syvitski et al., 2022).

#### **4. OBJECTIFS DE LA THESE**

Cette thèse a pour objectif général de **préciser la chronostratigraphie des dépôts et processus sédimentaires associés à la déglaciation de l’Inlandsis laurentidien et de la subséquente transition postglaciaire sur la marge continentale le long du Labrador et dans le détroit d’Hudson**. L’étude se base principalement sur l’analyse multi-traceurs de longues carottes sédimentaires provenant des trois secteurs (ouest du détroit d’Hudson, fjords Nachvak et Saglek et enfin le lac Melville). L’interprétation de données géophysiques aideront à analyser la séquence stratigraphique complète. Par cela même, il sera possible de comparer les séquences des trois secteurs en termes de propriétés, de chronologie et de dynamique sédimentaire. Plus concrètement, les objectifs spécifiques de cette thèse sont de :

- Préciser l'évolution du retrait de la marge glaciaire de l'Inlandsis laurentidien au Labrador et dans le détroit d'Hudson à partir de l'étude des séquences sédimentaires des bassins des différents secteurs. Qu'indiquent ces séquences sur le patron de retrait de chaque secteur ? Quels liens chronologiques peuvent être faits avec les moraines terrestres locales et régionales ? Au nord du Labrador, les fjords Nachvak et Saglek ont-ils expérimenté une déglaciation similaire et synchrone ? Comment la physiographie des différents secteurs influence le recul local ? Une combinaison de profils sismiques et de données lithologiques de carottes sédimentaires bien datées permettra d'obtenir une chronologie des changements d'environnements sédimentaires, eux-mêmes fortement conditionnés par la localisation de la marge. En plus de bonifier les études paléogéographiques locales, ces informations viendront s'ajouter aux nombreuses données permettant de reconstruire l'évolution du LIS au cours de la déglaciation.
- Identifier et distinguer les marqueurs sédimentaires des étapes de la déglaciation de la baie d'Hudson et préciser leur chronologie. Quels marqueurs sont identifiés et à quels événements correspondent-ils ? Les résultats indiquent-ils une dernière vidange du LAO vers 8,2 cal ka BP ou vers 8,45-8,55 cal ka BP ? En intégrant les études régionales récentes, quelle serait la chronologie des étapes de déglaciation de la baie ? Ces nouvelles données permettront d'éclaircir l'incertitude de la chronologie des événements. Outre la couche rouge, le taux de carbonates détritiques et de débris délestés par les glaces dans les sédiments sont des indicateurs sédimentaires clés de la déglaciation du secteur. Le tout dépendra cependant de la résolution des enregistrements.
- Caractériser et comparer la dynamique sédimentaire des différents environnements physiographiques de la marge continentale pendant la transition postglaciaire. Comment se comparent les bassins des trois secteurs en termes d'apports sédimentaires ? Comment se traduisent les processus paraglaciers à chaque endroit, et quelle part leurs apports prennent-ils dans la séquence ? Quelle période



couvre, approximativement, la transition postglaciaire dans chaque secteur ? Comment se manifeste cette transition du point de vue des propriétés sédimentaires ? Ces questions permettront de mieux cerner qualitativement l'évolution des différents environnements de la marge continentale à la suite du retrait des glaces jusqu'à la fin de la transition postglaciaire. Tout comme pour le premier objectif, les profils acoustiques de sous-surface vont compléter l'analyse des propriétés physiques des carottes sédimentaires, notamment pour quantifier les apports paraglaciers. Par ailleurs, les variations des propriétés chimiques et magnétiques du sédiment seront mises de l'avant pour identifier les changements s'opérant tout au long de la transition postglaciaire.

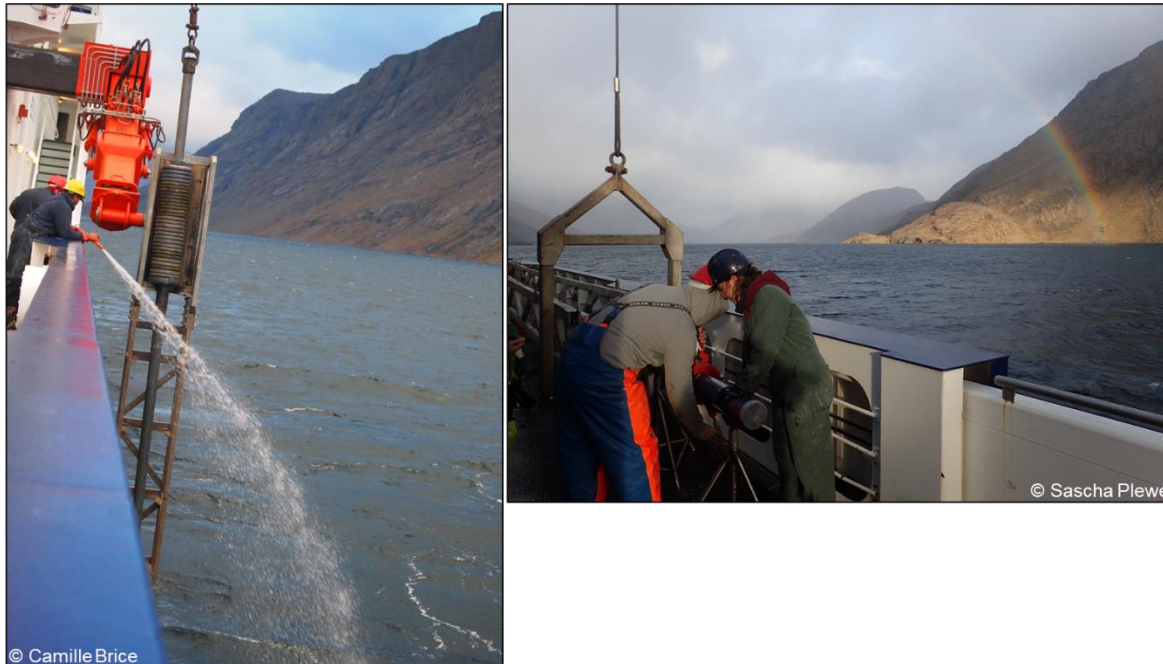
## **5. METHODOLOGIE**

### **5.1 Profils sismiques et carottage**

Les carottes sédimentaires dont les données sont détaillées dans cette thèse ont été prélevées lors de la mission MSM46 du N/R allemand Maria S. Merian ayant eu lieu du 25 août au 26 septembre 2015. Les sites d'échantillonnages ont été sélectionnés dans des bassins sédimentaires après l'analyse des profils sismiques afin de localiser les zones avec une épaisseur de séquence adaptée. Le but était d'optimiser la résolution temporelle tout en collectant la majeure partie de la période Holocène.

Les profils sismiques ont été réalisés à l'aide d'un système PARASOUND P70 opérant à des fréquences primaires de 18 à 28 kHz générant des séquences paramétriques secondaires de 0,5 à 10 kHz. Ce système permet techniquement d'obtenir des profils de sous-surface représentant les premiers 100 m de sédiments. Cependant, les lithologies sédimentaires plus denses telles que les sédiments de contact glaciaire sont difficilement distinguables de la roche-mère, limitant ainsi l'interprétation en profondeur des profils. Les fichiers SEG Y des

profils ont été visualisés à l'aide des programmes SeiSee et JP2 Viewer afin d'interpréter les différentes unités acoustiques.



**Figure 8.** Récupération de la carotte à gravité MSM46-28-04-GC dans le fjord Nachvak.

Le carottage s'est effectué à l'aide d'un carottier à gravité pouvant atteindre 18 m de longueur (Fig. 8). Une fois récoltées, les carottes ont été scindées à bord en tronçons de 1 m. Ensuite, ces tronçons ont été ouverts en deux sections égales, décrites, photographiées et sous-échantillonnées : des *u-channels* ont été prélevés pour effectuer des mesures paléomagnétiques, de même que des échantillons discrets pour des datations au radiocarbone sur des foraminifères.

Les carottes concernées par la présente thèse ont été prélevées dans trois secteurs : la MSM46-28-04-GC et la MSM46-14-05-GC dans les fjords Nachvak et Saglek respectivement, la MSM46-20-05-GC et la MSM46-24-01-GC dans l'ouest du détroit

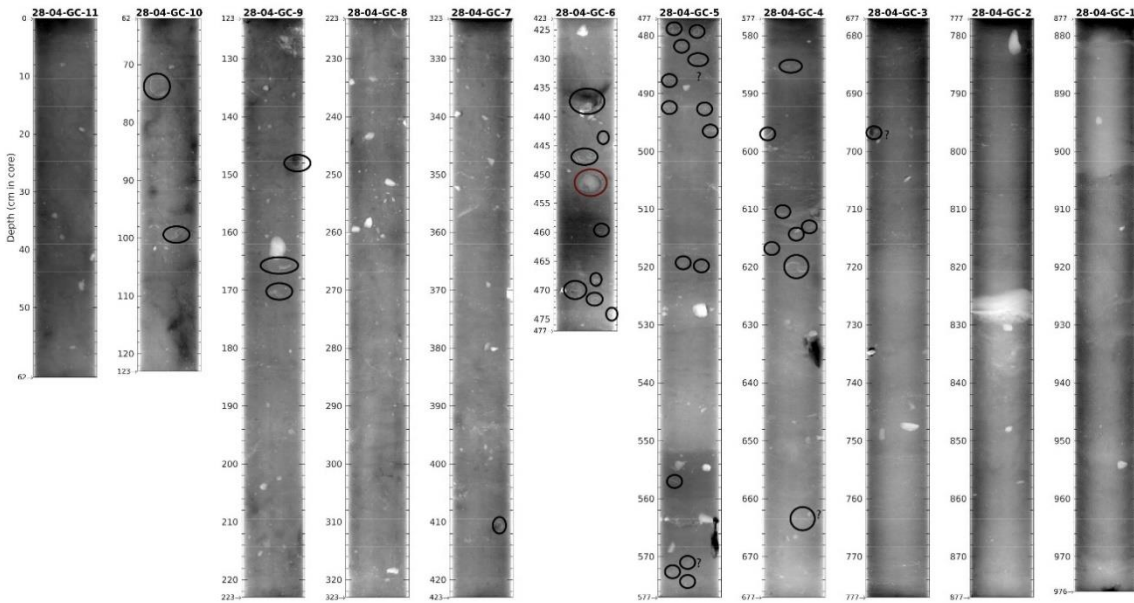
d'Hudson, et la MSM46-13-03-GC dans le lac Melville (Tableau 1). Les carottes sont ci-après référées sous les noms de carottes 28, 14, 20, 24 et 13, respectivement.

**Tableau 1.** Coordonnées, profondeur et longueur des carottes sédimentaires étudiées dans la présente thèse.

Carotte	Latitude	Longitude	Secteur	Profondeur d'eau (m)	Longueur de la carotte (cm)
MSM46-13-03-GC	53,8737	-59,2352	Lac Melville	122	1407
MSM46-14-05-GC	58,4918	-63,1507	Fjord Saglek	247	1335
MSM46-20-05-GC	63,0495	-74,3112	Détroit d'Hudson, bassin Ouest	426	807
MSM46-24-01-GC	62,765	-79,0043	Détroit d'Hudson, bassin Sud-Ouest	394	962
MSM46-28-04-GC	59,05	-63,65	Fjord Nachvak	165	976

## 5.2 Analyses tomodesitométriques

Les *u-channels* prélevés dans les carottes ont été passés dans un CT scan médical Siemens Somatom AS+ 128 au laboratoire de l'INRS-ETE à Québec pour obtenir des images tomodesitométriques. Celles-ci permettent de visualiser les variations de densité et les structures sédimentaires présentes dans les carottes (St-Onge et al., 2007, Fortin et al., 2013). De plus, à l'ISMER-UQAR, les demi-sections des carottes sédimentaires ont été scannées au MSCL-XCT de Geotek afin d'obtenir des images digitales plus générales des variations de densité du sédiment. Ces dernières, quoique moins précises, ont permis de repérer des coquilles de bivalves enfouies dans le sédiment qui ont pu être récupérées et utilisées pour la datation (Fig. 9).



**Figure 9.** Images tomographiques de la carotte 28 (Fjord Nachvak) obtenue avec le MSCL-XCT de l'ISMER-UQAR. Les cercles indiquent les coquilles de bivalves identifiées à l'aide de l'image. Les débris laissés par les glaces (IRDs) sont également bien visibles, ainsi qu'une couche de sédiments probablement déposée rapidement entre 824 et 830 cm.

### 5.3 Propriétés physiques et chimiques continues

Un banc de mesure MSCL (*Multi Sensor Core Logger*) a été utilisé pour mesurer, à un intervalle de 1 cm, la susceptibilité magnétique à faible champ  $k_{LF}$  avec un senseur ponctuel Bartington MS2E1, la réflectance par spectrophotométrie à l'aide d'un Minolta CM-2600d, ainsi que la composition chimique par fluorescence X (XRF) avec un Innov-X Olympus Delta Element. La susceptibilité magnétique caractérise la faculté du sédiment à s'aimanter, et est tout d'abord corrélée à la concentration de grains ferrimagnétiques (e.g., magnétite et titanomagnétite), mais augmente également avec la granulométrie du sédiment (St-Onge et al., 2007). La réflectance permet de représenter la couleur du sédiment selon les paramètres  $L^*$  (noir à blanc),  $a^*$  (vert à rouge) et  $b^*$  (bleu à jaune) de la Commission Internationale de l'Éclairage (St-Onge et al., 2007 ; Debret et al., 2011). Pour cette étude, seul  $a^*$  est utilisé

afin, par exemple, d'identifier la possible présence de la couche rouge du détroit d'Hudson dans les carottes. Finalement, les données XRF permettent d'obtenir les concentrations semi-quantitatives de certains éléments dans le sédiment tels que Fe, Ca, Ti, Zr, Mn, Rb, S, Al, Sr, etc. Des rapports d'éléments peuvent être ainsi calculés afin d'identifier des variations chimiques ou lithologiques (St-Onge et al., 2007 ; Croudace & Rothwell, 2015). Le Zr/Rb, par exemple, peut être utilisé comme indicateur de la taille des grains, le zirconium (Zr) étant généralement plus présent dans les grains grossiers et le rubidium (Rb) dans les sédiments fins. Ce rapport est très utile afin d'identifier la présence de couches déposées rapidement tel que des turbidites ou des hyperpycnites (Duboc et al., 2017). Le Ca/Ti est un bon indicateur des variations de proportions entre sédiments carbonatés et siliciclastiques. En outre, l'augmentation de ce rapport est souvent associée à une augmentation des sédiments carbonatés d'origine biogénique, ceux-ci étant riches en calcium (Ca). Cependant, dans les régions où les roches et sédiments peuvent être riches en carbonates d'origine détritique (comme la baie et le détroit d'Hudson), le rapport peut être utilisé comme discriminant des sources sédimentaires (Piva et al., 2008 ; Rashid et al., 2017). Dans ce cas, une augmentation du Ca/Sr permet de vérifier qu'il s'agit bien de carbonates détritiques, car le strontium (Sr) est également incorporé dans les carbonates biogéniques (Hodell et al., 2008). Le Fe/k<sub>LF</sub> est également utilisé dans la présente étude, afin de mettre en valeur les sédiments affectées par la dissolution de minéraux ferrimagnétiques (Funk et al., 2004 ; Hofmann et al., 2005 ; Korff et al., 2016). En effet, un tel processus affecte grandement k<sub>LF</sub> qui diminue alors que la quantité de fer (Fe) ne fluctue pas, celui-ci changeant simplement de phase pendant la dissolution. Finalement, le Mn/Ti est utilisé pour identifier les modifications de conditions redox dans le sédiment ou la relocalisation du manganèse (Mn) après dépôt (Kylander et al., 2011).

## 5.4 Analyses d'isotopes stables

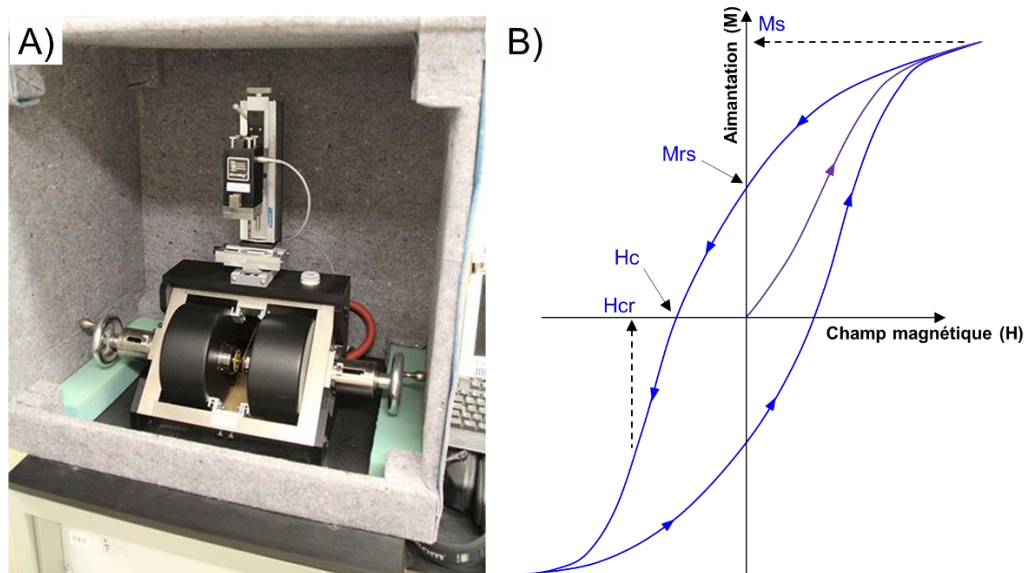
Des échantillons prélevés dans les carottes 13, 14 et 20 ont été analysés par spectrométrie de masse pour la détermination du  $\delta^{13}\text{C}$  et par un analyseur élémentaire (GC-EA-IRMS, ThermoElectron/ COSTECH) pour obtenir la teneur en carbone (C) et en azote (N). Chaque échantillon a été au préalable divisé en deux duplicatas afin d'en soumettre un à l'action de l'acide chlorhydrique dans le but d'en éliminer le carbone inorganique. Les données de  $\delta^{13}\text{C}$  et de  $\text{C}_{\text{org}}/\text{N}$  obtenues permettent de déterminer les variations de source de la matière organique du sédiment (Meyers, 1997 ; St-Onge & Hillaire-Marcel, 2001 ; Lamb et al., 2006) et d'évaluer l'évolution de l'influence relative des eaux de fonte glaciaire et des eaux marines au fil du temps dans un contexte de déglaciation.

## 5.5 Analyses granulométriques

Des échantillons de sédiment ont également été analysés à l'aide d'un granulomètre-laser Beckman Coulter LS13320 après avoir été préalablement dilués dans une solution de Calgon (hexametaphosphate de sodium à 1%). La moyenne géométrique des résultats compilée à l'aide de la macro EXCEL GRADISTAT (Blott & Pye, 2001) est utilisée comme représentant la taille moyenne des grains. Dans le cas des carottes 14, 20, 24 et 28, un travail de tamisage à 63  $\mu\text{m}$  et à 150  $\mu\text{m}$  a également été effectué sur des tranches de 2 cm d'épaisseur couvrant toute la partie inférieure (qui présentait des variations dans les données de MSCL). Le résultat est donné en pourcentage massique (wt%). Le wt% > 63  $\mu\text{m}$  indique la quantité de sable et de gravier présente dans l'échantillon, valeur plus représentative que les résultats du granulomètre pour cette fraction sédimentaire, car elle prend en compte un plus grand volume de sédiment. Les sédiments > 150  $\mu\text{m}$  peuvent être considérés comme des débris délestés par les glaces (IRDs; Moros et al., 2004), sauf dans les couches déposées rapidement.

## 5.6 Magnétomètre à gradient alternatif

Des échantillons représentatifs des différentes lithologies des carottes ont été analysés à l'aide d'un magnétomètre à gradient alternatif (AGM, MicroMag 2900 de *Princeton Measurement Corporation* ; Fig. 10A) afin de mesurer leurs propriétés magnétiques : le moment magnétique à saturation ( $M_s$ ), la rémanence de saturation ( $M_{rs}$ ), la coercivité ( $H_c$ ) et la coercivité rémanente ( $H_{cr}$ ). Les courbes (ou boucles) d'hystérésis obtenues (Fig. 10B) permettent de mettre en valeur les variations de minéralogie et de taille des grains magnétiques : la forme sigmoïdale des boucles indique la dominance de la (titano)magnétite comme vecteur de l'aimantation du sédiment, tandis que la largeur de la boucle augmente avec la coercivité, plus élevée dans les petits grains (Tauxe, 1993 ; Stoner & St-Onge, 2007). Le  $M_{rs}/M_s$  exprimé en fonction du  $H_{cr}/H_c$  donne le diagramme de Day (Day et al., 1977 ; Roberts et al., 1995 ; Tauxe et al., 1996) qui permet d'identifier le domaine des grains magnétiques : monodomaine (SD), pseudo-monodomaine (PSD) ou multidomaine (MD). Le type de domaine est souvent associé aux changements de granulométrie magnétique, mais peut dépendre de plusieurs facteurs tels que la minéralogie, la pureté ou la forme des grains (Stoner & St-Onge, 2007 ; Roberts et al., 2018).



**Figure 10.** A) Magnétomètre à gradient alternatif MicroMag 2900. B) Schéma d'une boucle d'hystérésis avec l'identification des paramètres principaux. Inspiré de Maher (2007).

## 5.7 Magnétomètre cryogénique

Les *u-channels* ont été passés dans un magnétomètre cryogénique 2G SRM-755 (ISMER-UQAR) afin de mesurer l'aimantation rémanente naturelle (NRM) du sédiment. Ils ont par la suite été démagnétisés par étapes incrémentées de 5 mT (jusqu'à 80 mT), et remesurés à chaque étape. Les résultats des mesures ont été ensuite compilés dans la macro Excel de Mazaud (2005) afin d'en extraire l'inclinaison et la déclinaison magnétique du sédiment par analyse en composante principale (Kirschvink, 1980) de même que le champ destructif médian (MDF) et la déviation angulaire maximale (MAD). Le MDF est un indicateur de la coercivité du sédiment qui change selon la minéralogie et augmente quand la taille des grains magnétiques diminue. La MAD est un indicateur de la qualité des données magnétiques, et doit être idéalement être inférieure à  $5^\circ$  pour s'assurer de cette qualité (Stoner & St-Onge, 2007).



Une aimantation rémanente anhystérétique (ARM) a ensuite été induite aux *u-channels*, puis mesurée par étapes successives suivant la même méthode que pour la NRM. Le processus a ensuite été répété avec une induction d'aimantation rémanente isothermale (IRM). L'ARM et l'IRM correspondent à des propriétés magnétiques intrinsèques du sédiment qui dépendent de la concentration et de la taille des grains magnétiques, ainsi que de la minéralogie. Si la magnétite est le principal vecteur d'aimantation du sédiment, alors l'ARM va surtout varier avec la proportion de grains SD et PSD ( $< 10 \mu\text{m}$ ), étant particulièrement renforcée par les grains entre 30 nm et  $1 \mu\text{m}$ , tandis que l'IRM est plus sensible aux grains  $> 10 \mu\text{m}$  (Stoner & St-Onge, 2007 ; Liu et al., 2012). La susceptibilité de la ARM ( $k_{\text{ARM}}$ ) est utilisée dans le  $k_{\text{ARM}}/k_{\text{LF}}$  qui varie de façon inversement proportionnelle à la taille des grains magnétiques.

## 5.8 Chronologie

Les carottes ayant été prélevées dans des zones relativement peu profondes en milieu subarctique, la profondeur de compensation des carbonates n'a pas été atteinte, et les carottes sont relativement riches en tests de foraminifères et en coquilles de mollusques. Plusieurs coquilles ont ainsi été prélevées, en bonne partie grâce aux images XCT ayant permis de les repérer dans le sédiment. Des profondeurs ont également été sélectionnées pour récupérer des foraminifères, le tout afin d'effectuer des datations au radiocarbone ( $^{14}\text{C}$ ). Les coquilles de mollusques ont été envoyées pour analyse au laboratoire Leibniz de datation radiométrique et de recherche isotopique de l'Université de Kiel en Allemagne, tandis que les échantillons de foraminifères ont été analysés à l'école polytechnique fédérale (ETH) de Zürich en Suisse. Les modèles d'âge ont été réalisés en privilégiant l'approche bayésienne avec le *R-package* Bacon (Blaauw & Christen, 2011) en utilisant la courbe de calibration Marine20 (Heaton et al., 2020). Une correction d'âge réservoir  $\Delta R$  a également été apportée en fonction de la région : la valeur de  $-2 \pm 69$  ans a été utilisée pour les carottes 14 et 28 dans les fjords du Labrador (Brouard et al., 2021) et celle de  $-73 \pm 64$  ans pour les carottes 20 et

24 du détroit d'Hudson (Pieńkowski et al., 2022). Pour la carotte 13 du lac Melville, en revanche, un  $\Delta R$  de  $0 \pm 0$  an a été appliqué, car aucune étude locale n'existe encore et les valeurs de  $\Delta R$  proposées pour le plateau continental ne peuvent être transférées au lac en raison de l'importante influence des eaux fluviales et de la connectivité limitée entre les différents milieux.

En outre, en plus de considérer la variation spatiale de l'âge réservoir, il est important de prendre en compte la variabilité temporelle de plusieurs facteurs océanographiques et glaciaires qui influencent l'âge réservoir du  $^{14}\text{C}$  d'une même région. Ainsi, l'âge réservoir va avoir tendance à augmenter avec la stratification de la colonne d'eau, la longévité du couvert de glace ou encore l'apport d'eau de fonte glaciaire appauvrie en  $^{14}\text{C}$  ou de carbonates détritiques paléozoïques qui en sont complètement dépourvus (Vickers et al., 2010 ; Ross et al., 2012 ; England et al., 2013 ; Lochte et al., 2019a). Pour ces raisons, l'âge réservoir aura tendance à être plus élevé dans des conditions de déglaciation. Ainsi, plusieurs études ajoutent entre 100 et 500 ans au  $\Delta R$  pour la période de déglaciation pour contrebalancer ces facteurs (e.g., Lewis et al., 2012 ; Rashid et al., 2017 ; Lochte et al., 2019a). Dans le cas de la présente étude, il a été décidé de conserver un  $\Delta R$  constant pour chacune des carottes, car il est difficile d'évaluer la variation temporelle des paramètres affectant cette valeur. Ce choix, de même que de nouvelles informations observées concernant le  $\Delta R$ , sont discutés dans le chapitre 2.

Par ailleurs, dans le cas de la carotte 13 du lac Melville, la réaction d'oxydation des sédiments sulfurés a attaqué les foraminifères après l'ouverture et il n'a pas été possible d'obtenir de matériel pour la datation au radiocarbone pour la partie supérieure de la carotte (0-700 cm). Les données d'inclinaison et de déclinaison magnétiques ont donc été comparées à celles d'autres enregistrements paléomagnétiques et à un modèle géomagnétique afin de compléter le modèle d'âge de la carotte (e.g. Lisé-Pronovost et al., 2009 ; Deschamps et al., 2018 ; Caron et al., 2019b). En effet, lors de leurs dépôts sur le fond marin, les sédiments magnétiques enregistrent les variations du champ magnétique terrestres, et ces variations

peuvent être corrélées d'un enregistrement à l'autre à l'échelle locale, régionale et même globale (Stoner & St-Onge, 2007).

## 6. ORGANISATION DE LA THESE

Cette thèse s'articule autour de trois chapitres rédigés sous forme d'articles scientifiques correspondant chacun à l'étude d'un des secteurs. Bien que la méthodologie soit en partie similaire d'un secteur à l'autre, chacun d'entre eux présente des spécificités qui font l'originalité de chaque chapitre.

Le **premier chapitre** présente une étude détaillée de la séquence sédimentaire quaternaire des fjords Nachvak et Saglek au nord du Labrador, à l'aide des données sismiques et de carottes sédimentaires. La chronologie de déglaciation des fjords y est discutée, de même que la présence de dépôts de mouvements de masse particulièrement épais, de couches riches en carbonates détritiques et d'anomalies magnétiques associées à la transition postglaciaire.

Duboc, Q., Lajeunesse, P., St-Onge, G., Moros, M., Perner, K., 2023. Holocene sedimentary sequences from Nachvak and Saglek Fjords (Northern Labrador) as a record of deglaciation of the Torngat Mountains and Hudson Bay. *Quaternary Science Reviews*, 307, 108046.

Le **deuxième chapitre** fait état d'une étude de carottes sédimentaires provenant de deux bassins de l'ouest du détroit d'Hudson contenant toutes deux les marqueurs sédimentaires associés aux derniers événements de déglaciation de la baie d'Hudson. Une chronostratigraphie de ces marqueurs y est détaillée, et la problématique de l'âge réservoir y est abordée en utilisant la comparaison des deux enregistrements.

Duboc, Q., St-Onge, G., Moros, M., Lajeunesse, P., Perner, K. Deglacial events surrounding the Lake Agassiz-Ojibway drainages constrained in high-resolution sedimentary records

from the western Hudson Strait and implications of marine reservoir age. Sera soumis prochainement à la revue *Nature Geoscience*.

Le **troisième chapitre** concerne le secteur du lac Melville et détaille la séquence sédimentaire correspondant à la transition d'un milieu glaciomarin à postglaciaire. Une chronologie détaillée complétée à l'aide du paléomagnétisme est présentée, permettant de lier l'évolution de la séquence à la dynamique de la marge glaciaire. Des conséquences de l'événement de 8.2 sur l'environnement sédimentaire sont également abordées.

Duboc, Q., St-Onge, G., Lajeunesse, P., Moros, M. Evolution of deglacial sedimentary processes and environmental conditions in Lake Melville, Labrador, since the last 9.2 ka. Sera soumis prochainement à *Boreas*.

Finalement, une **discussion générale** fait suite aux trois articles susmentionnés. Une analyse spatiotemporelle de la zone d'étude intégrant les informations des trois chapitres y est présentée en répondant aux objectifs de la thèse et aux différentes questions posées. Les limites de l'étude y sont ensuite abordées, de même que les perspectives futures de recherche qui en découlent.

# **CHAPITRE 1**

## **SEQUENCES SEDIMENTAIRES HOLOCENES DES FJORDS NACHVAK ET SAGLEK (NORD DU LABRADOR) COMME ENREGISTREMENT DE LA DEGLACIATION DES MONTS TORNGAT ET DE LA BAIE D'HUDSON**

### **1.1 RÉSUMÉ EN FRANÇAIS DU PREMIER ARTICLE**

La reconstruction du retrait final de l'Inlandsis laurentidien offre une opportunité de comprendre les impacts du retrait glaciaire sur les paysages et les processus sédimentaires, ainsi que leur relation avec l'océanographie et les variations climatiques dans l'est de l'Amérique du Nord. Dans le nord du Labrador, une région où peu de données terrestres donnent des contraintes chronologiques, l'étude de la dynamique de déglaciation est également cruciale car les importants ajouts d'eau de fonte dans la mer du Labrador peuvent affecter la formation d'eau profonde qui a lieu à cet endroit. Dans cet article, nous étudions les séquences sédimentaires des fjords Nachvak et Saglek, situés dans les monts Torngat, au nord du Labrador. Les profils sismiques révèlent que les deux fjords contiennent une séquence sédimentaire de plus de 100 m, y compris d'importants dépôts de mouvements de masse atteignant 40 m d'épaisseur. Ces événements ont possiblement été déclenchés par des tremblements de terre d'origine glacio-isostatique pendant le Dryas récent et le début de l'Holocène. Les estimations basées sur des carottes gravimétriques bien datées prélevées dans les deux fjords suggèrent une déglaciation avant le Dryas récent pour le bassin extérieur de Nachvak, mais seulement 2000 ans plus tard pour le bassin équivalent dans le fjord Saglek. Ce recul asynchrone s'explique par la présence de la baie de Saglek, qui agit comme une zone tampon contre le forçage océanique à l'entrée du fjord homonyme. Dans les carottes de sédiments, de fortes concentrations de carbonates détritiques et un équivalent de la couche rouge du détroit d'Hudson sont associés à des événements majeurs de déglaciation survenus entre 9,2 et 8,1 cal ka BP dans la région de la baie d'Hudson. Une transition postglaciaire

progressive s'est amorcée vers 8,0 cal ka BP avec une diminution des apports de carbonates détritiques et une influence croissante des eaux de l'Atlantique Nord. Cette transition s'est terminée brusquement par un changement environnemental régional majeur vers 6,3 cal ka BP après la fin de la fonte de l'Inlandsis laurentidien. Les propriétés magnétiques reflétant une consommation accrue d'oxygène au fond révèlent une productivité primaire plus élevée entre 6,3 et 3,8 cal ka BP dans les bassins principaux de Saglek et de Nachvak, et probablement une plus importante stratification de la colonne d'eau. Dans l'ensemble, ces résultats indiquent que la dynamique sédimentaire glaciomarine et postglaciaire des fjords Nachvak et Saglek a été influencée par (1) de volumineux dépôts de mouvements de masse probablement générés par des tremblements de terre, (2) l'exportation de sédiments par des processus de déglaciation à partir des zones locales et de la baie d'Hudson et (3) l'influence des eaux de la mer du Labrador.

## **1.2 HOLOCENE SEDIMENTARY SEQUENCES FROM NACHVAK AND SAGLEK FJORDS (NORTHERN LABRADOR) AS A RECORD OF DEGLACIATION OF THE TORNGAT MOUNTAINS AND HUDSON BAY**

Constraining the final retreat of the Laurentide Ice Sheet offers the best opportunities to understand the impacts of glacial retreat on landscapes and sedimentary processes, and their relation to oceanography and climate variations in Eastern North America. In Northern Labrador, an area that lacks chronological constraints on terrestrial data, investigating deglacial dynamics is also important as meltwater pulses may affect the deepwater formation that takes place in the Labrador Sea. In this paper, we investigate the deglacial sedimentary sequences from Nachvak and Saglek Fjords located in the Torngat Mountains of Northern Labrador. Sub-bottom profiles reveal that both fjords contain a deglacial sequence thicker than 100 m, including important mass-movement deposits reaching thicknesses of 40 m. These events were possibly triggered by glacio-isostatically induced earthquakes during the Younger Dryas and the Early Holocene. Estimations based on well-dated gravity cores sampled in both fjords suggest a deglaciation before the Younger Dryas for the Nachvak Outer Basin, but only 2000 yr later for the equivalent basin in Saglek Fjord. Such asynchronous retreat is explained by the presence of Saglek Bay acting as a buffer zone against oceanic forcing at the entrance of Saglek Fjord. In the sediment cores, high concentrations of detrital carbonates and an equivalent of the Hudson-Strait red bed are correlated with major deglacial events occurring between 9.2 and 8.1 cal ka BP in the Hudson Bay area. A progressive postglacial transition began around 8.0 cal ka BP with a decrease of detrital carbonate inputs and an increasing influence of North Atlantic waters. This transition ended abruptly with a regional major environmental change around 6.3 cal ka BP after the end of the Laurentide Ice Sheet melting. Magnetic properties reflecting enhanced bottom oxygen consumption reveal a high primary productivity from 6.3 to 3.8 cal ka BP in Saglek and Nachvak main basins, and probably a stronger water stratification. Overall, these results indicate that the deglacial and postglacial sedimentary dynamics of Nachvak and Saglek Fjords was influenced by (1) massive mass-movement deposits possibly generated by

earthquakes, (2) sediment export by deglacial processes from both the local and the Hudson Bay areas and (3) the influence of Labrador Sea waters.

### 1.3 INTRODUCTION

At the end of Last Glacial Maximum (LGM) around 21 cal ka BP, Québec-Labrador and its adjacent continental margins were covered by the Laurentide Ice Sheet (LIS) that was then progressively reduced following global and regional climatic fluctuations. Several studies focused on the evolution of the LIS margin during this deglaciation in order to improve our understanding of relationships between ice, ocean and climate dynamics in today's climatic context (e.g., Dyke et al., 2004; Occhietti et al., 2011; Dietrich et al., 2017; Dalton et al., 2020). Many of these studies are based on identification and dating of glacial deposits and landforms left by the fluctuating ice margins, such as lateral and frontal moraines (e.g., Clark, 1988; Occhietti et al., 2011; Margreth et al., 2017). While these LIS margin retreat and fluctuation patterns are well constrained in some areas, they lack precision in others that are more remote or where the terrestrial deglacial morphosedimentary and radiochronological record is scarce, making the reconstruction more challenging. The Torngat Mountains correspond to such an area of still-lacking chronological constraints, where most of expeditions occurred on land during and prior to the 1960s, with more recent cosmogenic exposure dating of glacial landforms in specific sectors (Ives, 1957; Evans and Rogerson, 1985; Clark, 1988; Gallagher, 1989; Dubé-Loubert et al., 2018). In this region, different weathering zones were identified as markers of successive glaciations, the lowermost one being delimited by an extensive system of lateral moraines named the Saglek Moraines (Ives, 1976; Clark, 1988; Clark et al., 2003). These moraines dated around 12-13 <sup>10</sup>Be ka might mark the last highest stand of LIS outlet glaciers in the Torngat Mountains area, or a change in ice regime (Ives, 1976; Clark et al., 2003). New studies are needed to better constrain the deglacial pattern of the Torngat area, particularly in the fjords that were the main pathway for the ice flowing from the Québec-Labrador Sector of the LIS towards the continental margin.



As they are major transition zones between ocean and continent, subarctic fjords are efficient sediment traps and their basins generally contain thick, high-resolution sedimentary sequences deposited at high rates by glacial, fluvial and marine processes, as well as by mass-failure events (e.g., Syvitski and Shaw, 1995; St-Onge and Hillaire-Marcel, 2001; Howe et al., 2010; St-Onge et al., 2012). These sequences can be used for reconstructing both past ice margin dynamics (e.g., Storms et al., 2012; Bellwald et al., 2019; Trottier et al., 2020) and marine and terrestrial climate variations (e.g., Hald et al., 2003; Howe et al., 2010; Richerol et al., 2016). The typical sequence formed during an ice margin retreat transits from ice-contact to glaciomarine/glaciofluvial and paraglacial, and finally postglacial sediments (Syvitski and Praeg, 1989; Syvitski, 1991), providing information on the relative position of the ice margin (e.g., Dietrich et al., 2017). Paraglacial sedimentation corresponds to sediment remobilization by a range of processes enhanced by rapid relative sea-level (RSL) variations and ice-sheet changes. These processes, particularly active in fjords, include mass-movement and the reworking of unconsolidated glacial or glaciofluvial sediments forming prograding deltaic wedges (Church and Ryder, 1972; Syvitski, 1991; Stoker et al., 2010; Dietrich et al., 2017). Once the deglaciated landscapes are stabilized, the sedimentation records the postglacial transition and the setup of modern-like environmental conditions. Investigating the resulting sediment sequence with acoustic sub-bottom profiles and gravity-cores allow identifying sedimentary units associated with the different depositional environment following the ice retreat (e.g., Syvitski and Lee, 1997; Duchesne et al., 2007; St-Onge et al., 2008; Normandeau et al., 2013; Bellwald et al., 2019; Lévesque et al., 2019). Sediment gravity-cores may then provide detailed continuous Holocene records of deglacial events and regional environmental change (e.g., St-Onge et al., 2012; Richerol et al., 2016; Caron et al., 2019; Lochte et al., 2019a, 2019b; Allan et al., 2021).

The Torngat fjords are also a relevant location for their opening on Labrador Sea, which plays a major role in regional and global climate as it is one of the major sites of deepwater formation that partly drives the Atlantic Meridional Overturning Circulation (AMOC) (e.g. Hoogakker et al., 2015; Thornalley et al., 2018). These sites are known to be sensitive to meltwater runoff, and the AMOC has been disturbed many times by massive freshwater

inputs triggered by major deglacial events in the Labrador Sea and the North Atlantic (Condrón and Windsor, 2012; Keigwin et al., 2018). The latest of these events was the last Lake Agassiz-Ojibway (LAO) outburst involved in the 8.2 ka cold event, the most pronounced Holocene cold snap (Barber et al., 1999; Lajeunesse and St-Onge, 2008; Hoffman et al., 2012; Matero et al., 2017). Recent studies have demonstrated that this drainage occurred in at least two times between 8.6 and 8.0 cal ka BP, and that the collapse of the Hudson Bay Ice Saddle that acted as a dam for the LAO also massively contributed to the freshwater input (Matero et al., 2017; Lochte et al., 2019a; Brouard et al., 2021). However, the timing of these events is still a matter of debate, as well as which event formed the layer of red, muddy, hematite-rich sediment spilled from northwestern Hudson Bay and previously associated with the last LAO drainage (Kerwin, 1996; Barber et al., 1999; St-Onge and Lajeunesse, 2007; Jennings et al., 2015).

On the Eastern coast of the Torngat Mountains, Nachvak and Saglek Fjords are of the longest and deepest fjords of the area. Moreover, their marine basins contain thick Quaternary sequences and are the site of an efficient exchange with continental shelf waters (Bentley and Kahlmeyer, 2012; Brown et al., 2012). These elements make these fjords good candidates for documenting both the regional ice margin retreat and the deglacial events occurring upstream the Labrador Current. In this paper, a combination of swath bathymetry imagery, sub-bottom acoustic profiles, sediment gravity-core data and radiocarbon dates are used in order to (1) establish the sedimentary sequence of Nachvak and Saglek Fjords, (2) reconstruct the patterns and rate of deglaciation of the fjords, (3) document the sedimentary record of regional and local deglaciation and of the following changes in sedimentary regimes.

## **1.4 STUDY AREA**

### **1.4.1 Physiographic setting**

Saglek and Nachvak Fjords are two subarctic fjords located in the Torngat Mountains National Park, on the Eastern coast of Northern Labrador (Fig. 11), an area also named

Nunatsiavut that is geologically composed by Archean and Early Proterozoic gneisses and metasedimentary rocks (Wardle et al., 1993).

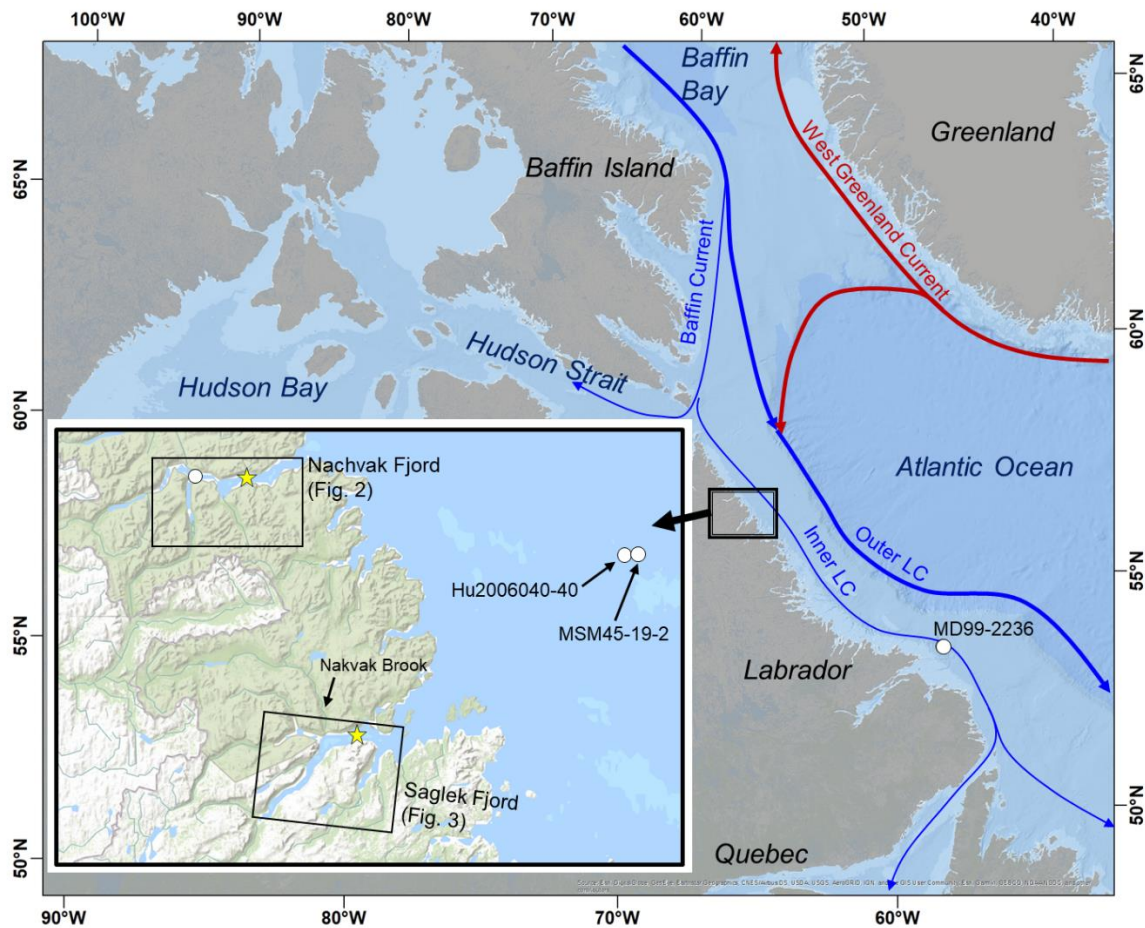
Nachvak Fjord is a 2-4 km wide glacial trough extending 45 km inland in the Torngat Mountains that produces up to 1000-m high sidewalls. This fjord is composed from west to east of four basins named Townlet, Koktortoaluk, Ivitin and Outer basins, which have respectively mean depths of 90, 160, 170 and 210 m, and are separated by sills ranging from 10 to 180 m-deep named Kogarsok, Ivitak and Tinutyarvik sills (Fig. 12; Gallagher, 1989; Bell and Josenhans, 1997; Bastick, 2009). Nachvak Fjord is continued by Tasiuyak and Tallek Arms westward and southward from Koktortoaluk Basin respectively.

Saglek Fjord is about 65 km long and opens out eastward to Saglek Bay, which is 14 km-wide, about 30 km-long and opens itself to the Labrador Sea. Saglek Fjord is prolonged to the southwest by Ugjuktok Fjord and is joined at the west by the tributary West arm complex (Fig. 13; Bastick, 2009; Bentley and Kahlmeyer, 2012).

Both fjords are influenced by tides, which have a range of 2 m and high tidal velocities in the inlets (Bentley and Kahlmeyer, 2012). Fjord basins have a well oxygenated water-column due to a good water circulation between fjords and the proximal Labrador continental shelf (Bentley and Kahlmeyer, 2012; Brown et al., 2012). Their deep waters are thus not subject to the lack of oxygen often characterizing such environments (Syvitski and Shaw, 1995; Howe et al., 2010; Brown et al., 2012). The climate of the Northern Labrador is significantly influenced by the Labrador Current (LC) that carries cold, fresh and nutrient-rich waters from the Arctic and the Hudson Bay system along Labrador and Newfoundland (Lazier and Wright, 1993; Cuny et al., 2002; Straneo and Saucier, 2008). This current maintains a strong climatic contrast between inland and coastal Labrador and enhances marine productivity (Engstrom and Hansen, 1985; Harrington, 2004).

In Nunatsiavut, the RSL record is poorly documented, and the few Holocene data obtained from raised-marine sequences and archeological evidences indicate that coastal areas experienced a continuous RSL fall of about 30 m since 10 cal ka BP, most of it

occurring before 6.0 cal ka BP (Vacchi et al., 2018). However, data from raised beaches closer to the Nachvak Fjord head indicate a RSL fall higher than 50 m (Gallagher, 1989).



**Figure 11.** Map of the study area with the Northwest Atlantic Circulation (adapted from Lochte et al., 2019b), with the location of Nachvak and Saglek Fjords. Yellow stars and white circles are the location of cores from this study and other cores referred in this work, respectively.

### 1.4.2 Background

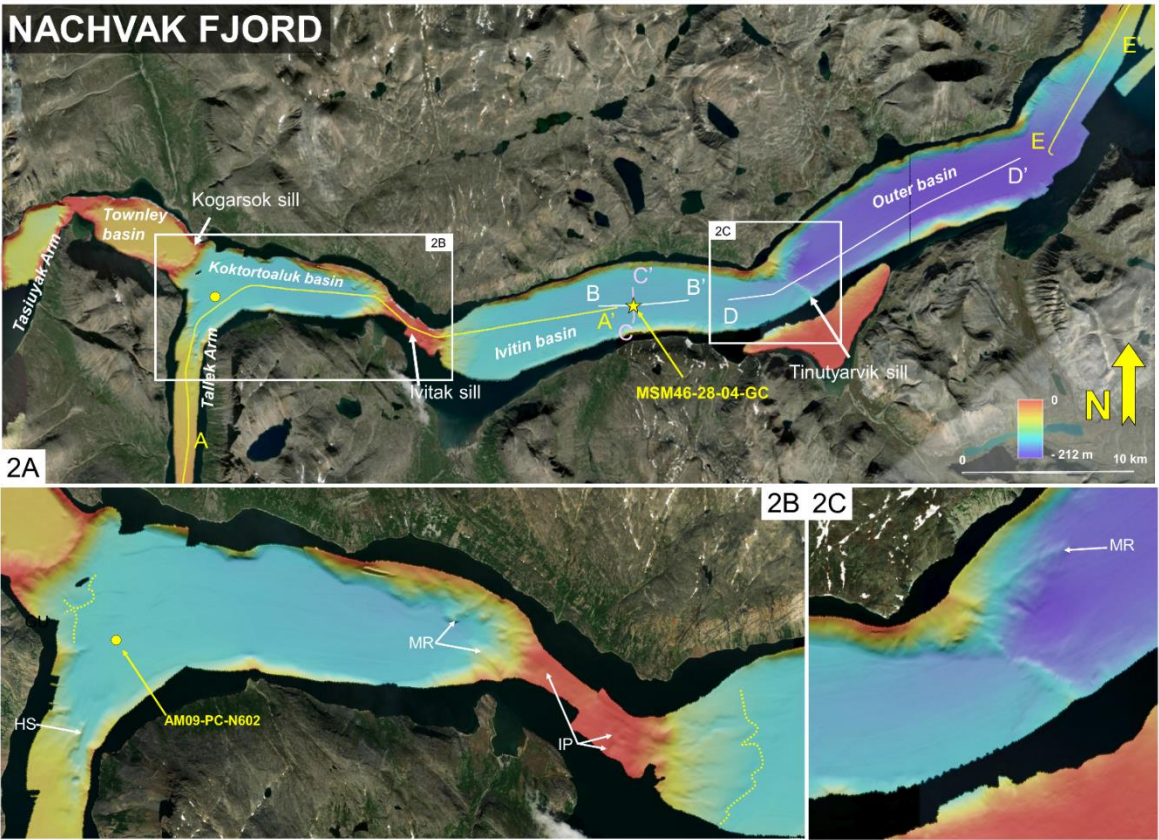
Terrestrial fieldwork had been done in the area since the 1950s and contributed to identify lateral moraines called the Saglek moraines that are interpreted as the LGM local limit (Ives, 1976; Clark, 1988; Occhietti et al., 2011), while cosmogenic  $^{10}\text{Be}$  ages suggested

that they were formed during the YD around 12-13  $^{10}\text{Be}$  ka (Clark et al., 2003). On another hand, despite a relatively controversial deglacial history of the Nunatsiavut coast (Evans and Rogerson, 1986; Clark and Josenhans, 1990; Occhietti et al., 2011), most of the studies considered an LGM limit close to the shelf break (Josenhans et al., 1986; Dalton et al., 2020) and an ice-free continental margin by at least 12 cal ka BP (Hall et al., 1999).

In the 1980 and 1990's, the pristine Nachvak Fjord received more attention than Saglek Fjord (Bell, 1987; Gallagher, 1989; Bell and Josenhans, 1997). Gallagher (1989) suggested, from radiocarbon dating on paleo-shorelines, that Nachvak Fjord was deglaciaded by 9000 BP –  $\approx$  10.3 cal ka BP. Extensive sub-bottom profiles in this fjord revealed a >180 m-thick sedimentary sequence apparently formed by at least two deglacial cycles that were not temporally constrained (Bell and Josenhans, 1997). In Saglek Fjord, only Chirp profiles showing the upper tens of meters of sediment had been published (Bentley and Kahlmeyer, 2012).

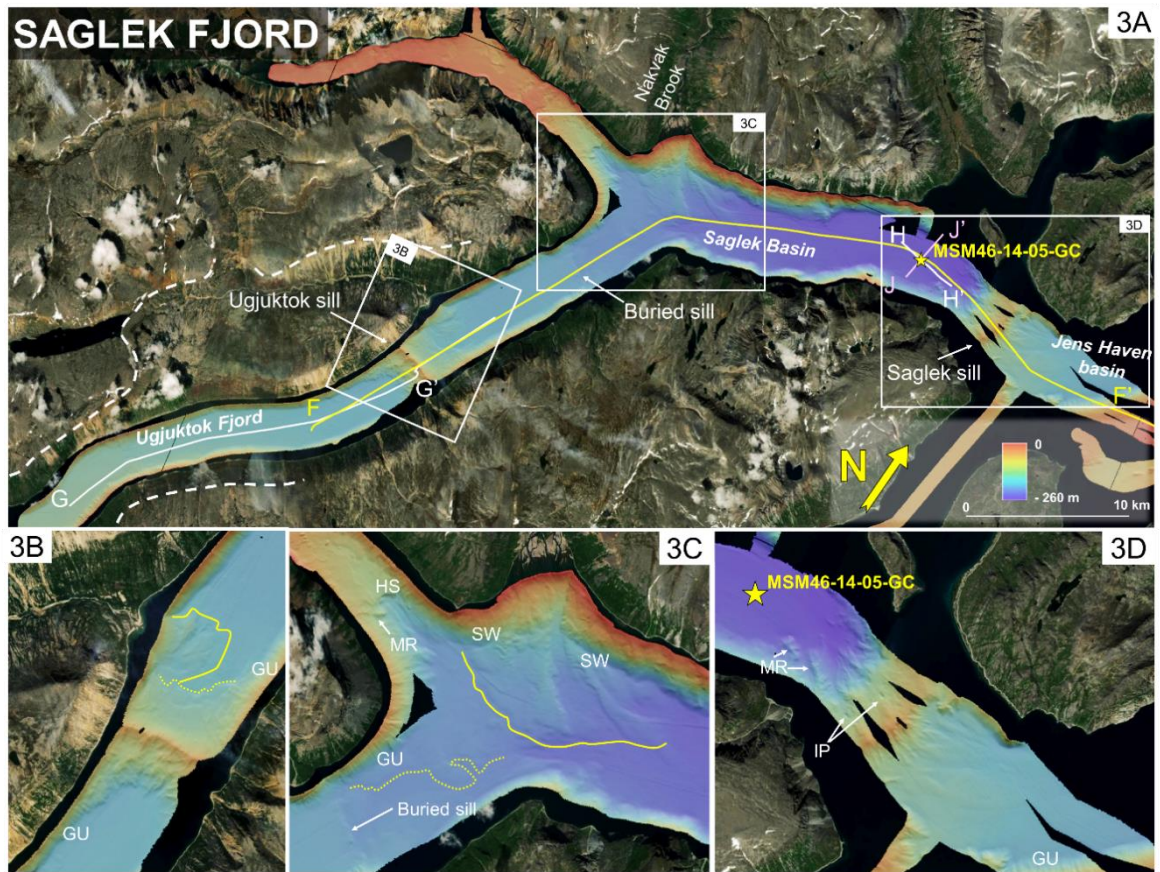
Box-cores have been sampled in both fjords for investigating fluvial sediment flux (Bentley and Kahlmeyer, 2012), dinoflagellates, diatoms and pollens (Richerol et al., 2014) and detrital organic matter (Barber et al., 2017) over the last centuries. However, longer cores were obtained only in Nachvak Fjord (Bell, 1987; Richerol et al., 2016) and suggested that the postglacial transition occurred between 7300 and 5200 BP -  $\approx$  8.2 – 6 cal. ka BP (Gallagher, 1989).

On the Labrador continental shelf, some basins with high sedimentation rates have also been investigated for paleoceanographic studies, such as Karlsefni Trough (Hall et al., 1999; Lochte et al., 2019a, 2019b; Rashid et al., 2017), Hopedale Saddle (Keigwin et al., 2005) and Cartwright Saddle (Keigwin et al., 2005; Jennings et al., 2015).



**Figure 12.** Swath bathymetry map of Nachvak Fjord, with location of seismic lines AA', BB', CC', DD' and EE' (Fig. 14) and coring sites of core 28-04-GC (this study) and core AM09-PC-N602 (Richerol et al., 2015). GU = gullies; HS = headscarps; IP = icebergs pits; MR = morainic ridges. Yellow dotted lines show the limit of depositional lobes.





**Figure 13.** Swath bathymetry map of Saglek Fjord, with location of seismic lines FF', GG', HH' and JJ' (Fig. 15) and coring sites of core 14-05-GC. All the names of Saglek basins and sill are proposed in this study. GU = gullies; HS = headscarps; IP = icebergs pits; MR = morainic ridges. Yellow dotted lines show the limit of depositional lobe. Yellow plain lines are the limits of sediment fans. White dotted lines are the location of the Saglek Moraines as identified by Ives (1976).

## **1.5 MATERIALS AND METHODS**

### **1.5.1 Geophysical data**

Swath (multibeam) bathymetry data were obtained from the ArcticNet Basemaps database, where the Ocean Mapping Group have compiled multibeam echosounder surveys realised onboards the NGCC Amundsen and the CSL Heron between 2006 and 2013. Most of these surveys were realised with a Kongsberg EM302 30 kHz multibeam echosounder. These allow identifying deposits and landforms related to deglacial and postglacial dynamics in the fjords.

Parts of the acoustic sub-bottom profiler dataset used here were collected during leg 4b of the CCGS Amundsen campaign in 2009 with a Knudsen K320R 3.5 kHz Chirp that sweeps through a band of frequencies between 2-7 kHz. More recent data were obtained during the MSM46 expedition of the RV Maria S. Merian in 2015 with a PARASOUND P70 operating at primary frequencies between 18 – 28 kHz with parametric secondary frequencies in the range of 0.5 – 10 kHz. Sediment thicknesses have been estimated with a sediment velocity of 1500 m/s, as in other similar environments (Hjelstuen et al., 2009; Bellwald et al., 2016).

### **1.5.2 Sampling**

Two gravity cores were sampled during RV Maria S. Merian expedition MSM46 in 2015 (Fig. 12 to 15). In Nachvak Fjord, a 9.76 m-long gravity core named MSM46-28-04-GC was sampled in the Ivitin Basin (59°02.995'N; 63°39.000'W; 165 m water depth; hereafter core 28-04-GC). In Saglek Fjord, the 13.35 m-long gravity core MSM46-14-05-GC, was sampled in the eastern Saglek Basin (58°29.510'N; 63°09.027'W; 247 m water depth; hereafter core 14-05-GC). The sub-bottom profiles were used to select sites with enough sediment thickness for high-resolution deglacial and postglacial analyses, thus with sedimentation rates in the range of 1 m/ka.



### 1.5.3 Physical properties analyses

Core 28-04-GC was opened, described and photographed on board the ship directly after core collection, and digital X-ray images were obtained on U-channels with a CT-scan at the INRS-ETE in Québec City. Core 14-05-GC was opened later at ISMER, where it was also described and photographed.

At ISMER, all the split cores have been run into a Geotek XCT digital x-ray system, and then into a Multi Sensor Core Logger (MSCL) to measure several parameters at 1 cm intervals: the low-field magnetic susceptibility ( $k_{LF}$ ) with a Bartington point sensor, diffuse spectral reflectance using a Minolta CM-2600d spectrophotometer, and elemental composition and concentration with an Innov-X Olympus Delta Element x-ray fluorescence (XRF) spectrometer.  $k_{LF}$  is a first order measure of the concentration of ferrimagnetic material, such as (titano)magnetite, and can be enhanced by large grains ( $>10 \mu\text{m}$ ) or decreased with dilution by detrital carbonates and organic matter (Stoner and St-Onge, 2007; Korff et al., 2016). Spectral reflectance was used to acquire colour data reported in the  $a^*$  colour space, a green to red scale of the International Commission on Illumination (CIE) (e.g., St-Onge et al. 2007; Debret et al. 2011). Elemental ratios obtained by XRF data provide information about sediment characteristics and associated processes. Here, we use the Ca/Ti as a proxy for carbonate content, Ca/Sr to verify if variations in carbonate content are driven by detrital or biogenic material, and Zr/Rb to follow grain-size variations in the core and help identify important terrigenous inputs such as turbidites (e.g., Croudace et al., 2006; Hodell et al., 2008; Piva et al., 2008; Croudace and Rothwell, 2015; Duboc et al., 2017). The Fe/ $k_{LF}$  is also investigated, as this proxy compares magnetite content with total iron content and can highlight changes of ferrimagnetic minerals concentration when bulk sediment composition is steady (Funk et al., 2004; Hofmann et al., 2005; Korff et al., 2016).

#### **1.5.4 Grain-size analyses**

Discrete samples were collected every 10 cm on the sections covering noticeable changes in MSCL data in cores 28-04-GC, 14-05-GC and 13-03-GC, and every 20 cm on the rest of the cores. The samples were diluted into a Calgon solution (1% sodium hexametaphosphate) and then analysed with a Beckman Coulter LS13320 laser sizer. The results were computed with GRADISTAT to determine grain-size statistical data (Blott and Pye, 2001). Lower halves of cores 14-05-GC and 28-04-GC were also sieved at 63  $\mu\text{m}$  and then 150  $\mu\text{m}$  in order to evaluate proportions of sand and IRDs in these sections.

#### **1.5.5 Magnetic properties analysis**

An alternating gradient force magnetometer (AGM) was used on discrete samples from cores 28-04-GC and 14-05-GC to measure rock magnetic properties of the sediment: the magnetic moment at saturation ( $M_s$ ), the saturation remanence ( $M_{rs}$ ), the bulk coercive force ( $H_c$ ) and the remanent coercivity ( $H_{cr}$ ). The resulting  $M_{rs}/M_s$  and  $H_{cr}/H_c$  are used to plot the data in the so-called Day-diagram in order to investigate variations of the magnetite grain-size through the sediment sequences (e.g., Day et al., 1977; Roberts et al., 1995; Channell and Hodell, 2013). This works only if (titano)magnetite is the dominant magnetic carrier, which can be determined with the measured hysteresis loops. The shape of the hysteresis loops yields information on the mineralogy and grain size of the magnetic carrier and can thus highlight variations in the sediment composition (e.g., Tauxe et al., 1996).

#### **1.5.6 Organic geochemistry**

Variations in the amount and the composition of organic matter reflect changes in environmental conditions and sediment provenance through time (Meyers, 1997; Lamb et al., 2006). For this study, sediment samples were analysed in core 14-05-GC every 20 cm in sections where MSCL properties revealed major changes and every 40 cm in the rest of the core. For each sample, percentages of nitrogen and carbon content were first measured. Sediment was dried, crushed, then split in two subsamples, and one of these two subsamples

was treated with HCl by fumigation to remove inorganic carbon (Harris et al., 2001; Ranmarine et al., 2011). All samples were then analyzed at the organic geochemistry environmental laboratory of GEOTOP (UQAM) with a gas chromatograph coupled to a mass spectrometer for stable isotope ( $\delta^{13}\text{C}$ ) and an elemental analyzer (GC-EA-IRMS, ThermoElectron/ COSTECH) to measure C and N contents (%C, %N). By combining the data from the treated and untreated samples, we can determine  $C_{\text{total}}$ ,  $N_{\text{total}}$ ,  $C_{\text{org}}$ , the  $C_{\text{org}}/N_{\text{total}}$  elemental ratio and the  $\delta^{13}\text{C}$  isotopic ratio.

### **1.5.7 Radiocarbon chronology**

Chronologies of both cores are first based on a total of 25 radiocarbon ages obtained on mollusc shells and foraminifera samples (Table 2). Mollusc shells were directly sampled in the cores and sent for analysis to the Leibniz Laboratory for Radiometric Dating and Isotope Research of Kiel University (CAU), Germany. The foraminifera were picked in sediment samples previously sieved at 63  $\mu\text{m}$  and then analysed at the ETH Zürich (Switzerland).

The obtained  $^{14}\text{C}$  ages were then calibrated online with Calib 8.2 (Stuiver et al., 2020) using the Marine20 radiocarbon curve (Heaton et al., 2020) after choosing an age reservoir correction ( $\Delta\text{R}$ ) as discussed after, and the R software package BACON was used to produce the best-fit linearly interpolated age models (Blaauw and Christen, 2011). All the  $^{14}\text{C}$  ages were integrated in the model, even those which seem reversed but are still coherent with their standard deviation.

There is no proposed  $\Delta\text{R}$  for Saglek and Nachvak fjords yet, but the values for cores 14-05-GC and 28-04-GC should be similar to those from the continental margin of Northern Labrador, as the cores sites are located in basins well connected to the shelf. McNeely et al. (2006) established regional value of  $\Delta\text{R}$  for the different Canadian coastal areas, including the Labrador Sea where this value is  $144 \pm 38$  yr when using Marine09 and Marine13 calibration curves. Nevertheless, the new Marine20 calibration curve (Heaton et al., 2020)

requires new regional reservoir corrections that were calculated by Brouard et al. (2021). We thus use the  $\Delta R$  of  $-2 \pm 69$  they obtained for Labrador Sea.

Some studies added another 200 yr to the  $\Delta R$  for the ages older than 6.0  $^{14}\text{C}$  ka BP or 7.0  $^{14}\text{C}$  ka BP in cores from Labrador Sea, in order to make the correction for the longer duration of sea-ice cover at this time (Lewis et al., 2012; Rashid et al., 2017; Lochte et al., 2019a, 2019b). However, Jennings et al. (2015) chose to not increase the  $\Delta R$  value for older ages in core MD99-2236 sampled in Cartwright Saddle, as well as Brouard et al. (2021) when they recalibrated ages from core MSM45-19-2 previously published by Lochte et al., (2019a). We chose to do the same, and keep a consistent  $\Delta R$  value through time, as we cannot evaluate the impact of freshwater discharge and sea-ice cover inside the fjords. However, the real values could be younger than those obtained after calibration.

**Table 2.** List of AMS radiocarbon ages analyzed and calibrated in Calib8.2 (Stuiver et al., 2020) using the Marine20 dataset (Heaton et al., 2020).

Core	Depth (cm)	Dated material	Uncorrected $^{14}\text{C}$ age ( $^{14}\text{C}$ yr BP)	Reservoir correction $\Delta\text{R}$ ( $^{14}\text{C}$ yr BP)	2 sigma age range (cal. yr BP)	Median probability age (cal. yr BP)	AMS laboratory number
MSM46-14-05- GC	339	Mollusk shell	3805 ± 27	-2 ± 69	3368-3820	<b>3582</b>	KIA-54306
<i>Saglek Fjord</i>	522	Mollusk shell	4782 ± 28	-2 ± 69	4588-5121	<b>4854</b>	KIA-54307
	647	Mollusk shell	5630 ± 30	-2 ± 69	5593-6040	<b>5822</b>	KIA-54308
	759	Mollusk shell	6175 ± 35	-2 ± 69	6207-6633	<b>6413</b>	KIA-54309
	926	Mix. benthic forams	7325 ± 70	-2 ± 69	7402-7849	<b>7613</b>	ETH-107319
	991	Mix. benthic forams	7950 ± 60	-2 ± 69	7998-8458	<b>8241</b>	ETH-102149
	1031	Mix. benthic forams	8220 ± 60	-2 ± 69	8308-8858	<b>8544</b>	ETH-102150
	1071	Mix. benthic forams	8490 ± 70	-2 ± 69	8583-9208	<b>8894</b>	ETH-102152
	1071	Mollusk shell	8430 ± 60	-2 ± 69	8528-9098	<b>8815</b>	ETH-102151
	1241	Mix. benthic forams	8770 ± 70	-2 ± 69	8993-9491	<b>9257</b>	ETH-102153
	MSM46-28-04- GC	69	Mix. benthic forams	1320 ± 55	-2 ± 69	503-915	<b>718</b>
<i>Nachvak Fjord</i>	369	Mix. benthic forams	4115 ± 55	-2 ± 69	3701-4267	<b>3986</b>	ETH-65449
	469	Mollusk shell	4569 ± 26	-2 ± 69	4359-4821	<b>4588</b>	UOC-2523
	569	Mollusk shell	5336 ± 21	-2 ± 69	5305-5712	<b>5511</b>	UOC-2524
	569	Mix. benthic forams	5450 ± 60	-2 ± 69	5407-5892	<b>5638</b>	ETH-101082
	596	Mollusk shell	5580 ± 30	-2 ± 69	5570-5983	<b>5772</b>	KIA-54320
	620	Mollusk shell	5835 ± 30	-2 ± 69	5856-6271	<b>6055</b>	KIA-54321
	636	Mix. benthic forams	6300 ± 60	-2 ± 69	6298-6788	<b>6547</b>	ETH-101084
	696	Mollusk shell	6740 ± 35	-2 ± 69	6813-7260	<b>7048</b>	KIA-54322
	721	Mix. benthic forams	7020 ± 60	-2 ± 69	7124-7554	<b>7333</b>	ETH-101085
	775	Mix. benthic forams	7585 ± 70	-2 ± 69	7627-8108	<b>7862</b>	ETH-107331
	819	Mix. benthic forams	7825 ± 70	-2 ± 69	7880-8350	<b>8112</b>	ETH-101086
	861	Mix. benthic forams	8505 ± 70	-2 ± 69	8598-9226	<b>8915</b>	ETH-107332
	911	Mix. benthic forams	8390 ± 70	-2 ± 69	8456-9053	<b>8766</b>	ETH-101087
	969	Mix. benthic forams	8620 ± 80	-2 ± 69	8753-9394	<b>9080</b>	ETH-101088

## 1.6 RESULTS

### 1.6.1 Fjord geomorphology

Both Nachvak and Saglek Fjords have the same general morphology with several basins separated by sills of different depths. Nachvak Fjord general morphology and bathymetry has already been described (Bell, 1987; Gallagher, 1989; Bell and Josenhans, 1997). Therefore, the focus will be first on Saglek Fjord and then on the detailed bathymetric features of both fjords.

## 1.6.2 Saglek Fjord general geomorphology

If Ugjuktok Fjord is included in Saglek Fjord, they contain together two long basins named here, from West to East, Ugjuktok Basin and Saglek Basin. Ugjuktok Basin is a 28 km-long and 2.5 km-wide trough bounded by steep walls, and slightly dipping seaward with a maximum depth of about 180 m at its northeastern end. It is separated from Saglek Basin by an 80 m-deep sill named here the Ugjuktok sill. The Saglek Basin is about 40 km-long, 3 to 6 km-large and turns East at its center where it is joined by the West arm complex, which has a 40 to 60 m-deep seafloor. The Saglek Basin can be divided in three parts: the western, central and eastern Saglek Basins. While the western and eastern Saglek Basins are relatively flat with mean depths of about 180 and 250 m, respectively, the central Saglek Basin is rather a transition between them with a more hummocky seafloor. Saglek Basin is separated from Saglek Bay by a 180 m-high and 80 m-deep sill, here named the Saglek sill. Swath bathymetry imagery also cover a smaller basin in Saglek Bay on the other side of Saglek Sill, here named the Jens Heaven Basin, like the island beside.

### 1.6.2.1 Sills and moraines

In both fjords, sills of different shapes are the predominant bathymetric features (Figs. 2, 3). In Nachvak Fjord, the high Kogarsok sill has the typically high, thin and arched shape of frontal morainal ridge. The smaller Tinutyarvik sill is also likely formed by a frontal moraine (Bell, 1987). The Ivitak sill, however, was described as a bedrock sill with a 4 km-wide plateau at 100 m above the adjacent basins, with about 20 m of glaciomarine sediment at its top (Fig. 12 and 14; Gallagher, 1989; Bell and Josenhans, 1997).

In Saglek Fjord, Ugjuktok and Saglek sills are also typical frontal moraines. Another frontal moraine is located about 12 km north from Ugjuktok, noticeable by a short steep bathymetric transition on the northeastern side. This morainic sill marks the limit between western and central Saglek Basins, named hereafter the Buried sill, is better observed on the acoustic profile FF' (Fig. 15).

#### 1.6.2.2 Sediment-filled basins and sediment fans

Saglek and Nachvak Fjords basins show a tabular seafloor that often characterizes sediment-filled fjord basins (Batchelor et al. 2019; Brouard and Lajeunesse, 2019). During and after deglaciation, basin depressions were filled by proglacial, paraglacial and postglacial hemipelagic sediment. The central Saglek Basin, however, is not as flat as the others, and shows many bathymetric features, particularly a large, 5 km-wide semi-circular bulges located at the mouth of Nakvak Brook. This feature is likely a sediment fan that started as an ice-proximal fan and is still fed by sediments from the huge watershed of Nakvak Brook that largely contributes to the contemporary sediment budget of Saglek Fjord (Bentley and Kahlmeyer, 2012). Swath bathymetry imagery shows some sand-waves on the sediment fan and a 0.2-1.0 km-wide channel incising it. A smaller fan is also observed downstream Ugjuktok sill and is associated with a minor tributary valley.

#### 1.6.2.3 Scarps and depositional lobes


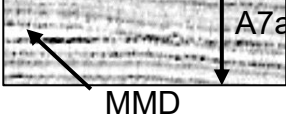
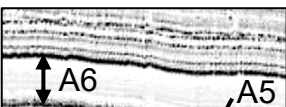

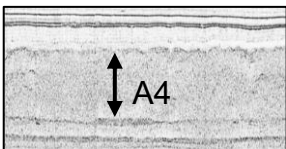
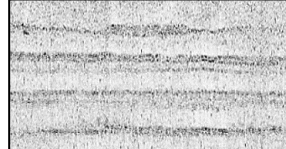
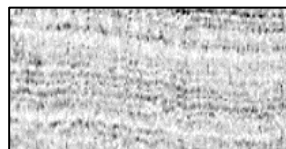
The seafloor around the sills is particularly hummocky, which is evidence of a more dynamic deposition and sediment destabilization along the sills after the ice retreat. In some cases, this destabilization formed depositional lobes such as the one on the seaward toe of Ivitak sill that appears like a sediment fan. Tens of meter-high headscarps are also visible on the transition from basins to shallower plateaus, such as in Tallek Arm and the West arm complex; they are correlated to mass-movement deposits (MMDs) that are observed on acoustic profiles (Fig. 14 and 15).

#### 1.6.2.4 Other submarine landforms

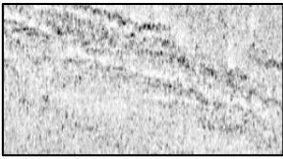
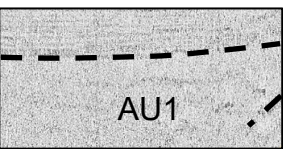
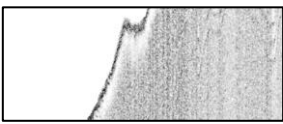
Numerous gullies are also observed along basin flanks on the swath bathymetry imagery and are particularly obvious in Ugjuktok Fjord. These small v-shaped linear depressions are typically formed where slopes are higher than 10°.

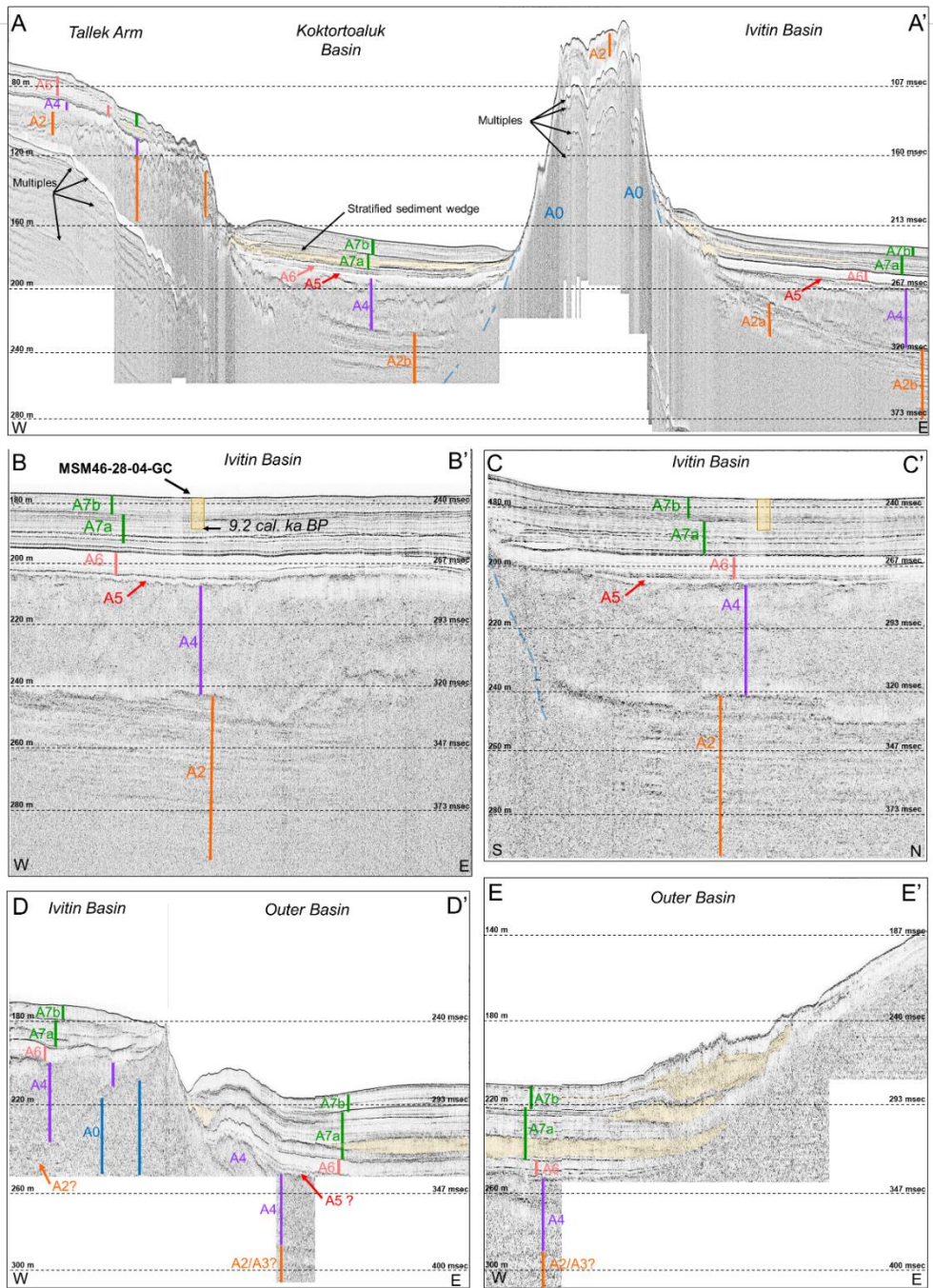
Finally, small pseudo-circular depressions are located on the seafloor of shallower sectors such as Tallek Arm and Ivitak sill. These depressions are probably iceberg pits – or ploughmarks – formed by grounded or flipping icebergs. In the Tallek Arm, a pronounced iceberg pit is located near an MMD headscarp. This MMD, and maybe others, could have been triggered by the movement of icebergs on the seafloor (Normandeau et al., 2021).

**Table 3.** Acoustic units in the sedimentary sequences of Nachvak and Saglek Fjords.

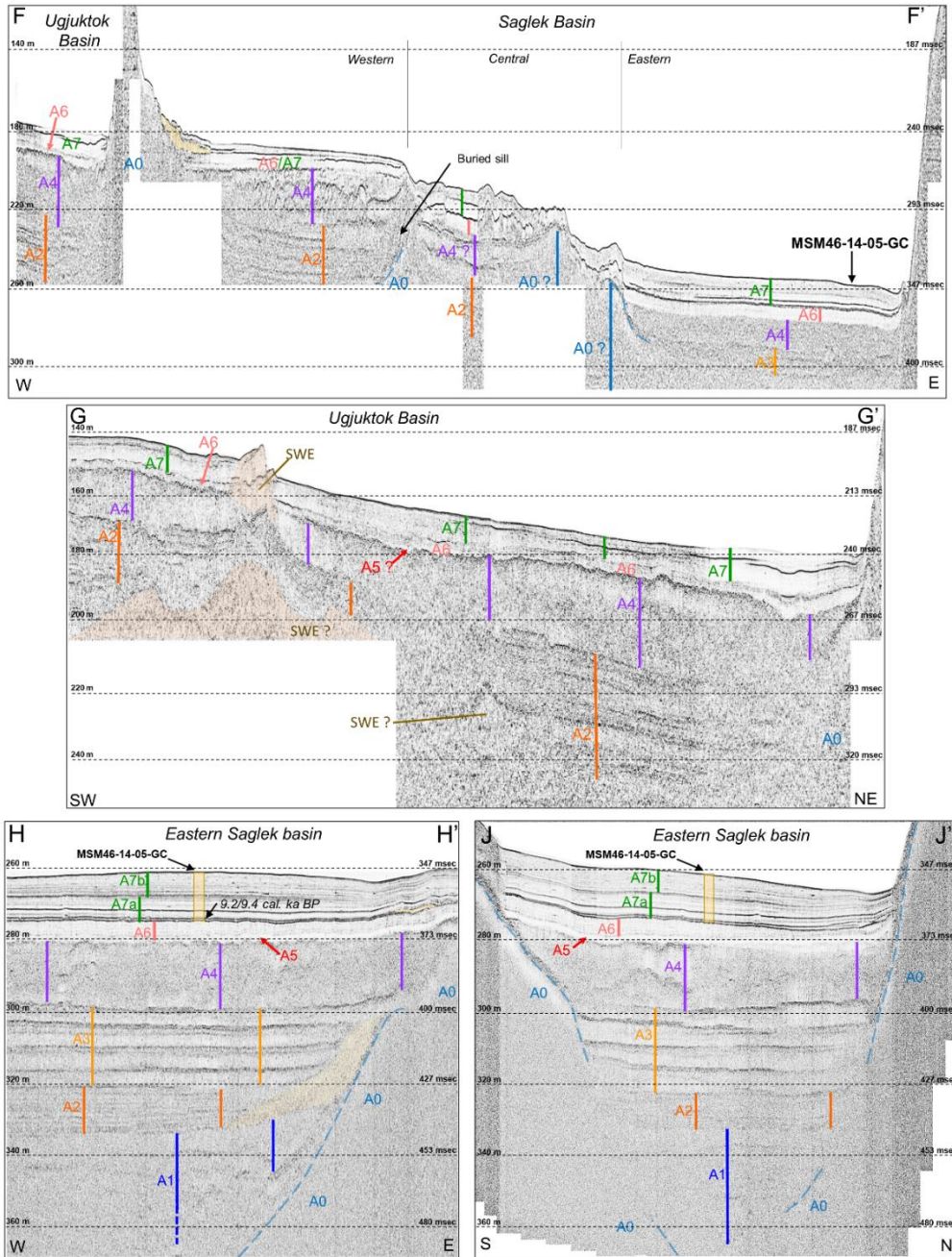
Acoustic unit	Acoustic properties	Acoustic profile	Thickness (m)	Interpretation
<b>7b</b>	Low- to medium-amplitude reflectors with a draping geometry		5-15	Hemipelagic postglacial sediments
<b>7a</b>	High- to medium-amplitude reflectors interbedded with transparent lenses		5-25	Hemipelagic and paraglacial sediments with MMDs & RDLs
<b>6</b>	Low-amplitude parallel reflectors that conformably drape lower units		~5	Distal glaciomarine sediments
<b>5</b>	Transparent, irregular unit, draping A4		1-5	Proximal glaciomarine sediments
<b>4</b>	Semi-transparent, internal chaotic reflectors. Strong and hummocky upper reflector. Ponded geometry		20-40	Massive MMDs
<b>3</b>	Transparent horizontal, ponded lenses transiting progressively upward to pseudo-parallel medium to strong reflectors		~20	Thick RDLs intercalated with glaciomarine sediments
<b>2b</b>	Medium to strong amplitude, parallel and closely spaced reflectors		20-40	Distal proglacial sediments



<b>2a</b>	Medium to strong amplitude, sub-parallel, wavy to chaotic reflectors		20-40	Proximal proglacial sediments
<b>1</b>	Harshly visible transparent unit with chaotic strong internal reflectors.		> 15 m	MMDs or ice-contact sediment
<b>0</b>	Absence of acoustic penetration. Upper strong reflector		N/A	Bedrock or glacial till



**Figure 14.** Acoustic profiles from Nachvak Fjord. Location of the profiles are indicated on Fig. 12. The different acoustic units are indicated and delimited. Zone highlighted in light yellow represent the identified MMDs. Profiles AA', BB' and CC' were obtained during the MSM46 cruise, whereas profiles DD' and EE' are from the Amundsen Science Data Collection and was obtained during the ArcticNet campaign of November 2009.



**Figure 15.** Acoustic profiles from Saglek Fjord. Location of the profiles are indicated on Fig. 13. The different acoustic units are indicated and delimited. Light yellow patches represent the identified MMDs, while the orange ones represent the sidewall echoes interfering with the signal (SWE). Profile HH' and JJ' were obtained during the MSM46 cruise, whereas profiles FF' et GG' come from Amundsen Science Data Collection and were obtained during the leg4b of the ArcticNet campaign of November 2009.

### 1.6.3 Sub-bottom profiles

The acoustic sub-bottom profiles reveal up to 110 m of sediment thickness in both fjords (Fig. 14, 15 and 16). They thus do not cover the entire 180 m-thick Quaternary sequence of Nachvak Fjord presented by Bell and Josenhans (1997), and likely do not reach the bedrock under the Saglek Fjord basins either. However, these profiles give a first overview of most of the Quaternary sequence in Saglek Fjord, which is mostly similar to one in Nachvak Fjord. The sequences presented here are composed by seven acoustic (A) units presented in Table 3, with more details in the text below. Units A0, A1, A2, and A4 likely correspond respectively to units A, B, C and D in Bell and Josenhans (1997), whereas A6 and A7 together correspond to unit E. Units A3 and A5 are described for the first time in the area. The particular case of the central Saglek Basin is presented after the units. Some features may be caused by sidewall echoes and may not represent the real stratigraphy, particularly where the valley is narrower. This is the case in Ugjuktok Basin where the ship got closer to a bathymetric high. Some other reflectors in the deepest units might be also produced by sidewall effects.

The lowermost unit A0 could represent bedrock or glacial till, as the acoustic frequencies used do not differentiate the two materials. This is evident for the morainic sills, such as the Ugjuktok sill, that are made of ice-contact sediments but not penetrated by the acoustic signal.

A1 is the lowermost unit having internal reflectors, although it possible corresponds to unit B in Bell and Josenhans (1997) interpreted as glacial diamicton. This unit, observed only in the eastern Saglek Basin here, could also be made of MMDs but the signal does not permit a definite interpretation.

A2 corresponds to unit C in Bell and Josenhans (1997), which is 80 to 130 m thick in Nachvak Fjord. In Saglek Fjord, A2 is only about 10-15 m-thick in the eastern Saglek Basin but reaches a thickness of at least 40 m in the Ugjuktok and western Saglek Basin where the unit base is not detected. A2 generally shows a higher thickness and steepness on the seaward side of the sills. This unit can be divided in two subunits: a more chaotic A2a that drapes the basin slopes, mostly on the landward side, and an A2b with more horizontal reflectors that continue A2a seaward and tends to fill the depressions. Unit A2 likely correspond to proglacial, glaciomarine sediments as often been

observed in other deglaciated troughs or basins (Hjelstuen et al., 2013; Hjelstuen and Brendryen, 2014; Trottier et al., 2020).

The ponded unit A3 is well defined in the eastern Saglek Basin where it forms a 20 m-thick stack of four lenses over A2. A3 is possibly present in the Nachvak Outer Basin, but this was not observed by Bell and Josenhans (1997) and the signal accuracy is insufficient. Unit A3 is likely a stack of 4 MMDs or turbidites separated from each other by glaciomarine sediments. Similar stacks were found in Canadian, Chilean, Patagonian or Norwegian fjords (Waldmann et al., 2011; St-Onge et al., 2012; Hjelstuen and Brendryen., 2014; Bellwald et al., 2016).

A4 is a medium-tone massive unit with a basin-fill geometry and a hummocky surface and corresponds to unit D in Bell and Josenhans (1997). A4 is 20 to 30 m-thick in Saglek Fjord but reaches 40-50 m in Nachvak Fjord. In some cases, A4 is transparent, but in other cases it shows internal chaotic reflectors. These reflectors are particularly strong in the Koptortoaluk and the western Saglek Basins. The unit base seems erosive in some cases, as in the Ivitin Basin where A2 is truncated by more than 10 m locally (Fig. 14-BB'). Bell and Josenhans (1997) suggested that this unit consists of ice-contact sediment and was shaped by a glacial readvance. However, its homogeneous signal with rare to inexistant internal strong reflectors rather corresponds to a MMD signature. Similar thick homogeneous acoustic units observed in fjords were interpreted as MMDs (Hjelstuen et al., 2009; Broom et al., 2017).

The irregularly thin unit A5 was not described by Bell and Josenhans (1997), probably due to its thinness, but its properties make it distinct from A4 and A6. This unit is well constrained in the western half of Ivitin Basin where it is pinched towards the fjord walls, and in the Koptortoaluk and eastern Saglek Basins. A less defined unit 5 is also found in the Nachvak Outer Basin and in the Ugjuktok basin, but the unit is not observed in the western and central Saglek Basins. This unit was maybe associated with the A4 MMD as fine suspended sediment remobilized during the event, or a subsequent smaller turbidite.

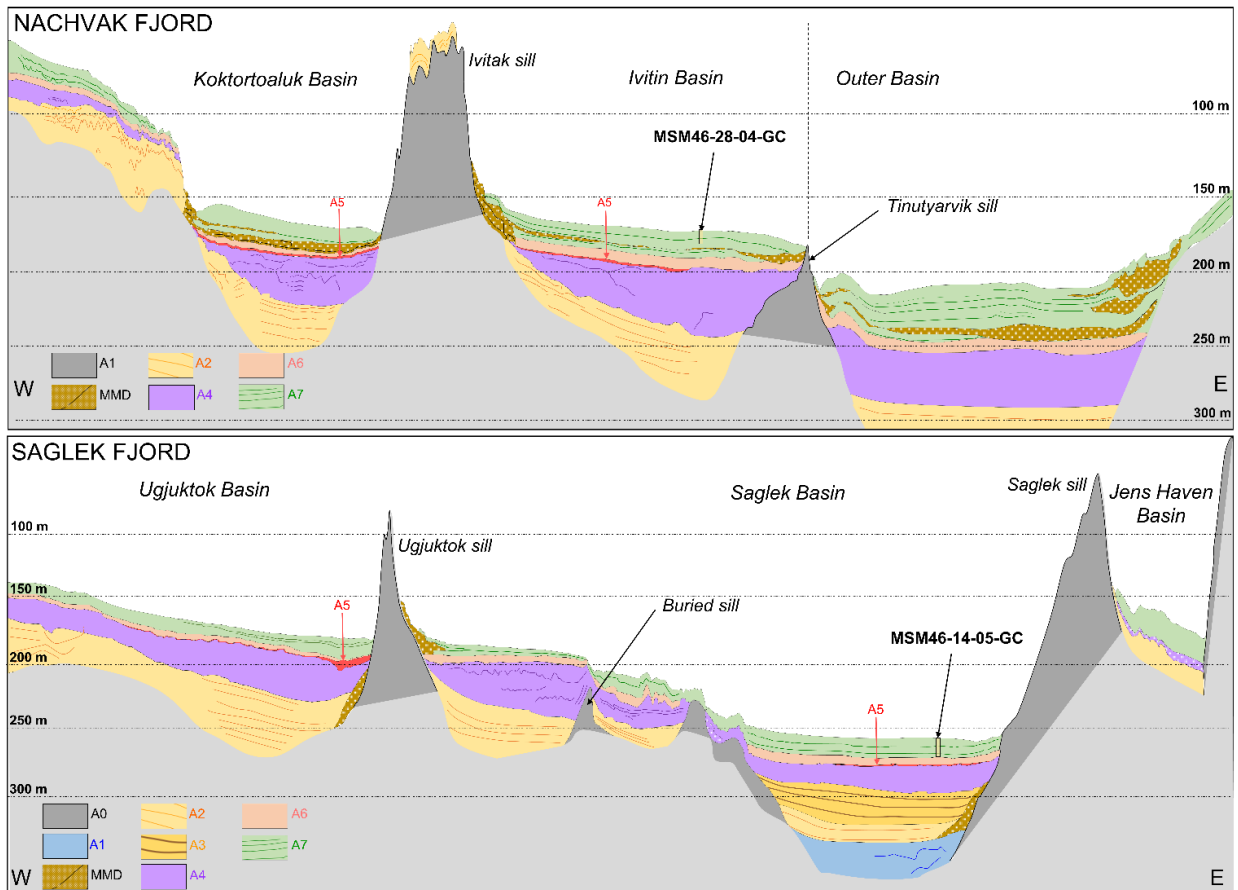


A6 often shows one to three moderately stronger reflectors at the base and a strong one at the upper boundary. It sometimes transits more progressively upward to slightly stronger and less parallel reflectors in unit 7, but do not contain MMDs or turbidites. This unit is almost transparent in the Nachvak Ivitin and Outer Basins, and in the eastern Saglek Basin. A6 is likely made of distal glaciomarine sediments (Normandeau et al., 2013).

A7, the upper unit, can be divided in two subunits not always distinct on the profiles. The lowermost, A7a, is generally less than 10 m-thick but reaches 15 and 25 m in Nachvak Ivitin and Outer Basins respectively. A7a contains chaotic to transparent lenses generally located at basin edges but sometimes spread over on a few km and often continued by strong reflectors along the basins. In the Kоктортоалук Basin, A7a is mostly composed by such lenses, including a basin-wide, 6 to 7 m-thick one looking slightly stratified. Just over this lens is localized a 5-6 m-thick wedge of acoustically stratified sediments. The uppermost subunit A7b is more homogeneous with weaker reflectors and generally no remarkable RDLs. Only one late MMD occurred on the eastern flank of the Nachvak Outer Basin. A7b tends to conformably drape lower units, but is often pinched in the end of basins, particularly pronounced in the Kоктортоалук Basin where the unit reaches a maximum thickness of 15 m. The entire unit A7 probably consists of paraglacial and postglacial sediment, as observed in other similar settings (e.g., Gagnon-Poiré et al., 2018). In A7a, the lenses and strong reflectors are likely MMDs and turbidites respectively (Hjelstuen et al., 2009; Bellwald et al., 2019), caused by paraglacial processes (Syvitski and Praeg, 1989; Syvitski, 1991; Stoker et al., 2010). A7a is thus a mixture of paraglacial and hemipelagic sediments, while A7b is mostly hemipelagic and deposited in a calmer setting after the postglacial transition. The A7b pinching indicates sediment drifts caused by local currents and forming contourites.

The acoustic sequence in the center of the Saglek Basin is very chaotic and difficult to interpret. However, it appears that this basin is limited to the west by the Buried Sill and by another moraine to the east that is still hard to constrain. Nevertheless, an interpretation is proposed in Fig. 16, but still needs to be confirmed.

Finally, apart from those of unit A4, many MMDs are located on basin flanks as transparent wedges. Some of them predate A2 deposition while most of them are concomitant with A7a deposition.



**Figure 16.** Stratigraphic framework of Nachvak and Saglek Fjords made from acoustic data. The different units are represented, as well as their internal reflectors. Light grey represents where we do not have sufficient acoustic penetration.

#### 1.6.4 Cores sedimentology

Both cores 14-05-GC and 28-04-GC mainly consist of brown to olive-gray silty-clay with several millimeter- to centimeter-thick IRDs visible on the XCT images. IRDs are more concentrated in core 28-04-GC, and XCT images of both cores also show numerous cm-large

bivalve shells, mostly in the upper halves. Lower halves of both cores contain light clayey, carbonate-rich layers. Geochemical, physical and sedimentological properties show similar patterns for both cores (Fig. 17), which can be divided in 4 main lithological units (1 to 4) from base to top, based on variations of the different parameters. This division is highlighted in Figures 7 C and D where units L2 and L3 have noticeably higher Ca/Ti values than other units, which are themselves differentiated by their magnetic susceptibilities.

Unit L1 was only sampled in core 14-05-GC and shows a homogeneous, carbonate-poor grey mud, with a slightly decreasing upward grain-size and magnetic susceptibility. This unit contains a very low percentage of sand and IRDs (<0.3%), as shown by sieving data (Fig. 18).

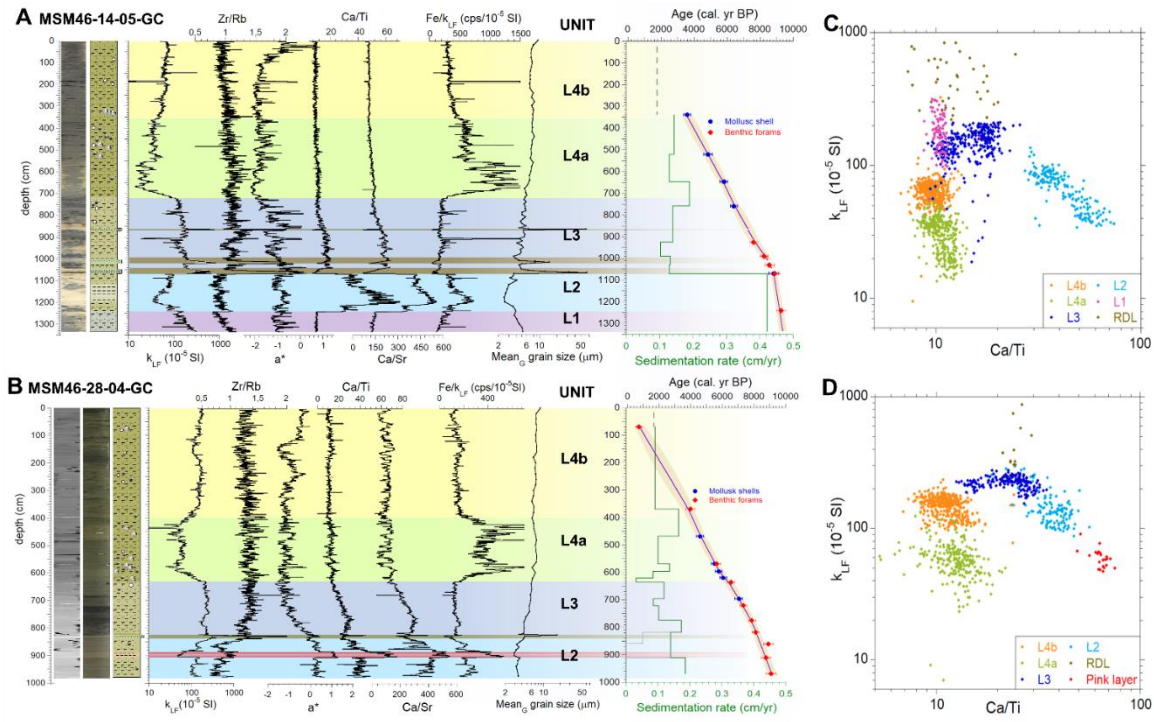
Unit L2, which overlain unit L1 with a sharp transition of the different physical and geochemical parameters, is composed by a light, carbonate-rich clayey mud, with a Ca/Ti 4 to 6 times higher than in units 1 and 4, and a lower magnetic susceptibility. The Ca/Sr, higher than in other units, suggests that these carbonates have mostly a detrital origin. In core 14-05-GC, unit L2 is 180 cm thick including a major 90 cm-thick peak of detrital carbonates (DC) that decreases upward with an increase of IRD (Fig. 8A). In this core, L2 is also topped by a RDL that have an erosive base, explaining the sharp upper transition. In core 28-04-GC, the base of unit L2 was not sampled and its top was not eroded. The highest Ca/Ti peak corresponds to a pinkish, 22 cm thick layer with a higher value of  $a^*$ , which is topped by a very thin – about 0.5 cm – layer of sand (Fig. 18B). This pinkish layer has no equivalent in core 14-05-GC and its structure, only visible on the CT-scan of the U-channel, consists of 8 to 10 wavy laminations, which is quite different from the rest of unit L2 (Fig. 18C). Above the pinkish layer, the sediment has a decreasing upward DC content and a slightly coarsening upward grain-size starting at 850 cm and ending with a double coarser peak between 836 and 826 cm. The upper of these two peaks is 5 cm-thick, contains 10% of fine sand, and is overlain by a 2 cm-thick DC layer (Fig. 18B). We thus chose to put the transition to unit L3 just above this last DC layer of core 28-04-GC.



Unit L3 corresponds to an olive-grey silty-mud characterized by a high magnetic susceptibility and relatively high – still lower than in unit L2 – Ca/Ti and Ca/Sr values (Fig. 18). These ratios are first stable in core 14-05-GC and slightly increasing in core 28-04-GC, and then progressively decrease upward in both cores. The sediment also has a slightly increasing mean grain-size towards the top, with an increasing content of sandy particles. This unit also contains three RDLs in core 14-05-GC that have a turbidite structure with fining upward trends from fine sand to clay. They all have a sharp lower, maybe erosive contact, and are respectively 26, 15 and 5 cm-thick from the lower to the upper one. Ca/Ti, Zr/Rb,  $k_{LF}$  and sieving data were combined to precisely determine their limits. Sieving data are very useful to delimitate the top of the turbidites, as their upper parts are exclusively made of mud (Fig. 18).

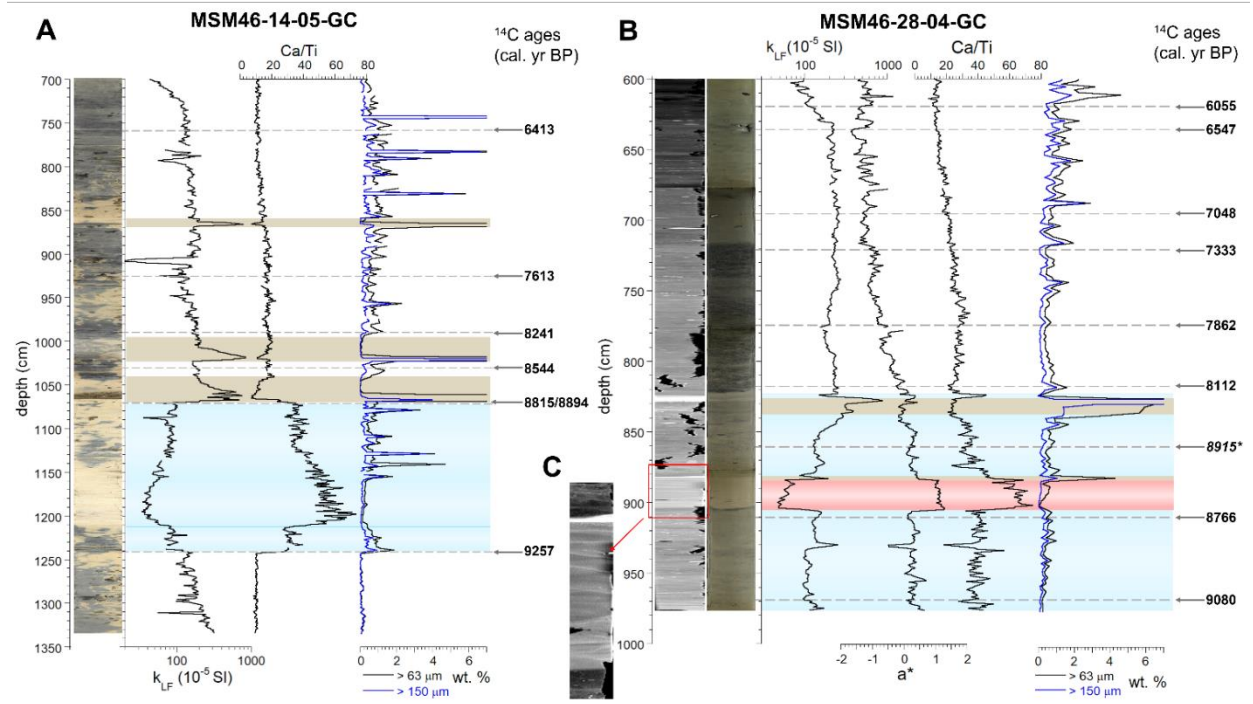
The transition between units 3 and 4 is highlighted by variations of all parameters, particularly  $k_{LF}$  that has values decreasing quickly by about 75% in both cores (Fig. 17). Unit L4 is composed of brown to grey silt with a more important fraction of coarse silt in core 28-04-GC, explaining the higher magnetic susceptibility in this core. Unit L4 shows near-homogeneous physical and chemical parameters except for the magnetic susceptibility, allowing us to split unit L4 in two subunits. Subunit L4a shows the lowest magnetic susceptibility of all units in both cores, with 2 to 4 times lower values than in subunit L4b, and Fe/ $k_{LF}$  values consequently much higher, as Fe content does not much change through unit L4. However, this low-magnetic susceptibility interval does not show the same trend in both cores. In core 28-04-GC, subunit L4a has a symmetrical pattern of magnetic susceptibility values with two peaks of low values around  $30 \cdot 10^{-5}$  SI centered at 435 and 575 cm. In core 14-05-GC, magnetic-susceptibility of subunit L4a varies between the very low values of 15 and  $30 \cdot 10^{-5}$  SI in the lower half between 700 and 550 cm, to around  $35 \cdot 10^{-5}$  SI in the upper half. XCT images and direct observations also revealed the presence of many bivalve shells in life position in unit L4a in both cores – except for the 700-550 cm interval in core 14-05-GC – with a concentration up to ten times higher than in the rest of the cores. In subunit L4b, corresponding to the upper 3.6 and 3.8 m of cores 14-05-GC and 28-04-GC respectively, parameters depict similar homogeneous trends of sediment properties in both

cores. Magnetic susceptibility values are, however, higher in core 28-04-GC than in core 14-05-GC, which is probably caused by differences of sedimentation dynamics between the sites.



**Figure 17.** A) and B) Physical, geochemical and sedimentological properties of cores 14-05-GC and 28-04-GC respectively along with their CT-scan images (for core 28-004-GC), pictures, logs and age-models. Note that the magnetic susceptibility has a logarithmic scale.

Colors are associated with the different units described in section 4.3 plus the RDLs (in brown) and the pinkish layer in core 28-04-GC (in red). The age-models are made with AMS  $^{14}\text{C}$  ages from foraminifera and mollusc shells. Also represented is the sedimentation rate calculated by interpolation between all of the ages (green plain line) and the same without including ages that generate aberrant variations in sedimentation rates (grey line). The dashed line at the top represents the theoretical sedimentation rate if there is no loss at the core top. C) and D) Diagram of  $k_{LF}$  versus Ca/Ti of cores 14-05-GC and 28-04-GC respectively, with logarithmic scales.



**Figure 18.** A) and B) Magnetic susceptibility Ca/Ti and weighted percentage of two sieve sizes (>63  $\mu\text{m}$  and >150  $\mu\text{m}$ ) for the lower parts – units L1, L2 and L3 – of cores 14-05-GC and 28-04-GC respectively, along with the core pictures. The  $a^*$  is also added for core 28-04-GC. Detrital carbonate (DC) layers of unit 2 are highlighted in blue, the pinkish layer in pink and the RDLs in grey. The median probability of  $^{14}\text{C}$  ages obtained on these sections are also indicated. C) Zoom on the CT-scan of the pinkish layer.

### 1.6.5 Hysteresis parameters

Hysteresis loops from all units of both cores show the typical sigmoidal shape characterizing the predominance of ferrimagnetic minerals such as magnetite and titanomagnetites (Fig. 21).  $M_r/M_s$  and  $H_{cr}/H_c$  plotted in the Day diagram should thus be good indicators of variations in the magnetic domain state and the magnetic grain-size (Roberts et al., 1995).

Day diagrams show that most of the samples have pseudo-single domain (PSD) magnetic assemblages. Only samples from subunit L4a are mostly multidomain (MD) and are thus associated with coarser magnetic grains. Such a coarser magnetic granulometry is

consistent with the lower coercivity and remanence of these samples, illustrated by their thinner hysteresis loops.

It also appears that the loops of samples from units L2 and L4a are slightly flatter, with a greater difference between values of the raw magnetic moment and the moment adjusted for paramagnetic and diamagnetic components. This difference indicates greater influences of diamagnetic and paramagnetic phases for these samples compared to those from other units (Demory et al., 2005). For unit L2, this is explained by the noticeable higher carbonate content, as carbonates have a diamagnetic behaviour and dilute the ferrimagnetic signal. In the case of subunit L4a, the hypothesis of changes in sediment source that could explain the difference with subunit L4b is not preferred, as non-magnetic parameters are quite homogeneous in unit L4. A modification of the magnetic assemblage is rather suspected.

#### **1.6.6 Organic matter geochemistry**

Organic carbon content of core 14-05-GC increases upwards from values around 0.25-0.3% at the bottom to a mean of 1.9 % in the uppermost 5 m (Fig. 22). This increase might have several origins, such as a progressive organic matter degradation with depth, or an increase in productivity with time (Meyers, 1997; Thibodeau et al., 2013). Distinct negative  $C_{org}$  peaks are also recorded in the three identified turbidites. This makes sense as such remobilized material originating from recently deglaciated lands contain less organic matter than hemipelagic sediments. The  $C_{org}/N$  varies between 6 and 10 in the lower core half, before stabilizing between 7 and 8 in unit L4. These values are typical of marine organic matter (Meyers, 1997; Lamb et al., 2006). The low values in unit L1 and in the lowermost turbidite might not faithfully represent organic matter origin, as the organic content is very low (< 0.3%) and a higher proportion of inorganic nitrogen might artifactually depress the ratio (Meyers, 1997). Finally,  $\delta^{13}C$  values increases towards the top of the core, with values around -25‰ in units L1 and L2 increasing to about -23‰ in unit L3 and then slightly increasing to -22‰ in unit L4. Lowest values might reflect fresher water sources, and/or colder water sources, as polar water can hold substantially more dissolved  $CO_2$ , thus decreasing  $^{13}C$

content (Meyers, 1997; Lamb et al, 2006). Combination of  $C_{org}/N$  and  $\delta^{13}C$  values indicate that organic matter of core 14-05-GC originates mostly from marine algae, with a higher influence of colder/fresher source in lower units.

### **1.6.7 Core chronology**

Cores 14-05-GC and 28-04-GC span approximately the last 9400 and 9200 years respectively (Fig. 17). The sedimentation rates are relatively high with values generally between 0.1 and 0.2 cm/yr for both cores. Unit L2 shows the highest sedimentation rate, about 0.2 cm/yr in core 28-04-GC and 0.4 cm/yr in core 14-05-GC.

As the RDLs of core 14-05-GC are considered to be deposited instantaneously, they were removed from the age-models. The three RDLs have erosive bases, which implies that some sediment was removed by the turbiditic flows that deposited them. The resulting sediment loss is estimated by extrapolating sedimentation rates obtained on hemipelagic sediment between  $^{14}C$  ages. These estimations indicate that the turbiditic flows causing the top, central, and bottom RDLs have likely eroded respectively 2, 4 and 16 cm of previously deposited sediment. In core 28-04-GC, the age-model was made without removing any sediment. The sandy layer was likely not deposited by a short event, as explained further.

## **1.7 DISCUSSION**

### **1.7.1 Sedimentary sequences**

Acoustic stratigraphy and gravity-cores provide information about the succession of local sediment processes and depositional environments in the fjords. Sub-bottom profiles in all the basins contain a similar main acoustic sequence including, from bottom to top, units A0, A1, A2, A4, A6 and A7. Unit A1 is probably ubiquitous in the basins, as shown by Bell and Josenhans (1997) for Nachvak Fjord. However, A3 is only observed in the eastern Saglek Basin, while A5 is not observed in the western and central Saglek Basin, though maybe just not detected. The sedimentary sequence made by A2, A3 A6 and A7 represents a typical

deglacial sequence from glaciomarine to postglacial sedimentation that accompanies the progressive ice margin retreat, including paraglacial deposits generally consisting of MMDs and turbidites (Syvitski and Praeg, 1989; Syvitski, 1991). These RDLs, located on basin wedges or in units A3, A4 and A7, are discussed in section 5.2.

The ice-proximal glaciomarine unit A2 deposition directly followed the ice retreat and its thick seaward dipping architecture in most of the basins is characteristic of ice-terminus grounding at the successive sills (e.g., Syvitski, 1989; Hjelstuen et al., 2009; Trotter et al., 2021). This retreat pattern generated the deposition of the steepest and more chaotic A2a on the western basin flanks (Turner et al., 2012; Dowdeswell et al., 2015). In the Koktortoaluk Basin in Nachvak Fjord, the geometry of unit A2 confirms the Bell (1987) hypothesis proposing that the ice-tongue retreated south in the Tallek Arm and not west in the Townley basin.

A6 corresponds to the next stage consisting mostly of fine sediment carried from a distal ice margin by glaciofluvial and marine processes. When almost transparent, such as in the eastern Saglek Basin and the Nachvak Ivitin Basin, unit A6 is very similar to unit U3 observed in a former glaciomarine basin of southern Québec (Normandeau et al., 2013) and suggests a rapid sedimentation probably enhanced by mud flocculation in the saline waters entering the fjords (Syvitski and Praeg, 1989; Normandeau et al., 2013). This interpretation is consistent in these basins with a higher influence of marine waters. In the other basins, where A6 reflectors are slightly stronger, this process is less preponderant and the sedimentation dynamic was rather controlled by rates of sediment delivering either directly from tidewater glaciers or from glaciofluvial runout (Syvitski and Lee, 1997; Normandeau et al., 2013).

Unit A7 was sampled by cores 28-04-GC and 14-05-GC in Nachvak and Saglek Fjords, respectively. Both cores are very well correlated as they span the same time period with comparable sedimentation rates and show a similar evolution of sediment lithologies through time (Fig. 17). Units L2 and L3 likely correspond to A7a in the acoustic profiles, while unit L4 corresponds to unit A7b. With its geochemical homogeneity and its fining upward grain-

size, unit L1 is similar to the top of a thick turbidite. In this case, L1 should be considered deposited instantaneously, which put the age of core 14-05-GC's base at 9.2 cal ka BP, as for core 28-04-GC. The transition from unit L3 to unit L4 is dated at 6.24 and 6.30 cal ka BP in cores 14-05-GC and 28-04-GC respectively, and the one between subunits L4a and L4b at 3.68 and 3.82 cal ka BP. However, the correlation of unit L2 between both cores is not so evident. The DC layers nature, provenance and timing, as well as the decrease of DC-content in unit L3 are discussed in section 5.4. The RDLs in unit L3 are possibly the continuity of distal MMDs located closer to basin edges and were deposited in the paraglacial environment concomitant with the entire subunit A7a. Finally, unit A7b corresponds to modern-like postglacial sediments richer in organic matter and bivalves and poorer in detrital carbonate, which deposition was influenced by stronger current producing sediment drifts along basin flanks.

### **1.7.2 Mass-movement deposits**

Three types of MMDs are identified in the deglacial sequences: 1) the stack of four basin-wide 2-3 m-thick MMDs of unit A3 only observed in the eastern Saglek Basin, 2) the massive basin-wide MMDs of unit A4, and 3) the smaller MMDs shaped as lenses or wedges located at slope toes and continued by turbidites, mostly in unit A7a.

While the MMD of units A3 are very similar in size to deposits generally found in fjord above glaciomarine units (Hjelstuen et al., 2009; St-Onge et al., 2012; Bellwald et al., 2019; Trottier et al., 2020), the MMDs of unit A4 are particularly voluminous. In the eastern Saglek and Ivitin basins the single MMD forming A4 corresponds to volumes of about  $290 \cdot 10^6 \text{ m}^3$  and  $540 \cdot 10^6 \text{ m}^3$  of material, respectively, thus about 25 and 30% of their total sediment volume. These volumes are considerable for unique events. MMDs with similar volumes are rare but were observed in some Norwegian and Baffin Island fjords (Broom et al., 2017; Bellwald et al., 2019; Syvitski et al., 2022). It is not likely that a single gravity-flow event went through all the basins of each fjord, as they could not transit above bathymetric highs such as the Ugjuktok or Ivitak sills. However, several gravity-flows were possibly triggered

by a single major regional event or by several local events. While A4 was also made by a unique event in the Ugjuktok Basin, the structure of this unit is more complex in the Kuktortoaluk and the western and central Saglek Basins, and possibly caused by more than one massive MMD. The presence of tributary valleys may have favored the multiplicity of important gravity-flows in these basins.

MMDs of units A3 and A4 occurred relatively quickly after the deglaciation of their respective basins, and are possibly the response of paraglacial landscape readjustment associated with the glacioisostatic rebound. These processes are common in a context of fjord deglaciation and enhanced by the steep slopes and the important amounts of unstable material (Stoker et al., 2010; Bellwald et al., 2019). Many factors may trigger MMDs in such environment after deglaciation, such as earthquakes, delta collapses, or RSL variations (Bellwald et al., 2019). In Northern Labrador, modern earthquakes of magnitude up to 4.5-5.5 still occur along the passive margin, about 300 km away from the Torngat Mountains (Bent and Hasegawa, 1992). However, deglaciation was probably a period of enhanced seismotectonic activity, caused by the glacio-isostatic rebound that may reactivate faults and the orogenic topography reset after long-term glacial erosion (Stewart et al., 2000; Bellwald et al., 2016; Steffen et al., 2021). There is therefore a possibility that earthquakes occurred in the Torngat Mountains in the millennia following deglaciation.

Paraglacial processes also occurred in the mid-Holocene, forming the small MMDs of A7a, possibly also by earthquakes, despite a reduced glacioisostatic rebound, or by other processes such as river floods, slope failure or delta collapses (Bellwald et al., 2016; 2019). The chaotic sequence and the hummocky surface on the central Saglek Basin probably share common origins with the depositional lobes and the headscarps of the surroundings, and could have been affected by the presence of the Nakvak Brook fan. This sedimentary system was probably highly nourished in this paraglacial environment, with sediments available in the large Nakvak Brook watershed and the possible occurrence of delta collapses (Bellwald et al., 2019). Proglacial lake drainages may have also occurred from Nakvak Brook directly in the Saglek Basin (Jansson and Kleman, 2004). In the Kuktortoaluk Basin, the thick basin-



wide MMD in unit A7 was possibly related to the drainage of Lake Korok from the Tallek Arm (Bell and Josenhans, 1997). The wedge of stratified sediments over this MMD was then fed by fluvial discharge. Finally, the seaward flank of the Nachvak Outer Basin was also the site of many gravity-flows corresponding with local headscarps.

### **1.7.3 Timing of deglaciation and deposition of massive MMDs**

Both fjords have the typical morphology shaped by glaciers retreating by steps, with occasional stillstands forming the moraines that split the fjords in different basins (e.g., Hjelstuen et al., 2009; Waldmann et al., 2010). Kogarsok and Ivitak sills were already identified as sites of major stillstands during ice recession in Nachvak Fjord (Bell, 1987), as are also probably Ugjuktok and Saglek sills in Saglek Fjord. The smaller Tinutyarvik and Buried moraines were potentially the location of shorter stillstands. Trying to precisely date these retreat stages and the events triggering the A4 MMDs is challenging, as the sediment cores did not reach this unit. Ice retreat in the fjords, however, occurred after the beginning of ice retreat on the continental margin during the Bølling-Allerød warm interval around 14 cal ka BP (Dyke et al, 2004; Dalton et al., 2020) and before 9.2 cal ka BP – i.e., the age of the cores.

By estimating sedimentation rates from the bases of the cores towards the top of unit A4, it is possible to estimate the age of A4 deposition in both the Ivitin and the eastern Saglek Basin, and then the successive retreat steps. By using the sedimentation rates of unit L4, the resulting ages are too old, at least in the Ivitin Basin where A4 would have been deposited at 17.4 cal ka BP. However, unit A6 probably had a higher sedimentation rate than unit A7, still not as high as at the beginning of deglacial sedimentation. Using a sedimentation rate of 0.5 cm/yr for downward extrapolation from cores 14-05-GC and 28-04-GC appears thus consistent, also with other datasets (Syvitski et al, 2022). This sedimentation rate would place the deposition of A4 MMD around 12.5 cal ka BP in the Nachvak Ivitin Basin – during the YD – and at 10.2 cal ka BP in the eastern Saglek Basin. These estimations are sensitive to the chosen sedimentation rate that can vary with time and must therefore be taken with

caution. However, irrespective of the selected sedimentation rate, it appears that unit A4 was not deposited at the same time in the different basins, and that several events triggering MMDs occurred between 14 and 10 cal ka PB. This age difference also suggests an asynchronous ice margin retreat from Nachvak and Saglek main basins. Nachvak Outer and Ivitin Basins were possibly already ice-free during the YD, while the ice was still covering the Saglek Basin, maybe forming the 180 m-high Saglek Sill during a YD stillstand. This interpretation is consistent with the formation of the Saglek Moraine around 12.8-13.2 cal ka BP (Ives, 1976; Clark et al., 2003). This age is obtained from a recalculation of the  $^{10}\text{Be}$  ages from Clark et al. (2003) with the production rate proposed by Borchers et al., (2016); it is more adapted to the area than the one for the Arctic from Young et al. (2013) used by Dubé-Loubert et al. (2018) that probably overestimates the age for the Labrador region. Thus, the Saglek Moraines and the Saglek Sill were probably formed during an important YD stillstand. The asynchronous ice retreat of neighboring valleys might be surprising, as they were influenced by similar climatic and oceanic variations, but this has been observed in West Greenland, and mostly explained by topographic and bathymetric controls (Lane et al., 2014). In the present case, both fjords have similar morphologies and bathymetries, but their entrance sills are not in the same physiographic context. While the wide Nachvak sill is directly located on the continental shelf, Saglek sill is separated from it by Saglek Bay with its islands, basins, sills and smaller tributary valleys. Therefore, Saglek Sill is less exposed to the oceanic forcing from Labrador Sea and the ice margin grounded on it was probably more stable than at the Nachvak entrance, explaining a later deglaciation of Saglek Basin.

The morainic sills located deeper in both fjords could have been formed by subsequent ice margin stillstands during cold Holocene events. These events were probably associated with those that caused the Gold Cove and Noble Inlet advances of the Québec-Labrador Dome in Hudson Strait, respectively from 11.0 to 10.6 and from 9.7 to 9.1 cal ka BP (Kaufman et al., 1993; Jennings et al., 1998; Jennings et al., 2015). In Nachvak Fjord, Gallagher (1989) showed that the ice sheet left Townley Basin before 10.3 cal ka BP and thus probably occupied this basin during the Gold Cove event and grounded at Kogarsok Sill. In Saglek Fjord, the ice margin formed the Buried Sill and then the high Ugjuktok Sill.

However, the thinner unit A2 in the eastern Saglek Basin suggests that the margin did not stay long on the Buried Sill, and was probably grounded on the Ugjuktok Sill during the Gold Cove event.

#### **1.7.4 Regional and local deglacial and postglacial events**

##### **1.7.4.1 Origin of the detrital carbonates**

Both core chronologies indicate that the DC layers of unit L2 were deposited between 9.19 and 8.17 cal ka BP. These DC cannot originate from Labrador lands, as there are no Paleozoic platforms that could act as local sources (Wheeler et al., 1996; Brown et al., 2012). These DC are thus allochthonous, as those found in the Labrador Sea Quaternary sequence, and were likely brought by ice and meltwaters in the LC from upstream deglaciation of carbonate platforms in Baffin Bay and the Hudson Bay System (e.g. Andrews and Tedesco, 1992; Naafs and Stein, 2013; Jennings et al., 2015). The presence of these DC-rich sediments in Labrador fjords coming from so far might be surprising, but can be explained by the deflection of LC waters in the fjords. It has already been observed that allochthonous icebergs may enter fjords and even reach their head (Normandeau et al., 2021), and so low-density meltwaters might follow the same path. Moreover, the important tides with high velocities occurring in Nachvak and Saglek Fjords facilitate waters and sediments transfer from the continental margin (Bentley and Kahlmeyer, 2012).

##### **1.7.4.2 Correspondence of the detrital-carbonate layers with deglacial events**

By looking at Ca/Ti data, the strongest DC-peak in core 14-05-GC could correspond to the DC-rich pinkish layer of core 28-04-GC. However, these peaks are 400 yr delayed and have different colors and structures, and are therefore not concordant. The pinkish layer, if ever deposited in the eastern Saglek Basin, was likely eroded by the lowest turbidite of core 14-05-GC that erased more than 100 yr of record (Fig. 19). The different connections of the sampled basins with the continental margin may also explain the mismatch between the DC-layers between both cores. There are therefore three distinct DC-peaks : one main peak in

each core that are related to distinct events, plus a last and very thin DC-peak only found in core 28-04-GC dated around 8.17 cal ka BP.

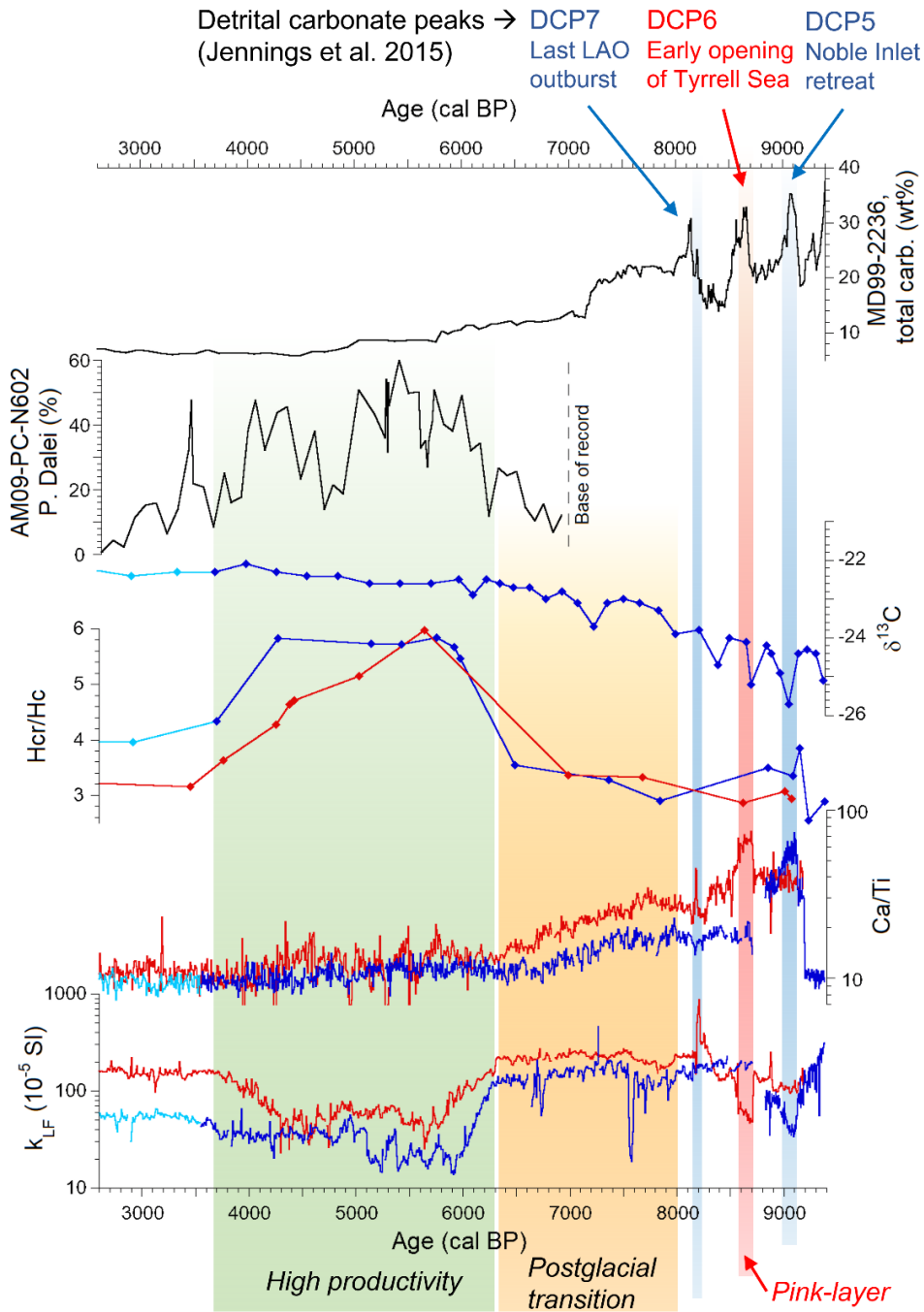
These three DC-peaks well correlate chronologically with DC-peaks 7, 6 and 5 in core MD99-2236 sampled in Cartwright Saddle, farther south on the Labrador continental margin (Jennings et al. 2015), and identified as markers of the Noble-Inlet retreat, the opening of the Tyrrell Sea and the LAO drainages (Andrews et al., 1995; Hall et al., 1999; Jennings et al., 2015; Lochte et al., 2019a).

The retreat of the Noble Inlet ice-advance of the Labrador Dome over Hudson Strait occurred around 9.13 cal ka BP (Andrews et al., 1995; Jennings et al., 2015). This event contributed to our oldest DC-peak, dated at about 9.10 cal ka BP, and probably to the high DC content at the bottom of core 28-04-GC.

The chronology of core 28-04-GC indicates that the pinkish layer, centered at 8.64 cal ka BP, corresponds to DCP6a in core MD99-2236, just before the reddish DCP6b, and also to the red bed in core MSM19-2 if a constant  $\Delta R$  is kept in this core (Jennings et al., 2015; Lochte et al., 2019; Brouard et al., 2021). We thus suppose that the pinkish layer corresponds to the same event, which triggered the deposition of the red bed found in Hudson Strait and Labrador Shelf (Kerwin, 1996; Lajeunesse and St-Onge, 2008; Lochte et al., 2019a). The new chronology of this red bed equivalent makes it better corresponding to the opening of the Tyrrell Sea than to a first LAO drainage (Jennings et al., 2015; Brouard et al., 2021).

The pinkish layer is, however, particularly light comparing to other red beds sampled. This suggests a high dilution of the red sediment, such as in the Eastern Basin of Hudson Strait (Kerwin, 1996). The wavy-laminated structure of the pinkish layer suggests that it was deposited in a short time, maybe a few weeks. The fjord trapping of deflected waters and sediments explain the higher thickness of the resulting pinkish layer compared to its equivalents in Labrador Shelf sedimentary records (Jennings et al., 2015; Rashid et al., 2017; Lochte et al., 2019a). This is actually the first time that the Hudson-Strait red bed is identified in a coastal inlet.

Finally, the youngest DC-peak, in core 28-04-GC, is dated at about 8.18 cal ka BP and corresponds well with DCP7 of core MD99-2236 and to the last LAO drainage often dated between 8.16 and 8.18 cal ka BP (Roy et al., 2011; Jennings et al. 2015; Brouard et al., 2021). This peak is underlain by the sandy-mud layer, which is structurally more similar to a hyperpycnite than a turbidite, as it has a slightly increasing upward content of silt and sand, with a relatively low DC content. This material could originate from a local source, there is no studies supporting local meltwater event that could form a hyperpycnite-like deposit in the Ivitin Basin at this time (Jansson and Kleman, 2004; Dubé-Loubert et al., 2018). This coarse sediment could also be made of IRDs from an external source. Jennings et al. (2015) also noticed a DC-poor layer of higher sand content just below DCP7. The Hudson Bay ice saddle collapse, happening just before the last LAO drainage, could be the cause of such IRDs deposition by triggering massive iceberg discharge towards Labrador Sea and Fjords.



**Figure 19.** Comparison of detrital carbonate record in core MD99-2236 (Jennings et al., 2015) and percentage of dinocyst *P. Dalei* (Richerol et al., 2016) against magnetic susceptibility, Ca/Ti and Hcr/Hc of cores 14-05-GC (in blue) and 28-04-GC (in red) and  $\delta^{13}\text{C}$  of core 14-05-GC. Gaps are left in core 14-05-GC for the record eroded by the turbidites. The blue and red bars correspond to the three DC peak identified in our cores.

#### 1.7.4.3 Decreasing meltwater discharge and the establishment of postglacial conditions

The first studies conducted on Labrador Shelf sediment sequences put the postglacial transition at 8000 yr BP, at the timing of the transition from the carbonate-rich Qeovik Silt to the postglacial Makkaq Clay (Josenhans et al., 1986; Clark and Josenhans, 1990; Bentley and Kahlmeyer, 2012). In Saglek and Nachvak Fjords, this timing corresponds to the transition from unit L2 to unit L3 with the end of massive DC input, but is only the beginning of a gradual transition to postglacial sedimentary conditions. This transition is marked by a progressive decline of DC input in Saglek and Nachvak fjords until 6.6 and 6.3 cal ka BP respectively. The same declining trend of DC content was identified in core Hu2006040-40 sampled in Karlsefni Trough, with also a stabilization around 6.3 cal ka BP (Rashid et al., 2017), showing that this trend is regional and not restricted to the fjords.

This DC content decrease is coherent with the final steps of LIS deglaciation that contributed to export detrital carbonates from Hudson Bay and Foxe Basin areas (Jennings et al., 2015; Utting et al., 2016). Moreover, this decreasing DC content from 7.5 to 6.2 cal ka BP is correlated with an increase of marine organic matter in core 14-05-GC, and thus an increasing influence of marine water in the eastern Saglek Basin. This observation is coherent with the rapid reduction of the LIS extent between 8.0 and 6.0 cal ka BP, which reduced the freshwater input in the fjords both from inland and from northern locations by the LC (Occhietti et al., 2011; Ullman et al., 2016; Dalton et al., 2020). Richerol et al. (2015) also noticed with dinocyst assemblages an increase in productivity and a decrease of cold surface Arctic waters in Nachvak Fjord between 7.0 –at least– and 6.2 cal ka BP.

#### 1.7.4.4 Postglacial magnetic properties and environmental variations

In the postglacial unit L4 of both cores, magnetic properties show important variations, while non-magnetic parameters are quite homogeneous, reflecting a modification of the magnetic assemblage. Hysteresis data and  $Fe/k_{LF}$  values show that ferrimagnetic grains are coarser and less concentrated in unit L4a than in unit L4b. Both these differences can be

explained by an enhanced partial dissolution of magnetite in a reductive environment. In such environments, the smaller magnetic grains are predominantly dissolved, as they have a higher surface-volume ratio, including biogenic magnetite that is a major constituent of magnetite assemblages in postglacial marine environment (Roberts et al., 2012; Yamakazi, 2020). This preferential dissolution thus increases the mean magnetic grain-size (Liu et al., 2004), which causes a loss of SD particles and explains the transition from PSD to MD grains in unit L4a in the Day-Diagram (Fig. 21).

Total or partial magnetite dissolution is generally caused by bacterial reduction for organic matter consumption and happens mostly in deep-sea in suboxic and anoxic sediments, but also on continental-margins with higher sedimentation rates (Liu et al., 2004; Rowan et al., 2009; Roberts, 2015). Reduction of magnetite and other iron-oxides is enhanced with higher organic matter influx or with reduced bottom water ventilation (Roberts, 2015).

In cores 14-05-GC and 28-04-GC, this enhanced reduction occurs likely in sediment deposited from 6.3 to 3.8 cal ka BP (Fig. 19). This interval is well correlated with a period of colder conditions, more important sea-ice cover and higher productivity in Nachvak Fjord (Richerol et al., 2016). In that core, the relative abundance (25 to 60%) of cysts of *Pentapharsodinium dalei* between 6.3 and 3.8 cal ka BP (Fig. 19) suggests an important water column stratification and a high productivity (Radi et al., 2007; Richerol et al., 2016; Allan et al., 2020). Higher productivity enhanced bottom influx of organic matter and its concentration in sediment, and thus favored a higher oxygen consumption by bacteria and an increase of magnetite dissolution in sediment deposited at this time. The important concentration of life-position shells in unit L4a, ten times higher than in unit L4b, might also reflect the higher nutrient content in sediments. However, the lower part of unit L4a in core 14-05-GC, dated from 6.0 to 5.0 cal ka BP, shows an even higher magnetite dissolution and a lower shell concentration. This difference inside unit L4a suggests that reducing conditions were at a higher level between 6.0 and 5.0 ka cal BP in the eastern Saglek Basin, maybe reflecting suboxic conditions in bottom waters caused by a higher stratification. The absence of such an interval with a higher level of magnetite dissolution in core 28-04-GC is maybe



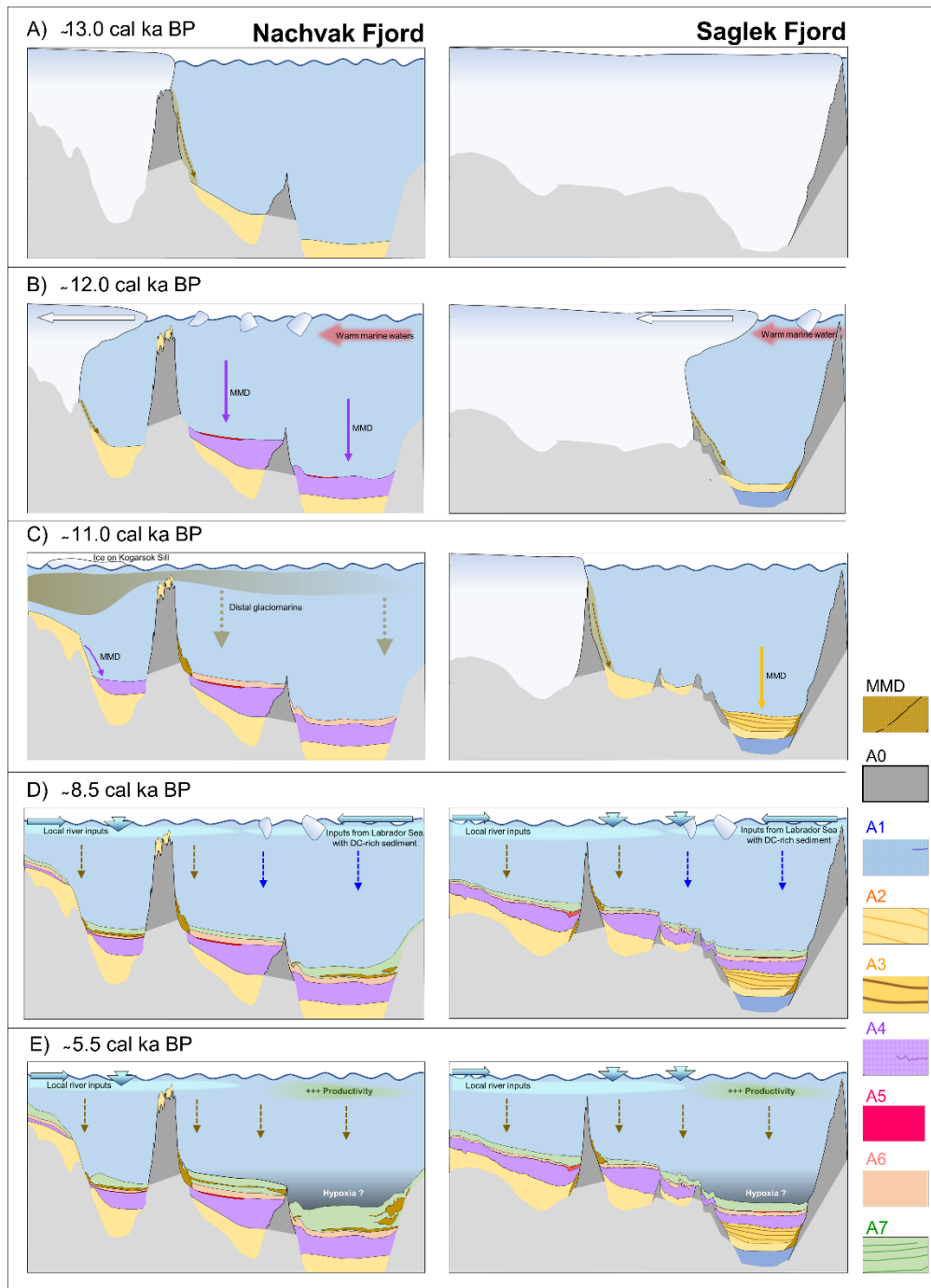
related to Nachvak Fjord specificity or to the core location, as it was sampled in the shallower Ivitin Basin. Deep fjords troughs and basins are known to have a weaker bottom ventilation. This is however not the case anymore in both fjords that are well oxygenated through the water column (Bentley and Kalhmeyer, 2012, Brown et al., 2012), conditions that are likely the same since 3.7 cal ka BP.

### **1.7.5 Deglacial to postglacial history and changes in sedimentary regimes**

During the Bølling-Allerød warm interval from 14.7 to 12.9 cal ka BP, the LIS margin retreated from the Labrador continental shelf to reach Nachvak Fjord and Saglek Bay but not Saglek Fjord. At the YD onset, the ice margin was probably grounded at Ivitak and Saglek Sill (Fig. 20A) to form the Saglek Moraines. Between the YD (12.9 – 11.7 cal ka BP) and the Gold Cove event (about 11.0 – 10.6 cal ka BP), the ice retreated from the Koptortoaluk Basin towards the Tallek Arm (Fig. 20B), while an ice-tongue stayed in the Townley Basin, forming the Kogarsok Sill during the Gold Cove event. At the same time, the ice margin retreated in the Saglek Basin and possibly in the West Arm, leaving an ice tongue in the Ugjuktok Basin during the Gold Cove event (Fig. 20C). The ice margin then probably retreated from Nachvak Fjord area earlier than in Saglek Fjord. This diachronic retreat is recorded by a transition from A6 to A7 in the Ivitin Basin that occurred before the same transition in the Saglek Basin. It appears that the deglaciation of each basin was quickly followed by the deposition of A4 MMDs, explaining the succession of units A2-A4-A6.

From 9.2 to about 6.5 cal ka BP, both fjords received a mixture of paraglacial and hemipelagic sediments. Paraglacial processes included mostly slope destabilization, fluvial remobilization and lake drainages that formed fans, wedges and turbidites in the basins. At this time, the hemipelagic sedimentation contained DC-rich sediment from the deglaciation of the Hudson Bay area, mostly from 9.2 to 8.1 cal ka BP (Fig. 20D). The period from 8.0 to 6.5 is marked by a relative increase of marine influence, and a decrease of LIS meltwaters arriving both by the fjords and Labrador Sea. At about 6.3 cal ka BP, an important regional climatic transition to higher temperatures favored an increase in productivity that enhanced

bottom oxygen consumption in both fjords until about 3.8 cal ka BP, particularly from 6.0 to 5.0 in the eastern Saglek Basin (Fig. 20E). However, in the last millennia, the water-column was well oxygenated, probably due to a lower productivity and a better water exchange between the fjords and the continental shelf.



**Figure 20.** Conceptual models representing the successive depositional environments in Nachvak and Saglek Fjords during and after the deglaciation. Arrows show different MMDs (plain arrows), hemipelagic or glacial (dotted brown arrows) and DC-rich (blue dotted arrows) sediment inputs.

## 1.8 CONCLUSIONS

The combination of swath bathymetry, sub-bottom profiles and sediment cores from Nachvak and Saglek Fjords provide insights on the local and regional retreat of the Laurentide Ice Sheet and on environmental changes that influenced sedimentation since deglaciation.

The post-LGM sedimentary sequence is similar in both fjords and reaches thicknesses higher than 100 m in most of the basins, characterized by the presence of a thick glaciomarine unit overlain by huge MMDs in fjord basins. These MMDs suggest the possible occurrence of earthquakes triggered by the local rapid glacio-isostatic uplift during the YD and the Early Holocene.

Despite similarities in their morphologies and sedimentary sequences, Saglek and Nachvak experienced an asynchronous last ice retreat, with a deglaciation of the outer Saglek Fjord delayed by about 2000 yr. This delay was probably caused by the buffering of Saglek Bay that limited the oceanic forcing on the ice margin.

Following local deglaciation, fjord sedimentation was still influenced by paraglacial processes, but also by sediment rich in detrital carbonates from the Hudson Bay area and transiting by Labrador waters deflected in the fjords. The resulting DC layers that also include a Hudson Strait red bed equivalent – which are here reported for the first time in a continental inlet – were correlated to the last deglacial events of Hudson Bay. The presence of these beds in the fjords suggests that the sediment dispersion following deglacial events in Hudson Bay was massive, even downstream Hudson Strait, and did not only follow the main oceanographic current paths.

The postglacial transition in the fjords occurred between 8.0 and 6.3 cal ka BP with the increasing influence of marine waters and the decrease of sediment inputs associated with deglaciation. The end of the transition was marked by an increased productivity and water stratification in outer basin that caused a lack of oxygen in the bottom of outer basins. These

conditions prevailed until about 3.8 cal ka BP with the set-up of modern-like oxygenated waters conditions.

The asynchronous deglaciation of the neighbouring Nachvak and Saglek Fjords provide an opportunity to investigate the spatial variability of ice-ocean interactions in a context of major role of the oceanic forcing during the retreat and ablation of the Laurentide Ice Sheet in Québec-Labrador. Moreover, despite the presence of a few RDLs in their mid- and late-Holocene sequences, Nachvak and Saglek outer basins are good candidate for investigating regional environmental variations through these periods.

## **1.9 ACKNOWLEDGMENTS**

We thank the captain, crew and scientist of the MSM46 expedition onboard the R/V Maria S. Merian. We acknowledge the Natural Science and Engineering Research Council (NSERC) of Canada and the Fonds de Recherche du Québec Nature et Technologie (FRQNT) for their financial support, as well as ArcticNet for the geophysical data collected by the NGCC Amundsen. We also thank Q. Beauvais, M. St-Onge, J. Major, J.-G. Auger and D. Lavallée for their help at the ISMER laboratory, as well as A. Adamowicz-Walczak and J.-F. Hélie at the Geotop research center. Finally, we thank P.-O. Couette, P.-A. Desiagne, and journal reviewers J. S. and A. Newton for the helpful comments that allowed improving the quality of the manuscript.

## **1.10 REFERENCES**

- Allan, E., de Vernal, A., Seidenkrantz, M., Briner, J.P., Hillaire-Marcel, C., Pearce, C., Meire, L., Røy, H., Mathiasen, A.M., Nielsen, M.T., Plesner, J.L., Perner, K., 2021. Insolation vs. meltwater control of productivity and sea surface conditions off SW Greenland during the Holocene. *Boreas* 50, 631–651. <https://doi.org/10.1111/bor.12514>
- Andrews, J.T., Tedesco, K., 1992. Detrital carbonate-rich sediments, northwestern Labrador Sea: Implications for ice-sheet dynamics and iceberg rafting (Heinrich) events in the North Atlantic. *Geology*, 20, 1087. [https://doi.org/10.1130/0091-7613\(1992\)020<1087:DCRSNL>2.3.CO;2](https://doi.org/10.1130/0091-7613(1992)020<1087:DCRSNL>2.3.CO;2)

- Andrews, J.T., MacLean, B., Kerwin, M., Manley, W., Jennings, A.E., Hall, F., 1995. Final stages in the collapse of the Laurentide Ice Sheet, Hudson Strait, Canada, NWT: 14C AMS dates, seismic stratigraphy, and magnetic susceptibility logs. *Quaternary Science Reviews* 14, 983e1004.
- Barber, A., Sirois, M., Chaillou, G., Gélinas, Y., 2017. Stable isotope analysis of dissolved organic carbon in Canada's eastern coastal waters: Stable isotope analysis of DOC. *Limnology and Oceanography*, 62, S71–S84. <https://doi.org/10.1002/lno.10666>
- Barber, D.C., Dyke, A., Hillaire-Marcel, C., Jennings, A.E., Andrews, J.T., Kerwin, M.W., Bilodeau, G., McNeely, R., Southon, J., Morehead, M.D., Gagnon, J.-M., 1999. Forcing of the cold event of 8,200 years ago by catastrophic drainage of Laurentide lakes. *Nature* 400, 344–348. <https://doi.org/10.1038/22504>
- Bastick, J., 2009. Evaluating marine ecological integrity monitoring measures for Nachvak and Saglek fjords, northern Labrador. M.Sc. thesis, 183 p., Royal Military College of Canada.
- Batchelor, C.L., Dowdeswell, J.A., Rignot, E., Millan, R., 2019. Submarine Moraines in Southeast Greenland Fjords Reveal Contrasting Outlet-Glacier Behavior since the Last Glacial Maximum. *Geophysical Research Letters*. 46, 3279–3286. <https://doi.org/10.1029/2019GL082556>
- Bell, T.J., 1987. Quaternary geomorphology, glacial history and relative sea level change in outer Nachvak Fiord, northern Labrador. Ph.D. thesis, 291 p., Memorial University of Newfoundland.
- Bell, T., Josenhans, H., 1997. The seismic record of glaciation in Nachvak Fjord, Northern Labrador. In: Davies, T. A., Bell, T., Cooper, A. K. et al. (eds) *Glaciated Continental Margins: An Atlas of Acoustic Images*. London: Chapman & Hall, pp. 190–193.
- Bellwald, B., Hjelstuen, B.O., Sejrup, H.P., Stokowy, T., Kuvås, J., 2019. Holocene mass-movements in west and mid-Norwegian fjords and lakes. *Marine Geology* 407, 192–212. <https://doi.org/10.1016/j.margeo.2018.11.007>
- Bent, A. L., Hasegawa, H. S., 1992. Earthquakes along the northwestern boundary of the Labrador Sea. *Seismological Research Letters* 63, No 4, 587-602.
- Bentley, S.J., Kahlmeyer, E., 2012. Patterns and mechanisms of fluvial sediment flux and accumulation in two subarctic fjords: Nachvak and Saglek Fjords, Nunatsiavut, Canada. *Canadian Journal of Earth Sciences*, 49, 1200–1215. <https://doi.org/10.1139/e2012-052>
- Blaauw, M., Christen, J.A., 2011. Flexible paleoclimate age-depth models using an autoregressive gamma process. *Bayesian Analysis*. 6. <https://doi.org/10.1214/11-BA618>

- Blott, S.J., Pye, K., 2001. GRADISTAT: a grain size distribution and statistics package for the analysis of unconsolidated sediments. *Earth surface processes and Landforms* 26, 1237–1248. <https://doi.org/10.1002/esp.261>
- Borchers, B., Marrero, S., Balco, G., Caffee, M., Goehring, B., Lifton, N., Nishiizumi, K., Phillips, F., Schaefer, J., Stone, J., 2016. Geological calibration of spallation production rates in the CRONUS-Earth project. *Quaternary Geochronology* 31, 188–198. <https://doi.org/10.1016/j.quageo.2015.01.009>
- Broom, L.M., Campbell, D.C., Gosse, J.C., 2017. Investigation of a Holocene marine sedimentary record from Pond Inlet, northern Baffin Island, Nunavut 12. Summary of Activities, 93-104.
- Brown, T., Reimer, K., Sheldon, Bell, T., Bentley, S., Pienitz, R., Gosselin, M., Blais, M., Carpenter, M., Estrada, E., Richerol, T., Kahlmeyer, E., Luque, S., Sjare, B., Fisk, A., Iverson, S., 2012. A first look at Nunatsiavut Kangi dualuk (‘fjord’) ecosystems. In: Nunavik and Nunatsiavut: from science to policy. An Integrated Regional Impact Study (IRIS) of climate change and modernization. ArcticNet Inc., Quebec City, QC, 271-301. <https://doi.org/10.13140/2.1.4784.9924>
- Brouard, E., Lajeunesse, P., 2019. Glacial to postglacial submarine landform assemblages in fiords of northeastern Baffin Island. *Geomorphology* 330, 40–56. <https://doi.org/10.1016/j.geomorph.2019.01.007>
- Brouard, E., Roy, M., Godbout, P.-M., Veillette, J.J., 2021. A framework for the timing of the final meltwater outbursts from glacial Lake Agassiz-Ojibway. *Quaternary Science Reviews* 274, 107269. <https://doi.org/10.1016/j.quascirev.2021.107269>
- Caron, M., Rochon, A., Montero-Serrano, J., St-Onge, G., 2019. Evolution of sea-surface conditions on the northwestern Greenland margin during the Holocene. *Journal of Quaternary Sciences*. 34, 569–580. <https://doi.org/10.1002/jqs.3146>
- Channell, J.E.T., Hodell, D.A., 2013. Magnetic signatures of Heinrich-like detrital layers in the Quaternary of the North Atlantic. *Earth and Planetary Science Letters* 369–370, 260–270. <https://doi.org/10.1016/j.epsl.2013.03.034>
- Church, M., Ryder, J. M., 1972. Paraglacial sedimentation: a consideration of fluvial processes conditioned by glaciation. *Geological Society of America Bulletin*, v. 83, 3059-3072. [https://doi.org/10.1130/0016-7606\(1972\)83\[3059:PSACOF\]2.0.CO;2](https://doi.org/10.1130/0016-7606(1972)83[3059:PSACOF]2.0.CO;2)
- Clark, P.U., 1988. Glacial geology of the Torngat Mountains, Labrador. *Canadian Journal of Earth Sciences* 25, 1184–1198. <https://doi.org/10.1139/e88-116>
- Clark, P.U., Brook, E.J., Raisbeck, G.M., Yiou, F., Clark, J., 2003. Cosmogenic  $^{10}\text{Be}$  ages of the Saglek Moraines, Torngat Mountains, Labrador. *Geology* 31, 617. [https://doi.org/10.1130/0091-7613\(2003\)031<0617:CBAOTS>2.0.CO;2](https://doi.org/10.1130/0091-7613(2003)031<0617:CBAOTS>2.0.CO;2)

- Clark, P.U., Josenhans, H.W., 1990. Reconstructed ice-flow patterns and ice limits using drift pebble lithology, outer Nachvak Fiord, northern Labrador: Discussion. *Canadian Journal of Earth Sciences* 27, 1002–1006. <https://doi.org/10.1139/e90-103>
- Condrón, A., Winsor, P., 2012. Meltwater routing and the Younger Dryas. *Proceedings of the National Academy of Sciences* 109, 19928–19933. <https://doi.org/10.1073/pnas.1207381109>
- Croudace, I.W., Rindby, A., Rothwell, R.G., 2006. ITRAX: description and evaluation of a new multi-function X-ray core scanner. *Geological Society, London, Special Publications* 267, 51–63. <https://doi.org/10.1144/GSL.SP.2006.267.01.04>
- Croudace, I.W., Rothwell, R.G. (Eds.), 2015. *Micro-XRF Studies of Sediment Cores: Applications of a non-destructive tool for the environmental sciences*, 1st ed. 2015. ed. *Developments in Paleoenvironmental Research*. Springer Netherlands : Imprint: Springer, Dordrecht. <https://doi.org/10.1007/978-94-017-9849-5>
- Cuny, J., Rhines, P.B., Niiler, P.P., Bacon, S., 2002. Labrador Sea Boundary Currents and the Fate of the Irminger Sea Water. *Journal of Physical Oceanography* 32, 627–647. [https://doi.org/10.1175/1520-0485\(2002\)032<0627:LSBCAT>2.0.CO;2](https://doi.org/10.1175/1520-0485(2002)032<0627:LSBCAT>2.0.CO;2)
- Dalton, A.S., Margold, M., Stokes, C.R., Tarasov, L., Dyke, A.S., Adams, R.S., Allard, S., Arends, H.E., Atkinson, N., Attig, J.W., Barnett, P.J., Barnett, R.L., Batterson, M., Bernatchez, P., Borns, H.W., Breckenridge, A., Briner, J.P., Brouard, E., Campbell, J.E., Carlson, A.E., Clague, J.J., Curry, B.B., Daigneault, R.-A., Dubé-Loubert, H., Easterbrook, D.J., Franzi, D.A., Friedrich, H.G., Funder, S., Gauthier, M.S., Gowan, A.S., Harris, K.L., Héту, B., Hooyer, T.S., Jennings, C.E., Johnson, M.D., Kehew, A.E., Kelley, S.E., Kerr, D., King, E.L., Kjeldsen, K.K., Knaeble, A.R., Lajeunesse, P., Lakeman, T.R., Lamothe, M., Larson, P., Lavoie, M., Loope, H.M., Lowell, T.V., Lusardi, B.A., Manz, L., McMartin, I., Nixon, F.C., Occhietti, S., Parkhill, M.A., Piper, D.J.W., Pronk, A.G., Richard, P.J.H., Ridge, J.C., Ross, M., Roy, M., Seaman, A., Shaw, J., Stea, R.R., Teller, J.T., Thompson, W.B., Thorleifson, L.H., Utting, D.J., Veillette, J.J., Ward, B.C., Weddle, T.K., Wright, H.E., 2020. An updated radiocarbon-based ice margin chronology for the last deglaciation of the North American Ice Sheet Complex. *Quaternary Science Reviews* 234, 106223. <https://doi.org/10.1016/j.quascirev.2020.106223>
- Day, R., Fuller, M., Schmidt, V.A., 1977. Hysteresis properties of titanomagnetites: Grain-size and compositional dependence. *Physics of the Earth and Planetary Interiors* 13, 260–267. [https://doi.org/10.1016/0031-9201\(77\)90108-X](https://doi.org/10.1016/0031-9201(77)90108-X)
- Debret, M., Sebag, D., Desmet, M., Balsam, W., Copard, Y., Mourier, B., Susperrigui, A.-S., Arnaud, F., Bentaleb, I., Chapron, E., Lallier-Vergès, E., Winiarski, T., 2011. Spectrocolorimetric interpretation of sedimentary dynamics: The new “Q7/4 diagram.” *Earth-Science Reviews* 109, 1–19. <https://doi.org/10.1016/j.earscirev.2011.07.002>



- Demory, F., Oberhänsli, H., Nowaczyk, N.R., Gottschalk, M., Wirth, R., Naumann, R., 2005. Detrital input and early diagenesis in sediments from Lake Baikal revealed by rock magnetism. *Global and Planetary Change* 46, 145–166. <https://doi.org/10.1016/j.gloplacha.2004.11.010>
- Dietrich, P., Ghienne, J.-F., Normandeau, A., Lajeunesse, P., 2017. Reconstructing ice margin retreat using delta morphostratigraphy. *Scientific reports* 7, 16936. <https://doi.org/10.1038/s41598-017-16763-x>
- Dowdeswell, J.A., Hogan, K.A., Arnold, N.S., Mugford, R.I., Wells, M., Hirst, J.P.P., Decalf, C., 2015. Sediment-rich meltwater plumes and ice-proximal fans at the margins of modern and ancient tidewater glaciers: Observations and modelling. *Sedimentology* 62, 1665–1692. <https://doi.org/10.1111/sed.12198>
- Dubé-Loubert, H., Roy, M., Schaefer, J.M., Clark, P.U., 2018. 10Be dating of former glacial Lake Naskaupi (Québec-Labrador) and timing of its discharges during the last deglaciation. *Quaternary Science Reviews* 191, 31–40. <https://doi.org/10.1016/j.quascirev.2018.05.008>
- Duboc, Q., St-Onge, G., Lajeunesse, P., 2017. Sediment records of the influence of river damming on the dynamics of the Nelson and Churchill Rivers, western Hudson Bay, Canada, during the last centuries. *The Holocene* 27, 712–725. <https://doi.org/10.1177/0959683616670465>
- Duchesne, M.J., Pinet, N., Bolduc, A., Bédard, K., Lavoie, D., 2007. Seismic stratigraphy of the lower St. Lawrence River estuary (Quebec) Quaternary deposits and seismic signature of the underlying geological domains Geological Survey of Canada Current Research 2007-D2, 1-14. <https://doi.org/10.4095/224408>
- Dyke, A.S., 2004. An outline of North American deglaciation with emphasis on central and northern Canada, in: *Developments in Quaternary Sciences*. Elsevier, 373–424. [https://doi.org/10.1016/S1571-0866\(04\)80209-4](https://doi.org/10.1016/S1571-0866(04)80209-4)
- Engstrom, D.R., Hansen, B.C.S., 1985. Postglacial vegetational change and soil development in southeastern Labrador as inferred from pollen and chemical stratigraphy. *Canadian Journal of Botany* 63, 543–561. <https://doi.org/10.1139/b85-070>
- Evans, D.J.A., Rogerson, R.J., 1986. Glacial geomorphology and chronology in the Selamut Range – Nachvak Fiord area, Torngat Mountains, Labrador. *Canadian Journal of Earth Science* 23, 66–76. <https://doi.org/10.1139/e86-007>
- Funk, J. A., Von Dobeneck, T., Reitz, A., 2004. Integrated rock magnetic and geochemical quantification of redoxomorphic iron mineral diagenesis in Late Quaternary sediments from the Equatorial Atlantic. In : *The South Atlantic in the Late Quaternary: Reconstruction of material budgets and current systems*. Berlin, Heidelberg : Springer Berlin Heidelberg, 2004. pp. 237-260.

- Gagnon-Poiré, A., Lajeunesse, P., Normandeau, A., Francus, P., St-Onge, G., Nzekwe, O.P., 2018. Late-Quaternary glacial to postglacial sedimentation in three adjacent fjord-lakes of the Québec North Shore (eastern Canadian Shield). *Quaternary Science Reviews* 186, 91–110. <https://doi.org/10.1016/j.quascirev.2018.02.013>
- Gallagher, J., 1989. Glacial geomorphology and late Quaternary chronology of inner Nachvak Fiord, northern Labrador, M.Sc. thesis, 217 p., Memorial University of Newfoundland, St. John's, Canada.
- Hald, M., Husum, K., Vorren, T., Grøsfjeld, K., Jensen, H., Sharapova, A., 2003. Holocene climate in the subarctic fjord Malangen, northern Norway: a multi-proxy study. *Boreas* 32, 543–559. <https://doi.org/10.1080/03009480310004134>
- Hall, F.R., Andrews, J.T., Jennings, A., Vilks, G., Moran, K., 1999. Late Quaternary sediments and chronology of the northeast Labrador Shelf (Karlsefni Trough, Saglek Bank): Links to glacial history. *Geological Society of America Bulletin* 111, 1700–1713. [https://doi.org/10.1130/0016-7606\(1999\)111<1700:LQSACO>2.3.CO;2](https://doi.org/10.1130/0016-7606(1999)111<1700:LQSACO>2.3.CO;2)
- Harrington, G. J., 2004. Structure of the North American vegetation gradient during the late Paleocene/early Eocene warm climate. *Evolutionary Ecology Research*, 6(1), 33-48.
- Harris, D., Horwáth, W.R., van Kessel, C., 2001. Acid fumigation of soils to remove carbonates prior to total organic carbon or carbon-13 isotopic analysis. *Soil Science Society of America Journal* 65, 1853–1856. <https://doi.org/10.2136/sssaj2001.1853>
- Heaton, T.J., Köhler, P., Butzin, M., Bard, E., Reimer, R.W., Austin, W.E.N., Bronk Ramsey, C., Grootes, P.M., Hughen, K.A., Kromer, B., Reimer, P.J., Adkins, J., Burke, A., Cook, M.S., Olsen, J., Skinner, L.C., 2020. Marine20—The Marine Radiocarbon Age Calibration Curve (0–55,000 cal BP). *Radiocarbon* 62, 779–820. <https://doi.org/10.1017/RDC.2020.68>
- Hjelstuen, B.O., Brendryen, J., 2014. Submarine Mass-movements and Trigger Mechanisms in Byfjorden, Western Norway, in: Krastel, S., Behrmann, J.-H., Völker, D., Stipp, M., Berndt, C., Urgeles, R., Chaytor, J., Huhn, K., Strasser, M., Harbitz, C.B. (Eds.), *Submarine Mass-movements and Their Consequences, Advances in Natural and Technological Hazards Research*. Springer International Publishing, Cham, 351–359. [https://doi.org/10.1007/978-3-319-00972-8\\_31](https://doi.org/10.1007/978-3-319-00972-8_31)
- Hjelstuen, B.O., Haflidason, H., Sejrup, H.P., Lyså, A., 2009. Sedimentary processes and depositional environments in glaciated fjord systems — Evidence from Nordfjord, Norway. *Marine Geology* 258, 88–99. <https://doi.org/10.1016/j.margeo.2008.11.010>
- Hjelstuen, B.O., Kjennbakken, H., Bleikli, V., Ersland, R.A., Kvilhaug, S., Euler, C., Alvheim, S., 2013. Fjord stratigraphy and processes - evidence from the NE Atlantic Fensfjorden system. *Journal of Quaternary Science* 28, 421–432. <https://doi.org/10.1002/jqs.2636>

- Hodell, D.A., Channell, J.E.T., Curtis, J.H., Romero, O.E., Röhl, U., 2008. Onset of “Hudson Strait” Heinrich events in the eastern North Atlantic at the end of the middle Pleistocene transition (~640 ka)? *Paleoceanography* 23, 1-16.  
<https://doi.org/10.1029/2008PA001591>
- Hoffman, J.S., Carlson, A.E., Winsor, K., Klinkhammer, G.P., LeGrande, A.N., Andrews, J.T., Strasser, J.C., 2012. Linking the 8.2 ka event and its freshwater forcing in the Labrador Sea. *Geophysical Research Letters* 39, 1-5.  
<https://doi.org/10.1029/2012GL053047>
- Hoogakker, B.A.A., McCave, I.N., Elderfield, H., Hillaire-Marcel, C., Simstich, J., 2015. Holocene climate variability in the Labrador Sea. *Journal of the Geological Society* 172, 272–277. <https://doi.org/10.1144/jgs2013-097>
- Howe, J.A., Austin, W.E.N., Forwick, M., Paetzel, M., Harland, R., Cage, A.G., 2010. Fjord systems and archives: a review. *Geological Society, London, Special Publications* 344, 5–15. <https://doi.org/10.1144/SP344.2>
- Ives, J.D., 1976. The Saglek Moraines of Northern Labrador: A Commentary. *Arctic and Alpine Research* 8, 403-408. <https://doi.org/10.2307/1550444>
- Ives, J.D., 1957. Glaciation of the Torngat Mountains, Northern Labrador. *Arctic* 10, 66-87.  
<https://doi.org/10.14430/arctic3755>
- Jansson, K.N., Kleman, J., 2004. Early Holocene glacial lake meltwater injections into the Labrador Sea and Ungava Bay. *Paleoceanography* 19, 1-12.  
<https://doi.org/10.1029/2003PA000943>
- Jennings, A., Andrews, J., Pearce, C., Wilson, L., Ólfasdóttir, S., 2015. Detrital carbonate peaks on the Labrador shelf, a 13–7ka template for freshwater forcing from the Hudson Strait outlet of the Laurentide Ice Sheet into the subpolar gyre. *Quaternary Science Reviews* 107, 62–80. <https://doi.org/10.1016/j.quascirev.2014.10.022>
- Jennings, A.E., Manley, W.F., Maclean, B., Andrews, J.T., 1998. Marine evidence for the last glacial advance across eastern Hudson Strait, eastern Canadian Arctic. *Journal of Quaternary Science* 13, 501–514. [https://doi.org/10.1002/\(SICI\)1099-1417\(1998110\)13:6<501::AID-JQS391>3.0.CO;2-A](https://doi.org/10.1002/(SICI)1099-1417(1998110)13:6<501::AID-JQS391>3.0.CO;2-A)
- Josenhans, H.W., Zevenhuizen, J., Klassen, R.A., 1986. The Quaternary geology of the Labrador Shelf. *Can. Journal of Earth Sciences* 23, 1190–1213.  
<https://doi.org/10.1139/e86-116>
- Kaufman, D.S., Miller, G.H., Stravers, J.A., Andrews, J.T., 1993. Abrupt early-Holocene (9.9-9.6 kyr BP) ice stream advance at the mouth of Hudson Strait, Arctic Canada. *Geology* 21, 1063-1066.

- Keigwin, L.D., Klotsko, S., Zhao, N., Reilly, B., Giosan, L., Driscoll, N.W., 2018. Deglacial floods in the Beaufort Sea preceded Younger Dryas cooling. *Nature Geosci* 11, 599–604. <https://doi.org/10.1038/s41561-018-0169-6>
- Keigwin, L.D., Sachs, J.P., Rosenthal, Y., Boyle, E.A., 2005. The 8200 year B.P. event in the slope water system, western subpolar North Atlantic. *Paleoceanography* 20, 1-14. <https://doi.org/10.1029/2004PA001074>
- Kerwin, M.W., 1996. A Regional Stratigraphic Isochron (ca. 8000 <sup>14</sup>C yr B.P.) from Final Deglaciation of Hudson Strait. *Quaternary Research* 46, 89–98. <https://doi.org/10.1006/qres.1996.0049>
- Korff, L., von Dobeneck, T., Frederichs, T., Kasten, S., Kuhn, G., Gersonde, R., Diekmann, B., 2016. Cyclic magnetite dissolution in Pleistocene sediments of the abyssal northwest Pacific Ocean: Evidence for glacial oxygen depletion and carbon trapping: Magnetite Dissolution in the NW Pacific. *Paleoceanography* 31, 600–624. <https://doi.org/10.1002/2015PA002882>
- Lajeunesse, P., St-Onge, G., 2008. The subglacial origin of the Lake Agassiz–Ojibway final outburst flood. *Nature Geoscience* 1, 184–188. <https://doi.org/10.1038/ngeo130>
- Lamb, A., Wilson G., Leng, M., 2006 A review of coastal palaeoclimate and relative sea-level reconstructions using  $\delta^{13}\text{C}$  and C/N ratios in organic material. *Earth Science Reviews* 75, 29-57. <https://doi.org/10.1016/j.earscirev.2005.10.003>
- Lane, T. P., Roberts, D. H., Rea, B. R., Cofaigh, C. Ó., Vieli, A., Rodés, A., 2014. Controls upon the Last Glacial maximum deglaciation of the northern Ummannaq ice stream system, West Greenland. *Quaternary Science Reviews* 92, 324-344. <https://doi.org/10.1016/j.quascirev.2013.09.013>
- Lazier, J. R. N., Wright, D. G., 1993. Annual velocity in the Labrador Current. *American Meteorological Society* 23, 659-678. [https://doi.org/10.1175/1520-0485\(1993\)023<0659:AVVITL>2.0.CO;2](https://doi.org/10.1175/1520-0485(1993)023<0659:AVVITL>2.0.CO;2)
- Lévesque, Y., St-Onge, G., Lajeunesse, P., Desiège, P., Brouard, E., 2020. Defining the maximum extent of the Laurentide Ice Sheet in Home Bay (eastern Arctic Canada) during the Last Glacial episode. *Boreas* 49, 52–70. <https://doi.org/10.1111/bor.12415>
- Lewis, C.F.M., Miller, A.A.L., Levac, E., Piper, D.J.W., Sonnichsen, G.V., 2012. Lake Agassiz outburst age and routing by Labrador Current and the 8.2 ka cold event. *Quaternary International* 260, 83–97. <https://doi.org/10.1016/j.quaint.2011.08.023>
- Liu, J., 2004. High-resolution analysis of early diagenetic effects on magnetic minerals in post-middle-Holocene continental shelf sediments from the Korea Strait. *Journal of Geophysical Research* 109, B03103. <https://doi.org/10.1029/2003JB002813>
- Lochte, A.A., Repschläger, J., Kienast, M., Garbe-Schönberg, D., Andersen, N., Hamann, C., Schneider, R., 2019a. Labrador Sea freshening at 8.5 ka BP caused by Hudson Bay

- Ice Saddle collapse. *Nature Communication* 10, 586. <https://doi.org/10.1038/s41467-019-08408-6>
- Lochte, A.A., Repschläger, J., Seidenkrantz, M.-S., Kienast, M., Blanz, T., Schneider, R.R., 2019b. Holocene water mass changes in the Labrador Current. *The Holocene* 29, 676–690. <https://doi.org/10.1177/0959683618824752>
- Margreth, A., Gosse, J.C., Dyke, A.S., 2017. Wisconsinan and early Holocene glacial dynamics of Cumberland Peninsula, Baffin Island, Arctic Canada. *Quaternary Science Reviews* 168, 79–100. <https://doi.org/10.1016/j.quascirev.2017.04.033>
- Matero, I.S.O., Gregoire, L.J., Ivanovic, R.F., Tindall, J.C., Haywood, A.M., 2017. The 8.2 ka cooling event caused by Laurentide ice saddle collapse. *Earth and Planetary Science Letters* 473, 205–214. <https://doi.org/10.1016/j.epsl.2017.06.011>
- McNeely, R., Dyke, A.S., Southon, J.R., 2006. Canadian marine reservoir ages, preliminary data assessment. Geological Survey of Canada, openfile No. 5049, 1-3. <https://doi.org/10.4095/221564>
- Meyers, P.A., 1997. Organic geochemical proxies of paleoceanographic, paleolimnologic, and paleoclimatic processes. *Organic Geochemistry* 27, 213–250. [https://doi.org/10.1016/S0146-6380\(97\)00049-1](https://doi.org/10.1016/S0146-6380(97)00049-1)
- Naafs, B.D.A., Hefter, J., Stein, R., 2013. Millennial-scale ice rafting events and Hudson Strait Heinrich(-like) Events during the late Pliocene and Pleistocene: a review. *Quaternary Science Reviews* 80, 1–28. <https://doi.org/10.1016/j.quascirev.2013.08.014>
- Normandeau, A., Lajeunesse, P., Philibert, G., 2013. Late-Quaternary morphostratigraphy of Lake St-Joseph (southeastern Canadian Shield): Evolution from a semi-enclosed glacial-marine basin to a postglacial lake. *Sedimentary Geology* 295, 38–52. <https://doi.org/10.1016/j.sedgeo.2013.07.005>
- Normandeau, A., MacKillop, K., Macquarrie, M., Richards, C., Bourgault, D., Campbell, D.C., Maselli, V., Philibert, G., Clarke, J.H., 2021. Submarine landslides triggered by iceberg collision with the seafloor. *Nature Geoscience* 14, 599–605.
- Occhietti, S., Parent, M., Lajeunesse, P., Robert, F., Govare, É., 2011. Late Pleistocene–Early Holocene Decay of the Laurentide Ice Sheet in Québec–Labrador, in: *Developments in Quaternary Sciences*. Elsevier, pp. 601–630. <https://doi.org/10.1016/B978-0-444-53447-7.00047-7>
- Piva, A., Asioli, A., Schneider, R.R., Trincardi, F., Andersen, N., Colmenero-Hidalgo, E., Dennielou, B., Flores, J.-A., Vigliotti, L., 2008. Climatic cycles as expressed in sediments of the PROMESS1 borehole PRAD1-2, central Adriatic, for the last 370 ka: 1. Integrated stratigraphy. *Geochemistry, Geophysics, Geosystems* 9, :Q01R01. <https://doi.org/10.1029/2007GC001713>

- Radi, T., Pospelova, V., de Vernal, A., Vaughn Barrie, J., 2007. Dinoflagellate cysts as indicators of water quality and productivity in British Columbia estuarine environments. *Marine Micropaleontology* 62, 269–297. <https://doi.org/10.1016/j.marmicro.2006.09.002>
- Ramnarine, R., Voroney, R.P., Wagner-Riddle, C., Dunfield, K.E., 2011. Carbonate removal by acid fumigation for measuring the  $\delta^{13}\text{C}$  of soil organic carbon. *Canadian Journal of Soil Science* 91, 247–250. <https://doi.org/10.4141/cjss10066>
- Rashid, H., Piper, D.J.W., Lazar, K.B., McDonald, K., Saint-Ange, F., 2017. The Holocene Labrador Current: Changing linkages to atmospheric and oceanographic forcing factors. *Paleoceanography* 32, 498–510. <https://doi.org/10.1002/2016PA003051>
- Richerol, T., Fréchette, B., Rochon, A., Pienitz, R., 2016. Holocene climate history of the Nunatsiavut (northern Labrador, Canada) established from pollen and dinoflagellate cyst assemblages covering the past 7000 years. *The Holocene* 26, 44–60. <https://doi.org/10.1177/0959683615596823>
- Richerol, T., Pienitz, R., Rochon, A., 2014. Recent anthropogenic and climatic history of Nunatsiavut fjords (Labrador, Canada): Paleoceanography of Nunatsiavut fjords. *Paleoceanography* 29, 869–892. <https://doi.org/10.1002/2014PA002624>
- Roberts, A.P., 2015. Magnetic mineral diagenesis. *Earth-Science Reviews* 151, 1–47. <https://doi.org/10.1016/j.earscirev.2015.09.010>
- Roberts, A.P., Chang, L., Heslop, D., Florindo, F., Larrasoana, J.C., 2012. Searching for single domain magnetite in the “pseudo-single-domain” sedimentary haystack: Implications of biogenic magnetite preservation for sediment magnetism and relative paleointensity determinations. *Journal of Geophysical Research*. 117, 1-26. <https://doi.org/10.1029/2012JB009412>
- Roberts, A.P., Cui, Y., Verosub, K.L., 1995. Wasp-waisted hysteresis loops: Mineral magnetic characteristics and discrimination of components in mixed magnetic systems. *Journal of Geophysical Research* 100, 17909–17924. <https://doi.org/10.1029/95JB00672>
- Rowan, C.J., Roberts, A.P., Broadbent, T., 2009. Reductive diagenesis, magnetite dissolution, greigite growth and paleomagnetic smoothing in marine sediments: A new view. *Earth and Planetary Science Letters* 277, 223–235. <https://doi.org/10.1016/j.epsl.2008.10.016>
- Roy, M., Dell'Oste, F., Veillette, J.J., de Vernal, A., Helie, J.-F., Parent, M., 2011. Insights on the events surrounding the final drainage of Lake Ojibway based on James Bay stratigraphic sequences. *Quaternary Science Reviews* 30, 682-692. <https://doi.org/10.1016/j.quascirev.2010.12.008>
- Steffen, H., Olesen, O., Sutinen, R., 2021. Glacially-triggered faulting. Cambridge University Press. <https://doi.org/10.1017/9781108779906>

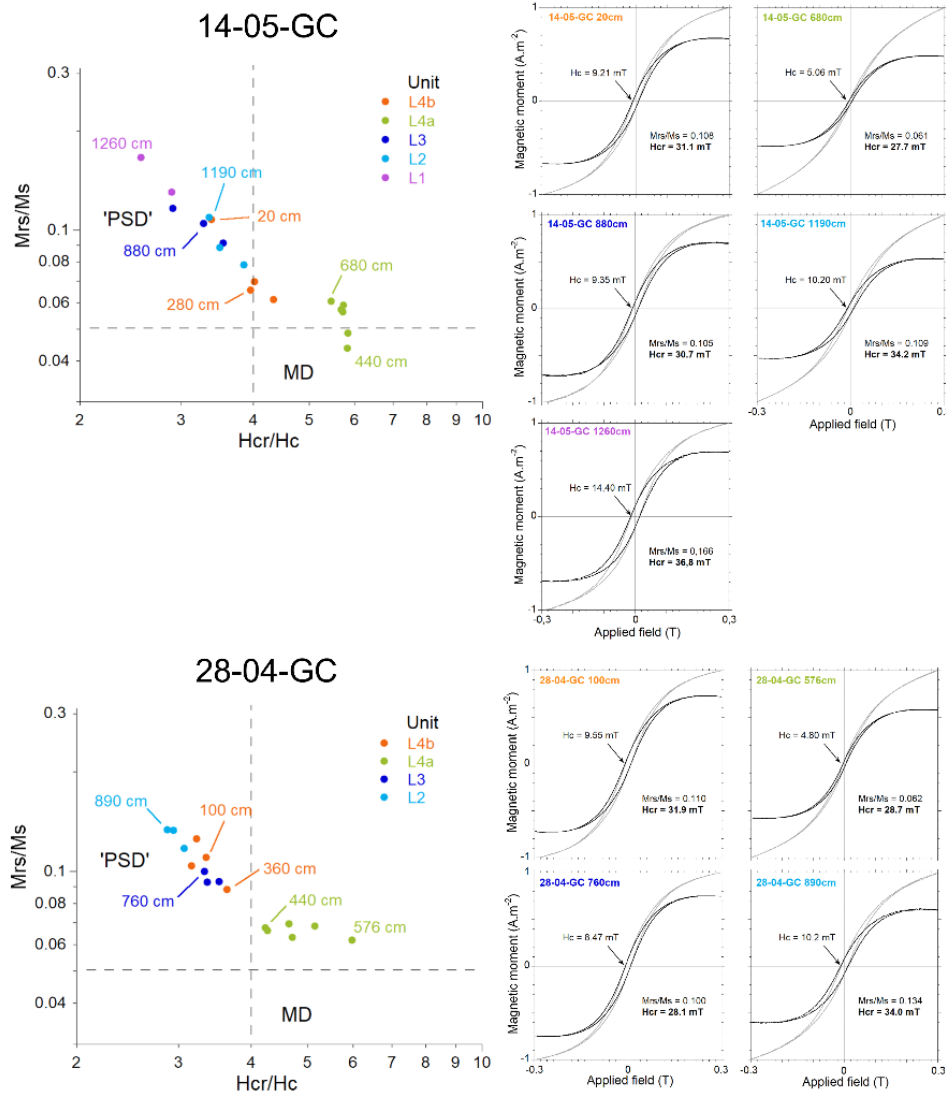
- Stewart, I., Sauber, J., Rose, J., 2000. Glacio-seismotectonics: ice sheets, crustal deformation and seismicity. *Quaternary Science Reviews* 19, 1367-1389.  
[https://doi.org/10.1016/S0277-3791\(00\)00094-9](https://doi.org/10.1016/S0277-3791(00)00094-9)
- Stoker, M.S., Wilson, C.R., Howe, J.A., Bradwell, T., Long, D., 2010. Paraglacial slope instability in Scottish fjords: examples from Little Loch Broom, NW Scotland. *Geological Society, London, Special Publications* 344, 225–242.  
<https://doi.org/10.1144/SP344.16>
- Stoner, J.S., St-Onge, G., 2007. Chapter Three Magnetic Stratigraphy in Paleoceanography: Reversals, Excursions, Paleointensity, and Secular Variation, in: *Developments in Marine Geology* 1, 99–138. [https://doi.org/10.1016/S1572-5480\(07\)01008-1](https://doi.org/10.1016/S1572-5480(07)01008-1)
- St-Onge, G., Chapron, E., Mulsow, S., Salas, M., Viel, M., Debret, M., Foucher, A., Mulder, T., Winiarski, T., Desmet, M., Costa, P.J.M., Ghaleb, B., Jaouen, A., Locat, J., 2012. Comparison of earthquake-triggered turbidites from the Saguenay (Eastern Canada) and Reloncavi (Chilean margin) Fjords: Implications for paleoseismicity and sedimentology. *Sedimentary Geology* 243–244, 89–107.  
<https://doi.org/10.1016/j.sedgeo.2011.11.003>
- St-Onge, G., Hillaire-Marcel, C., 2001. Isotopic constraints of sedimentary inputs and organic carbon burial rates in the Saguenay Fjord, Quebec. *Marine Geology* 176, 1–22. [https://doi.org/10.1016/S0025-3227\(01\)00150-5](https://doi.org/10.1016/S0025-3227(01)00150-5)
- St-Onge, G., Lajeunesse, P., 2007. Flood-Induced Turbidites From Northern Hudson Bay And Western Hudson Strait: A Two-Pulse Record Of Lake Agassiz Final Outburst Flood?, in: Lykousis, V., Sakellariou, D., Locat, J. (Eds.), *Submarine Mass-movements and Their Consequences*. Springer Netherlands, Dordrecht, 129–137.
- St-Onge, G., Lajeunesse, P., Duchesne, M.J., Gagné, H., 2008. Identification and dating of a key Late Pleistocene stratigraphic unit in the St. Lawrence Estuary and Gulf (Eastern Canada). *Quaternary Science Reviews* 27, 2390–2400.  
<https://doi.org/10.1016/j.quascirev.2008.08.023>
- St-Onge, G., Mulder, T., Francus, P., Long, B., 2007. Chapter Two Continuous Physical Properties of Cored Marine Sediments. *Developments in Marine Geology* 1, 63–98.  
[https://doi.org/10.1016/S1572-5480\(07\)01007-X](https://doi.org/10.1016/S1572-5480(07)01007-X)
- Storms, J.E.A., de Winter, I.L., Overeem, I., Drijkoningen, G.G., Lykke-Andersen, H., 2012. The Holocene sedimentary history of the Kangerlussuaq Fjord-valley fill, West Greenland. *Quaternary Science Reviews* 35, 29–50.  
<https://doi.org/10.1016/j.quascirev.2011.12.014>
- Straneo, F., Saucier, F., 2008. The outflow from Hudson Strait and its contribution to the Labrador Current. *Deep Sea Research Part I: Oceanographic Research Papers* 55, 926–946. <https://doi.org/10.1016/j.dsr.2008.03.012>
- Stuiver, M., Reimer, P. J., Reimer, R. W., 2020. CALIB 8.2 [WWW Program]. 2021.

- Syvitski, J.P.M., 1989. On the deposition of sediment within glacier-influenced fjords: oceanographic controls. *Marine Geology* 85, 301-329. [https://doi.org/10.1016/0025-3227\(89\)90158-8](https://doi.org/10.1016/0025-3227(89)90158-8)
- Syvitski, J.P.M., 1991. Towards an understanding of sediment deposition on glaciated continental shelves. *Continental Shelf Research* 11, 897-937. [https://doi.org/10.1016/0278-4343\(91\)90085-K](https://doi.org/10.1016/0278-4343(91)90085-K)
- Syvitski, J.P.M., Lee, H.J., 1997. Postglacial sequence stratigraphy of Lake Melville, Labrador. *Marine Geology* 143, 55-79. [https://doi.org/10.1016/S0025-3227\(97\)00090-X](https://doi.org/10.1016/S0025-3227(97)00090-X)
- Syvitski, J.P.M., Praeg, D.B., 1989. Quaternary Sedimentation in the St. Lawrence Estuary and Adjoining Areas, Eastern Canada: An Overview Based on High-Resolution Seismo-Stratigraphy. *Géographie physique et Quaternaire* 43, 291-310. <https://doi.org/10.7202/032784ar>
- Syvitski, J.P.M., Shaw, J., 1995. Chapter 5 Sedimentology and Geomorphology of Fjords. *Developments in Sedimentology* 1, 113-178. [https://doi.org/10.1016/S0070-4571\(05\)80025-1](https://doi.org/10.1016/S0070-4571(05)80025-1)
- Syvitski, J., Andrews, J. T., Schafer, C. T., Stravers, J. A., 2022. Sediment fill of Baffin Island Fjords: Architecture and rates. *Quaternary Science Reviews* 284, 107474 <https://doi.org/10.1016/j.quascirev.2022.107474>
- Tauxe, L., Mullender, T.A.T., Pick, T., 1996. Potbellies, wasp-waists, and superparamagnetism in magnetic hysteresis. *Journal of Geophysical Research* 101, No. B1, 571-583.
- Thibodeau, B., de Vernal, A., Limoges, A., 2013. Low oxygen events in the Laurentian Channel during the Holocene. *Marine Geology* 346, 183-191. <https://doi.org/10.1016/j.margeo.2013.08.004>
- Thornalley, D.J.R., Oppo, D.W., Ortega, P., Robson, J.I., Brierley, C.M., Davis, R., Hall, I.R., Moffa-Sanchez, P., Rose, N.L., Spooner, P.T., Yashayaev, I., Keigwin, L.D., 2018. Anomalously weak Labrador Sea convection and Atlantic overturning during the past 150 years. *Nature* 556, 227-230.
- Trottier, A., Lajeunesse, P., Gagnon-Poiré, A., Francus, P., 2020. Morphological signatures of deglaciation and postglacial sedimentary processes in a deep fjord-lake (Grand Lake, Labrador). *Earth Surface Processes and Landforms* 45, 928-947. <https://doi.org/10.1002/esp.4786>
- Trottier, A., Brouard, E., Lajeunesse, P., Normandeau, A., 2021. The morphosedimentary record of glacial to postglacial environmental changes in fjord-lake Mékinac and adjacent areas (southeastern Canadian Shield). *Geomorphology* 376, 107565. <https://doi.org/10.1016/j.geomorph.2020.107565>

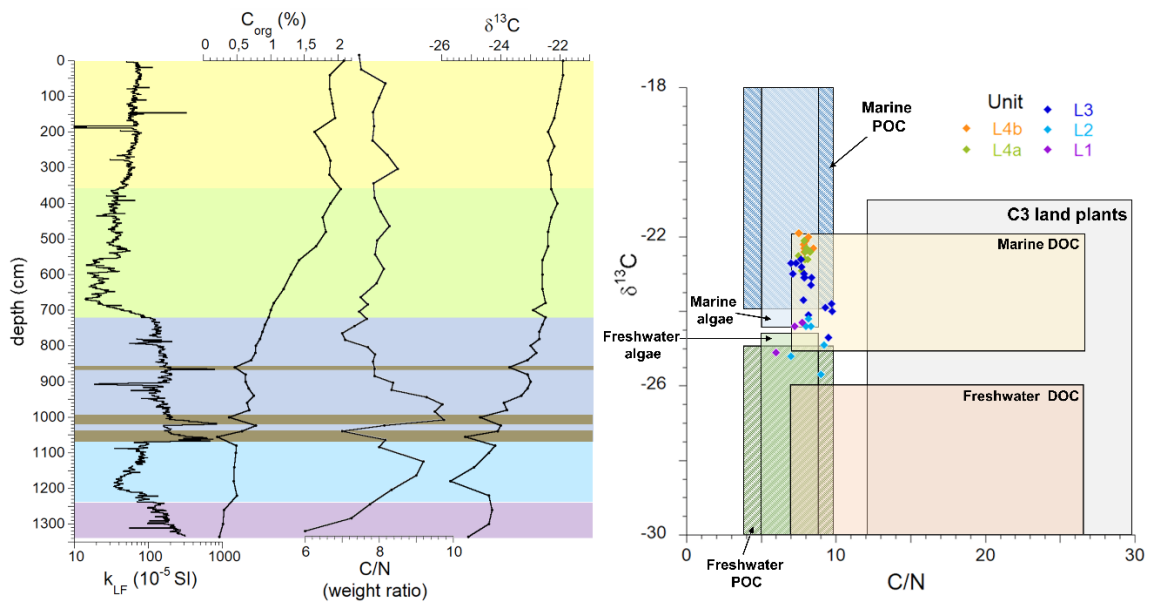


- Turner, A.J., Woodward, J., Dunning, S.A., Shine, A.J., Stokes, C.R., Cofaigh, C.Ó., 2012. Geophysical surveys of the sediments of Loch Ness, Scotland: implications for the deglaciation of the Moray Firth Ice Stream, British-Irish Ice Sheet. *Journal of Quaternary Science* 27, 221–232. <https://doi.org/10.1002/jqs.1538>
- Ullman, D.J., Carlson, A.E., Hostetler, S.W., Clark, P.U., Cuzzone, J., Milne, G.A., Winsor, K., Caffee, M., 2016. Final Laurentide ice-sheet deglaciation and Holocene climate-sea level change. *Quaternary Science Reviews* 152, 49–59. <https://doi.org/10.1016/j.quascirev.2016.09.014>
- Utting, D.J., Gosse, J.C., Kelley, S.E., Vickers, K.J., Ward, B.C., Trommelen, M.S., 2016. Advance, deglacial and sea-level chronology for Foxe Peninsula, Baffin Island, Nunavut. *Boreas* 45, 439–454. <https://doi.org/10.1111/bor.12167>
- Vacchi, M., Engelhart, S.E., Nikitina, D., Ashe, E.L., Peltier, W.R., Roy, K., Kopp, R.E., Horton, B.P., 2018. Postglacial relative sea-level histories along the eastern Canadian coastline. *Quaternary Science Reviews* 201, 124–146. <https://doi.org/10.1016/j.quascirev.2018.09.043>
- Waldmann, N., Anselmetti, F.S., Ariztegui, D., Austin Jr, J.A., Pirouz, M., Moy, C.M., Dunbar, R., 2011. Holocene mass-wasting events in Lago Fagnano, Tierra del Fuego (54°S): implications for paleoseismicity of the Magallanes-Fagnano transform fault: Holocene mass-wasting events in Lago Fagnano, Tierra del Fuego (54°S). *Basin Research* 23, 171–190. <https://doi.org/10.1111/j.1365-2117.2010.00489.x>
- Wardle, R. J., Van Kranendonk, M. J., Mengel, F., Scott, D., Schwarz, S., Ryan, B., Bridgwater, D., 1993. Geological mapping in the Torngat Orogen, northernmost Labrador: report 2. Newfoundland Department of Mining and Energy Report, 93-1, 77-89.
- Yamazaki, T., 2020. Reductive dissolution of biogenic magnetite. *Earth Planets Space* 72, 150. <https://doi.org/10.1186/s40623-020-01290-3>
- Young, N.E., Schaefer, J.M., Briner, J.P., Goehring, B.M., 2013. A <sup>10</sup>Be production-rate calibration for the Arctic. *Journal of Quaternary Science* 28, 515–526. <https://doi.org/10.1002/jqs.2642>

## 1.11 SUPPLEMENTARY MATERIAL (FIGURES)



**Figure 21.** Day-diagrams made with AGM data from cores 14-05-GC and 28-04-GC, along with hysteresis curves of representative samples for each unit of the core. Grey hysteresis curves correspond to raw hysteresis data, whereas the black ones are corrected for paramagnetic and diamagnetic components.



**Figure 22.** Carbon and nitrogen properties for cores 14-05-GC and 13-03-GC along with their magnetic susceptibility. Also shown is a diagram of  $\delta^{13}C$  versus C/N for each core for comparison with the values of different sources of organic matter, based on Lamb et al. (2006).

## **CHAPITRE 2**

### **TROIS VIDANGES DU LAC AGASSIZ-OJIBWAY IDENTIFIÉES DANS DE NOUVEAUX ENREGISTREMENTS SEDIMENTAIRES A HAUTE RESOLUTION DE L'OUEST DU DETROIT D'HUDSON**

#### **2.1 RÉSUMÉ EN FRANÇAIS DU DEUXIÈME ARTICLE**

Des enregistrements sédimentaires à haute résolution sont nécessaires pour étudier avec précision la série des événements de déglaciation de la baie d'Hudson qui sont à l'origine de l'important ajout d'eau douce dans l'Atlantique Nord, responsable du déclenchement de l'événement froid de 8.2 ka. Ces événements sont survenus en quelques siècles et comprennent l'ouverture de la mer de Tyrrell, plusieurs événements de drainage du lac proglaciaire Agassiz-Ojibway et l'effondrement du barrage de glace de la baie d'Hudson. Des carottes à gravité représentant les 9 000 dernières années ont été prélevées dans deux bassins de l'ouest du détroit d'Hudson et couvrent ces événements de déglaciation avec des taux de sédimentation atteignant 0,4 cm/an. Avec une correction constante  $\Delta R$  de l'âge réservoir, les chronologies robustes de ces carottes indiquent que la couche rouge du détroit d'Hudson s'est déposée à environ  $8,67 \pm 0,15$  cal ka BP. Cet âge confirme que la couche serait associée à un drainage sous-glaciaire du lac Agassiz-Ojibway plutôt qu'à son drainage final. Ce drainage a été suivi d'un important afflux d'icebergs, comme l'indique un événement d'IRDs dans les carottes, puis d'un ralentissement du retrait des glaces pendant environ 200 ans à la faveur du début d'un refroidissement général à long terme. Vers 8,2 cal ka BP, le dernier drainage du lac Agassiz-Ojibway s'est produit en deux étapes séparées par quelques décennies et concomitantes avec la chute du barrage de glace de la baie d'Hudson, formant un double pic d'IRDs et de carbonates détritiques dans la séquence sédimentaire. Cependant, la considération d'un âge-réservoir temporellement variable pourrait invalider ces interprétations. Quoi qu'il en soit, les événements étant bien corrélés entre les carottes des

deux bassins, il s'avère que l'âge réservoir marin était supérieur d'environ 700 ans dans le bassin Sud-ouest par rapport au bassin Ouest pendant l'ouverture de la mer de Tyrrell et le drainage sous-glaciaire qui a suivi. Cette différence illustre l'impact des marges glaciaires proximales et/ou de la circulation marine sur le réservoir d'âge marin local.

## **2.2 THREE LAKE AGASSIZ-OJIBWAY DRAINAGES EVENTS CONSTRAINED IN NEW HIGH-RESOLUTION SEDIMENTARY RECORDS FROM THE WESTERN HUDSON STRAIT**

High-resolution sedimentary records are necessary for precisely studying the series of deglacial events characterizing the Hudson Bay deglaciation, which were involved in the massive freshwater input in the North Atlantic that triggered the 8.2 ka cold event. These deglacial events occurred in a few centuries and include the opening of Tyrrell Sea, several drainage events of the proglacial Lake Agassiz-Ojibway, and the Hudson Bay Ice Saddle collapse. Gravity cores spanning the last 9,000 yr were retrieved from two basins in western Hudson Strait and cover the last deglacial events with, for one of them, sedimentation rates reaching 0.4 cm/yr. With a constant age-reservoir correction  $\Delta R$ , strong chronologies of these cores indicate that the Hudson Strait red layer was deposited at about  $8.67 \pm 0.15$  cal ka BP. This age suggests that the layer would be associated with a subglacial drainage of the Lake Agassiz-Ojibway rather than to its final drainage. This subglacial drainage was followed by an iceberg surge as indicated by an IRD event, and then a slowdown of ice retreat for about 200 yr thanks to the start of a long-term general cooling. Around 8.2 cal ka BP, the last drainage of Lake Agassiz-Ojibway occurred in two stages separated by a few decades and concomitant with the Hudson Bay Ice Saddle collapse, forming a double peak of IRDs and detrital carbonates in the sedimentary sequence. However, using a time-varying age-reservoir correction might invalidate these interpretations. In any case, the good correlation of events between the cores from both basins reveal that the marine age reservoir was about 700 yr higher in the westernmost basin during the opening of Tyrrell Sea and the following subglacial drainage. This difference illustrates the impact of proximal ice margins and/or water circulation on local marine age reservoir.

## 2.3 INTRODUCTION

Investigating past ice sheet dynamics and major deglacial events is among the ways of understanding connections between climate, ocean and cryosphere variations in the actual context of accelerating decay of the Greenland and Western Antarctic Ice Sheets. During its deglaciation (21-6 ka), the Laurentide Ice Sheet (LIS) that covered large parts of Canadian lands progressively decayed in response to climatic and oceanic forcings (e.g., Dyke et al., 2004; Stokes, 2017; Dalton et al., 2020). This deglaciation was punctuated by major delivered of freshwater in short times, freshening the North Atlantic waters and disturbing the Atlantic Meridional Overturning Circulation (AMOC) (e.g., Keigwin et al., 1991; Barber et al., 1999; Clark et al., 2001;). The last major climatic perturbation caused by such events was the so-called “8.2 ka event”, a ~160-yr duration cold period identified in many climatic records (e.g., Alley et al., 1997; Baldini et al., 2002; Rasmussen et al., 2006; Lutz et al., 2007; Morrill et al., 2013). This event is usually associated to the drainage of Lake Agassiz Ojibway (LAO), a large proglacial lake that was separated from marine waters of Tyrrell Sea –the Hudson Bay ancestor– by the Hudson Bay Ice Saddle (HBIS) (Barber et al., 1999; Lajeunesse and St-Onge, 2008; Matero et al., 2017). The drainage of this extensive lake occurred as multiple events that injected freshwater in the North Atlantic through Hudson Strait, perturbing the AMOC (e.g., St-Onge and Lajeunesse, 2007; Hillaire-Marcel et al., 2007; Gauthier et al., 2020). Modelling studies also showed that freshwater input from the HBIS collapse itself should have contributed to the weakening of the AMOC and the attendant climate cooling occurring around 8.2 ka BP (Gregoire et al., 2012; Matero et al., 2017; Lochte et al., 2019a).

However, the timing of this series of events and some of their respective sedimentary markers are still a matter of debate (Brouard et al., 2021). A reddish, hematite-rich mud layer found in sediment cores in Hudson Strait have been for long associated with sediment spilled from Northwestern Hudson Bay by the last LAO drainage (Kerwin, 1996; Barber et al., 1999; St-Onge and Lajeunesse, 2007). This red layer, first dated at  $8.47 \pm 0.30$  cal ka BP, was used as a chronostratigraphic marker for the LAO drainage (Barber et al., 1999; Haberzettl et al., 2010; Lewis et al., 2012), but recent studies argued it was rather produced during the opening

of the Tyrrell Sea, centuries before LAO drainages (Jennings et al., 2015; Brouard et al., 2021). Moreover, there is no consensus about the timing of the LAO drainages. Some studies consider a main drainage around 8.45-8.55 cal ka BP (Barber et al., 1999; Rashid et al., 2017; Lochte et al., 2019a). Subglacial channel mapping in western Hudson Bay combined with chronologies based on marine and freshwater mollusks rather suggests a first, subglacial drainage around 8.57 cal ka BP and a last and main drainage around 8.11 cal ka BP, following the HBIS demise (Gauthier et al., 2020). Recently, Brouard et al. (2021) used a compilation of 597 recalibrated  $^{14}\text{C}$  ages to constrain a partial drainage at  $8.22 \pm 0.02$  cal ka BP and a final one at  $8.16 \pm 0.02$  cal ka BP, together bracketing the end of the HBIS collapse. This theory of two closely-spaced drainages is supported by varve sequences from eastern LAO basin (Godbout et al., 2019, 2020). However, the only continuous records strengthening this last theory are in the North Atlantic (Ellison et al., 2006; Jennings et al., 2015; Lochte et al., 2019a), and more detailed sediment sequences are needed to improve the chronology of the Hudson Bay deglacial events.

The study and comparison of marine sedimentary records of the deglaciation is further complicated by the use of different Early and Middle Holocene age-reservoir corrections  $\Delta R$  for a same oceanographically consistent region. Some studies choose to keep using the modern  $\Delta R$  through the sedimentary record when building their age-models (e.g., Jennings et al., 2015; Gauthier et al., 2020; Brouard et al., 2021), while others increase the  $\Delta R$  by 100-500 yr for older samples to compensate for the influence of  $^{14}\text{C}$ -depleted meltwaters (e.g., Ross et al., 2012; Rashid et al., 2017; Lochte et al., 2019). In a context of high-resolution paleoclimate studies, the centennial-scale differences in the resulting calibrated age may impact the correlation of marine proxies with specific climatic events.

This study presents new high-resolution sediment records from two western Hudson Strait basins containing the same markers of the last regional deglacial events, in order to better constrain their chronology. These well dated records allow comparison with the latest LAO drainage studies and discussion of the issues surrounding the choice of  $\Delta R$  for the regional events.

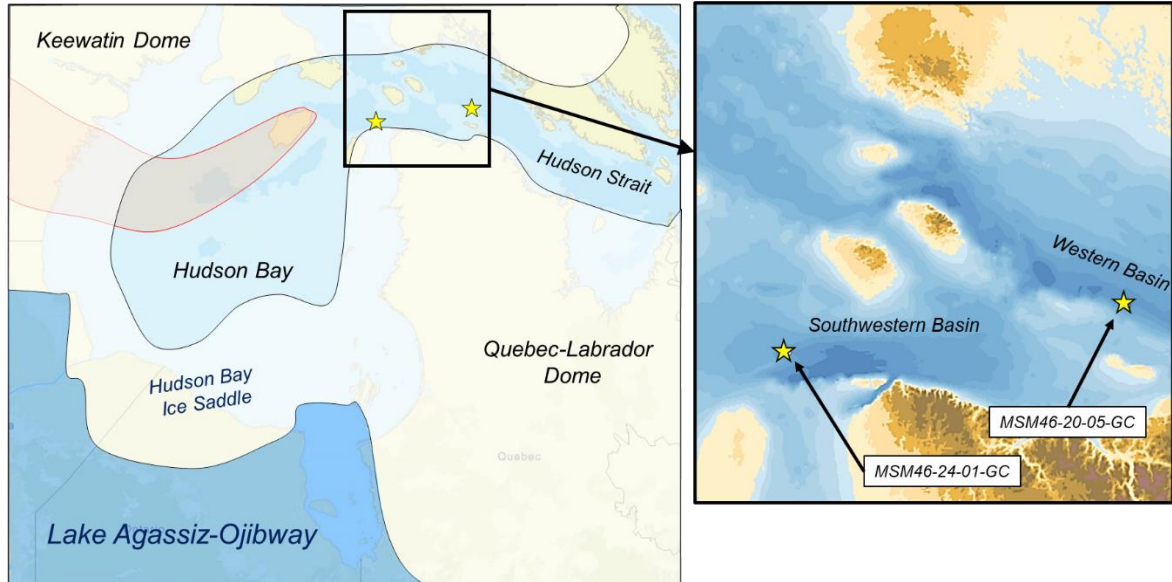
## 2.4 STUDY AREA

### 2.4.1 Physiography and oceanography

Hudson Strait is a major marine waterway of about 800 km long and 90 km wide that links Hudson Bay and Foxe Basin to the Labrador Sea and the North Atlantic (Andrews and MacLean, 2003). While Hudson Bay has a mean depth of about 125 m and a gentle bathymetry, Hudson Strait is deeper (200-400 m) and is characterized by three sedimentary basins formed by half-graben structures parallel to the Hudson Strait main axis (Fig. 23), informally referred to the Southwestern, Western and Eastern Basins (Prinsenber, 1986; MacLean, 2001a; Andrews and MacLean, 2003). The Southwestern and Western Basins, situated close to the western end of Hudson Strait, are about 400-500 m deep, whereas the Eastern Basin, at the eastern end, is the largest and deepest with depths below 900 m (MacLean, 2001a; Andrews and MacLean, 2003). Hudson Bay and Strait bedrock is mainly composed by Early Paleozoic carbonate rocks, surrounded beneath them and near the coasts by Precambrian metamorphic rocks (MacLean, 2001b).

In Hudson Bay, the water circulation pattern is counter-clockwise, with waters flowing from Foxe Basin and rivers and evacuating at the Northeast towards Hudson Strait (Prinsenber, 1986). In Hudson Strait, the circulation is mostly from west to east and is generally influenced by runoff and polar waters coming from Hudson Bay, Foxe Basin and Ungava Bay (Drinkwater, 1986; Vilks et al, 1989). Bottom waters with higher salinities also enter Hudson Strait from the Labrador Sea and are mixed with low-salinity waters in the eastern part of Hudson Strait. High-amplitude tides and strong tidal currents favorize a well-mixed water column in Hudson Strait (Drinkwater, 1986; Hill et al., 2011).





**Figure 23.** Map of the study area with extension of the Laurentide Ice Sheet before the drainage of Lake Agassiz-Ojibway. Yellow stars represent locations of the cores used in the study. The red patch is the principal area of red erratics dispersed by the ice-sheet from the Dubawnt Group at the northwest.

#### 2.4.2 Deglaciation and Quaternary sequence

During the last glaciation, Hudson Strait was host to a large and fast ice-stream that drained an extensive part of the LIS (Laymon, 1992; Andrews and Maclean, 2003; Tarasov et al., 2012). This ice-stream played a major role in the Heinrich Events and the deglaciation of Eastern Canada, during which it enhanced massive sedimentation out and in Hudson Strait. The deglaciation of Hudson Strait occurred between 12.8 and 8.7 cal ka BP (Dalton et al. 2020). During this period of general westward retreat of the ice-margin, two major ice-readvances were initiated by the drawdown of the Labrador Dome located over central Quebec: the Gold Cove at 11-10.6 cal ka BP and the subsequent Noble Inlet advance around 9.7-9.1 cal ka BP (Kaufman et al., 1993; Jennings et al., 1998; Jennings et al., 2015). Once deglaciated, Hudson Strait became the main pathway for icebergs and meltwaters from Hudson Bay and Foxe Basin areas towards the North Atlantic during the final steps of the

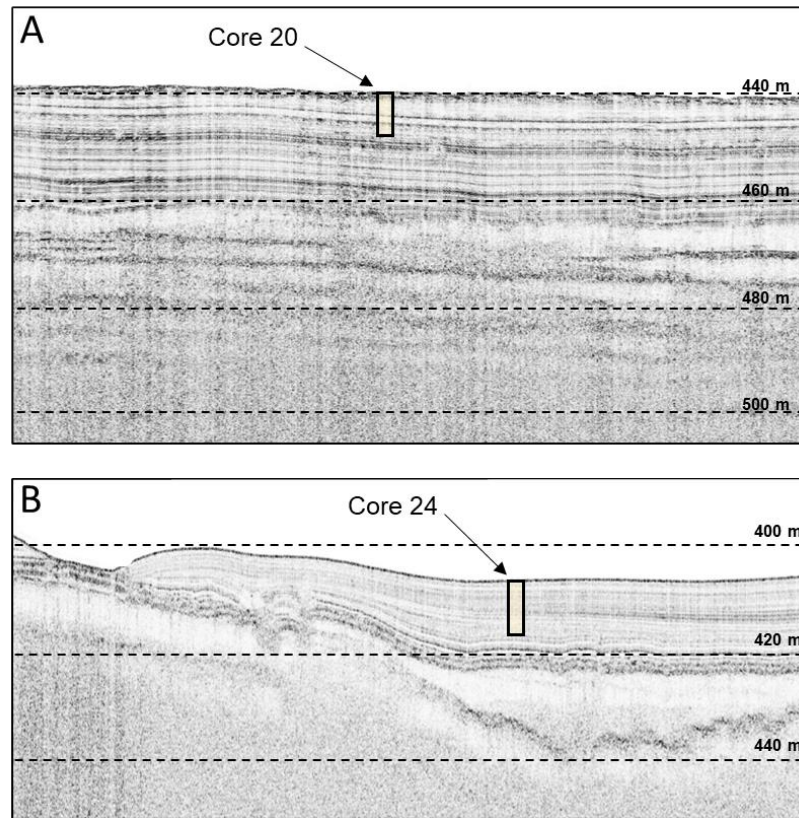
LIS retreat. (e.g., Lajeunesse and St-Onge, 2008; Ross et al., 2012). After ice retreat, the relative sea-level dropped by about 120-160 m in western Hudson Strait area due to glacio-isostatic recovery, as determined from paleo-shorelines and marine samples recovered on coastlines (Ross et al., 2012; Vacchi et al., 2018). About 50-70% of this readjustment was completed by 6.5 cal ka BP.

While a thick unit or sequence of ice-contact sediment is ubiquitous in Hudson Bay and Hudson Strait, locations containing continuous glaciomarine and postglacial sediment sequences are rare. In Hudson Strait, such sequences are only localized in the three basins and in some other rare locations. Several cores have already been retrieved in these basins and revealed the presence of the red layer with various thicknesses (e.g., Kerwin, 1996; Hall et al., 2001; St-Onge and Lajeunesse, 2007; Haberzettl et al., 2010). Outside of the basins, postglacial sediments consist of a 10-15 cm-thick surface veneer of sand or gravel formed by the winnowing action of bottom currents combined with ice rafted debris (IRDs) deposition (MacLean et al., 2001).

## **2.5 METHODS**

### **2.5.1 Sampling**

Cores MSM46-20-05-GC and MSM46-24-01-GC, hereafter referred as cores 20 and 24 respectively, were retrieved during RV Maria S. Merian expedition MSM46 in 2015. Sub-bottom sediment profiles were also obtained during the mission with a PARASOUND P70 and helped to select locations with sufficient Holocene sediment thicknesses for coring (Fig. 24). Core 20 was sampled in the Western Basin (63.0495; -74.3112; 426 m water depth) and measures 8.07 m, while core 24 was retrieved in the Southwestern Basin (62.7650; -79.0043; 394 m water depth) and is 9.62 m-long. Both cores were opened, described and photographed onboard, and u-channels for paleomagnetic analyses were also directly sampled, as well as some sediment at selected depths for radiocarbon dating on foraminifera.



**Figure 24.** Sub-bottom profiles of the coring locations of A) Core 20 in the Western Basin and B) Core 24 in the Southwestern Basin. A sediment velocity of 1500 m/s is used to correlate the cores with the acoustic signal.

### 2.5.2 Sediment analyses

X-ray digital images of cores 20 and 24 were obtained on the U-channels with a CT-scan at the INRS-ETE in Québec City, while the split cores were run into a Multi Sensor Core Logger (MSCL) at ISMER to measure several parameters at 1 cm intervals. These parameters include the low-field magnetic susceptibility  $k_{LF}$  with a Bartington point sensor, the  $a^*$  green to red scale of the International Commission on Illumination (CIE) measured with a Minolta CM-2600d spectrophotometer, as well as Ca, Ti, Zr and Rb concentrations with an Innov-X Olympus Delta Element x-ray fluorescence (XRF) spectrometer.  $k_{LF}$  is

mostly related to ferrimagnetic grain concentration but also enhanced by large ( $>10\ \mu\text{m}$ ) grains (Stoner and St-Onge, 2007). An increase in  $a^*$  values is observed in reddish sediment, and is used to eventually find the Hudson Strait red layer (e.g., St-Onge and Lajeunesse, 2007; Jennings et al., 2015; Lochte et al., 2019a). The Ca/Ti is used as a proxy for carbonate content, while the Zr/Rb was used to infer grain-size variations and for identifying important terrigenous inputs (Croudace et al., 2006; Croudace and Rothwell, 2015; Duboc et al., 2017).

An anhysteretic remanent magnetization (ARM) was also imparted to the U-channels by inducing a peak alternating field of 100 mT with a superimposed 0.05 mT direct current biasing field. This ARM was then measured with a 2G SRM-755 u-channel cryogenic magnetometer after each step of demagnetization with an alternative field from 0 to 80 mT, with 5-mT increments. Derived from ARM, the anhysteretic susceptibility  $k_{\text{ARM}}$  is combined with  $k_{\text{LF}}$  to obtain the  $k_{\text{ARM}}/k_{\text{LF}}$  that varies inversely with the magnetic grain-size, particularly in the 1-10  $\mu\text{m}$  range (King et al., 1983; Stoner and St-Onge, 2007) and is thus a grain-size indicator when chemical processes did not affect the primary magnetic assemblage.

Lower halves of cores 20 and 24 were also sieved at 63  $\mu\text{m}$  and then 150  $\mu\text{m}$  in order to evaluate the relative quantities of sand and gravel, as well as IRDs before the postglacial transition.

### **2.5.3 Chronology**

A total of 33 radiocarbon ages were obtained on mollusc shells and foraminifera samples (Table 4) in order to develop the cores chronologies. The shells, directly sampled in the opened cores, were sent for analysis to the Leibniz Laboratory for Radiometric Dating and Isotope Research of Kiel University (CAU), Germany. The foraminifera were picked in sediment previously sieved at 63 $\mu\text{m}$ , and were then sent to the ETH Zürich, Switzerland, for  $^{14}\text{C}$  analyses. The obtained ages were then calibrated with the Calib 8.2 software (Stuiver et al., 2020) and best-fit linearly interpolated age models were made with the R software

package BACON (Blaauw and Christen, 2011) with the Marine 20 calibration curve (Heaton et al., 2020) and an age-reservoir correction ( $\Delta R$ ).

Pieńkowski et al. (2022) proposes regional  $\Delta R$  values for molluscs and foraminifera from Arctic North America adapted for the Marine 20 curve. These  $\Delta R$  correspond to modern values, as they are based on pre-industrial molluscs (Coulthard et al., 2010; Pieńkowski et al., 2022). However, local reservoir age may fluctuate by several centuries through time, as they depend on water mass ventilation that varies with water stratification and meltwater runoff, which are generally enhanced during deglaciation (Vickers et al., 2010). Moreover, meltwaters originating from old and  $^{14}\text{C}$ -depleted ice contribute to increase the  $\Delta R$  value and even more if these waters transport  $^{14}\text{C}$ -depleted detrital carbonates eroded from Paleozoic platforms such as in Hudson Bay, Hudson Strait, and Foxe Basin areas (England et al., 2013; Lougheed et al., 2013). Therefore, many studies applied different  $\Delta R$  corrections for Mid- and Early-Holocene  $^{14}\text{C}$  ages in order to compensate for sea-ice and other processes that may increase age reservoir (e.g., Vickers et al., 2010; Lewis et al., 2012; Ross et al., 2012; Rashid et al., 2017; Lochte et al., 2019b), while others decided to keep a same  $\Delta R$  value through time (e.g., Jennings et al., 2015; Caron et al., 2019; Brouard et al., 2021; Allan et al., 2021).

Here, as there are no clear constraints on past reservoir age changes, we were conservative and used the same  $\Delta R$  value of  $-73 \pm 64$  yr proposed by Pieńkowski et al. (2022) for Hudson Strait for all cores. This choice is further discussed in section 5.2.

**Table 4.** List of AMS radiocarbon ages analyzed and calibrated in Calib8.2 (Stuiver et al., 2020) using the Marine20 dataset (Heaton et al., 2020) and the  $\Delta R$  value of  $-73 \pm 64$  yr proposed by Pieńkowski et al. (2022).

Core	Depth (cm)	Dated material	Uncorrected $^{14}\text{C}$ age ( $^{14}\text{C}$ yr BP)	2 sigma age range (cal. yr BP)	Median probability age (cal. yr BP)	AMS laboratory number
MSM46-20-05-GC	71	N. labradorica	580 $\pm$ 50	0-289	<b>129</b>	ETH-102154
<i>Western Basin</i>	126	N. labradorica	4470 $\pm$ 60	4287-4817	<b>4552</b>	ETH-102155
	145	Mollusk shell	4087 $\pm$ 28	3810-4295	<b>4042</b>	KIA-54310
	280	Mollusk shell	6045 $\pm$ 30	6158-6569	<b>6351</b>	KIA-54311
	319	Benthic forams	6670 $\pm$ 60	6793-7272	<b>7048</b>	ETH-87308
	369	Benthic forams	6895 $\pm$ 60	7050-7490	<b>7282</b>	ETH-87309
	383	Mollusk shell	6770 $\pm$ 40	6931-7361	<b>7156</b>	Poz-110849
	385	Mollusk shell	6735 $\pm$ 35	6896-7318	<b>7117</b>	KIA-54312
	417	Mollusk shell	7195 $\pm$ 35	7376-7744	<b>7555</b>	Poz-110851
	428	Benthic forams	7700 $\pm$ 60	7842-8293	<b>8059</b>	ETH-87310
	519	Benthic forams	7885 $\pm$ 60	8009-8457	<b>8247</b>	ETH-87311
	669	Benthic forams	8265 $\pm$ 70	8423-8981	<b>8698</b>	ETH-87312
	683	Benthic forams	8375 $\pm$ 80	8516-9145	<b>8835</b>	ETH-87313
	694	Benthic forams	8340 $\pm$ 70	8499-9082	<b>8792</b>	ETH-87314
	731	Benthic forams	8290 $\pm$ 60	8457-8993	<b>8729</b>	ETH-102786
	734	Mollusk shell	8555 $\pm$ 35	8838-9340	<b>9091</b>	KIA-54313
	752	Mollusk shell	8505 $\pm$ 70	8693-9310	<b>9022</b>	ETH-102787
	800	Benthic forams	9200 $\pm$ 70	9564-10160	<b>9877</b>	ETH-87315
MSM46-24-01-GC	39	Mollusk shell	1068 $\pm$ 23	413-715	<b>564</b>	KIA-54314
<i>Southwestern Basin</i>	119	Benthic forams	2140 $\pm$ 50	1399-1866	<b>1634</b>	ETH-102156
	219	Benthic forams	2770 $\pm$ 60	2163-2690	<b>2425</b>	ETH-102157
	306	Mollusk shell	2950 $\pm$ 27	2394-2834	<b>2631</b>	KIA-54315
	456	Mollusk shell	3656 $\pm$ 27	3268-3708	<b>3488</b>	KIA-54316
	469	Benthic forams	4070 $\pm$ 60	3732-4301	<b>4020</b>	ETH-102158
	519	Benthic forams	4290 $\pm$ 60	4019-4586	<b>4310</b>	ETH-102159
	537	Mollusk shell	4358 $\pm$ 29	4146-4647	<b>4402</b>	KIA-54317
	569	Benthic forams	4770 $\pm$ 60	4667-5240	<b>4933</b>	ETH-102160
	600	Mollusk shell	4805 $\pm$ 35	4767-5257	<b>4974</b>	KIA-54318
	631	Benthic forams	5900 $\pm$ 70	5936-6428	<b>6195</b>	ETH-102161
	694	Mollusk shell	6720 $\pm$ 35	6882-7306	<b>7101</b>	KIA-54319
	769	Mollusk shell	7560 $\pm$ 60	7688-8140	<b>7909</b>	ETH-102162
	829	Ostracods	8620 $\pm$ 70	8901-9434	<b>9167</b>	ETH-102163
	829	Benthic forams	8650 $\pm$ 70	8953-9459	<b>9201</b>	ETH-102164

## 2.6 RESULTS

### 2.6.1 Lithology

In order to facilitate the comparison between cores 20 and 24, they are divided in three units following variations in their properties.

#### 2.6.1.1 Unit 1

Unit 1 corresponds to the sediment sequence below the red bed and is not similar from one core to another. In core 20, unit 1 is relatively homogenous, composed by clayey silt with a weight percentage of particles  $> 63 \mu\text{m}$  below 4%, and a slightly increasing upward  $a^*$ . In contrast, unit 1 is much coarser in core 24 and mainly composed of sandy silt with pebbles. Sand and gravel contents highly vary between 2 and 40%, but follow a general decreasing upward trend. Most of this unit in core 24 is brownish, but a 30 cm-thick grayish layer at the center is finer and has lower values of Ca/Ti, Zr/Rb and  $a^*$  than the rest.

#### 2.6.1.2 Unit 2

Despite the fact that unit 2 is three times thicker in core 20 than in 24, it shows the same sediment sequence in both cores. At the base, the red layer, well identifiable in core photographs, is about 20 and 6 cm-thick in cores 20 and 24 respectively and is marked by lowering of all  $k_{LF}$ , Zr/Rb, Ca/Ti and grain-size parameters. Following  $a^*$  values, the red sediment concentration in the red layer progressively increases and decreases upward. In both cores, this layer is topped by a 20-25 cm-thick IRD-rich layer that reaches 10% of particles  $> 63 \mu\text{m}$ . This layer has no variations of carbonate content and pebbles found inside are not carbonated either, but it shows a small  $a^*$  peak in both cores. Above this IRD-layer, the sediment becomes much finer, and poor in carbonates and IRDs in comparison to unit 1 and the rest of unit 2. This fine layer is highlighted by a particularly high  $k_{ARM}/k_{LF}$  values in core 24, reflecting higher quantities of very fine magnetic grains. Finally, the top of unit 2 consists of a layer richer in detrital carbonates and IRDs that is about 60 and 20 cm-thick in cores 20

and 24 respectively. This layer, hereafter named DDCP (double detrital carbonate peak) is made of two main peaks, the upper one being thicker and more pronounced in both cores.

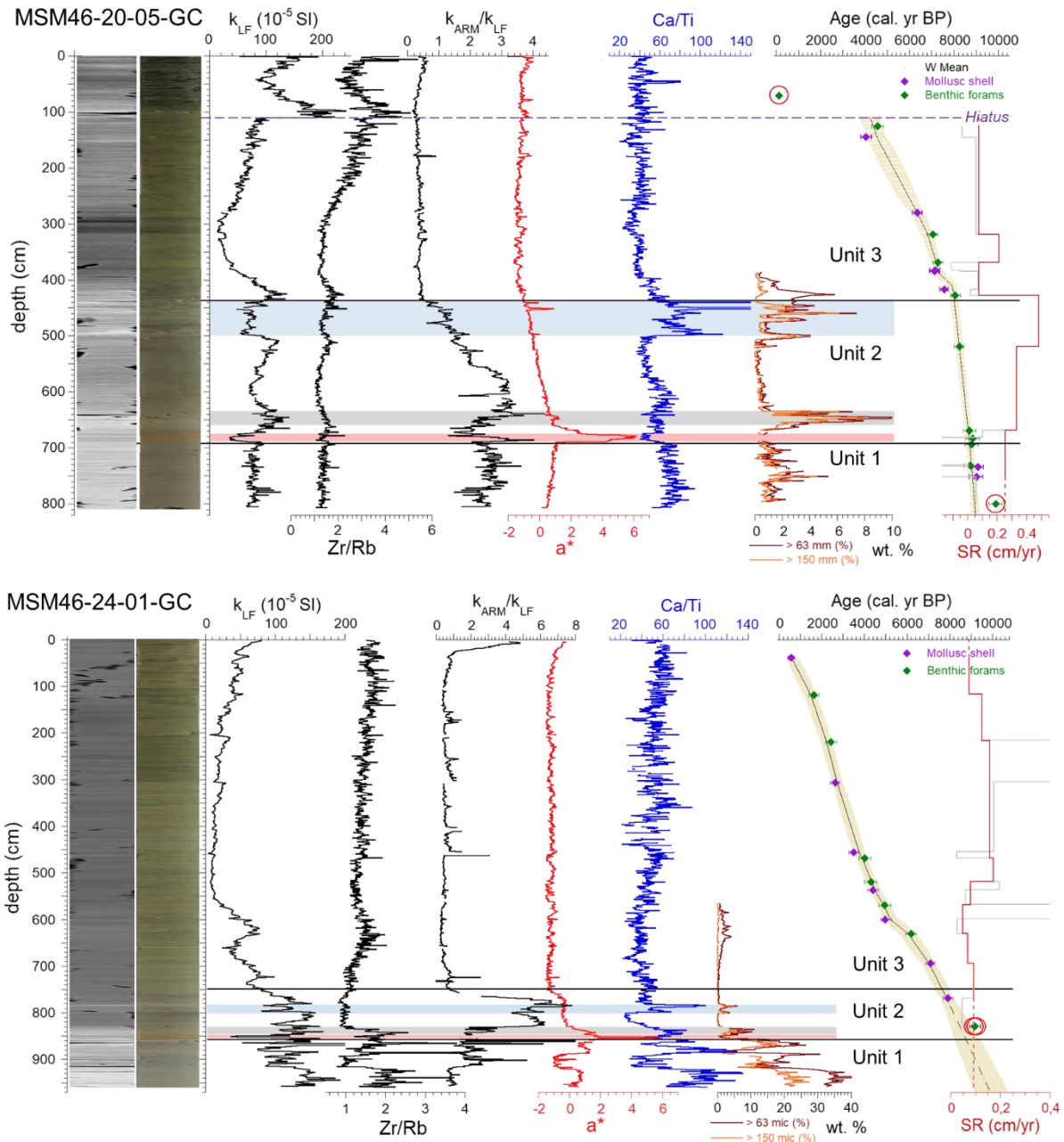
### 2.6.1.3 Unit 3

Unit 3 is characterized by relatively constant  $a^*$  and Ca/Ti values in both cores, but shows variations of magnetic and other grain-size parameters.

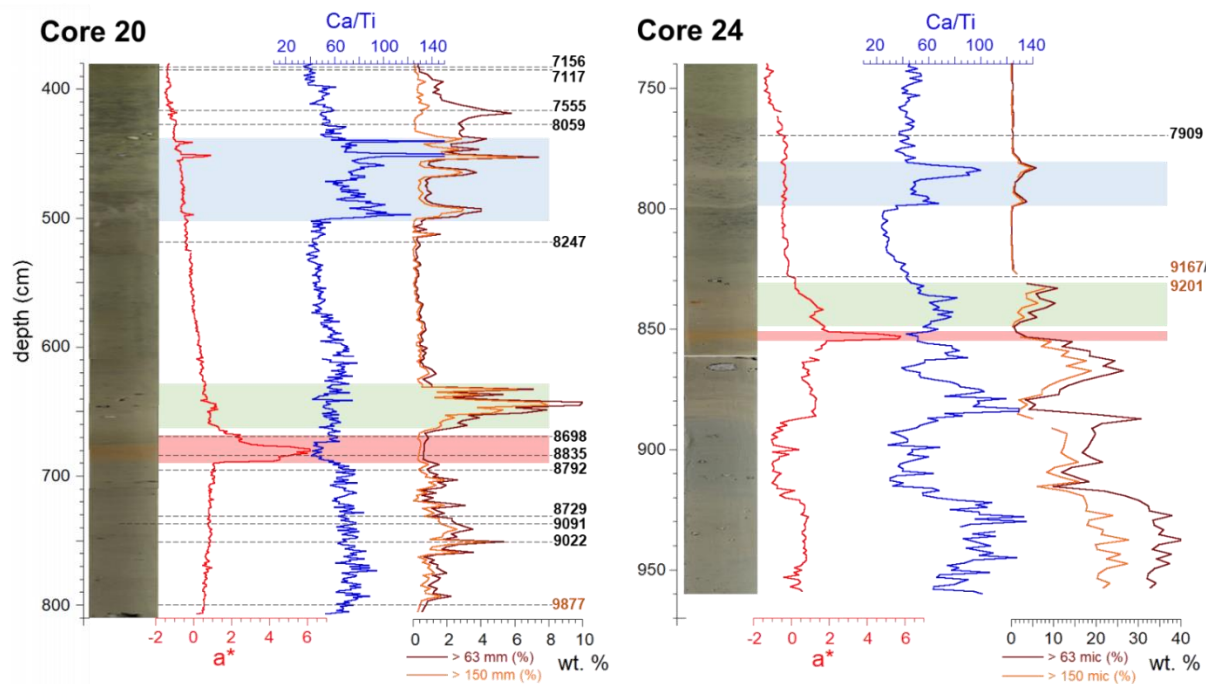
In core 20,  $k_{LF}$  is particularly low between 380 and 280 cm, reaching values lower than  $20 \cdot 10^{-5}$  SI where the sediment is particularly dark and richer in organic matter. At 280 cm, sediment starts to progressively coarse upward from clayey silt to sandy-silt, a trend followed by  $k_{LF}$  and Zr/Rb data. This progressive upward coarsening is stopped at 110 cm where is located the base of a 15 cm-thick unsorted coarse layer containing many pebbles and crushed shells. The transition to this layer is particularly sharp for  $k_{LF}$ , but not for the grain-size indicators. This coarse layer reminds the veneer of sand and gravel characterizing the seabed of Hudson Strait outside the basins (MacLean et al., 2001). In the upper 95 cm, the grain-size is first decreasing and then increasing towards the top, and the sediment is particularly rich in sulfidic layers.

In core 24, unit 1 is more uniform than in core 20, but the magnetic susceptibility also shows variations. Values in  $k_{LF}$  drop above 560 cm at very low values, around  $10 \cdot 10^{-5}$ SI, before to progressively increase towards the top.





**Figure 25.** Physical and chemical properties of cores 20 and 24 with their age-models, their photography and the CT-scan images of their respective u-channels. The results of sediment sieving at 63 and 150  $\mu$ m is also shown, as well as core age-models obtained from AMS  $^{14}\text{C}$  ages. The red circles indicate ages that were not included in the BACON age-models. Pale blue, grey and red rectangles highlight respectively the double detrital carbonate peak (DDCP), the 20 cm-thick IRD-rich layer and the red layer that are recognized in both cores.



**Figure 26.** Zoomed comparison of the lower sections of both cores 20 and 24 with their  $a^*$ , Ca/Ti and sieving data. Black numbers correspond to calibrated  $^{14}\text{C}$  ages. Ages in red are those not considered in the age-model building with Bacon.

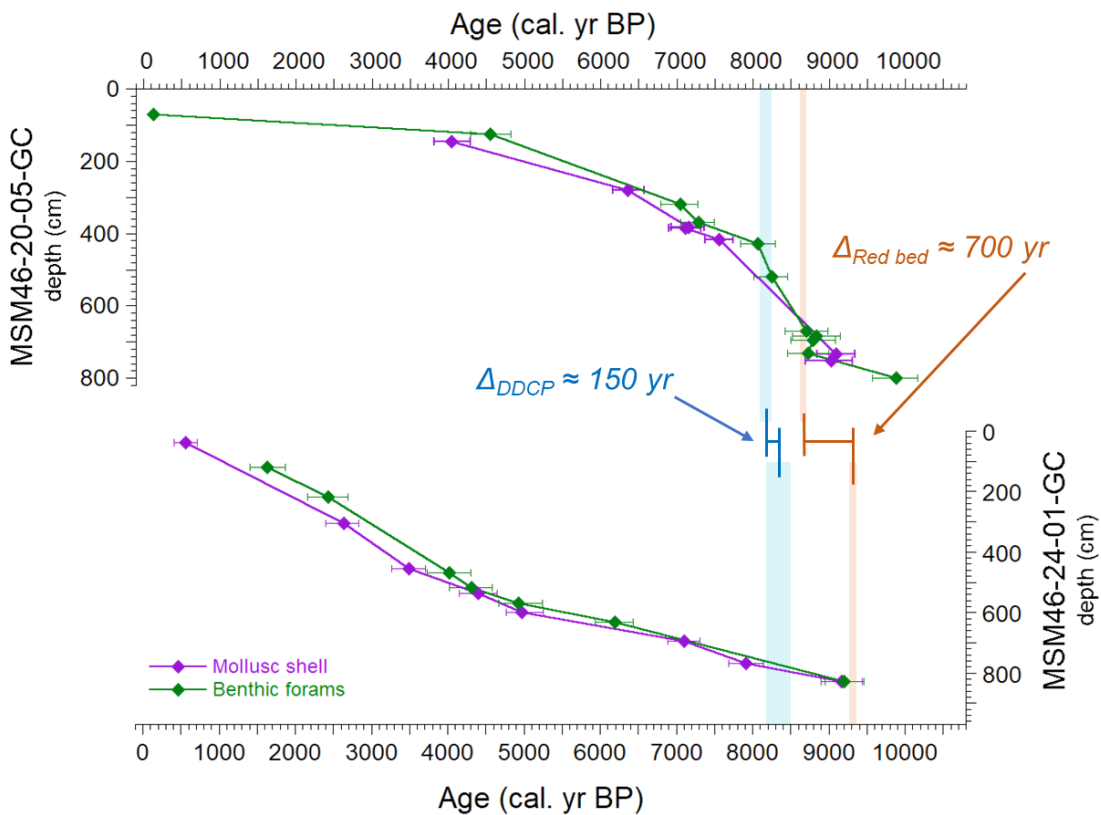
## 2.6.2 Chronologies

The age models resulting from the Bayesian calculation with Bacon are shown in Fig. 25. Resulting chronologies indicate that cores 20 and 24 span the last 8.7 and 9.2 ka, respectively. This maximal age is, however, an approximation, as age-models are mostly extrapolated in unit 1. The two ages at 829 cm in core 24 and the one at 800 cm in core 20 were not included in this calculation. These ages are likely too old, stretching age-models at the base and decreasing glaciomarine sedimentation rates. This aging is shown in Fig. 27, where the age of the DDCP and the red layer are given by interpolation between all the  $^{14}\text{C}$  ages. The resulting difference between similar layers of both cores increases towards the base and is about 700 yr for the red layer. This apparent aging is probably caused by different

local age reservoirs, as discussed in section 5.2. We thus chose to not include these “old” ages in the age-model, rather than subjectively change the  $\Delta R$ .

At the top of core 20, the veneer-like layer between 95 and 110 cm likely corresponds to a temporal hiatus, as strong tidal currents prevented continuous sediment deposition. This hiatus explains the great difference between the age above and those below it. The age-model was thus extrapolated upward to the veneer, but not above it, as there are not enough constraints to build it in the upper section.

Sedimentation rates were obtained by interpolation between calibrated ages. However, when using all the ages obtained, it appears that an alternation between mollusc and foraminifera samples generates a succession of high and low – and negative – sedimentation rates. These variations highlight the fact that mollusc seem generally younger than foraminifera at similar depths. This time-lag is well illustrated in Fig. 27, and its mean is about 230 and 340 yr in cores 20 and 24 respectively. Therefore, some ages were not used for the interpolation in order to keep positive and coherent sedimentation rates. In core 24, the sedimentation rate is relatively steady, varying between 0.05 and 0.17 cm/yr. In core 20, however, sedimentation rates reach values of about 0.48 cm/yr in unit 2, two to three times those in core 24 for the same unit, which corresponds to the thickness difference of the red layer and the DDCP between the cores. In contrast, sedimentation rates in core 20 decrease to about 0.075 cm/yr in unit 3, two times lower than in core 24.



**Figure 27.** Separated interpolations between mollusc and foraminifera samples from cores 20 and 24. Blue and red bars indicate the temporal occurrence of the DDCP and the red layer respectively.

## 2.7 DISCUSSION

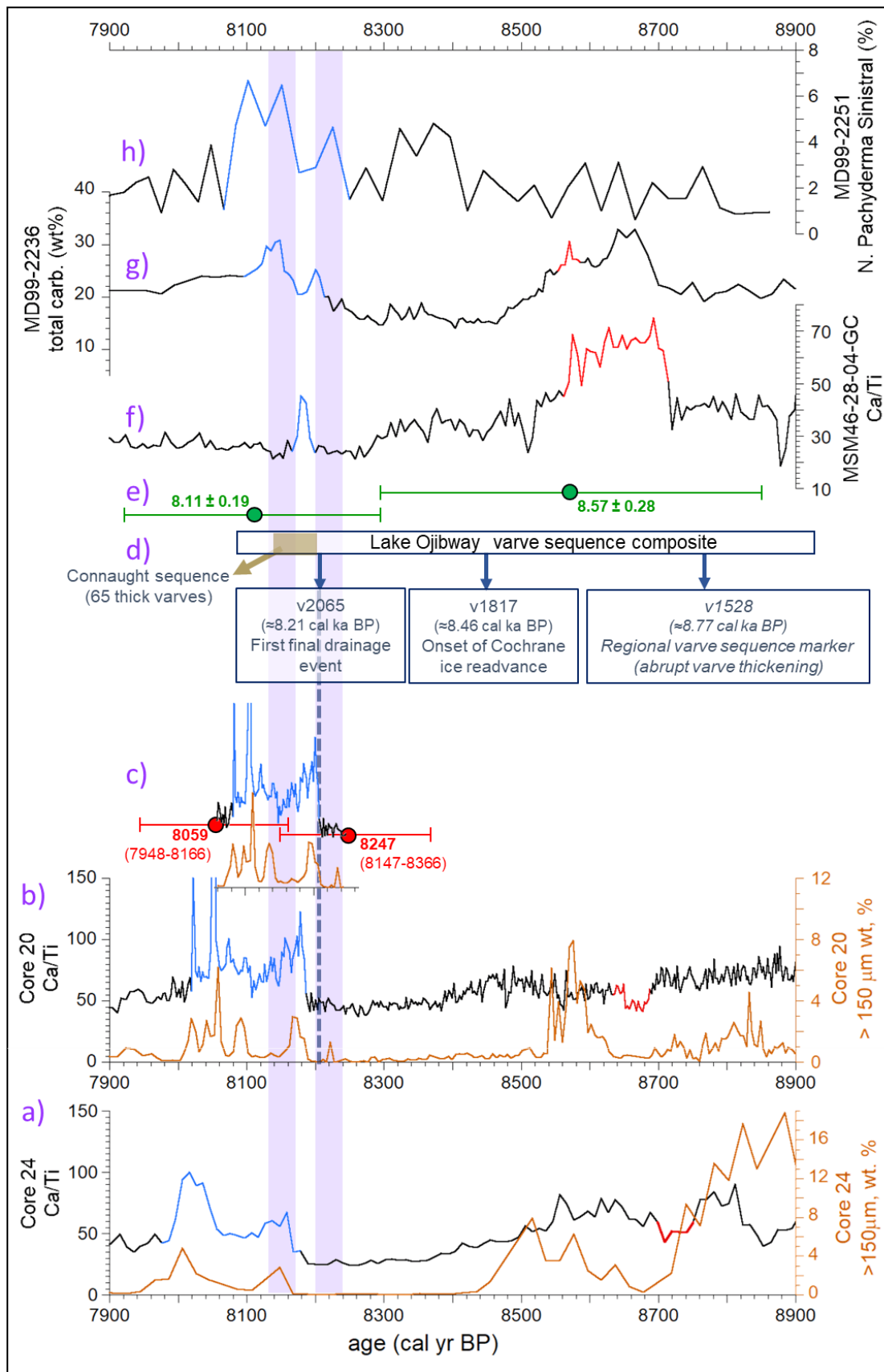
Sediment sequences of units 1 and 3 show many differences between cores 20 and 24, indicating that both sites experienced different sedimentary dynamics or environmental changes at these times. In contrast, despite a noticeable difference of sedimentation rates, the sedimentary sequence of unit 2 is structurally very well correlated between both cores. Therefore, both Western and Southwestern Basins recorded a series of similar sedimentary events consisting, from base to top, to the red layer formation, an IRD event, a period of fine sediment deposition and finally the DDCP deposition. This sequence may be correlated with the last Hudson Bay deglacial events as reported in recent studies with similar chronological

constraints – i.e., that keep a constant marine  $\Delta R$  through the record. Sequences of both cores are used for interpretation, but the resolution and chronology of core 20 make it way better to investigate temporally the successive events.

### **2.7.1 Detailed record of Hudson Bay deglacial events considering a consistent $\Delta R$**

#### **2.7.1.1 The double detrital carbonate peak**

The DDCP corresponds well to the double peak of detrital carbonates DCP7 of core MD99-2236 sampled on the Labrador Shelf (Jennings et al., 2015), with an upper and younger peak much larger and pronounced than the lower one (Fig. 28). It also approximately fits with the two-pulse LAO drainage constrained by Brouard et al. (2021). Therefore, the DDCP likely represents the double LAO drainage layer with a particularly high resolution in core 20. The high IRD content is caused by iceberg surges probably linked to the HBIS collapse that occurred at the same time and allowed a complete LAO drainage (Gauthier et al., 2020). A varved record from the former Lake Ojibway suggests that both events beginnings were separated by at least 65 yr (Godbout et al., 2019), but possibly more if a part of the record was eroded by the last flood. Our Bayesian chronology indicates that the whole event including both drainages lasted about 160 years – between 8.18 and  $8.02 \pm 0.15$  cal ka BP. However, an interpolation between the two foraminifera ages bracketing the DDCP suggests a period of 130 years, from 8.21 to 8.08 cal ka BP (Fig. 28). These last dates match much more corresponding records of DC or freshwater peaks from the Labrador Sea (Ellison et al., 2006; Jennings et al., 2015) and are also consistent with a final drainage around 8.11 cal ka BP suggested by Gauthier et al. (2020). By matching the date of 8.21 cal ka BP with the corresponding drainage layer in the Ojibway varve record proposed by Godbout et al. (2019), the onset of the Cochrane ice readvance that occurred 248 varve year before would be dated at about 8.46 cal ka BP (Fig. 28).



**Figure 28.** Comparison of Hudson Bay deglacial event markers from different records on a same time-frame. a) and b) Ca/Ti and >150 $\mu$ m sieving data from cores 24 and 20 respectively according to the Bacon age-model; c) Same data from core 20 according to an interpolation between the  $^{14}\text{C}$  indicated by red dots; d) Diagram of the Lake Ojibway varve sequence from Godbout et al. (2019) matched with core 20 record by considering the pre-final LAO drainage at 8.21 cal ka BP; e) ages of the subglacial drainage spilling the red layer and the last LAO drainage according to Gauthier et al. (2020); f) Ca/Ti of core MSM46-28-04-GC from Nachvak Fjord (Duboc et al., 2023); g) Total carbonate content of core MS99-2236 (Jennings et al., 2015); h) % of *Pachyderma Sinistral* of core MD99-2251 (Ellison et al, 2006). Sequences in red and blue correspond respectively to the red layer and the detrital-carbonate layer associated with the last LAO drainage in the different records. Vertical purple bars represent the timing of the LAO two-stage last drainage determined by Brouard et al. (2021).

#### 2.7.1.2 The red layer

Core chronologies indicate that the red layer is dated at  $8.67 \pm 0.15$  and  $8.72 \pm 0.59$  cal ka BP in cores 20 and 24, respectively, which is older than other recent records placing it around 8.55 cal ka BP (Jennings et al., 2015; Lochte et al., 2019), but still concordant with error ranges. The wide error range in core 24 is due to the age-model extrapolation downcore through the red layer, making its age less precise than in core 20.

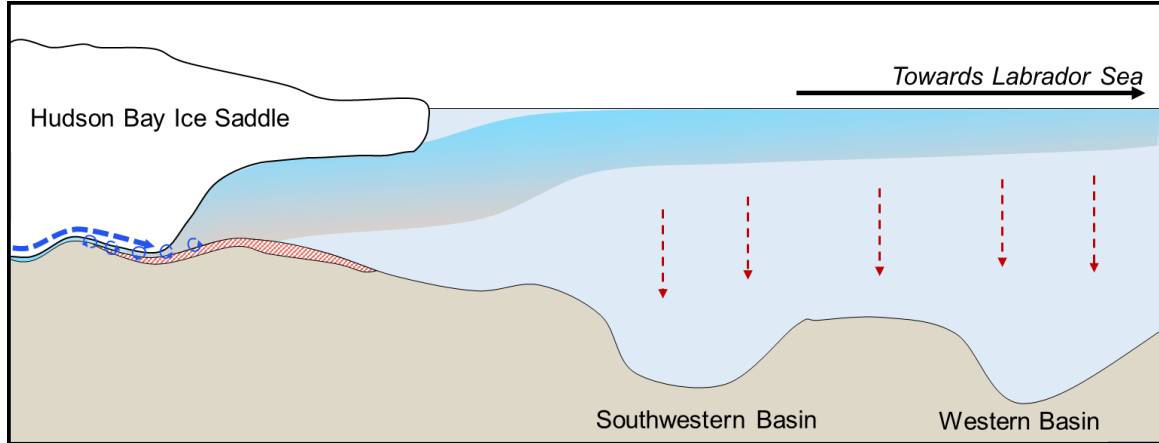
Making the DDCP fitting with the last LAO drainage implies that the red layer had to be formed about 400 yr before this drainage. Despite the red layer is sandwiched by two IRD-rich layers, it is itself muddy with no sand or coarse IRDs and was thus probably not associated with a local iceberg surge like the DDCP. Therefore, the red sediment dispersion was likely not caused by the opening of Tyrrell Sea as proposed by Jennings et al., (2015), but after it. This sediment was probably spilled from NW Hudson Bay by a limited LAO subglacial drainage, as past subglacial channels are located in SW Hudson Bay, just south of the red sediment dispersal train (St-Onge and Lajeunesse, 2007; Gauthier et al., 2020). However, the varved records from the former Lake Ojibway do not show any discontinuity at this time (Godbout et al., 2019), but the eastern part of the lake might have been less

affected if the drainage was only localized in Northern Manitoba. The only noticeable change in Ojibway varve sequences that could be associated with this subglacial drainage is the regional varve thickening at varve year 1528 that is used as a regional marker varve record (Breckenridge et al., 2012), as varve thickening may be associated with lake lowering. However, our matching place the varve year 1528 at about 8.77 cal ka BP (Fig. 28), which is slightly older than the red layer.

Red layers of cores 20 and 24 have a relatively low Ca/Ti, while equivalent layers in Labrador shelf area are correlated with detrital carbonate peaks (Jennings et al., 2015; Duboc et al., 2023), a contrast that may question their common origin. The distance from the source of the respective sampling locations may, however, explain this contrast. It has been observed that the red layer found in eastern Hudson Strait and Nachvak Fjord is lighter than in western Hudson Strait, the red sediment likely being diluted (Kerwin, 1996; Duboc et al., 2023). At proximal sites, the DC-poor red sediment is more concentrated and reduces the Ca/Ti relatively to the DC-rich background sedimentation of the Hudson Bay area. In contrast, meltwaters transport the red sediment together with detrital carbonates towards the Labrador Shelf. A mix of these material explain why the distal red layer has higher Ca/Ti values than the DC-poor background sedimentation of the Labrador Shelf and fjords.

The increasing then decreasing upward concentration of red sediment in the red layer reminds a hyperpycnite structure, as proposed by previous studies (St-Onge and Lajeunesse, 2007). However, it is not likely that a hyperpycnal flow could have travelled on thousands of kilometers to reach the Labrador Shelf across basins and sills on the path (Mulder and Chapron, 2011). Thus, after being released in Tyrrell Sea at the ice grounding line, the freshwater plume carrying the fine red sediment probably took the form of a homopycnal or mesopycnal flow (Mulder and Chapron, 2011), and the sediment deposition occurred along Hudson Strait and Labrador Shelf by reconcentration processes or simple particle fallout (Fig. 29), explaining the presence of intact foraminifera in the red sediment.



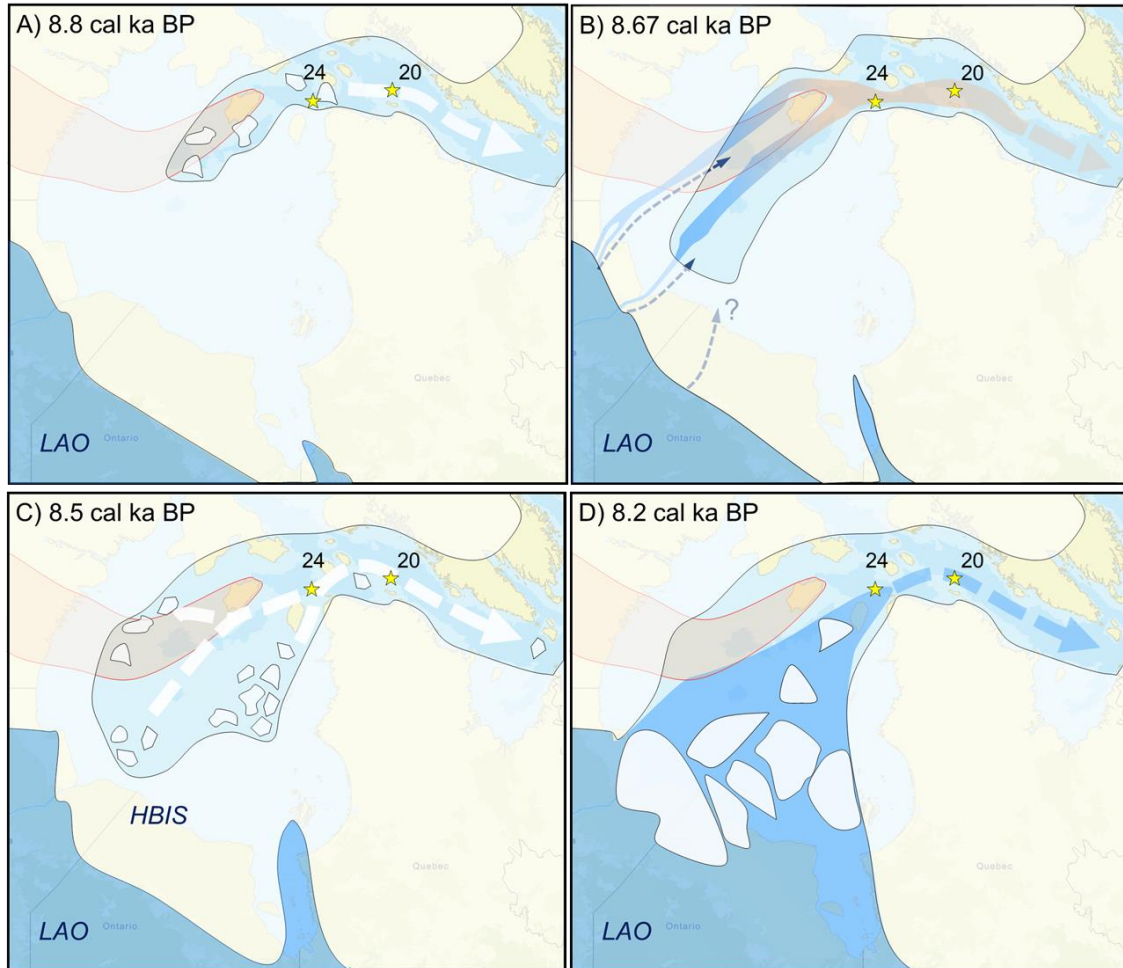


**Figure 29.** Schematic representation of red sediment dispersal with a freshwater plume formed by a subglacial drainage of Lake Agassiz-Ojibway (blue arrow) under the Hudson Bay Ice Saddle. Red dotted arrows represent particle fallout from the plume containing high concentration of fine red sediment.

### 2.7.1.3 Deglacial sequence of Hudson Bay

After the ice retreat in Hudson Strait and northern Hudson Bay, a calving bay started the opening of the Tyrrell Sea. At this time, the ice margin was for a while close to the Southwestern basin, providing it in proximal sand- and pebble-rich glaciomarine sediments while the Western Basin received more distal material, forming unit 1. The different lithologies of unit 1 in core 24 likely depict the provenance of ice-rafted material from different sectors of Hudson Bay, some of them being more metamorphic and others richer in Paleozoic carbonates (Shilts, 1980). The southwestward retreat of the ice grounding-line contributed to thin the HBIS separating the LAO from the Tyrrell Sea, and the pressure probably exerted by the lake generated a subglacial drainage around 8.65-8.60 cal ka BP (Lochte et al., 2019a; Gauthier et al., 2020). Freshwaters were drained subglacially towards Tyrrell Sea and eroded red erratics and other seafloor sediments on their pathway (Kerwin, 1996; St-Onge and Lajeunesse, 2007). Fine eroded sediments were then transported as a plume as far as the Labrador Sea, and formed the muddy red layer in Hudson Strait and in the Labrador Shelf and fjords (Jennings et al., 2015; Duboc et al., 2023).

The subglacial drainage event might have weakened the ice shelves that partly broke and triggered iceberg surges forming the IRD event that overlain the red layer in cores 20 and 24. Both the subglacial drainage and subsequent iceberg surge possibly caused a first North Atlantic freshening identified in sediment cores (Ellison et al., 2006; Lochte et al., 2019) that may have contributed to the long-term cooling starting around 8.60 cal ka BP (Rohling and Pälike, 2005; Jennings et al., 2015). This cooling likely contributed to slow down ice retreat and iceberg calving in the Hudson Bay area, marked by the reduction of IRD and DC concentration in cores 20 and 24. Very fine particles were deposited at site of core 24 at this time, reflecting an environment of particularly low energy. Climate cooling may have also allowed the southward Cochrane ice-readvance in Lake Ojibway at about 8.46 cal ka BP (v1816, Godbout et al., 2019). This period of ice stability was then abruptly stopped by another subglacial drainage around 8.21 cal ka BP, followed by the final LAO drainage a few decades after along with the HBIS collapse (Brouard et al., 2021). These two last drainages and the HBIS collapse together formed the IRD-rich double detrital-carbonate-peak observed in Hudson Strait – our DDCP – and on the Labrador Shelf in core MD99-2236 (Jennings et al., 2015). Therefore, the DDCP is likely the marker of the complex series of events that triggered the 8.2 ka cold event by injecting huge amounts of freshwater in the North Atlantic in a short period of time and disturbing the AMOC.



**Figure 30.** Schematic view of the last deglacial events in Hudson Bay. A) Early opening of the Tyrrell Sea. B) First, subglacial LAO drainage eroding and carrying red sediment downstream. C) Ice ablation caused by the LIS retreat, following the first drainage. 4) Collapse of the HBIS and catastrophic, final LAO drainage triggering the 8.2 ka event.

### 2.7.2 Implications of reservoir age variations

The precedent interpretations are made assuming a reservoir age similar to the modern one in Hudson Strait through the records. However, as reservoir ages were possibly higher during the deglaciation of these areas due to longer sea-ice cover and higher glacial freshwater input, it would not be uncoherent to increase the  $\Delta R$  by 100-500 yr for ages older than 7.0  $^{14}\text{C}$  (e.g., Vickers et al., 2010; Lewis et al., 2012; Rashid et al., 2017; Lochte et al., 2019b). Such modification would make matching the red layer with the last LAO drainage

and the DDCP to the Foxe Basin deglaciation, as done for core HU2006040-40 on the Labrador Shelf (Rashid et al., 2017). However, such a correspondence would challenge the chronologies of other studies based on marine cores containing the equivalent sedimentary layers (Jennings et al., 2015). Therefore, at which point can we assume and evaluate reservoir age variations? Another question about calibration is brought by the apparent 230-340 yr difference between foraminifera and mollusks. This difference is possibly caused by a difference of specific age-reservoir for the two types of material. This lag is not corrected during the Marine20 calibration and shows that  $\Delta R$  values from Pienkowski et al. (2022) are not suitable for benthic foraminifera.

Here, we can at least suggest that the reservoir age in both basins was higher during the opening of Tyrrell Sea than during subsequent events, as suggested by the old ages obtained from molluscs and foraminifera at the base of both cores. Though, the transition from higher to lower reservoir age values occurred later in the Southwestern Basin, as shown by the 700-year age difference of the red layer between both cores when all the radiocarbon ages are considered (Fig. 27). This reduction of reservoir age thus occurred before and after the red layer deposition in the Western and in the Southwestern Basin, respectively. The proximity of the ice margin from the basins is probably in cause. This ice margin was indeed very close to the Southwestern Basin until the enlarging of the Tyrrell Sea calving bay (Dalton et al., 2020) that likely occurred after the subglacial drainage of 8.6 cal ka BP. This ice margin proximity may have enhanced locally water stratification and the relative influence of  $^{14}\text{C}$ -depleted meltwaters in the Southwestern Basin. Such important regional differences of age reservoir were already shown between two areas of Foxe Basin during its deglaciation (Ross et al., 2012). Therefore, the good lithological correlation between cores 20 and 24 provides a quantitative example of how the age reservoir can vary in short space and time in a marine environment influenced by ice-margin dynamics.

## 2.8 CONCLUSIONS

High-resolution sedimentary sequences sampled in both Southwestern and Western Hudson Strait Basins provide a detailed record of the last Hudson Bay deglacial events, including three LAO drainages and the HBIS collapse. In core 20 from the Western Basin, this resolution is among the highest ever obtained and reached a mean of 0.4 cm/yr during the 500 yr that span these events. These records bring the few following insights:

- First, the opening of Tyrrell Sea triggered distal glaciomarine sedimentation in the Western Basin, while the Southwestern Basin received proximal coarse glaciomarine material from closer ice margins. Important meltwater fluxes likely increased  $^{14}\text{C}$  reservoir age of the carbonated material found at both core bases.
- The red layer is interpreted as resulting from a LAO subglacial drainage occurring at about  $8.67 \pm 0.15$  cal ka BP, thus about 500 years before its final outburst. This drainage probably formed a meltwater plume carrying fine red sediment in Hudson Strait and Labrador Sea, and was quickly followed by an iceberg surge from Hudson Bay. Subsequent slight cooling favored glaciers stabilization or advances and greatly decreased IRD and detrital carbonate export during at least 200 yr.
- The final Lake Agassiz-Ojibway outburst itself, that triggered the 8.2 ka cold event, likely started around 8.21 cal ka BP. It occurred in two drainage events recorded as an IRD-rich double detrital carbonate peak, which is about 60 cm-thick in core 20. These drainages were likely separated by a few decades, the second one being more important and concomitant with the HBIS collapse.
- Despite the coherence of the link between sediment and deglacial events, the reservoir age reservoir was possibly higher than modern values used in the study. A  $\Delta R$  higher by a few centuries could completely change the interpretations. Deeper analyses of the sediment provenance of the different events, particularly the IRDs, could certify the validity of the deglacial sequence.

## 2.9 ACKNOWLEDGMENTS

Many thanks to the captain, crew and scientist of the MSM46 expedition onboard the R/V Maria S. Merian. We also acknowledge the Natural Science and Engineering Research Council (NSERC) of Canada and the Fonds de Recherche du Québec Nature et Technologie (FRQNT) for their financial support. We also thank Q. Beauvais, M. St-Onge, D. Lavallée and M. Babin for their help for the analyses.

## 2.10 REFERENCES

- Allan, E., de Vernal, A., Seidenkrantz, M., Briner, J.P., Hillaire-Marcel, C., Pearce, C., Meire, L., Røy, H., Mathiasen, A.M., Nielsen, M.T., Plesner, J.L., Perner, K., 2021. Insolation vs. meltwater control of productivity and sea surface conditions off SW Greenland during the Holocene. *Boreas* 50, 631–651. <https://doi.org/10.1111/bor.12514>
- Alley, R.B., Mayewski, P.A., Sowers, T., Stuiver, M., Taylor, K.C., Clark, P.U., 1997. Holocene climatic instability: A prominent, widespread event 8200 yr ago. *Geology* 25, 483. [https://doi.org/10.1130/0091-7613\(1997\)025<0483:HCIAPW>2.3.CO;2](https://doi.org/10.1130/0091-7613(1997)025<0483:HCIAPW>2.3.CO;2)
- Andrews, J.T., MacLean, B., 2003. Hudson Strait ice streams: a review of stratigraphy, chronology and links with North Atlantic Heinrich events. *Boreas*, 32 (1) (2003), pp. 4-17. <https://doi.org/10.1080/03009480310001010>
- Baldini, J.U.L., McDermott, F., Fairchild, I.J., 2002. Structure of the 8200-Year Cold Event Revealed by a Speleothem Trace Element Record. *Science* 296, 2203–2206. <https://doi.org/10.1126/science.1071776>
- Barber, D.C., Dyke, A., Hillaire-Marcel, C., Jennings, A.E., Andrews, J.T., Kerwin, M.W., Bilodeau, G., McNeely, R., Southon, J., Morehead, M.D., Gagnon, J.-M., 1999. Forcing of the cold event of 8,200 years ago by catastrophic drainage of Laurentide lakes. *Nature* 400, 344–348. <https://doi.org/10.1038/22504>
- Blaauw, M., Christen, J.A., 2011. Flexible paleoclimate age-depth models using an autoregressive gamma process. *Bayesian Analysis* 6. <https://doi.org/10.1214/11-BA618>

- Breckenridge, A., Lowell, T. V., Stroup, J. S., Evans, G., 2012. A review and analysis of varve thickness records from glacial Lake Ojibway (Ontario and Quebec, Canada). *Quaternary International*, 260, 43-54. <https://doi.org/10.1016/j.quaint.2011.09.031>
- Brouard, E., Roy, M., Godbout, P.-M., Veillette, J.J., 2021. A framework for the timing of the final meltwater outbursts from glacial Lake Agassiz-Ojibway. *Quaternary Science Reviews* 274, 107269. <https://doi.org/10.1016/j.quascirev.2021.107269>
- Caron, M., St-Onge, G., Montero-Serrano, J.-C., Rochon, A., Georgiadis, E., Giraudeau, J., Massé, G., 2019. Holocene chronostratigraphy of northeastern Baffin Bay based on radiocarbon and palaeomagnetic data. *Boreas* 48, 147–165. <https://doi.org/10.1111/bor.12346>
- Clark, P.U., Marshall, S.J., Clarke, G.K.C., Hostetler, S.W., Licciardi, J.M., Teller, J.T., 2001. Freshwater Forcing of Abrupt Climate Change During the Last Glaciation. *Science* 293, 283–287. <https://doi.org/10.1126/science.1062517>
- Coulthard, R.D., Furze, M.F.A., Pieńkowski, A.J., Chantel Nixon, F., England, J.H., 2010. New marine  $\Delta R$  values for Arctic Canada. *Quaternary Geochronology* 5, 419–434. <https://doi.org/10.1016/j.quageo.2010.03.002>
- Croudace, I.W., Rindby, A., Rothwell, R.G., 2006. ITRAX: description and evaluation of a new multi-function X-ray core scanner. *Geological Society, London, Special Publications* 267, 51–63. <https://doi.org/10.1144/GSL.SP.2006.267.01.04>
- Croudace, I.W., Rothwell, R.G. (Eds.), 2015. *Micro-XRF Studies of Sediment Cores: Applications of a non-destructive tool for the environmental sciences*, 1st ed. 2015. ed, *Developments in Paleoenvironmental Research*. Springer Netherlands : Imprint: Springer, Dordrecht. <https://doi.org/10.1007/978-94-017-9849-5>

- Dalton, A.S., Margold, M., Stokes, C.R., Tarasov, L., Dyke, A.S., Adams, R.S., Allard, S., Arends, H.E., Atkinson, N., Attig, J.W., Barnett, P.J., Barnett, R.L., Batterson, M., Bernatchez, P., Borns, H.W., Breckenridge, A., Briner, J.P., Brouard, E., Campbell, J.E., Carlson, A.E., Clague, J.J., Curry, B.B., Daigneault, R.-A., Dubé-Loubert, H., Easterbrook, D.J., Franzi, D.A., Friedrich, H.G., Funder, S., Gauthier, M.S., Gowan, A.S., Harris, K.L., Héту, B., Hooyer, T.S., Jennings, C.E., Johnson, M.D., Kehew, A.E., Kelley, S.E., Kerr, D., King, E.L., Kjeldsen, K.K., Knaeble, A.R., Lajeunesse, P., Lakeman, T.R., Lamothe, M., Larson, P., Lavoie, M., Loope, H.M., Lowell, T.V., Lusardi, B.A., Manz, L., McMartin, I., Nixon, F.C., Occhietti, S., Parkhill, M.A., Piper, D.J.W., Pronk, A.G., Richard, P.J.H., Ridge, J.C., Ross, M., Roy, M., Seaman, A., Shaw, J., Stea, R.R., Teller, J.T., Thompson, W.B., Thorleifson, L.H., Utting, D.J., Veillette, J.J., Ward, B.C., Weddle, T.K., Wright, H.E., 2020. An updated radiocarbon-based ice margin chronology for the last deglaciation of the North American Ice Sheet Complex. *Quaternary Science Reviews* 234, 106223. <https://doi.org/10.1016/j.quascirev.2020.106223>
- Drinkwater, K.F., 1986. Physical oceanography of Hudson strait and Ungava Bay. In *Elsevier oceanography series*, Vol. 44, 237-264. [https://doi.org/10.1016/S0422-9894\(08\)70906-1](https://doi.org/10.1016/S0422-9894(08)70906-1)
- Duboc, Q., St-Onge, G., Lajeunesse, P., 2017. Sediment records of the influence of river damming on the dynamics of the Nelson and Churchill Rivers, western Hudson Bay, Canada, during the last centuries. *The Holocene* 27, 712–725. <https://doi.org/10.1177/0959683616670465>
- Duboc, Q., Lajeunesse, P., St-Onge, G., Moros, M., Perner, K., 2023. Holocene sedimentary sequences from Nachvak and Saglek Fjords (Northern Labrador) as a record of deglaciation of the Torngat Mountains and Hudson Bay. *Quaternary Science Reviews* 307, 108046. <https://doi.org/10.1016/j.quascirev.2023.108046>
- Dyke, A.S., 2004. An outline of North American deglaciation with emphasis on central and northern Canada, in: *Developments in Quaternary Sciences*. Elsevier, pp. 373–424. [https://doi.org/10.1016/S1571-0866\(04\)80209-4](https://doi.org/10.1016/S1571-0866(04)80209-4)
- Ellison, C. R., Chapman, M. R., Hall, I. R., 2006. Surface and deep ocean interactions during the cold climate event 8200 years ago. *Science*, 312(5782), 1929-1932. DOI: 10.1126/science.1127213
- England, J., Dyke, A.S., Coulthard, R.D., Mcneely, R., Aitken, A., 2013. The exaggerated radiocarbon age of deposit-feeding molluscs in calcareous environments: Exaggerated radiocarbon ages of molluscs. *Boreas* 42, 362–373. <https://doi.org/10.1111/j.1502-3885.2012.00256.x>



- Gauthier, M.S., Kelley, S.E., Hodder, T.J., 2020. Lake Agassiz drainage bracketed Holocene Hudson Bay Ice Saddle collapse. *Earth and Planetary Science Letters* 544, 116372. <https://doi.org/10.1016/j.epsl.2020.116372>
- Godbout, P.-M., Roy, M., Veillette, J.J., 2019. High-resolution varve sequences record one major late-glacial ice readvance and two drainage events in the eastern Lake Agassiz-Ojibway basin. *Quaternary Science Reviews* 223, 105942. <https://doi.org/10.1016/j.quascirev.2019.105942>
- Godbout, P. M., Roy, M., Veillette, J. J., 2020. A detailed lake-level reconstruction shows evidence for two abrupt lake drawdowns in the late-stage history of the eastern Lake Agassiz-Ojibway basin. *Quaternary Science Reviews*, 238, 106327. <https://doi.org/10.1016/j.quascirev.2020.106327>
- Gregoire, L.J., Payne, A.J., Valdes, P.J., 2012. Deglacial rapid sea level rises caused by ice-sheet saddle collapses. *Nature* 487, 219–222. <https://doi.org/10.1038/nature11257>
- Haberzettl, T., St-Onge, G., Lajeunesse, P., 2010. Multi-proxy records of environmental changes in Hudson Bay and Strait since the final outburst flood of Lake Agassiz–Ojibway. *Marine Geology* 271, 93–105. <https://doi.org/10.1016/j.margeo.2010.01.014>
- Heaton, T.J., Köhler, P., Butzin, M., Bard, E., Reimer, R.W., Austin, W.E.N., Bronk Ramsey, C., Grootes, P.M., Hughen, K.A., Kromer, B., Reimer, P.J., Adkins, J., Burke, A., Cook, M.S., Olsen, J., Skinner, L.C., 2020. Marine20—The Marine Radiocarbon Age Calibration Curve (0–55,000 cal BP). *Radiocarbon* 62, 779–820. <https://doi.org/10.1017/RDC.2020.68>
- Hill, D.F., Griffiths, S.D., Peltier, W.R., Horton, B.P., Törnqvist, T.E., 2011. High-resolution numerical modeling of tides in the western Atlantic, Gulf of Mexico, and Caribbean Sea during the Holocene. *Journal of Geophysical Research : Oceans* 116, C10014. <https://doi.org/10.1029/2010JC006896>
- Hillaire-Marcel, C., de Vernal, A., Piper, D.J.W., 2007. Lake Agassiz Final drainage event in the northwest North Atlantic. *Geophysical Research Letters* 34. <https://doi.org/10.1029/2007GL030396>
- Jennings, A.E., Manley, W.F., MacLean, B., Andrews, J.T., 1998. Marine evidence for the last glacial advance across eastern Hudson Strait, eastern Canadian Arctic. *Journal of Quaternary Science* 13, 501-514. [https://doi.org/10.1002/\(SICI\)1099-1417\(1998110\)13:6<501::AID-JQS391>3.0.CO;2-A](https://doi.org/10.1002/(SICI)1099-1417(1998110)13:6<501::AID-JQS391>3.0.CO;2-A)

- Jennings, A., Andrews, J., Pearce, C., Wilson, L., Ólfasdóttir, S., 2015. Detrital carbonate peaks on the Labrador shelf, a 13–7ka template for freshwater forcing from the Hudson Strait outlet of the Laurentide Ice Sheet into the subpolar gyre. *Quaternary Science Reviews* 107, 62–80.  
<https://doi.org/10.1016/j.quascirev.2014.10.022>
- Kaufman, D. S., Miller, G. H., Stravers, J. A., Andrews, J. T, 1993. Abrupt early Holocene (9.9-9.6 ka) ice-stream advance at the mouth of Hudson Strait, Arctic Canada. *Geology*, 21(12), 1063-1066. [https://doi.org/10.1130/0091-7613\(1993\)021<1063:AEHKIS>2.3.CO;2](https://doi.org/10.1130/0091-7613(1993)021<1063:AEHKIS>2.3.CO;2)
- Keigwin, L.D., Jones, G.A., Lehman, S.J., Boyle, E.A., 1991. Deglacial meltwater discharge, North Atlantic deep circulation, and abrupt climate change. *Journal of Geophysical Research: Oceans* 96, 16811-16826.  
<http://dx.doi.org/10.1029/91JC01624>
- Kerwin, M.W., 1996. A Regional Stratigraphic Isochron (ca. 8000 <sup>14</sup>C yr B.P.) from Final Deglaciation of Hudson Strait. *Quaternary Research* 46, 89–98.  
<https://doi.org/10.1006/qres.1996.0049>
- King, J. W., Banerjee, S. K., Marvin, J., 1983. A new rock-magnetic approach to selecting sediments for geomagnetic paleointensity studies: application to paleointensity for the last 4000 years. *Journal of Geophysical Research: Solid Earth* 88, 5911–5921. <https://doi.org/10.1029/JB088iB07p05911>
- Lajeunesse, P., St-Onge, G., 2008. The subglacial origin of the Lake Agassiz–Ojibway final outburst flood. *Nature Geoscience* 1, 184–188.  
<https://doi.org/10.1038/ngeo130>
- Laymon, C.A., 1992. Glacial geology of western Hudson Strait, Canada, with reference to Laurentide Ice Sheet dynamics. *Geological Society of America Bulletin* 104, 1169–1177. [https://doi.org/10.1130/0016-7606\(1992\)104<1169:GGOWHS>2.3.CO;2](https://doi.org/10.1130/0016-7606(1992)104<1169:GGOWHS>2.3.CO;2)
- Lewis, C.F.M., Miller, A.A.L., Levac, E., Piper, D.J.W., Sonnichsen, G.V., 2012. Lake Agassiz outburst age and routing by Labrador Current and the 8.2 cal ka cold event. *Quaternary International* 260, 83–97.  
<https://doi.org/10.1016/j.quaint.2011.08.023>
- Lochte, A.A., Repschläger, J., Kienast, M., Garbe-Schönberg, D., Andersen, N., Hamann, C., Schneider, R., 2019a. Labrador Sea freshening at 8.5 ka BP caused by Hudson Bay Ice Saddle collapse. *Nature Communication* 10, 586.  
<https://doi.org/10.1038/s41467-019-08408-6>

- Lochte, A.A., Repschläger, J., Seidenkrantz, M.-S., Kienast, M., Blanz, T., Schneider, R.R., 2019b. Holocene water mass changes in the Labrador Current. *The Holocene* 29, 676–690. <https://doi.org/10.1177/0959683618824752>
- Lougheed, B.C., Filipsson, H.L., Snowball, I., 2013. Large spatial variations in coastal <sup>14</sup>C reservoir age – a case study from the Baltic Sea. *Climate of the Past* 9, 1015–1028. <https://doi.org/10.5194/cp-9-1015-2013>
- Lutz, B., Wiles, G., Lowell, T., Michaels, J., 2007. The 8.2-ka abrupt climate change event in Brown’s Lake, northeast Ohio. *Quaternary Research* 67, 292–296. <https://doi.org/10.1016/j.yqres.2006.08.007>
- MacLean, B. (ed.) 2001a. *Marine Geology of Hudson Strait and Ungava Bay, Eastern Arctic Canada: Late Quaternary Sediments, Depositional Environments, and Late Glacial–Deglacial History Derived from Marine and Terrestrial Studies*. Geological Survey of Canada Bulletin 566, 199 pp. Queen’s Printer, Ottawa.
- MacLean, B. 2001b. Bedrock geology of Hudson Strait and Ungava Bay. In MacLean, B. (ed.): *Marine Geology of Hudson Strait and Ungava Bay, Eastern Arctic Canada; Late Quaternary Sediments, Depositional Environments, and Late Glacial–Deglacial History Derived from Marine and Terrestrial Studies*, 65–69. Geological Survey of Canada Bulletin 566. Queen’s Printer, Ottawa.
- MacLean, B., Vilks, G., Hardy, I., Deonarine, B., Jennings, A., Manley, W.F., 2001. Quaternary sediments in Hudson Strait and Ungava Bay. In MacLean, B. (ed.): *Marine Geology of Hudson Strait and Ungava Bay, Eastern Arctic Canada; Late Quaternary Sediments, Depositional Environments, and Late Glacial–Deglacial History Derived from Marine and Terrestrial Studies*, 71–126. Geological Survey of Canada Bulletin 566. Queen’s Printer, Ottawa.
- Matero, I.S.O., Gregoire, L.J., Ivanovic, R.F., Tindall, J.C., Haywood, A.M., 2017. The 8.2 ka cooling event caused by Laurentide ice saddle collapse. *Earth and Planetary Science Letters* 473, 205–214. <https://doi.org/10.1016/j.epsl.2017.06.011>
- Morrill, C., Anderson, D.M., Bauer, B.A., Buckner, R., Gille, E.P., Gross, W.S., Hartman, M., Shah, A., 2013. Proxy benchmarks for intercomparison of 8.2 ka simulations. *Climate of the Past* 9, 423–432. <https://doi.org/10.5194/cp-9-423-2013>
- Mulder, T., Chapron, E., 2011. Flood deposits in continental and marine environments: Character and significance, in R. M. Slatt and C. Zavala, eds., *Sediment transfer from shelf to deep water—Revisiting the delivery system: AAPG Studies in Geology* 61, p. 1–30. DOI:10.1306/13271348St613436

- Pieńkowski, A.J., Coulthard, R.D., Furze, M.F.A., 2022. Revised marine reservoir offset ( $\Delta R$ ) values for molluscs and marine mammals from Arctic North America. *Boreas* bor.12606. <https://doi.org/10.1111/bor.12606>
- Prinsenberg, S. J., 1986. The circulation pattern and current structure of Hudson Bay. *Elsevier oceanography series*, 44, 187-204. [https://doi.org/10.1016/S0422-9894\(08\)70903-6](https://doi.org/10.1016/S0422-9894(08)70903-6)
- Rashid, H., Piper, D.J.W., Lazar, K.B., McDonald, K., Saint-Ange, F., 2017. The Holocene Labrador Current: Changing linkages to atmospheric and oceanographic forcing factors. *Paleoceanography* 32, 498–510. <https://doi.org/10.1002/2016PA003051>
- Rasmussen, S.O., Andersen, K.K., Svensson, A.M., Steffensen, J.P., Vinther, B.M., Clausen, H.B., Siggaard-Andersen, M.-L., Johnsen, S.J., Larsen, L.B., Dahl-Jensen, D., Bigler, M., Röthlisberger, R., Fischer, H., Goto-Azuma, K., Hansson, M.E., Ruth, U., 2006. A new Greenland ice core chronology for the last glacial termination. *J. Geophys. Res.* 111, D06102. <https://doi.org/10.1029/2005JD006079>
- Rohling, E. J., Pälike, H., 2005. Centennial-scale climate cooling with a sudden cold event around 8,200 years ago. *Nature*, 434(7036), 975-979.
- Ross, M., Utting, D.J., Lajeunesse, P., Kosar, K.G.A., 2012. Early Holocene deglaciation of northern Hudson Bay and Foxe Channel constrained by new radiocarbon ages and marine reservoir correction. *Quaternary Research* 78, 82–94. <https://doi.org/10.1016/j.yqres.2012.03.001>
- Shilts, W.W., 1980. Flow patterns in the central North American ice sheet. *Nature* 286, 213–218. <https://doi.org/10.1038/286213a0>
- Stokes, C.R., Tarasov, L., Dyke, A.S., 2012. Dynamics of the North American Ice Sheet Complex during its inception and build-up to the Last Glacial Maximum. *Quaternary Science Reviews* 50, 86–104. <https://doi.org/10.1016/j.quascirev.2012.07.009>
- Stoner, J.S., St-Onge, G., 2007. Chapter Three Magnetic Stratigraphy in Paleooceanography: Reversals, Excursions, Paleointensity, and Secular Variation, in: *Developments in Marine Geology* 1, 99–138. [https://doi.org/10.1016/S1572-5480\(07\)01008-1](https://doi.org/10.1016/S1572-5480(07)01008-1)
- St-Onge, G., Lajeunesse, P., 2007. Flood-Induced Turbidites From Northern Hudson Bay And Western Hudson Strait: A Two-Pulse Record Of Lake Agassiz Final Outburst Flood?, in: Lykousis, V., Sakellariou, D., Locat, J. (Eds.), *Submarine Mass Movements and Their Consequences*. Springer Netherlands, Dordrecht, pp. 129–137. [https://doi.org/10.1007/978-1-4020-6512-5\\_14](https://doi.org/10.1007/978-1-4020-6512-5_14)

- Stuiver, M., Reimer, P. J., Reimer, R. W., 2020. CALIB 8.2 [WWW Program]. 2021.
- Tarasov, L., Dyke, A.S., Neal, R.M., Peltier, W.R., 2012. A data-calibrated distribution of deglacial chronologies for the North American ice complex from glaciological modeling. *Earth and Planetary Science Letters* 315–316, 30–40. <https://doi.org/10.1016/j.epsl.2011.09.010>
- Vacchi, M., Engelhart, S.E., Nikitina, D., Ashe, E.L., Peltier, W.R., Roy, K., Kopp, R.E., Horton, B.P., 2018. Postglacial relative sea-level histories along the eastern Canadian coastline. *Quaternary Science Reviews* 201, 124–146. <https://doi.org/10.1016/j.quascirev.2018.09.043>
- Vickers, K.J., Ward, B.C., Utting, D.J., Telka, A.M., 2010. Deglacial reservoir age and implications, Foxe Peninsula, Baffin Island. *Journal of Quaternary Science* 25, 1338–1346. <https://doi.org/10.1002/jqs.1419>
- Vilks, G., MacLean, B., Deonarine, B., Currie, C.G., Moran, K., 1989. Late Quaternary Paleooceanography and Sedimentary Environments in Hudson Strait. *Géographie physique et Quaternaire* 43, 161–178. <https://doi.org/10.7202/032767ar>

### **CHAPITRE 3**

## **ÉVOLUTION DES PROCESSUS SEDIMENTAIRES ET DES CONDITIONS ENVIRONNEMENTALE DANS LE LAC MELVILLE, LABRADOR, DEPUIS 9200 ANS**

#### **3.1 RÉSUMÉ EN FRANÇAIS DU TROISIÈME ARTICLE**

Les enregistrements sédimentaires marins continus provenant de bassins déglacés permettent de compléter les données géomorphologiques terrestres afin d'étudier la dynamique passée des marges glaciaires. En outre, ils peuvent fournir des informations sur l'évolution des conditions environnementales locales et régionales pouvant être associées à la déglaciation. Dans cet article, nous présentons un cadre chronologique continu de l'évolution des environnements sédimentaires associés au retrait de la marge glaciaire et aux variations environnementales du lac estuarien Melville, afin d'étudier la dynamique de déglaciation du sud du Labrador. Cette étude est basée sur l'analyse multi-proxy d'une carotte à gravité longue de 14 m qui couvre les derniers 9,1 ka et représente la transition progressive d'un environnement glaciomarin distal à un environnement postglaciaire. Les cinq premiers mètres à la base de la carotte sont principalement composés de boues glaciomarines et paraglaciaires déposées pendant le retrait continu vers l'ouest de la marge glaciaire entre 9,1 et 8,4 cal ka BP, concomitant avec une augmentation de l'influence des eaux marines. Les propriétés magnétiques et la couleur des sédiments ont révélé que, pendant l'événement froid de 8,2 ka, les conditions redox ont changé dans les sédiments, soulignant l'impact des conditions plus froides sur l'environnement. Une transition soudaine s'est ensuite produite vers 7,8 cal ka BP, lorsque les conditions ont basculé vers un environnement postglaciaire proche de l'actuel. Les derniers 7,8 ka ont été principalement marqués par une réduction du taux de sédimentation et une diminution de l'influence des eaux marines causée par la baisse relative du niveau de la mer qui a réduit la profondeur du seuil à l'entrée du lac.

### **3.2 EVOLUTION OF DEGLACIAL SEDIMENTARY PROCESSES AND ENVIRONMENTAL CONDITIONS IN LAKE MELVILLE, LABRADOR, SINCE THE LAST 9.2 KA**

Continuous marine sedimentary records from deglaciated basins are helpful to complete terrestrial landforms for investigating past ice margin dynamics. Moreover, they may provide information on the evolution of local and regional environmental conditions that can be assessed as deglaciation causes or consequences. Here, we present a continuous chronological framework of the evolution of sedimentary environments associated with the ice margin retreat and environmental variations in Lake Melville, a large fjord-like estuary, to investigate deglacial dynamics in Southern Labrador. This study is based on the multiproxy analysis of a 14 m-long gravity-core spanning the last 9.1 ka that represents the progressive transition from a distal glaciomarine to a postglacial environment. The lowest 5 meters of the core are mostly composed of glaciomarine and paraglacial mud deposited during the continuous westward ice margin retreat occurring between 9.1 and 8.4 cal ka BP, with an increase of marine waters influence. Magnetic properties and sediment colour revealed that, during the 8.2 ka cold event, redox conditions changed in the sediment, highlighting the impact of the colder conditions on the environment. A sudden transition then occurred around 7.8 cal ka BP when conditions switched to a modern-like postglacial environment. The last 7.8 ka were mostly marked by a reduction of the sedimentation rate and a decrease of marine waters influence caused by the relative sea-level drop.

### **3.3 INTRODUCTION**

Investigating chronological constraints on regional deglacial dynamic is crucial to evaluate the impact of the North-American ice-sheets melting on Holocene climate and environment. The input of important amounts of glacial water in the ocean together with the isostatic adjustment following the retreat of kilometer-thick ice-masses involved variations of up to 250 m of the relative-sea-level in the deglaciated areas (e.g. Shaw et al., 1998; Gregoire et al., 2016; Vacchi et al., 2018). Moreover, massive injection of glacial freshwater in the North Atlantic contributed to a slowdown of the Atlantic Meridional Overturning Circulation and thus triggered a cold snap such as the 8.2 ka event (e.g., Alley et al., 1997; Clark et al., 2001; Lajeunesse and St-Onge, 2008). Therefore, better

constraining ice-sheet retreat may provide information on their link with climatic fluctuations and the resulting environmental, as well as geographic and oceanographic changes. During their retreat, ice sheets erode, transport, and deliver huge amounts of sediments that form terrestrial landforms such as moraines and thick sedimentary sequences in continental margins, fjords and lacustrine basins (e.g., Hjelstuen et al., 2009; Dietrich et al., 2017; Poiré et al., 2018). Continued deglacial and postglacial marine sequences, if well chronologically constrained, may therefore provide additional information on the evolution of regional sedimentary environments and processes that affect landscapes during deglaciation. The sediments reflect changes in temperatures, salinities, sea-ice cover, productivity, or vegetation cover (e.g., Moros et al., 2016; Richerol et al., 2017; Caron et al., 2019; Allan et al., 2021; Weiser et al., 2021), but also punctual events such as floods, glacial meltwater inputs, icebergs discharges or mass-movement deposits (MMDs; e.g., St-Onge et al., 2004; Jennings et al., 2015; Broom et al., 2017; Trottier et al., 2021). They also help to quantify the sediment budget through the successive sedimentary environments (Syvitski et al., 2022).

In Southern Labrador, Lake Melville offers the opportunity to retrieve high-resolution sedimentary sequences spanning the Holocene since the deglaciation. This lake is a particular case as it corresponds to a large water body located more than 200 km inland and connected to the continental shelf by straits where sills limit the water exchange with Labrador Sea (Vilks and Mudie, 1983; Syvitski and Lee, 1997). Moreover, Lake Melville was likely the location of a calving bay during the deglaciation and played an important role in the local ice-margin dynamic by enhancing regional calving (Occhietti et al., 2011). Several studies contributed to better constraining the timing of formation of different morainic systems in the area, and give a general timeframe of the regional margin dynamic (e.g., King, 1985; Ullman et al., 2016; Couette et al., 2023). These ice margin landforms were well correlated to the Holocene climate. Cold events of 11.2, 10.3 and 9.3 ka are correlated with the abandonment of the Belles-Amours, Paradise and Little-Drunken-North-Shore Moraines that are located south and southeast of Lake Melville (Ullman et al., 2016; Couette et al. in press). In the Lake Melville area itself, the Sebaskachu Moraine located west of the lake is the only major morainic system and is dated at about  $8.4 \pm 0.6$  cal ka BP (Couette et al., 2023). Therefore, the LIS, within Lake Melville, likely



experienced two stabilizations before the one forming the Sebaskachu Moraine, during the 10.3 and 9.2 ka events, probably corresponding to moraines identified on previous seismic data (Syvitski and Lee, 1997). There are however not enough chronological constraints to assess this correspondence.

This study provides a new high-resolution continuous sedimentary record from Lake Melville with a detailed chronology built from a combination of  $^{14}\text{C}$  ages and paleomagnetism. This record helps to complete recent terrestrial fieldwork and establish the evolution of regional sedimentary environments in Lake Melville during the last 9.1 ka.

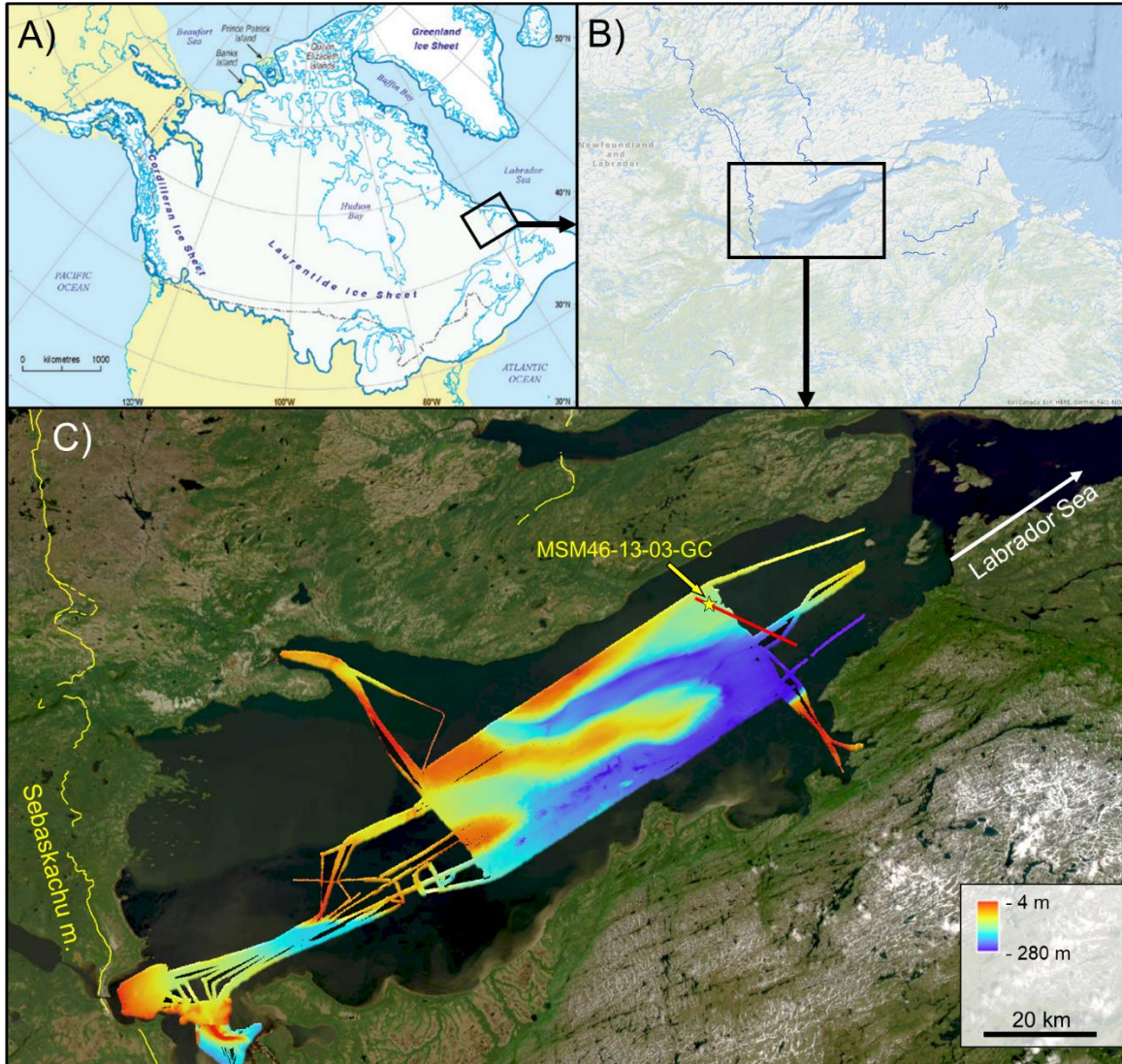
### **3.4 STUDY AREA**

Lake Melville is a semi-enclosed estuary which is part of the Hamilton Inlet system (Fig. 31) extending 250 km inland from the coastline in the intrusive and high-grade metamorphic rocks of the Grenville Province (Vilks and Mudie, 1983; Vilks et al., 1987; Syvitski and Shaw, 1995; Syvitski and Lee, 1997). Lake Melville is formally classified as a fjärd, more than a fjord (Brown et al., 2012), as its bathymetry is irregular and it is surrounded by flat lowlands, except the Mealy Mountains Massif flanking the southern shore that reaches more than 1,000 m (Vilks and Mudie, 1983; Brown et al., 2012; Kamula et al., 2020). It comprises an area of  $\sim 2,100 \text{ km}^2$  and is fluvially dominated, as it receives about  $94 \text{ km}^3$  of water a year from the Churchill, Goose, North West, Naskaupi and Kenamu Rivers, draining a total of  $150,000 \text{ km}^2$  of the hinterland (Syvitski and Shaw, 1995; Kamula et al., 2017). Lake Melville is dominated by depths less than 100 m, but has four sedimentary depressions from 120 to 250 m deep located in the eastern sector. The eastern boundary of this basin contains a 28 m-deep sill separating Lake Melville from the 50 m deep Narrows that lead to Groswater Bay and the continental shelf (Syvitski and Lee, 1997). The tidal amplitude is about 0.4 m with tidal currents varying between 0.05 to 1 m/s (Vilks et al., 1987; Nijhuis, 2013).

The large freshwater input from the rivers enhances the strong stratification with a fresher surface layer –  $\sim 10$  psu – flowing seaward and more salty bottom waters – 20-28 psu – flowing from Groswater Bay. Due to the strong stratification and shallow sill

presence, only waters with less than 30 psu are able to enter the Lake, which prevents water stagnation and anoxic conditions at depth. (Vilks and Mudie, 1983). Most organic and inorganic sediments come from rivers, particularly from Churchill River that is responsible for 47% of the input, whereas coastal erosion is not an important source in the Lake Melville system (Kamula et al., 2020).

During the LIS retreat, Lake Melville was likely a calving bay and played a role in the topographic control of the eastward ice-flow (Vilks et al., 1987; Syvitski and Lee, 1997; Occhietti et al., 2011; Trottier et al., 2019). Extensive moraine systems located in southeast Labrador indicate major positions of the ice margin during deglaciation (e.g., Occhietti et al., 2011; Couette et al., in press). In Lake Melville itself, the ice-margin experienced a single retreat phase starting after 11.0 cal ka BP, punctuated by small readvances that formed submarine moraines now buried under postglacial sediments (Syvitski and Lee, 1997). The main lake channel was ice-free before 9.2 cal ka BP and the margin reached the head of Lake Melville before  $8.4 \pm 0.6$  cal ka BP, when ice stabilized and deposited the Sebaskachu moraine (King, 1985; Couette et al., in press). After this stillstand, the ice sheet ablation occurred mainly on land, yielding the formation of paraglacial deltaic deposits including mass-failures (Syvitski and Lee, 1997). After the complete ablation of the ice sheet, postglacial muds with high organic content were deposited across much of the marine basin.



**Figure 31.** Map of the Lake Melville area. A) Extension of the Laurentide Ice Sheet over North America at the Last Glacial Maximum, from Stokes (2017). B) Zoom on Southeastern Labrador with *yellow scattered* lines representing moraines systems. C) Map of Lake Melville with multibeam data from the ArcticNet Basemaps Database, the localisation of core MSM46-13-03-GC and of the Sebaskachu Moraine system. The red line shows the location of the acoustic profile of Figure 32.

Just after local deglaciation, the marine limits were higher than present day with values increasing inland from about 110 m at the Narrows to 150 m a.s.l. west of the lake (Fitzhugh, 1973; Vilks and Mudie, 1983; Nijhuis, 2013). The Lake Melville area then

experienced a continuous relative sea-level (RSL) drop with a decreasing rate, reaching a level of 67 m at the head of the lake around 7.8 cal ka BP. This drop is still active today with a rate of about 3-4 mm/yr (Shaw et al., 1998; Batterson and Liverman, 2010; Vacchi et al., 2018; Couette et al., 2022, chap. 4). The sill at the entrance was thus 90 m deeper than now at 7.5 <sup>14</sup>C ka BP (7.8 cal ka BP), 50 m deeper at 7.0 <sup>14</sup>C ka BP (7.3 cal ka BP) and 20 m deeper at 5.0 <sup>14</sup>C ka BP (5.1 cal ka BP) (Vilks and Mudie, 1983).

### **3.5 MATERIALS AND METHODS**

#### **3.5.1 Acoustic profiling and sampling**

Acoustic sub-bottom profiling and gravity-coring were done in Lake Melville during the MSM46 expedition of the RV Maria S. Merian in the summer 2015 with a PARASOUND P70 operating at primary frequencies between 18 – 28 kHz and parametric secondary frequencies in the range of 0.5 – 10 kHz.

The 14.07 m-long sediment core MSM46-13-03-GC – hereafter referred as core 13-03-GC – was retrieved from a basin shallower than the main lake troughs (Fig. 32) at a depth of 122 m (53.8737; -59.2352). Onboard the ship, the core was opened, described, and photographed. U-channels were also directly sampled, as well as some sediment for <sup>14</sup>C analyses on foraminifera. However, the upper 7 m of the core were highly sulfidic. As such, significant calcium carbonate dissolution occurred when the sediment was oxidized after the opening (Reaves, 1986) and subsampling in this section was not done in time for recovering tests of foraminifera.

#### **3.5.2 Physical and chemical measurements**

U-channels were run into a CT-scan at the INRS-ETE in Quebec City to obtain digital x-ray images of the cores. At ISMER-UQAR, the core was run into a Multi Sensor Core logger (MSCL) equipped with a Bartington point-sensor to measure the low-field magnetic susceptibility  $k_{LF}$ , a Minolta CM-2600d spectrophotometer to obtain the  $a^*$  colour space, and an Innov-X Olympus Delta Element x-ray fluorescence (XRF) spectrometer for

measuring several elemental concentrations including Zr, Rb, Mn and Ti concentrations.  $k_{LF}$  is used as a proxy for ferrimagnetic grain concentration, but also increases with particle grain-size  $> 10 \mu\text{m}$  (Stoner and St-Onge, 2007).  $a^*$  corresponds to the green-red scale of sediment colour (St-Onge et al. 2007; Debret et al. 2011), and in our case reflects the level of sediment surface oxidation as the measurements were done 3 years after the core opening. The Zr/Rb is used as a grain-size proxy, as Zr and Rb are more concentrated in coarse-grain sediments and in clays respectively, while the Mn/Ti is a proxy for redox transition (Rothwell et al., 2006; Kylander et al., 2011; Croudace and Rothwell, 2015; Duboc et al., 2017).

### 3.5.3 Cryogenic magnetometer

Continuous paleomagnetic measurements were performed on U-channels from core 13-03-GC at 1-cm intervals with a 2G SRM-755 u-channel cryogenic magnetometer. The natural remanent magnetization (NRM) was measured a first time on u-channels that were then demagnetized by an alternating field at peak fields from 0 to 80 mT (5-mT increments) in order to determine the characteristic remanent magnetization (ChRM). An anhysteretic remanent magnetization (ARM) was then imparted to the sediment by inducing a peak alternating field of 100 mT with a superimposed 0.05 mT direct current (DC) biasing field, and then measured with the same demagnetization steps as for the NRM. This process was again repeated after inducing an isothermal remanent magnetization (IRM) in a DC field of 0.3 T with a pulse magnetizer. ARM and IRM are inherent magnetic properties that are primarily related to the concentration of ferrimagnetic grains but also by their sizes (King et al., 1982; Stoner et al., 1996; Dunlop and Özdemir, 2007). ARM is more enhanced by very fine-grained, single to pseudo-single domain magnetite ( $30 \text{ nm} < d < 1 \mu\text{m}$ ) which are particularly affected by dissolution under reducing conditions (Bloemendal et al., 1992; Funk et al., 2004), whereas IRM is more sensitive to coarser grains ( $>10 \mu\text{m}$  and up to a few tenths of microns). The anhysteretic susceptibility  $k_{ARM}$  derived from ARM, is used to obtain the  $k_{ARM}/k_{LF}$  that varies inversely with the magnetic grain-size, particularly in the 1-10  $\mu\text{m}$  range (King et al., 1983; Stoner and St-Onge, 2007).

Using the Excel macro developed by Mazaud (2005) on NRM measurements, characteristic declinations and inclinations were then computed by principal component analysis (Kirschvink 1980) from NRM measurements. This computation also provides the maximum angular deviation (MAD) and the median destructive field (MDF) for NRM, ARM and IRM measurements. The MAD gives a quantitative estimation of the paleomagnetic data quality with value below 5° indicating high-quality directional data (Stoner and St-Onge, 2007). The MDF corresponds to the peak AF needed to remove half of the magnetic remanence and varies depending on the type of magnetization induced, providing different information on the sediment magnetic properties (Stoner and St-Onge, 2007).

### **3.5.4 Discrete analyses**

Discrete sediment samples from every 10 or 20 cm were analyzed with a Beckman Coulter LS13320 laser sizer after being diluted into a Calgon solution (1% sodium hexametaphosphate). The results were computed with GRADISTAT to determine the mean sediment grain-size (Blott and Pye, 2001).

Sediment samples from every 20 or 40 cm were also analyzed for stable isotopic analyses. They were first dried, crushed, and split in two duplicates. One duplicate of each sample was then treated with HCl by fumigation to remove inorganic carbon (Harris et al., 2001; Ranmarine et al., 2011). All samples were analysed with a gas chromatograph coupled to a mass spectrometer for stable isotope ( $\delta^{13}\text{C}$ ) and an elemental analyzer (GC-EA-IRMS, ThermoElectron/ COSTECH) to measure C and N contents (%C, %N) at the geochemistry environmental laboratory of GEOTOP (UQAM). By combining the data from the treated and untreated samples, we can determine the  $C_{\text{org}}/N_{\text{total}}$  elemental ratio and the  $\delta^{13}\text{C}$  isotopic ratio. These proxies give information on the provenance of the organic matter, and thus on variations of elemental conditions (e.g., Meyers, 1997; St-Onge and Hillaire-Marcel, 2001; Lamb et al., 2006).

Finally, discrete samples were also analyzed with a Princeton Measurements alternating gradient force magnetometer (AGM) to measure rock magnetic properties of the sediment: the magnetic moment at saturation ( $M_s$ ), the saturation remanence ( $M_{rs}$ ), the

bulk coercive force ( $H_c$ ) and the remanent coercivity ( $H_{cr}$ ). In this case, the samples were chosen in order to represent the different lithological variations. Hysteresis loops were obtained during the measurements and can be used to confirm if (titano)magnetite is the main magnetic carrier in the magnetic assemblage, which is required to reconstruct reliable paleomagnetic records (Tauxe, 1993; Stoner and St-Onge, 2007). The data derived from the AGM measurements can also be used to investigate variations of the magnetite grain-size by plotting the  $M_{rs}/M_s$  vs  $H_{cr}/H_c$  in a Day-diagram (e.g., Day et al., 1977; Roberts et al., 1995; Tauxe et al., 1996; Channell and Hodell, 2013).

### 3.5.5 Chronology

Three mollusk shells were retrieved in core 13-03-GC, as well as eight samples of mixed benthic foraminifera for AMS radiocarbon dating (Table 5). The shells were sent for analysis to the Leibniz Laboratory for Radiometric Dating and Isotope Research of Kiel University (CAU), Germany, while the foraminifera were analysed at the ETH Zürich (Switzerland). The obtained  $^{14}\text{C}$  ages were calibrated with the online software Calib 8.2 with the Marine20 curve and a reservoir age correction  $\Delta R$  of  $0 \pm 0$ . Choosing a  $\Delta R$  is of critical importance in such high-resolution studies, but many factors may influence the reservoir age, particularly water stratification and glacial meltwater inputs (e.g., Vickers et al., 2010; Ross et al., 2012; Duboc et al., in prep). So far, no  $\Delta R$  was estimated in Lake Melville, and it can be difficult to estimate an appropriate value for this enclosed area where the relative influence of meltwaters, river runoff and seawater changed through time during the Holocene. We thus chose to keep a conservative value of  $\Delta R = 0 \pm 0$  yr through the entire record.

However, as the upper part of core 13-03-GC (above 7.0 m) did not provide datable carbonate material, we used the paleomagnetic directional data to complete the age-model. We thus compared inclination and declination data from core 13-03-GC with those from the global geomagnetic model CALS10k.2 (Korte et al., 2011) and other regional records. Such correlations allow tie-points to be determined that can be used to build a strong age-model together with the radiocarbon data (e.g. Lisé-Pronovost et al., 2009; Barletta et al., 2010a; Deschamps et al, 2018; Caron et al., 2018).

**Table 5.** List of AMS radiocarbon ages analyzed and calibrated in Calib8.2 (Stuiver et al., 2020) using the Marine20 dataset (Heaton et al., 2020) and a  $\Delta R$  value of  $0 \pm 0$  yr.

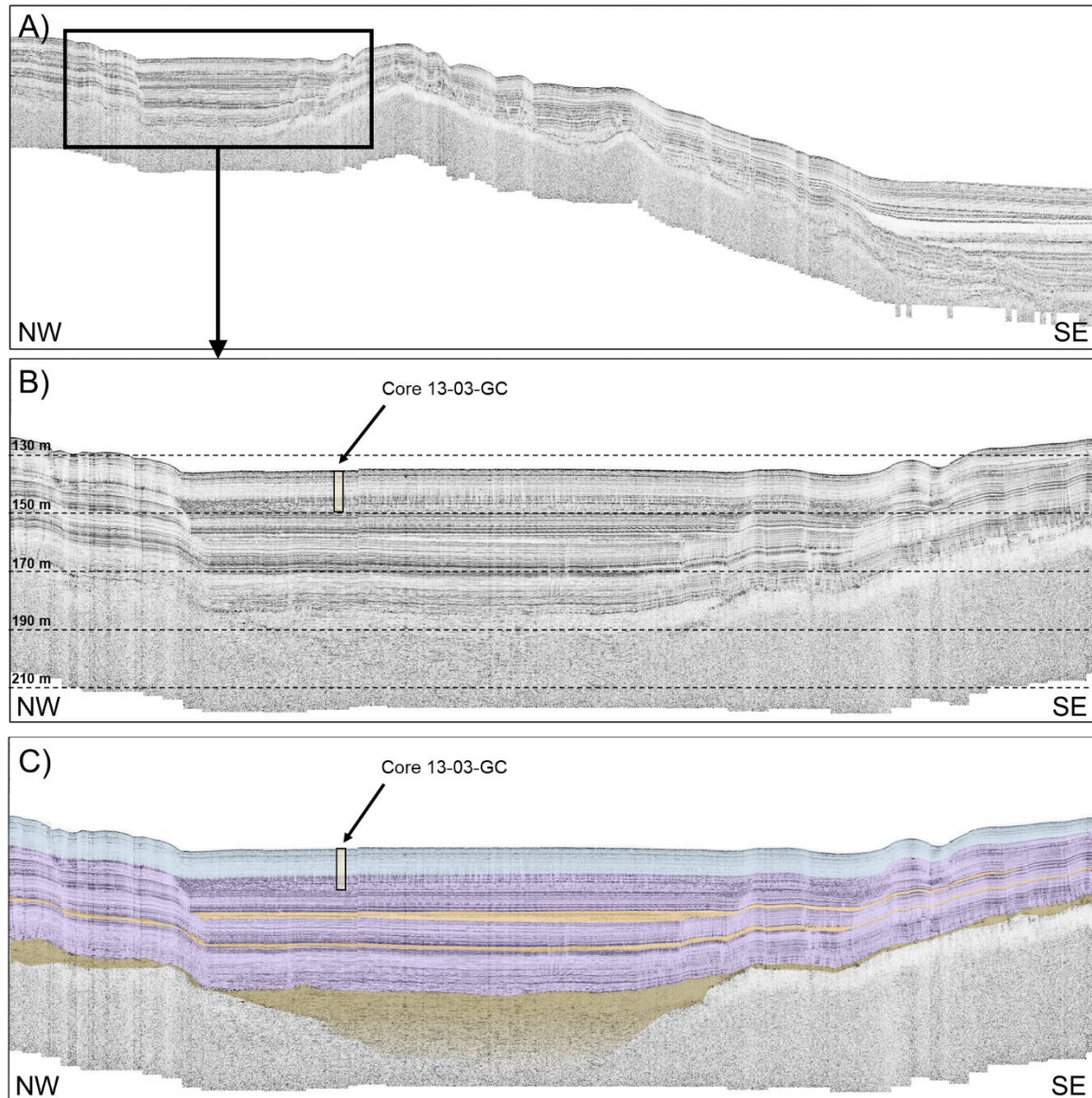
Depth (cm)	Dated material	Uncorrected $^{14}\text{C}$ age ( $^{14}\text{C}$ yr BP)	$2\sigma$ age range (cal. yr BP)	Median prob. age (cal. yr BP)	AMS laboratory number
703	Mix. benthic forams	$7170 \pm 60$	7300-7625	<b>7469</b>	ETH-102145
841	Mollusk shell	$7840 \pm 35$	7985-8294	<b>8131</b>	KIA-54303
876	Mix. benthic forams	$7480 \pm 60$	7590-7927	<b>7758</b>	ETH-102146
926	Mix. benthic forams	$8532 \pm 101$	8625-9264	<b>8952</b>	UOC-2339
949	Mix. benthic forams	$6842 \pm 75$	6930-7360	<b>7155</b>	UOC-2340
980	Mix. benthic forams	$8184 \pm 32$	8348-8631	<b>8485</b>	UOC-2335
1065	Mollusk shell	$8275 \pm 40$	8410-8803	<b>8599</b>	KIA-54304
1137	Mix. benthic forams	$8427 \pm 32$	8628-8987	<b>8816</b>	UOC-2341
1301	Mix. benthic forams	$8571 \pm 35$	8818-9212	<b>9017</b>	UOC-2342
1403	Mollusk shell	$8635 \pm 40$	8933-9286	<b>9097</b>	KIA-54305
1405	Mix. benthic forams	$8500 \pm 80$	8622-9181	<b>8906</b>	ETH-102147

## 3.6 RESULTS

### 3.6.1 Acoustic stratigraphy

Acoustic profiles reveal a Quaternary sedimentary sequence at least 60 m-thick composed of 4 acoustic units – A1 to A4 from base to top (Fig. 32). The acoustic basement corresponds either to the bedrock or ice-contact sediment. A1 is a transparent ponded 10 m-thick unit that could be interpreted to ice-contact sediments or mass failure deposits. Unit A2 is about 40 m-thick and is composed by parallel reflectors with varying intensities that conformably drape lower units. This second unit is interpreted as glaciomarine sediments, and some of the strong reflectors are probably turbidites. Unit A3 corresponds to two ponded thin sequences located inside unit 2 and are continued on the basin flanks by strong wavy reflectors. This thin unit located in the middle of the glaciomarine sequence is interpreted here as MMDs triggered by paraglacial processes, and the uppermost and thickest of them stratigraphically corresponds to a thick MMD identified as unit M-1 by Vilks et al. (1987, profile A-B). Finally, unit A4 is about 10 m-thick and is also made of parallel reflectors that drape lower units but are generally weaker than in unit A2. This uppermost unit likely corresponds to postglacial sediments.





**Figure 32.** Acoustic profile obtained during the MDM46 cruise. A) Complete profile with location indicated in figure 31. B) Zoom on the shallow basin with position of core 13-03-GC. Sediment thicknesses have been estimated with a sediment velocity of 1500 m/s, as in other fjord-like environments (Hjelstuen et al., 2009; Bellwald et al., 2016). C) Same as B) but with colors highlighting the different units described in section 3.1: A1 in brown with an uncertain base at the basin bottom; A2 in purple, A3 in yellow and A4 in blue at the top.

### 3.6.2 Core lithology

Core 13-03-GC is generally made of silt varying in size, but generally fining upward between the base and 700 cm, and homogeneous fine silt between 700 cm and the top (Fig. 33). Most of the core is characterized by numerous black, sulfidic traces, well observable on the core pictures. They however became reddish with time after opening – not shown on the picture – particularly between 800 cm and the top. This color change explains the high values of  $a^*$ , which was measured 3 yr after, and do not corresponds to the picture. Interestingly, these enhanced  $a^*$  values reflecting sediment oxidation are well correlated to the  $K_{ARM}/K_{LF}$ . Magnetic properties, reflectance and grain-size variations allow to identify 4 different units – 1 to 4 from base to top – and a major transition around 800 cm.

Unit 1, from the core base to about 1335 cm, is mainly composed by a background of grey, fine silt without black traces, and contains several layers of coarser sediment up to medium sand. These layers show smooth transitions with the background, with a coarsening upward base and a fining upward top. At the bottom of unit 1 – below 1360 cm –, the layers are about 2-3 cm thick and regularly spaced by a few centimeters. These layers then become thinner and finer toward the top and gradually merge with the background. These grain-size alternations are well represented by highly variable Zr/Rb values (Fig. 33 and 34). Values of  $\delta^{13}C$  and C/N are low in unit 1, and likely represent organic matter originating from freshwater.

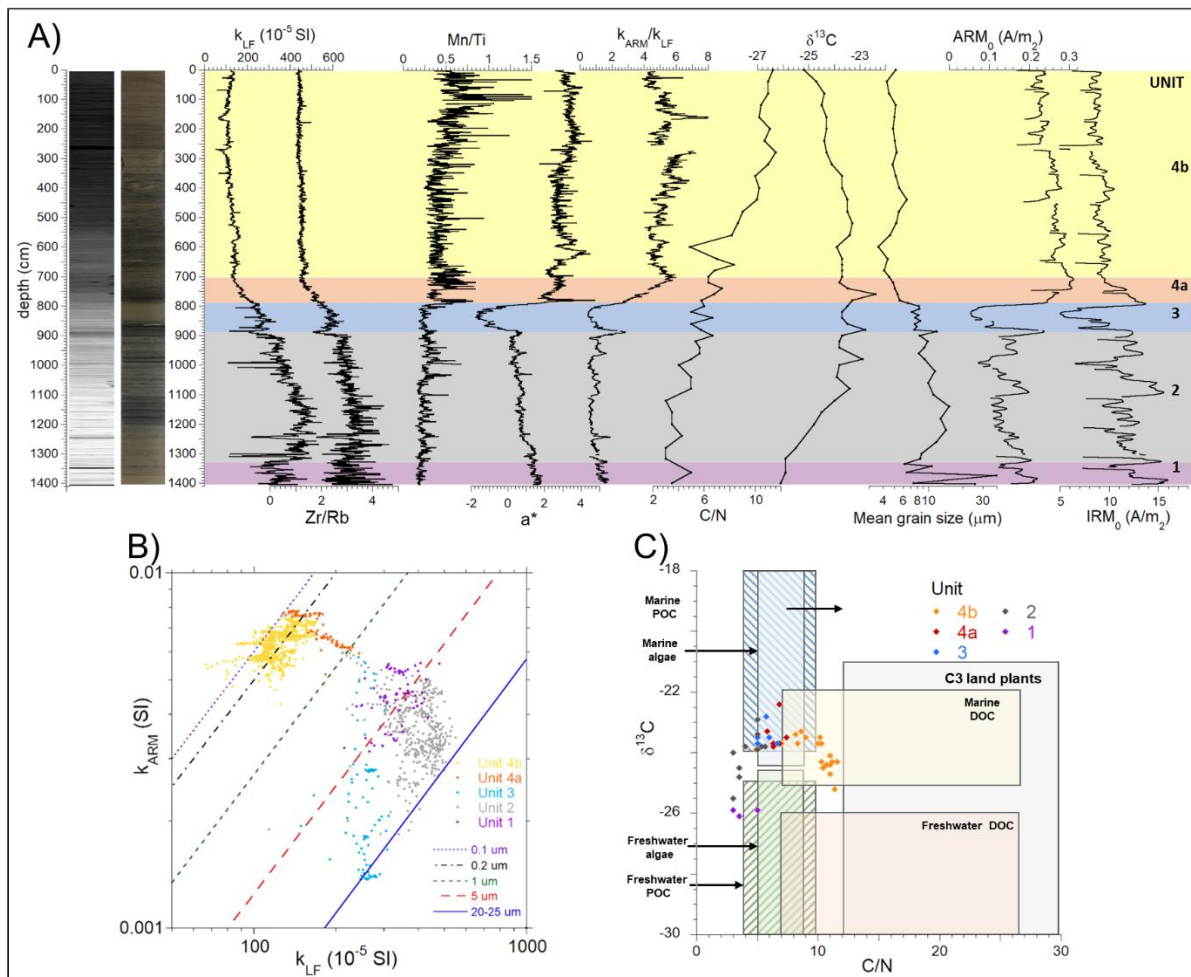
Unit 2, from 1335 to 880 cm, is characterized by the presence of black sulfidic traces. Their concentration increases from 1330 to 1200 cm, and include some 2-3 cm-thick black layers. Grain-size proxies show an upward coarsening from 1330 to 1200 cm and then fining from 1150 to 880 cm. The  $\delta^{13}C$  shows a net increase from 1300 to 1080 cm and then stabilizes, while C/N slightly increases as it approximately does in all units above. The top of unit 2 is marked by a 5 cm-thick black layer that has higher ARM values than the rest of the unit.

Unit 3, from 880 to 790 cm, is characterized by lower values of  $a^*$ , ARM and IRM in comparison to the rest of the core. This is particularly true between 850 and 795 cm where black traces are completely absent. Grain-size parameters slightly increase then

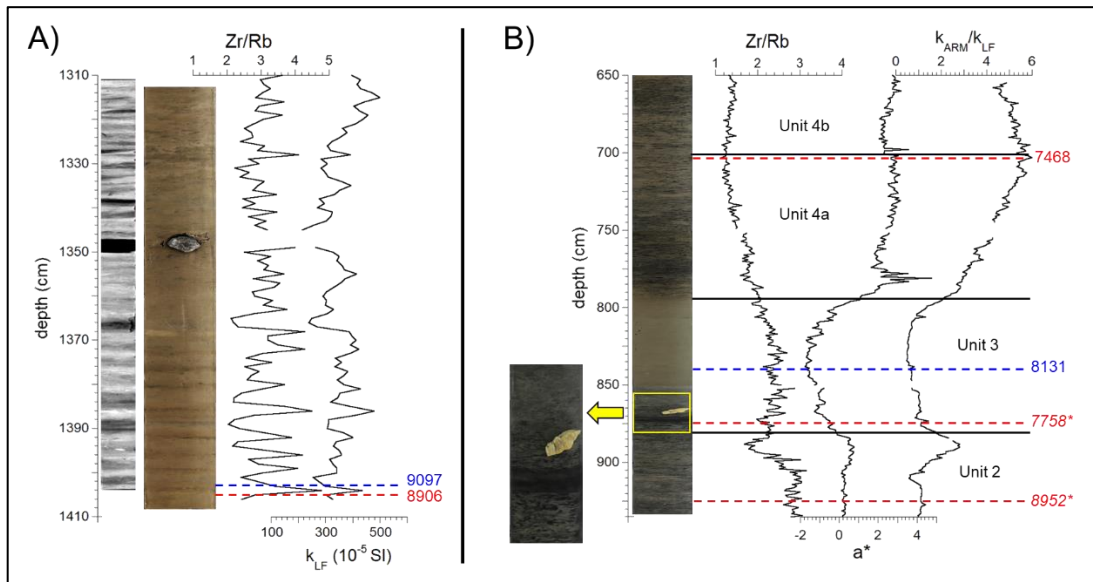
decrease upward and magnetic susceptibility do not show such variations. A 5 cm-large carbonated rock, likely calcite, was found at 865 cm (Fig. 34).

The most prominent transition in core 13-03-GC is the one from unit 3 to unit 4 around 790 cm. This transition is highlighted by a pronounced peak of  $a^*$  and Mn/Ti and sharp increases of ARM and IRM values, as well as a decrease in mean grain-size. The  $k_{ARM}$  vs  $k_{LF}$  diagram indicates that magnetic grain-size transits below 1  $\mu\text{m}$ . Unit 4 is composed of brown fine silt studded with many black sulfidic traces that became reddish afterwards, increasing the  $a^*$  value. Subunit 4a corresponds to a continuation of the transition with bulk and magnetic grain-size decreases highlighted by all parameters. The combination of an ARM increase and an IRM decrease indicates an increasing proportion of magnetic particle  $< 1 \mu\text{m}$  at the expenses of a loss of particles  $> 10 \mu\text{m}$ . Subunit 4a also has high Mn/Ti values, that decrease at the base of 4b. Subunit 4b is particularly homogenous in comparison to other units, with just a slight sediment coarsening upward from about 600 to 450 cm. The  $\delta^{13}\text{C}$  values, which were relatively steady after its increase in unit 2, starts an upward decrease at about 550 cm, while the C/N continues to progressively increase.

Based on sub-bottom profile and lithological data, we assume that the upper 9 m of core 13-03-GC – units 3 and 4 – correspond to the postglacial acoustic unit A4, while units 2 and 1 were deposited mostly by glaciomarine and fluvio-glacial processes and are the top of acoustic unit A2.



**Figure 33.** **A)** Physical, chemical, sedimentological and magnetic properties of core 13-03-GC versus depth, along with its photography and the CT-scan image from the u-channels. Colors are associated to the different units described in section 4.2. **B)** Diagram of  $k_{ARM}$  VS  $k_{LF}$  with lines representing different magnetic grain-size threshold proposed by King et al. (1983). **C)** Diagram of  $\delta^{13}C$  versus C/N for comparison with the values of different sources of organic matter, based on Lamb et al. (2006).

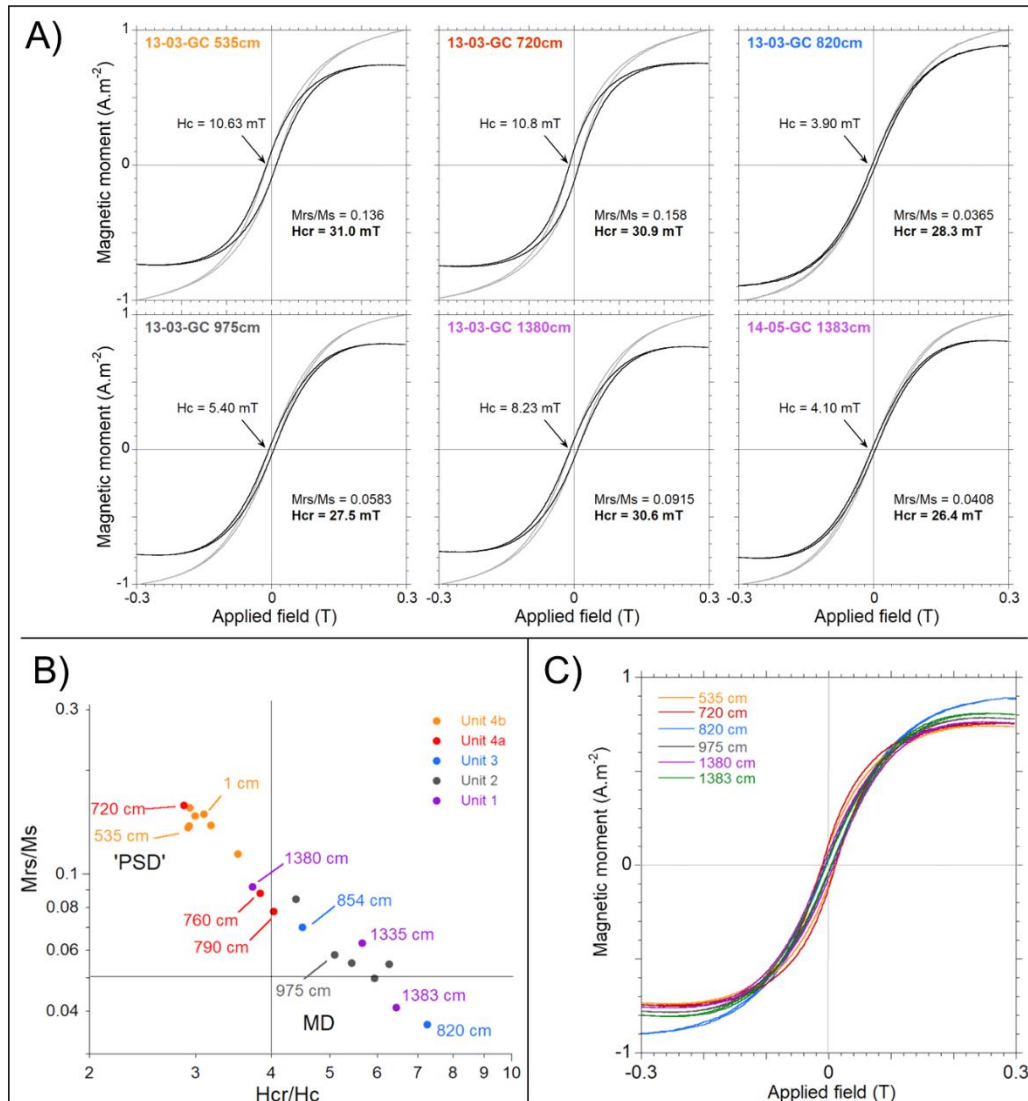


**Figure 34.** Zoom on specific sections of core 13-03-GC with their photographs, some chemical, physical or magnetic properties and the location of calibrated AMS  $^{14}\text{C}$  ages from foraminifera (in red) and mollusc shells (in blue). **A)** Unit 1, also with the CT-scan from u-channels. **B)** Section covering the transition of units 3 and 4a, also with an image with the thick carbonated IRD found in the core.

### 3.6.3 Rock-magnetic analyses

The sigmoidal shapes of hysteresis loops from all units are typical of magnetic assemblages dominated by (titano)magnetite (Fig. 35A). Variations of  $M_{rs}/M_s$  and  $H_{cr}/H_c$  should therefore mostly depend on the magnetic grain-size. We note however that the loop shape is slightly different for samples from unit 3 (Fig. 35C), maybe reflecting mineralogical differences despite the predominance of (titano)magnetite. The resulting Day diagram (Fig. 35B), together with the  $k_{ARM}/k_{LF}$ , shows that the magnetic grain-size generally follows the bulk grain-size and Zr/Rb variations, except for unit 3. The great variability of the hysteresis ratios in unit 1 highlights the variations between the silty-clayey background and the sandy

layers. Sediment samples from unit 2 and 3 vary in the multidomain (MD) magnetic range, while those from unit 4 are in the pseudo-single domain (PSD) range and thus finer. The finer grain-size of unit 4 is also emphasized by the high values of ARM in comparison to other units. Despite samples from unit 3 are all in the MD range, their hysteresis ratios are highly variable, and values from 820 cm correspond to even coarser magnetic grains than the sandy layers of unit 1. In the section between 850 and 795 cm, where the sediment does not contain black traces, ARM, IRM and the coercivity parameters –  $MDF_{NRM}$  and  $H_c$  – have the lowest values of core 13-03-GC. However, other grain-size indicators do not show noticeable grain-size variations in unit 3. Therefore, ferrimagnetic minerals are possibly coarser in unit 3.



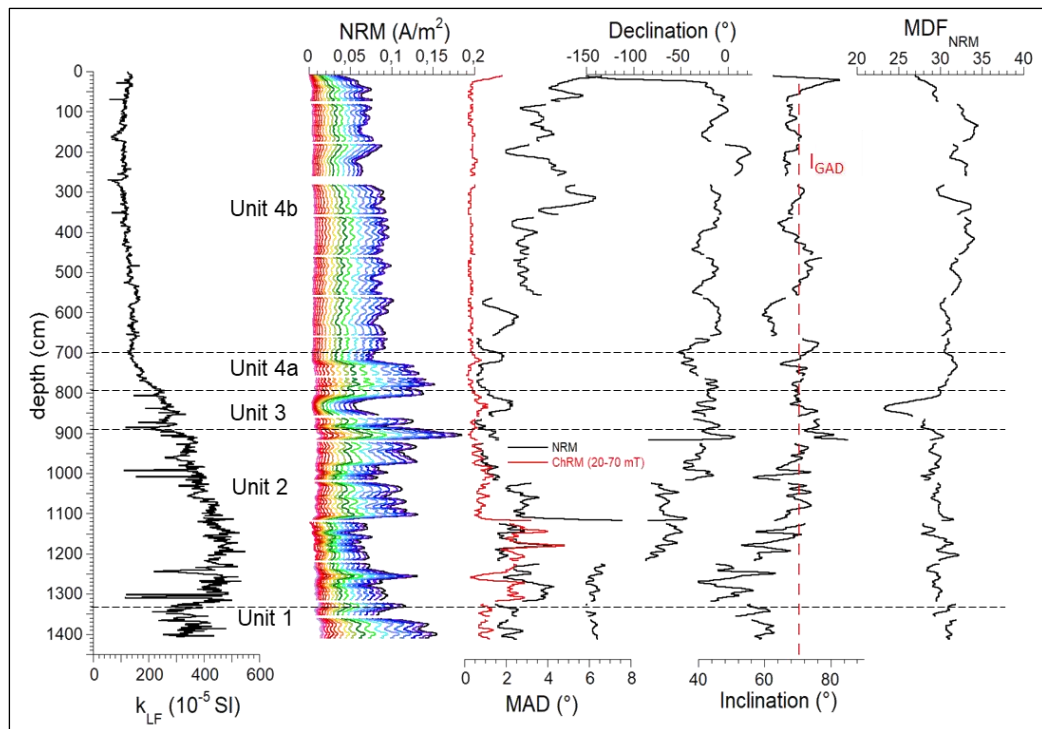
**Figure 35.** Data obtained from AGM measurements. A) Specific hysteresis curves from samples representing the different units of core 13-03-GC. Grey hysteresis curves correspond to raw hysteresis data, whereas the black ones are corrected for paramagnetic and diamagnetic components. B) Day diagram with all measured sampled. C) Combination of all normalized and corrected hysteresis curved showed above.

### 3.6.4 NRM and paleomagnetic directional data

Paleomagnetic measurements for core 13-03-GC yielded high-quality data with a  $MAD_{NRM}$  below  $6^\circ$  when including all the demagnetization steps. After removing the



demagnetization steps below 20 mT, the resulting ChRM has  $MAD_{NRM}$  values below  $2^\circ$  for units 1, 3 and 4 and below  $5^\circ$  for unit 2 (Fig. 35). The inclination varies around the expected inclination  $-70^\circ$  – for the site latitude based on a geocentric axial dipole model (GAD) from the top to 1,200 cm and has lower values for the lower part of the core. The declination is also relatively steady in the upper 1,000 cm where it varies into a range of  $80^\circ$ , but shows shifts at 1,000 and 1,200 cm. This information indicates that the ChRM is strong and stable for all the core, but paleomagnetic data should be carefully considered below 1200 cm. Data from core 13-03-GC are thus reliable for paleomagnetic secular variation reconstruction, particularly in unit 4.



**Figure 36.** Natural remanent magnetization measurements of core 13-03-GC along with its magnetic susceptibility. The MAD of NRM and ChRM are plotted, as well as the inclination of the geocentric axial dipole model ( $I_{GAD}$ ).



## 3.7 DISCUSSION

### 3.7.1 Deglacial sedimentary sequence

Core 13-03-GC sampled the 14 upper meters of the 60 m-thick sedimentary sequence and mostly reflects the transition from a glaciomarine to a postglacial environment that is typical of basins that experienced a local ice-retreat. Unit 1 and 2 are correlated with the top of acoustic unit A2 that likely corresponds to a thick glaciomarine sequence also containing paraglacial deposits (Fig. 32). By the time Unit 1 was formed, the glacial margin was not proximal to the sampling site, as most of the sediment is fine, thus reflecting suspension-dominated transport dynamics. The regularly spaced sandy layers give the sediment a varved appearance, which would be consistent in a lake. However, these varve-like laminations would be 5 cm thick, indicating a sedimentation rate ten times higher than calculated from the chronology. Moreover, the symmetric aspect with progressive transition of these layers makes them distinct of typical varves that have sharp transitions between them. These sandy layers rather have the typical structure of hyperpycnites deposited by increasing then decreasing hyperpycnal currents (e.g. Mulder and Chapron, 2011; Duboc et al., 2017). In such a deglacial context, these currents could be triggered by meltwater pulses released from under the ice-sheet. Moreover, the fact that these layers become finer with time illustrates the progressive retreat of the ice margin farther from the site.

The transition to unit 2 is correlated with an increase in marine organic matter, an apparition of the black stripes and a disappearance of the sandy layers. This marks the retreat of the ice-sheet from the surrounding, maybe inland. This retreat also allowed a decrease of the freshwater proportion and thus an increase of the relative influence of marine water in Lake Melville, as highlighted by  $\delta^{13}\text{C}$  data (Fig. 33). The sedimentary environment therefore began to transit from glaciomarine to postglacial. The high sedimentation rate in unit 2 is probably explained by paraglacial processes that remobilised high quantities of sediment from deglaciaded lands (Dietrich et al., 2017). As there is no turbidites found in the core, the

fluvial remobilization of glacial sediment was probably the main paraglacial process in action.

A transition then occurred at the top of unit 2 and continued in unit 4a, with a progressive sediment fining and reduction of the sedimentation rates. This transition is, however, intercepted by a temporary environmental change, highlighted by magnetic properties and sediment color in unit 3. The slightly lower Mn/Ti values in unit 3 overlain by a noticeable peak indicates change in redox conditions at the transition to unit 4. However, this peak is possibly an “artificial” feature as it corresponds to the most prominent a\* peak caused by the oxidation of the dark sediment after the core opening – XRF measurement being done 3 years after. Therefore, the sediment between 850 and 795 that did not contain black traces was possibly richer in oxygen than the overlying sediment of unit 4, and the Mn/Ti peak is an artefact. Nonetheless, this still highlights an important environmental change. The influx of organic matter was possibly reduced during the deposition of unit 3, preventing iron and sulfate reduction that increased again with organic matter flux in unit 4 (e.g. Liu et al., 2012).

Unit 4 corresponds to the postglacial sequence in which the only sedimentological changes are the quick fining in subunit 4a then slow coarsening upward from 700 to about 600 cm. The other noticeable change is the reduction of marine organic matter proportion highlighted by the  $\delta^{13}\text{C}$  decrease. This can be linked to the isostatic uplift that reduced the sill depth at eastern Lake Melville and increased the limitation of water exchange with the continental shelf. The progressive increase of the vegetation cover after the ice margin retreat is also involved in the evolution of organic matter provenance.

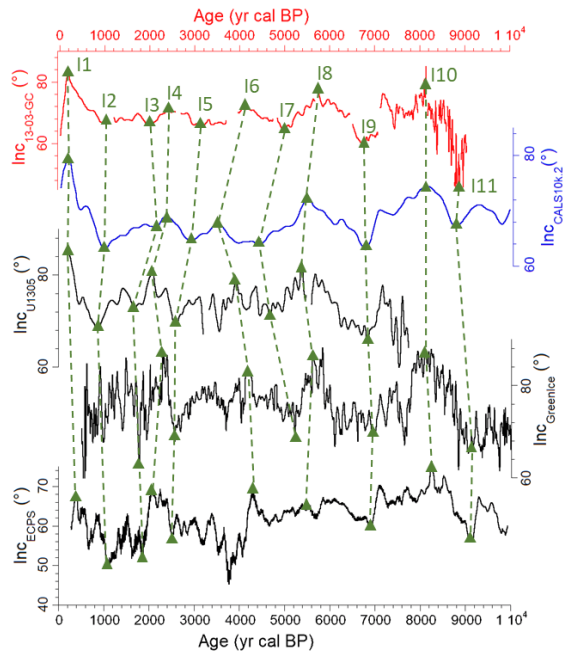
### **3.7.2 Age-modelling**

A preliminary age-model based on the obtained radiocarbon ages was made with a third-degree polynomial fit ( $R = 0.986$ ). Three foraminifera samples yielded too young or too old ages and were thus excluded from age-modelling. We then put inclination and declination data of core 13-03-GC on the resulting timescale and compared them with directional data

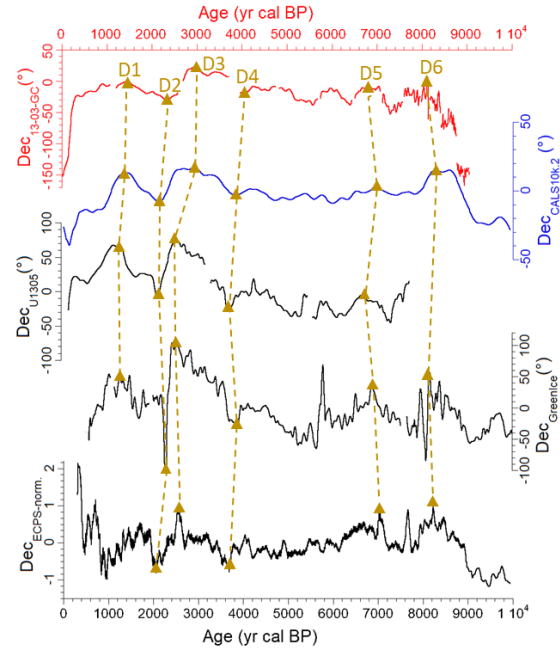
from the geomagnetic field model CALS10k.2 (Korte et al., 2011) for the location of the site, as well as with data from other records from the Northern Hemisphere (Fig. 37). The chosen records are those from site U1305 in the Labrador Sea (Stoner et al., 2013), from the PSV composite GreenIce made with two cores sampled between Greenland and Iceland (Stoner et al., 2007) and from the Eastern Canada Paleostack in the St. Lawrence area (Barletta et al., 2010b). The correlation between the 13-03-GC record and the CALS10k.2 model is particularly good, which again confirms the high quality of the record. The overall correlation with the model and the other records permitted a selection of 11 minima and maxima as tie-points for the inclination and 6 for the declination to better constrain the age-model of core 13-03-GC (Fig. 37). Weighted means and standard deviations were then calculated for each tie-points (Table 6). Because the correlation with the CALS10k.2 model is particularly good, and that other records are thousands km away from Lake Melville, we chose to give a two times higher weight for the geomagnetic model than for the records. Note also that values deduced from the preliminary age-model were only considered in the calculation of the tie-points below 700 cm, as the model was not constrained by  $^{14}\text{C}$  ages above that.

The final age-model including all  $^{14}\text{C}$  ages and paleomagnetic tie-points was then built with the Bacon R package (Fig. 38). The resulting model shows that core 13-03-GC spans the last 9.1 ka. The sedimentation rate has a value of about 1.0 cm/yr in unit 1 and decreases to 0.6 cm/yr in unit 2, 0.2-0.25 in units 3 and 4a and then transits progressively from 0.17 to 0.07 cm/yr towards the top in unit 4b. Deglacial and postglacial rates are therefore similar to Nachvak and Saglek Fjord rates in Northern Labrador (Duboc et al., 2023) and to the highest rates observed in Baffin Bay fjords (Syvitski et al., 2022), and resulted in the deposition of units 1 and 2 – thus 5 meters – in less than 1000 years, while the 8-9 m-thick postglacial unit 4 alone represents the last 7.8 ka.

## A Inclination



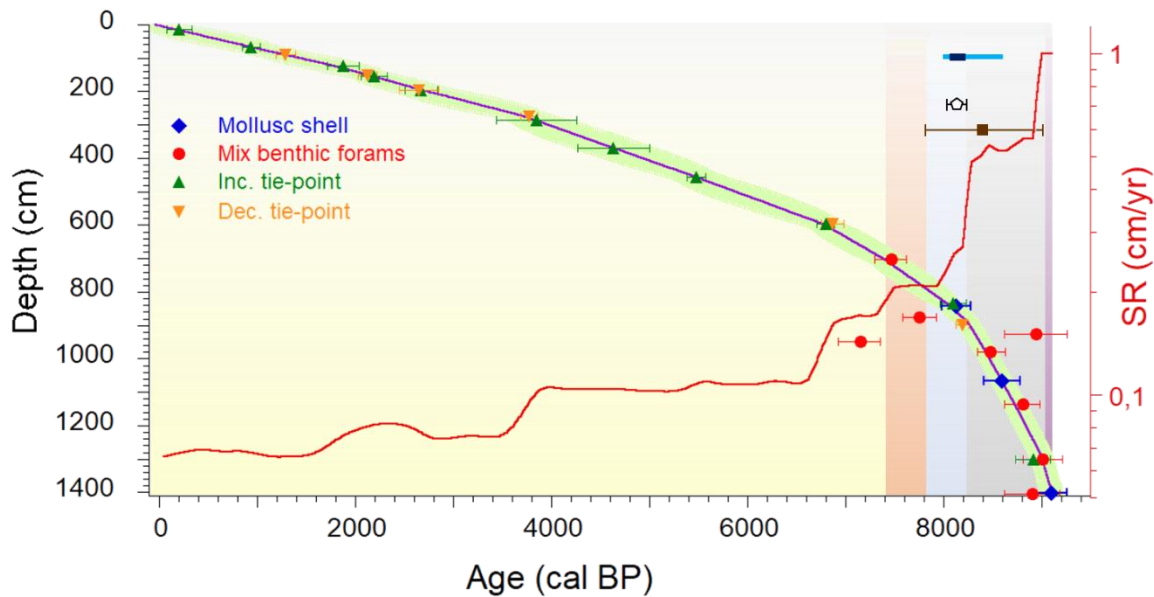
## B Declination



**Figure 37.** Paleomagnetic comparison of **(A)** inclination and **(B)** declination between core 13-03-GC from Lake Melville, the geomagnetic field model from Korte et al. (2011) and other regional records: the Greenland-Iceland PSV composite (GreenIce; Stoner et al., 2007), Site U1305 in Labrador Sea (Stoner et al., 2013) and the Eastern Canada Paleostack (Barletta et al., 2010*b*).

**Table 6.** Paleomagnetic chronostratigraphic markers (tie-points) based on correlation between core 13-03-GC, the geomagnetic field model CALS10k.2 (Korte et al., 2011) calculated for the localisation of core 13-03-GC and three other paleomagnetic records: Greenland-Iceland PSV composite (Stoner et al., 2007), Site U1305 in Labrador Sea (Stoner et al., 2013) and the Eastern Canada Paleostack (Barletta et al., 2010*b*). Tie-points labelled with I and D correspond respectively to inclination and declination and are identified in Fig. 37 .

Tie-points	Depth (cm)		Age (cal. yr BP)				Mean age	St. deviation
	13-03-GC	13-03-GC	CALS10k.2	Green-Ice	U1305	ECPS		
I1	14	189	125	—	185	402	<b>237</b>	146
I2	69	1115	910	—	869	1079	<b>953</b>	111
D1	90	1449	1370	1280	1158	—	<b>1269</b>	106
I3	124	1968	2050	1770	1680	1856	<b>1839</b>	158
D2	150	2347	2080	2295	2131	2058	<b>2141</b>	107
I4	154	2404	2290	2290	2078	2026	<b>2171</b>	139
D3	195	2968	2870	2440	2538	2544	<b>2598</b>	187
I5	196	2981	2850	2560	2600	2498	<b>2627</b>	154
D4	274	3953	3790	3900	3715	3683	<b>3772</b>	96
I6	285	4080	3430	4160	3926	4324	<b>3960</b>	389
I7	368	4963	4360	5135	4680	4616	<b>4698</b>	323
I8	455	5754	5440	5605	5370	5540	<b>5489</b>	104
I9	596	6778	6700	6925	6830	6897	<b>6838</b>	100
D5	597	6784	6950	6875	6721	7035	<b>6895</b>	133
I10	834	7948	8100	8230	—	8265	<b>8136</b>	144
D6	898	8124	8260	8165	—	8229	<b>8194</b>	62
I11	1300	8903	8730	9160	—	9083	<b>8969</b>	192

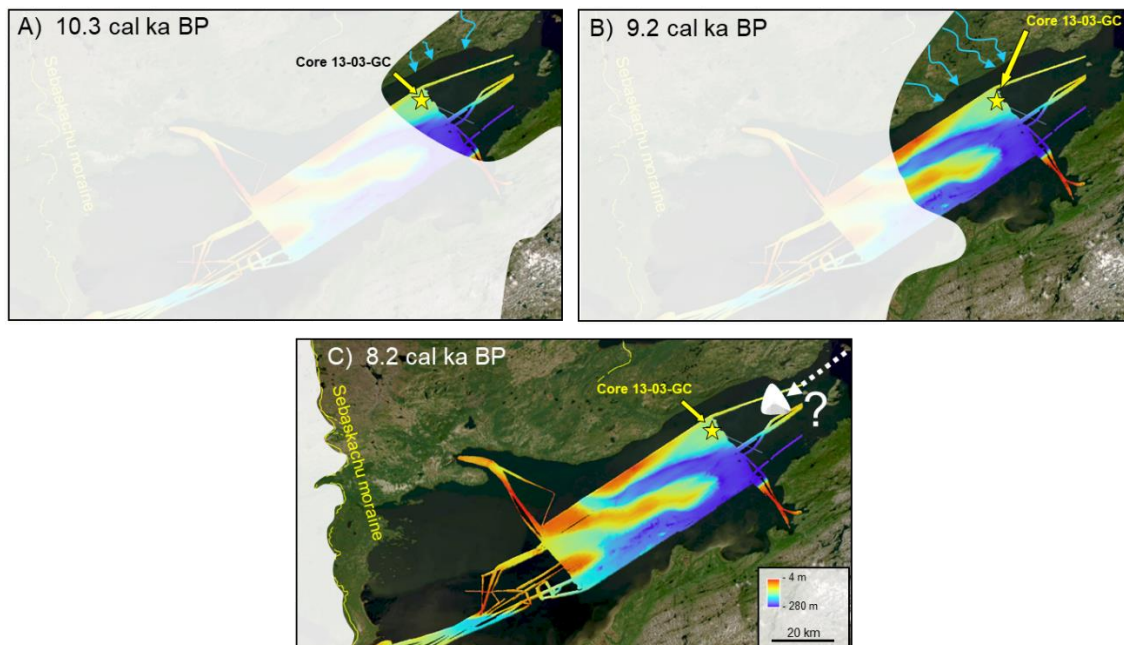


**Figure 38.** Final age model of core 13-03-GC based on AMS  $^{14}\text{C}$  ages from foraminifera and mollusc shells, and on tie-points from paleomagnetic correlations of inclination and declination. Variations of sedimentation rates are also plotted in red with a logarithmic scale. On the top right, the dark and the light blue bar represents respectively the 8.2 ka event and the long-term cooling starting around 8.6 ka cal BP (Rohling and Pälike, 2005). The white pentagon corresponds to the age of the thick carbonate IRD found in core 13-03-GC, while the brown square represents the age of the Sebaskachu moraine (Couette et al., 2023). Colours in the background correspond to the five units of core 13-03-GC as in Figure 33.

### 3.7.3 Evolution of sedimentary and environmental conditions

According to the acoustic profile and the core chronology, about 30-35 m of glaciomarine sediment were deposited before 9.2 cal ka BP at the core 13-03-GC sampling site. Considering that the ice margin began its retreat in the lake after 11.0 cal ka BP, it likely rapidly reached the location of the core site and the glaciomarine sequence was formed in 1.5-2.0 kyr with a mean sedimentation rate of about 2 cm/yr. The wide watershed of Lake Melville might explain this important sediment accumulation, with fluvio-glacial processes remobilizing glacial material from surrounding lands recently deglaciated. According to

previous studies, there was probably a margin stillstand or readvance during the 9.3 ka cold event, likely not far from the basin, which probably contributed to high sedimentation rates of unit 1 in core 13-03-GC and below (Syvitski and Lee, 1997; Couette et al., 2023). Therefore, the progressive thinning and fining of sandy layers in unit 1 likely depicts the beginning of the westward ice-retreat from its grounding zone.



**Figure 39.** Schematic representation of deglaciation steps in the Lake Melville area. Locations of core 13-03-GC and the Sebaskachu moraine are indicated. The blue arrows represent fluvio-glacial runoff from the LIS.

The ice margin then retreated westward and formed the Sebaskachu moraine at about  $8.4 \pm 0.6$  cal ka BP (Fig. 39)f, either during the 8.2 ka cold event or earlier with the general cooling that began at about 8.6 cal ka BP (Rohling and Pälike, 2005; Couette et al., 2023). The moraine formation also coincides with a reduction of the sedimentation rate at the core sample site. The ice margin was therefore still in the lake during the deposition of unit 2, but farther west and did not much control the sediment delivering in the basin and paraglacial sediments were more involved. At the base of unit 3, the depth where was found the 5 cm-

thick carbonated IRD is dated at  $8.16 \pm 0.11$  cal ka BP, which corresponds to the timing of the last Lake Agassiz-Ojibway (LAO) drainage and the concurrent collapse of the Hudson Bay Ice Saddle that was damming it (e.g., Barber et al., 1999; Jennings et al., 2015; Gauthier et al., 2020; Brouard et al., 2021; Duboc et al., in prep). This rock could therefore have come from the Hudson Bay region and been brought there by an iceberg following the Labrador Current. Icebergs can indeed be deflected in fjords and leave the IRD they carry (Normandeau et al., 2021). Moreover, detrital carbonates carried by meltwaters from the Hudson Bay System during several deglacial events were already found on the Labrador shelf, including in Cartwright Saddle just front of Hamilton Inlet (Jennings et al., 2015). At the time, the RSL was 75 and 150 m higher at the Hamilton Inlet entrance and at the Lake Melville head, respectively. Hamilton Inlet was then much larger, hence provided an easier pathway for the entrance of icebergs than the present-day narrow strait.

Unit 3 spans 400 yr from 8.19 to 7.82 cal ka BP, and thus partly corresponds to the 8.2 ka event that lasted about 160 yr, as suggested by Greenland ice cores and caused by the last LAO drainage and the collapse of its ice-dam (e.g. Alley et al, 1997; Thomas et al., 2007). Therefore, the environmental variation highlighted by changes in redox conditions may be caused by the colder temperatures characterizing the event. This climate change may have reduced the organic matter influx, thus leaving enough oxygen in it to prevent sulfate reduction.

Finally, at about 7.82 cal ka BP, the environment transitioned to postglacial conditions with sedimentation of organic-rich muds and a decrease of sedimentation rate caused by a reduction of sediment availability. The conditions were then mostly affected by the relative sea-level fall that progressively decreased the marine water incursion in Lake Melville

### **3.8 CONCLUSION**

The multiproxy study with high-resolution of core 13-03-GC combined with sub-bottom profile data and information about ice-margin stillstand from previous studies helped to better constrain the chronological evolution of sedimentary dynamics in north Lake Melville:



- During the 9.3 ka cold event, the ice margin was likely grounded in the lake, not that far from the basin, and distal glaciomarine muds alternated with sandy layers formed by subglacial meltwater pulses.
- The retreat westward of the ice margin allowed a transition from glaciomarine to postglacial sedimentation between  $9.0 \pm 0.1$  and  $8.4 \pm 0.1$  cal ka BP and was characterized by fluvial delivering of glacial muds enriched with organic matter with an increasing proportion of marine origin.
- The 8.2 ka cold event locally caused changes in sediment redox conditions, probably by reducing organic matter export in the sediment. Moreover, a carbonated rock was possibly brought by an iceberg from the Hudson Bay area during the last LAO outburst when the RSL was about 100 m higher in Hamilton Inlet.
- Postglacial sedimentation from 7.8 cal ka BP corresponds to a reduction of sedimentation rate and a shallowing of the sill at the lake entrance that reduced the marine water influx.

### **3.9 ACKNOWLEDGMENTS**

This project was funded by the Natural Science and Engineering Research Council (NSERC) of Canada grants to G.S. and the Fonds de Recherche du Québec Nature et Technologie (FRQNT) grants to Q.D. We thank the captain, crew and scientist of the MSM46 expedition for their work onboard the R/V Maria S. Merian. We also thank Q Beauvais, M St-Onge and D Lavallée for their help at ISMER, as well as A Adamowicz-Walczak and J-F Hélie at the Geotop research center.

### 3.10 RÉFÉRENCES

- Allan, E., de Vernal, A., Seidenkrantz, M., Briner, J.P., Hillaire-Marcel, C., Pearce, C., Meire, L., Røy, H., Mathiasen, A.M., Nielsen, M.T., Plesner, J.L., Perner, K., 2021. Insolation vs. meltwater control of productivity and sea surface conditions off SW Greenland during the Holocene. *Boreas* 50, 631–651. <https://doi.org/10.1111/bor.12514>
- Alley, R.B., Mayewski, P.A., Sowers, T., Stuiver, M., Taylor, K.C., Clark, P.U., 1997. Holocene climatic instability: A prominent, widespread event 8200 yr ago. *Geology* 25, 483. [https://doi.org/10.1130/0091-7613\(1997\)025<0483:HCIAPW>2.3.CO;2](https://doi.org/10.1130/0091-7613(1997)025<0483:HCIAPW>2.3.CO;2)
- Barber, D.C., Dyke, A., Hillaire-Marcel, C., Jennings, A.E., Andrews, J.T., Kerwin, M.W., Bilodeau, G., McNeely, R., Southon, J., Morehead, M.D., Gagnon, J.-M., 1999. Forcing of the cold event of 8,200 years ago by catastrophic drainage of Laurentide lakes. *Nature* 400, 344–348. <https://doi.org/10.1038/22504>
- Barletta, F., St-Onge, G., Channell, J.E.T., Rochon, A., 2010a. Dating of Holocene western Canadian Arctic sediments by matching paleomagnetic secular variation to a geomagnetic field model. *Quaternary Science Reviews* 29, 2315–2324. <https://doi.org/10.1016/j.quascirev.2010.05.035>
- Barletta, F., St-Onge, G., Stoner, J.S., Lajeunesse, P., Locat, J., 2010b. A high-resolution Holocene paleomagnetic secular variation and relative paleointensity stack from eastern Canada. *Earth and Planetary Science Letters* 298, 162–174. <https://doi.org/10.1016/j.epsl.2010.07.038>
- Batterson, M., Liverman, D., 2010. Past and future sea-level change in Newfoundland and Labrador: Guidelines for policy and planning. *Current Research. Newfoundland and Labrador Department of Natural Resources Geological Survey, Report, 10-1.*
- Bellwald, B., Hjelstuen, B.O., Sejrup, H.P., Haflidason, H., 2016. Postglacial mass movements and depositional environments in a high-latitude fjord system – Hardangerfjorden, Western Norway. *Marine Geology* 379, 157–175. <https://doi.org/10.1016/j.margeo.2016.06.002>
- Blaauw, M., Christen, J.A., 2011. Flexible paleoclimate age-depth models using an autoregressive gamma process. *Bayesian Analysis* 6. <https://doi.org/10.1214/11-BA618>

- Blott, S.J., Pye, K., 2001. GRADISTAT: a grain size distribution and statistics package for the analysis of unconsolidated sediments. *Earth Surface Processes and Landforms* 26, 1237–1248. <https://doi.org/10.1002/esp.261>
- Broom, L.M., Campbell, D.C., Gosse, J.C., 2017. Investigation of a Holocene marine sedimentary record from Pond Inlet, northern Baffin Island, Nunavut 12. *Summary of Activities*, 93-104.
- Brouard, E., Roy, M., Godbout, P.-M., Veillette, J.J., 2021. A framework for the timing of the final meltwater outbursts from glacial Lake Agassiz-Ojibway. *Quaternary Science Reviews* 274, 107269. <https://doi.org/10.1016/j.quascirev.2021.107269>
- Brown, T., Reimer, K., Sheldon, Bell, T., Bentley, S., Pienitz, R., Gosselin, M., Blais, M., Carpenter, M., Estrada, E., Richerol, T., Kahlmeyer, E., Luque, S., Sjare, B., Fisk, A., Iverson, S., 2012. A first look at Nunatsiavut Kangidualuk ('fjord') ecosystems. In: *Nunavik and Nunatsiavut: from science to policy. An Integrated Regional Impact Study (IRIS) of climate change and modernization*. ArcticNet Inc., Quebec City, QC, 271-301. <https://doi.org/10.13140/2.1.4784.9924>
- Caron, M., Rochon, A., Montero-Serrano, J., St-Onge, G., 2019. Evolution of sea-surface conditions on the northwestern Greenland margin during the Holocene. *Journal of Quaternary Science* 34, 569–580. <https://doi.org/10.1002/jqs.3146>
- Channell, J.E.T., Hodell, D.A., 2013. Magnetic signatures of Heinrich-like detrital layers in the Quaternary of the North Atlantic. *Earth and Planetary Science Letters* 369–370, 260–270. <https://doi.org/10.1016/j.epsl.2013.03.034>
- Clark, P.U., Marshall, S.J., Clarke, G.K.C., Hostetler, S.W., Licciardi, J.M., Teller, J.T., 2001. Freshwater Forcing of Abrupt Climate Change During the Last Glaciation. *Science* 293, 283–287. <https://doi.org/10.1126/science.1062517>
- Couette, P. O., Ghienne, J. F., Lajeunesse, P., Van der Woerd, J., 2023. Climatic control on the retreat of the Laurentide Ice Sheet margin in easternmost Québec-Labrador (Canada) revealed by cosmogenic exposure dating. *Journal of Quaternary Science* 3525.
- Couette, P. O., 2022. *Déglaciation et dynamiques morpho-sédimentaires des systèmes juxtaglaciaires: exemple de la marge orientale de l'Inlandsis laurentidien depuis le Dernier maximum glaciaire*. PhD Thesis, Université Laval, 237 p.
- Croudace, I.W., Rothwell, R.G. (Eds.), 2015. *Micro-XRF Studies of Sediment Cores: Applications of a non-destructive tool for the environmental sciences*, 1st ed. 2015. ed, *Developments in Paleoenvironmental Research*. Springer Netherlands : Imprint: Springer, Dordrecht, vol 17, 668 p. <https://doi.org/10.1007/978-94-017-9849-5>

- Day, R., Fuller, M., Schmidt, V.A., 1977. Hysteresis properties of titanomagnetites: Grain-size and compositional dependence. *Physics of the Earth and Planetary Interiors* 13, 260–267. [https://doi.org/10.1016/0031-9201\(77\)90108-X](https://doi.org/10.1016/0031-9201(77)90108-X)
- Debret, M., Sebag, D., Desmet, M., Balsam, W., Copard, Y., Mourier, B., Susperrigui, A.-S., Arnaud, F., Bentaleb, I., Chapron, E., Lallier-Vergès, E., Winiarski, T., 2011. Spectrocolorimetric interpretation of sedimentary dynamics: The new “Q7/4 diagram.” *Earth-Science Reviews* 109, 1–19. <https://doi.org/10.1016/j.earscirev.2011.07.002>
- Deschamps, C., St-Onge, G., Montero-Serrano, J., Polyak, L., 2018. Chronostratigraphy and spatial distribution of magnetic sediments in the Chukchi and Beaufort seas since the last deglaciation. *Boreas* 47, 544–564. <https://doi.org/10.1111/bor.12296>
- Dietrich, P., Ghienne, J.-F., Normandeau, A., Lajeunesse, P., 2017. Reconstructing ice-margin retreat using delta morphostratigraphy. *Scientific Reports* 7, 16936. <https://doi.org/10.1038/s41598-017-16763-x>
- Duboc, Q., Lajeunesse, P., St-Onge, G., Moros, M., Perner, K., 2023. Holocene sedimentary sequences from Nachvak and Saglek Fjords (Northern Labrador) as a record of deglaciation of the Torngat Mountains and Hudson Bay. *Quaternary Science Reviews* 307, 108046. <https://doi.org/10.1016/j.quascirev.2023.108046>
- Duboc, Q., St-Onge, G., Lajeunesse, P., 2017. Sediment records of the influence of river damming on the dynamics of the Nelson and Churchill Rivers, western Hudson Bay, Canada, during the last centuries. *The Holocene* 27, 712–725. <https://doi.org/10.1177/0959683616670465>
- Duboc, Q., St-Onge, G., Moros, M., Lajeunesse, P., in prep. Three Lake Agassiz-Ojibway drainages events constrained in new high-resolution sedimentary records from the western Hudson Strait.
- Fitzhugh, W., 1973. Environmental Approaches to the Prehistory of the North. *Journal of the Washington Academy of Sciences*, 39-53.
- Funk, J. A., Von Dobeneck, T., Reitz, A., 2004. Integrated rock magnetic and geochemical quantification of redoxomorphic iron mineral diagenesis in Late Quaternary sediments from the Equatorial Atlantic. In : *The South Atlantic in the Late Quaternary: Reconstruction of material budgets and current systems*. Berlin, Heidelberg : Springer Berlin Heidelberg, 2004. pp. 237-260.
- Gauthier, M.S., Kelley, S.E., Hodder, T.J., 2020. Lake Agassiz drainage bracketed Holocene Hudson Bay Ice Saddle collapse. *Earth and Planetary Science Letters* 544, 116372. <https://doi.org/10.1016/j.epsl.2020.116372>

- Gregoire, L.J., Otto-Bliesner, B., Valdes, P.J., Ivanovic, R., 2016. Abrupt Bølling warming and ice saddle collapse contributions to the Meltwater Pulse 1a rapid sea level rise: North American MWP1a Contribution. *Geophysical Research Letters* 43, 9130–9137. <https://doi.org/10.1002/2016GL070356>
- Harris, D., Horwáth, W. R., Van Kessel, C., 2001. Acid fumigation of soils to remove carbonates prior to total organic carbon or carbon-13 isotopic analysis. *Soil Science Society of America Journal* 65, 1853-1856. <https://doi.org/10.2136/sssaj2001.1853>
- Hjelstuen, B.O., Haflidason, H., Sejrup, H.P., Lyså, A., 2009. Sedimentary processes and depositional environments in glaciated fjord systems — Evidence from Nordfjord, Norway. *Marine Geology* 258, 88–99. <https://doi.org/10.1016/j.margeo.2008.11.010>
- Jennings, A., Andrews, J., Pearce, C., Wilson, L., Ólfasdóttir, S., 2015. Detrital carbonate peaks on the Labrador shelf, a 13–7ka template for freshwater forcing from the Hudson Strait outlet of the Laurentide Ice Sheet into the subpolar gyre. *Quaternary Science Reviews* 107, 62–80. <https://doi.org/10.1016/j.quascirev.2014.10.022>
- Kamula, C.M., Kuzyk, Z.Z.A., Lobb, D.A., Macdonald, R.W., 2017. Sources and accumulation of sediment and particulate organic carbon in a subarctic fjard estuary:  $^{210}\text{Pb}$ ,  $^{137}\text{Cs}$ , and  $\delta^{13}\text{C}$  records from Lake Melville, Labrador. *Canadian Journal of Earth Sciences* 54, 993–1006. <https://doi.org/10.1139/cjes-2016-0167>
- Kamula, C.M., Macdonald, R.W., Kuzyk, Z.Z.A., 2020. Sediment and particulate organic carbon budgets of a subarctic estuarine fjard: Lake Melville, Labrador. *Marine Geology* 424, 106154. <https://doi.org/10.1016/j.margeo.2020.106154>
- King, G.A., 2007. A Standard Method for Evaluating Radiocarbon Dates of Local Deglaciation: Application to the Deglaciation History of Southern Labrador and Adjacent Québec. *Géographie Physique et Quaternaire* 39, 163–182. <https://doi.org/10.7202/032600ar>
- Korte, M., Constable, C., Donadini, F., Holme, R., 2011. Reconstructing the Holocene geomagnetic field. *Earth and Planetary Science Letters* 312, 497–505. <https://doi.org/10.1016/j.epsl.2011.10.031>
- Kylander, M.E., Ampel, L., Wohlfarth, B., Veres, D., 2011. High-resolution X-ray fluorescence core scanning analysis of Les Echets (France) sedimentary sequence: new insights from chemical proxies. *Journal of Quaternary Science* 26, 109–117. <https://doi.org/10.1002/jqs.1438>

- Lajeunesse, P., St-Onge, G., 2008. The subglacial origin of the Lake Agassiz–Ojibway final outburst flood. *Nature Geoscience* 1, 184–188.  
<https://doi.org/10.1038/ngeo130>
- Lamb, A.L., Wilson, G.P., Leng, M.J., 2006. A review of coastal palaeoclimate and relative sea-level reconstructions using  $\delta^{13}\text{C}$  and C/N ratios in organic material. *Earth-Science Reviews* 75, 29–57. <https://doi.org/10.1016/j.earscirev.2005.10.003>
- Lisé-Pronovost, A., St-Onge, G., Brachfeld, S., Barletta, F., Darby, D., 2009. Paleomagnetic constraints on the Holocene stratigraphy of the Arctic Alaskan margin. *Global and Planetary Change* 68, 85–99.  
<https://doi.org/10.1016/j.gloplacha.2009.03.015>
- Liu, Q., Roberts, A.P., Larrasoana, J.C., Banerjee, S.K., Guyodo, Y., Tauxe, L., Oldfield, F., 2012. Environmental magnetism: Principles and applications. *Reviews of Geophysics* 50, RG4002. <https://doi.org/10.1029/2012RG000393>
- Meyers, P.A., 1997. Organic geochemical proxies of paleoceanographic, paleolimnologic, and paleoclimatic processes. *Organic Geochemistry* 27, 213–250.  
[https://doi.org/10.1016/S0146-6380\(97\)00049-1](https://doi.org/10.1016/S0146-6380(97)00049-1)
- Moros, M., Lloyd, J.M., Perner, K., Krawczyk, D., Blanz, T., de Vernal, A., Ouellet-Bernier, M.-M., Kuijpers, A., Jennings, A.E., Witkowski, A., Schneider, R., Jansen, E., 2016. Surface and sub-surface multi-proxy reconstruction of middle to late Holocene palaeoceanographic changes in Disko Bugt, West Greenland. *Quaternary Science Reviews* 132, 146–160.  
<https://doi.org/10.1016/j.quascirev.2015.11.017>
- Mulder, T., E. Chapron, 2011. Flood deposits in continental and marine environments: Character and significance, in R. M. Slatt and C. Zavala, eds., *Sediment transfer from shelf to deep water—Revisiting the delivery system: AAPG Studies in Geology* 61, 1–30.
- Normandeau, A., MacKillop, K., Macquarrie, M., Richards, C., Bourgault, D., Campbell, D.C., Maselli, V., Philibert, G., Clarke, J.H., 2021. Submarine landslides triggered by iceberg collision with the seafloor. *Nature Geoscience* 14, 599–605.
- Nijhuis, A. G., 2013. Fluvio-deltaic response to relative sea-level fall: A case study of the Goose River delta, Labrador, Canada (Doctoral dissertation, Boston College), 66 p.

- Occhiotti, S., Parent, M., Lajeunesse, P., Robert, F., Govare, É., 2011. Late Pleistocene–Early Holocene Decay of the Laurentide Ice Sheet in Québec–Labrador, in: *Developments in Quaternary Sciences*. Elsevier, pp. 601–630. <https://doi.org/10.1016/B978-0-444-53447-7.00047-7>
- Poiré, A.G., Lajeunesse, P., Normandeau, A., Francus, P., St-Onge, G., Nzekwe, O.P., 2018. Late-Quaternary glacial to postglacial sedimentation in three adjacent fjord-lakes of the Québec North Shore (eastern Canadian Shield). *Quaternary Science Reviews* 186, 91–110. <https://doi.org/10.1016/j.quascirev.2018.02.013>
- Ramnarine, R., Voroney, R.P., Wagner-Riddle, C., Dunfield, K.E., 2011. Carbonate removal by acid fumigation for measuring the  $\delta^{13}\text{C}$  of soil organic carbon. *Canadian Journal of Soil Science* 91, 247–250. <https://doi.org/10.4141/cjss10066>
- Reaves, C.M., 1986. Organic matter metabolizability and calcium carbonate dissolution in nearshore marine muds. *Journal of Sedimentary Research*, 56 486–494.
- Richerol, T., Fréchette, B., Rochon, A., Pienitz, R., 2016. Holocene climate history of the Nunatsiavut (northern Labrador, Canada) established from pollen and dinoflagellate cyst assemblages covering the past 7000 years. *The Holocene* 26, 44–60. <https://doi.org/10.1177/0959683615596823>
- Roberts, A.P., Cui, Y., Verosub, K.L., 1995. Wasp-waisted hysteresis loops: Mineral magnetic characteristics and discrimination of components in mixed magnetic systems. *Journal of Geophysical Research: Solid Earth* 100, 17909–17924. <https://doi.org/10.1029/95JB00672>
- Roberts, A.P., Tauxe, L., Heslop, D., Zhao, X., Jiang, Z., 2018. A Critical Appraisal of the “Day” Diagram. *Journal of Geophysical Research: Solid Earth* 123, 2618–2644. <https://doi.org/10.1002/2017JB015247>
- Rohling, E.J., Pälike, H., 2005. Centennial-scale climate cooling with a sudden cold event around 8,200 years ago. *Nature* 434, 975–979. <https://doi.org/10.1038/nature03421>
- Ross, M., Utting, D.J., Lajeunesse, P., Kosar, K.G.A., 2012. Early Holocene deglaciation of northern Hudson Bay and Foxe Channel constrained by new radiocarbon ages and marine reservoir correction. *Quaternary Research* 78, 82–94. <https://doi.org/10.1016/j.yqres.2012.03.001>
- Rothwell, R.G., Hoogakker, B., Thomson, J., Croudace, I.W., Frenz, M., 2006. Turbidite emplacement on the southern Balearic Abyssal Plain (western Mediterranean Sea) during Marine Isotope Stages 1–3: an application of ITRAX XRF scanning of sediment cores to lithostratigraphic analysis. *SP* 267, 79–98. <https://doi.org/10.1144/GSL.SP.2006.267.01.06>

- Shaw, J., Taylor, R.B., Forbes, D.L., Ruz, M.H., Solomon, S., 1998. Sensitivity of the coasts of Canada to sea-level rise. *GSC Bulletin* 505, 1-79.  
<https://doi.org/10.4095/210075>
- Stoner, J.S., Channell, J.E.T., Hillaire-Marcel, C., 1996. The magnetic signature of rapidly deposited detrital layers from the Deep Labrador Sea: Relationship to North Atlantic Heinrich layers. *Paleoceanography* 11, 309–325.  
<https://doi.org/10.1029/96PA00583>
- Stoner, J.S., Channell, J.E.T., Mazaud, A., Strano, S.E., Xuan, C., 2013. The influence of high-latitude flux lobes on the Holocene paleomagnetic record of IODP Site U1305 and the northern North Atlantic: Paleomagnetic Record of the N. Atlantic. *Geochemistry, Geophysics, Geosystems* 14, 4623–4646.  
<https://doi.org/10.1002/ggge.20272>
- Stoner, J.S., Jennings, A., Kristjánssdóttir, G.B., Dunhill, G., Andrews, J.T., Hardardóttir, J., 2007. A paleomagnetic approach toward refining Holocene radiocarbon-based chronologies: Paleoceanographic records from the north Iceland (MD99-2269) and east Greenland (MD99-2322) margins. *Paleoceanography* 22, 1-23.  
<https://doi.org/10.1029/2006PA001285>
- Stoner, J.S., St-Onge, G., 2007. Chapter Three Magnetic Stratigraphy in *Paleoceanography: Reversals, Excursions, Paleointensity, and Secular Variation*, in: *Developments in Marine Geology*. Elsevier, 99–138.  
[https://doi.org/10.1016/S1572-5480\(07\)01008-1](https://doi.org/10.1016/S1572-5480(07)01008-1)
- St-Onge, G., Hillaire-Marcel, C., 2001. Isotopic constraints of sedimentary inputs and organic carbon burial rates in the Saguenay Fjord, Quebec. *Marine Geology* 176, 1–22. [https://doi.org/10.1016/S0025-3227\(01\)00150-5](https://doi.org/10.1016/S0025-3227(01)00150-5)
- St-Onge, G., Mulder, T., Francus, P., Long, B., 2007. Chapter Two Continuous Physical Properties of Cored Marine Sediments, in: *Developments in Marine Geology*. Elsevier, 63–98. [https://doi.org/10.1016/S1572-5480\(07\)01007-X](https://doi.org/10.1016/S1572-5480(07)01007-X)
- St-Onge, G., Mulder, T., Piper, D.J.W., Hillaire-Marcel, C., Stoner, J.S., 2004. Earthquake and flood-induced turbidites in the Saguenay Fjord (Québec): a Holocene paleoseismicity record. *Quaternary Science Reviews* 23, 283–294.  
<https://doi.org/10.1016/j.quascirev.2003.03.001>
- Syvitski, J., Andrews, J.T., Schafer, C.T., Stravers, J.A., 2022. Sediment fill of Baffin Island fjords: Architecture and rates. *Quaternary Science Reviews* 284, 107474.  
<https://doi.org/10.1016/j.quascirev.2022.107474>



- Syvitski, J.P.M., Lee, H.J., 1997. Postglacial sequence stratigraphy of Lake Melville, Labrador. *Marine Geology* 143, 55–79. [https://doi.org/10.1016/S0025-3227\(97\)00090-X](https://doi.org/10.1016/S0025-3227(97)00090-X)
- Syvitski, J.P.M., Shaw, J., 1995. Chapter 5 Sedimentology and Geomorphology of Fjords, in: *Developments in Sedimentology*. Elsevier, pp. 113–178. [https://doi.org/10.1016/S0070-4571\(05\)80025-1](https://doi.org/10.1016/S0070-4571(05)80025-1)
- Tauxe, L., Mullender, T.A.T., Pick, T., 1996. Potbellies, wasp-waists, and superparamagnetism in magnetic hysteresis. *Journal of Geophysical Research* 101, No. B1, 571-583.
- Thomas, E.R., Wolff, E.W., Mulvaney, R., Steffensen, J.P., Johnsen, S.J., Arrowsmith, C., White, J.W.C., Vaughn, B., Popp, T., 2007. The 8.2ka event from Greenland ice cores. *Quaternary Science Reviews* 26, 70–81. <https://doi.org/10.1016/j.quascirev.2006.07.017>
- Trottier, A., Lajeunesse, P., Gagnon-Poiré, A., Francus, P., 2020. Morphological signatures of deglaciation and postglacial sedimentary processes in a deep fjord-lake (Grand Lake, Labrador). *Earth Surface Processes and Landforms* 45, 928–947. <https://doi.org/10.1002/esp.4786>
- Trottier, A.-P., Brouard, E., Lajeunesse, P., Normandeau, A., 2021. The morphosedimentary record of glacial to postglacial environmental changes in fjord-lake Mékinac and adjacent areas (southeastern Canadian Shield). *Geomorphology* 376, 107565. <https://doi.org/10.1016/j.geomorph.2020.107565>
- Ullman, D.J., Carlson, A.E., Hostetler, S.W., Clark, P.U., Cuzzone, J., Milne, G.A., Winsor, K., Caffee, M., 2016. Final Laurentide ice-sheet deglaciation and Holocene climate-sea level change. *Quaternary Science Reviews* 152, 49–59. <https://doi.org/10.1016/j.quascirev.2016.09.014>
- Vacchi, M., Engelhart, S.E., Nikitina, D., Ashe, E.L., Peltier, W.R., Roy, K., Kopp, R.E., Horton, B.P., 2018. Postglacial relative sea-level histories along the eastern Canadian coastline. *Quaternary Science Reviews* 201, 124–146. <https://doi.org/10.1016/j.quascirev.2018.09.043>
- Vickers, K.J., Ward, B.C., Utting, D.J., Telka, A.M., 2010. Deglacial reservoir age and implications, Foxe Peninsula, Baffin Island. *Journal of Quaternary Science* 25, 1338–1346. <https://doi.org/10.1002/jqs.1419>
- Vilks, G., Deonaraine, B., Winters, G., 1987. Late Quaternary marine geology of Lake Melville, Labrador. Geological Survey of Canada, paper No. 87, 1-50. <https://doi.org/10.4095/122409>

Vilks, G., Mudie, P.J., 1983. Evidence for Postglacial Paleoceanographic and Paleoclimatic Changes in Lake Melville, Labrador, Canada. *Arctic and Alpine Research* 15, 307. <https://doi.org/10.2307/1550827>

Weiser, J., Titschack, J., Kienast, M., McCave, I.N., Lochte, A.A., Saini, J., Stein, R., Hebbeln, D., 2021. Atlantic water inflow to Labrador Sea and its interaction with ice sheet dynamics during the Holocene. *Quaternary Science Reviews* 256, 106833. <https://doi.org/10.1016/j.quascirev.2021.106833>

## CONCLUSION GÉNÉRALE

Dans cette thèse, l'étude de séquences sédimentaires à haute résolution a permis de répondre à l'objectif principal qui était de préciser la chronostratigraphie des dépôts et processus sédimentaires associés à la déglaciation de l'Inlandsis laurentidien et de la subséquente transition postglaciaire sur la marge continentale le long du Labrador et du nord du Québec. Plus précisément, l'analyse multi-traceurs de cinq carottes sédimentaires, combinée à des chronologies précises basées sur 69 âges  $^{14}\text{C}$  et dans certains cas à des données géophysiques, a permis de mettre en évidence certaines étapes de l'évolution environnementale de trois secteurs différents dans un contexte de déglaciation. Chacun des secteurs en question a fait l'objet d'un chapitre de la thèse.

Le **chapitre 1**, qui a consisté en l'analyse des séquences sédimentaires des fjords Nachvak et Saglek, a permis de mettre en valeur 1) une déglaciation asynchrone des deux fjords, le recul du glacier du fjord Saglek ayant été retardé par l'effet tampon de la baie de Saglek : son bassin principal se serait libéré de sa glace environ 2000 ans après celui du fjord Nachvak ; 2) d'importants dépôts de mouvements de masse probablement causés par une activité sismique associée au rebond glacio-isostatique ; 3) la présence de couches riches en carbonates détritiques dans les deux fjords et d'une couche rouge diluée dans le fjord Nachvak, toutes associées aux derniers événements de déglaciation de la baie d'Hudson ; et 4) une fin de transition postglaciaire vers 6,3 cal ka BP qui se caractérise par des conditions devenant propices à la dissolution des minéraux ferrimagnétiques dans le sédiment, particulièrement dans les sédiments déposés entre 6,3 et 3,8 cal ka BP qui devaient être plus riches en matière organique.

Le **chapitre 2** s'est concentré sur les carottes récupérées dans les deux bassins à l'ouest du détroit d'Hudson. Ces deux carottes, 20 et 24, contiennent les mêmes indicateurs sédimentaires de déglaciation avec une résolution différente, mais particulièrement élevée

pour la carotte 20 du bassin Ouest. La comparaison et la chronologie de ces carottes ont permis d'identifier la séquence d'événements suivante : 1) un événement de drainage sous-glaciaire du LAO successif à l'ouverture de la mer de Tyrrell et qui aurait déposé la couche rouge ici datée de  $8,67 \pm 0,15$  cal ka BP ; 2) l'agrandissement de la mer de Tyrrell formant une importante débâcle d'icebergs identifiée par une couche riche en IRDs dans les carottes ; 3) une période de relative stabilité (avec possibles réavancées) de la marge glaciaire comme en témoigne une séquence de sédiments très fins avec peu d'IRDs ; 4) la vidange finale du LAO accompagnée de la chute du barrage de glace de la baie d'Hudson, formant un double pic d'IRDs et de carbonates détritiques dans les séquences sédimentaires et daté entre 8,21 et 8,03 cal ka BP. Ce chapitre a également pu mettre en valeur certains aspects de la complexité de l'utilisation de l'âge réservoir tels qu'une différence de  $\Delta R$  entre mollusques et foraminifères contemporains, ou l'influence d'une marge glaciaire très proximale sur l'effet réservoir.

Finalement, le **chapitre 3** détaille une séquence sédimentaire du lac Melville dont la chronologie a été complétée à l'aide de données paléomagnétiques de très bonne qualité. Les données sédimentaires ont permis de mieux cerner l'évolution de l'environnement glaciomarin, puis postglaciaire du secteur et indiquent que : 1) le nord du lac était déjà déglacé pendant l'événement de 9,3 ka, et probablement pendant celui de 10,2 ka ; 2) le recul de la marge glaciaire dans les terres marqué par la moraine de Sebaskachu s'est accompagné d'une baisse drastique du taux de sédimentation ; 3) l'influence des eaux marines était à son maximum entre 8,5 et 6,0 cal ka BP, puis a progressivement diminué avec la diminution de la profondeur du seuil à l'embouchure du lac ; 4) l'événement froid de 8,2 ka a temporairement réduit l'apport de matière organique, laissant une couche de sédiments bien oxygéné comparativement au reste de la carotte dont le sédiment riche en sulfures s'est oxydé seulement à l'ouverture de celle-ci ; 5) la présence d'un gros IRD carbonaté daté de la vidange finale du LAO pourrait laisser présager d'un acheminement d'iceberg(s) depuis la baie d'Hudson jusque dans le lac Melville.

Ensemble, ces trois chapitres ont permis de répondre aux trois grands objectifs de la thèse visant à investiguer 1) le retrait de la marge de l'Inlandsis laurentidien, 2) les étapes de déglaciation de la baie d'Hudson, et enfin 3) la dynamique sédimentaire des différents secteurs au cours de la transition postglaciaire.

### **Retrait de l'Inlandsis laurentidien**

Le premier objectif était de préciser l'évolution du retrait de la marge glaciaire de l'Inlandsis laurentidien autour du Québec et du Labrador à partir de l'étude des séquences sédimentaires des bassins des différents secteurs. Au Labrador, les études montraient déjà que le retrait de la marge glaciaire a été cadencé par un réchauffement ponctué par les périodes froides du Dryas récent et de 10,3, 9,3 et 8,2 ka au cours desquelles la marge a stagné, voir réavancé (e.g., Gallagher, 1989 ; Clark et al., 2003 ; Ullman et al., 2016 ; Couette et al., sous presse). Les séquences sédimentaires de cette étude-ci apportent de nouvelles indications sur la position de la marge aux différentes périodes. Ainsi, les profils acoustiques ont permis de visualiser l'épaisseur de sédiments glaciomarins en dessous des carottes prélevées et datées, et de proposer une période de déglaciation des bassins correspondants. Dans le cas des fjords Nachvak et Saglek, la structure des dépôts glaciomarins suggère des stabilisations successives des courants glaciaires au niveau des seuils dont la plupart sont des moraines frontales formées à ce moment-là. Pendant le Bolling-Allerod, seul le fjord Nachvak a subi une déglaciation, d'ailleurs plutôt précoce par rapport au reste de la côte (Occhietti et al., 2011 ; Dalton et al., 2020). Le glacier s'est probablement retrouvé ancré au seuil Ivitak pendant le Dryas récent, au moment où le glacier du fjord Saglek a atteint son dernier maximum en formant les moraines de Saglek. Après le Dryas récent, la marge glaciaire a rapidement reculé dans le fjord Saglek et dans le secteur du lac Melville. Au cours de l'événement froid de 10,3 ka ayant causé la réavancée de Gold Cove dans le détroit d'Hudson, la glace s'est arrêtée aux seuils de Kogarsok et de Ugjuktok dans les fjords Nachvak et Saglek respectivement. Dans les bras secondaires des fjords (i.e., bras de Tallek dans Nachvak et complexe du bras Ouest dans Saglek), les courants glaciaires avaient déjà reculé plus loin dans les vallées. Dans le lac Melville, la position est incertaine, mais

l'épaisseur de sédiments sous-jacents à la carotte 13 laisse penser que le site en question était déjà déglacé à ce moment. Quoiqu'il en soit, les chronologies des carottes indiquent que tous les secteurs à l'étude étaient déglacés pendant l'événement de 9,3 ka. La marge glaciaire était cependant proche du bassin Sud-ouest du détroit d'Hudson, de même que du bassin où la carotte 13 du lac Melville a été échantillonnée : les structures sédimentaires aux bases des carottes témoignent en effet de milieux de dépôt plus dynamiques. Par la suite, la marge glaciaire a subi un recul important de façon générale jusqu'à l'événement de 8,2 ka, ou du moins jusqu'au début du refroidissement vers 8,6 cal ka BP. Dans le lac Melville, la marge a reculé jusqu'à former la moraine de Sebaskachu à l'ouest du lac vers  $8,4 \pm 0,6$  cal ka BP (Couette et al., 2023).

Ainsi, cette thèse vient corroborer les études se focussant sur le recul de la marge de l'Inlandsis laurentidien dans le lac Melville et les fjords Saglek et Nachvak (e.g., Gallagher, 1989 ; Syvitski & Lee, 1997 ; Clark et al., 2003 ; Couette et al., sous presse). Elle démontre cependant que le fjord Nachvak s'est déglacé particulièrement tôt. De plus, le recul asynchrone de la glace entre les fjords Nachvak et Saglek met en lumière l'influence de la topographie et de la bathymétrie dans les systèmes de fjords échancrés, de même qu'observé dans l'étude de Couette (2022). L'ouverture directe du fjord Nachvak sur la marge continentale aurait favorisé l'infiltration des eaux marines sous la glace et accéléré le vèlage, tandis que les îles et seuils de la baie de Saglek ont ralenti le processus dans le fjord Saglek, le laissant complètement englacé au Dryas récent.

Par ailleurs, en baie d'Hudson, une vidange finale du LAO à partir de 8,2 cal ka BP implique que le barrage de glace de la baie d'Hudson a survécu jusque-là, ce qui remet en question les reconstructions passées du recul de la marge qui proposaient une séparation des dômes de Keewatin et du Labrador avant 8,5 cal ka BP (Dyke et al., 2004 ; Dalton et al., 2020). L'enchaînement des événements est plus détaillé dans la réponse au deuxième objectif, ci-dessous.

## Déglaciation de la baie d'Hudson

Le deuxième objectif de la thèse était d'identifier et distinguer les marqueurs sédimentaires des étapes de la déglaciation de la baie d'Hudson et préciser leur chronologie. La réalisation de cet objectif devait normalement être atteinte seulement avec l'étude des séquences du détroit d'Hudson. Cependant, les carottes des fjords contenaient également des marqueurs d'événements de déglaciation de la baie d'Hudson, renforçant ainsi la chronologie de ceux-ci.

Les marqueurs sédimentaires identifiés consistent en la couche rouge du détroit d'Hudson, des événements d'IRDs et des pics de concentration de carbonates détritiques. La couche rouge a été observée dans les carottes 20 (bassin Ouest), 24 (bassin Sud-Ouest) et 28 (Fjord Nachvak) et datée à 8,67, 8,72 et 8,64 cal ka BP respectivement. La date de  $8,67 \pm 0,15$  cal ka BP est préférentiellement considérée, car la chronologie de la carotte 20 est plus précise. L'absence d'IRDs dans la couche rouge indique qu'elle n'est pas associée à l'ouverture de la mer de Tyrrell comme proposé par Jennings et al. (2015), mais plutôt à une vidange sous-glaciaire du LAO correspondant à celle suggérée par Gauthier et al., (2020). Deux événements d'IRDs sont particulièrement marqués dans la carotte 20 et également enregistrés dans la 24. Le plus ancien, non-corrélé à une hausse des carbonates détritiques, dépeindrait un vêlage important d'icebergs dans la mer de Tyrrell. Le second événement d'IRDs n'est autre que le double pic de carbonates détritiques (DDCP). Cette couche trouve un équivalent dans la carotte 28, bien que réduite à un seul pic, et est très bien corrélée au DCP7 de la carotte MD99-2236 échantillonnée plus au sud sur la marge du Labrador, juste devant le bras de mer Hamilton au bout duquel est situé le lac Melville (Jennings et al., 2015). Cette couche met très bien en valeur les deux événements de drainage marquant la fin du LAO et du barrage de glace qui le retenait, et séparés de quelques décennies, tel que suggéré par Godbout et al. (2019), l'événement final étant plus important. Par ailleurs, la période entre les deux événements d'IRDs se caractérise par le dépôt de sédiments particulièrement fins dans les deux bassins du détroit d'Hudson, mais également par une diminution importante (et temporaire) de l'export de carbonates détritiques vers les fjords. Ceci traduit

une période relativement calme d'un point de vue d'événements de fonte ou de vêlage d'icebergs dans le système de la baie d'Hudson, et s'étendant approximativement de 8,55 à 8,2 cal ka BP. Cette période de stabilisation est bien corrélée à un début de refroidissement dès 8,6 ka cal BP (Rohling & Pälike, 2005) possiblement responsable de la réavancée glaciaire de Cochrane vers 8,45 cal ka BP précédant la vidange du LAO (Godbout et al., 2019) et à l'exposition de la moraine de Sebaskachu vers  $8,4 \pm 0,6$  cal ka BP (Couette et al., sous presse).

De plus, la présente étude, en particulier la haute résolution de la carotte 20, permet d'affirmer que la dernière vidange du LAO a bien eu lieu aux alentours de 8,2-8,1 plutôt que 8,55-8,45 cal ka BP. Ces enregistrements sédimentaires viennent donc corroborer les études de Jennings et al., (2015), Gauthier et al. (2020) et Brouard et al. (2021). Il n'y aurait donc pas eu de délai entre l'événement final et le début de l'événement froid de 8,2 ka qu'il a déclenché.

Par ailleurs, il est important de noter que les indicateurs sédimentaires n'ont pas tout à fait la même signature d'un secteur à l'autre. C'est le cas par exemple de la couche rouge, qui s'accompagne d'un pic de Ca/Ti négatif dans les bassins du détroit d'Hudson et positif dans la mer du Labrador. Ce contraste s'explique à la fois par la différence de concentration de sédiment rouge (pauvre en Ca) et par les différences de sources sédimentaires locales, beaucoup plus riches en Ca dans le système de la baie d'Hudson que dans la mer du Labrador. De tels facteurs sont donc importants à considérer lorsque l'on cherche à reconnaître les mêmes indicateurs pour identifier des événements d'un secteur à un autre.

### **Dynamique sédimentaire**

Le troisième objectif consistait à caractériser et comparer la dynamique sédimentaire des différents environnements physiographiques de la marge continentale pendant la transition postglaciaire. Pour ce faire, il est important de se rappeler que les sites de carottage ne correspondent pas aux zones d'épaisseur maximale de la séquence sédimentaire, en particulier dans le lac Melville. Cependant, les données renseignent sur l'importance relative

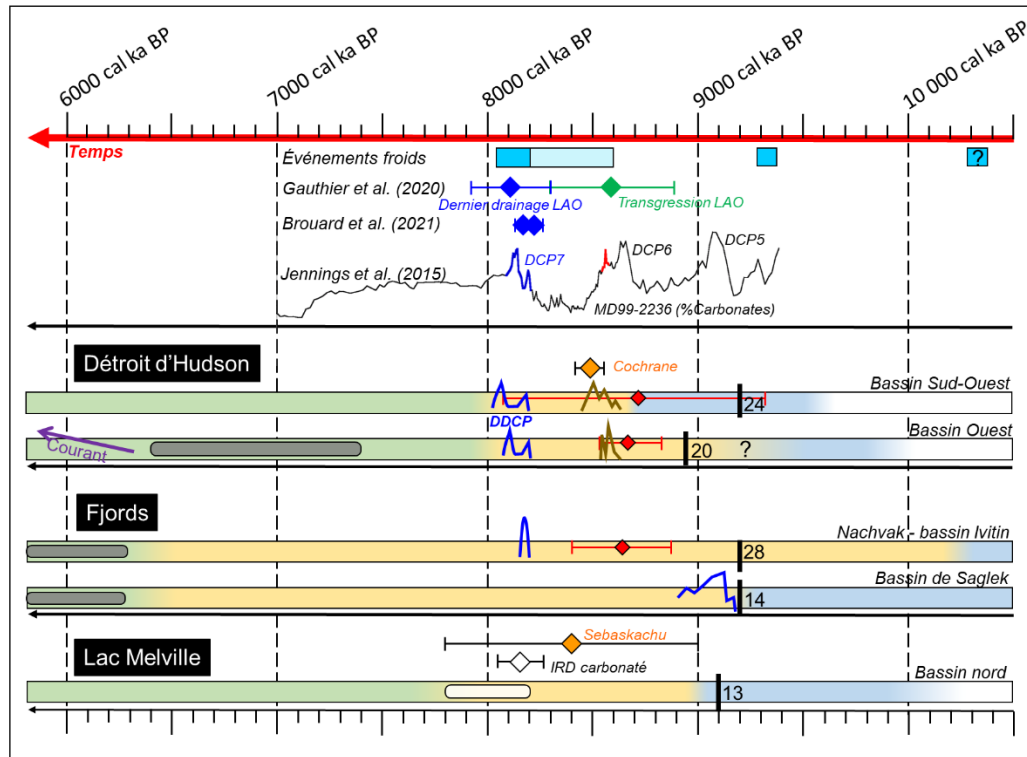


des dépôts glaciomarins, paraglaciacaires et postglaciacaires dans chaque secteur. Notez que les sédiments de contact glaciaire ne sont pas considérés dans cette analyse. Ainsi, les sédiments glaciomarins représentent environ 80% de l'épaisseur de sédiments déposés après le retrait des glaces dans le lac Melville et dans le bassin Ouest du détroit d'Hudson, 70% dans le bassin Sud-Ouest et seulement 30-35% dans les fjords Nachvak et Saglek. Cette faible proportion dans les fjords est due à la présence des MMDs et autres couches déposées rapidement qui représentent généralement 50% de leur séquence, contre à peine 10% dans le bassin du lac Melville et une infime proportion dans les bassins du détroit d'Hudson. Ces proportions contrastées reflètent les différents environnements physiographiques étudiés, les forts dénivelés et la proximité des parois des fjords étant plus propices aux mouvements de masse subaériens et subaquatiques (Stoker et al., 2010 ; Bellwald et al., 2019). L'occurrence possible de séismes générés par le réajustement isostatique expliquerait aussi l'ubiquité d'épais MMDs dans les différents bassins des fjords. Autre processus paraglaciacaire, la remobilisation de sédiments glaciaires par les eaux fluviales joue également un rôle important, en particulier dans le lac Melville qui a un grand bassin de drainage et est entouré de zones plus planes. Bien qu'il soit plus difficile d'identifier directement les dépôts associés à ces processus fluviaux, le haut taux de sédimentation de l'unité 2 de la carotte 13 est probablement corrélé à une importante remobilisation de sédiments.

D'un autre côté, l'évolution des taux de sédimentation des différents bassins reflète également une diversité de processus affectant la sédimentation, aussi bien pendant qu'après la transition postglaciaire. À l'exception de la carotte 24 du bassin Sud-Ouest, les séquences suivent la classique tendance à la réduction des apports sédimentaires avec la transition postglaciaire. Celle-ci s'explique notamment par la réduction, avec le temps, de l'influence glaciaire et de la disponibilité du matériel pour les processus paraglaciacaires. Cette tendance semble plus marquée dans le lac Melville que dans les fjords : cela peut s'expliquer par une végétalisation plus importante et une topographie plus plane au sud du Labrador, limitant l'érosion postglaciaire comparativement aux fjords encaissés du nord du Labrador. Par ailleurs, les deux carottes du détroit d'Hudson offrent un contraste saisissant entre une réduction drastique des apports sédimentaire dans la carotte 20 et une augmentation dans la

carotte 24. Cette différence reflète l'importance des courants de fond dans ce secteur. En effet, une augmentation des courants dans le bassin Ouest a engendré une déposition préférentielle et une augmentation de la granulométrie visible dans la carotte 20, jusqu'à former un pavage causant un hiatus temporel. À l'inverse, la carotte 24 a été échantillonnée dans une zone plus calme où les sédiments se concentrent, à proximité d'une zone de courant formant également un pavage visible et une dérive sédimentaire bien visible sur les profils de sous-surface. L'évolution des conditions océanographiques jouent ainsi un rôle majeur dans la sédimentation de la marge continentale, et ce même dans les bassins profonds.

Pour terminer, les données permettent de proposer une approximation de la durée de la transition postglaciaire dans chaque secteur, du moins pour la fin de celle-ci (Figure 40). Dans le nord du lac Melville, la transition se produit pendant l'éloignement de la marge glaciaire entre les événements de 9,3 et 8,2 ka. Elle se caractérise par une sédimentation contrôlée surtout par la remobilisation paraglaciale de sédiments, en particulier par les eaux fluviales, combinée à des apports riches en matière organique. Dans les bassins principaux des fjords du Labrador, le début de la transition correspond à la transition entre les unités A6 et A7. Cette transition est nette dans le bassin Ivitin du fjord Nachvak et se produit avant l'événement de 9,3 ka, possiblement à la fin de l'événement de 10,3 ka. C'est en effet à ce moment que la glace a quitté les bassins à l'ouest du fjord, limitant la sédimentation glaciomarine (Gallagher, 1989). Dans le fjord Saglek, encore une fois, cette transition débute plus tard, après l'événement froid de 9,3 ka. Cependant, la lentille d'eau de fonte qui a persisté dans le nord de la mer du Labrador (et qui a contribué à acheminer des carbonates détritiques jusque-là) a retardé la fin de la transition, qui se produit plutôt vers 6,5-6,3 cal ka BP dans les deux fjords. Cette transition est corrélée au début tardif du maximum thermal Holocène dans la région (Kaufman et al., 2004). Finalement, dans le détroit d'Hudson, la transition est plus floue mais semble se terminer après l'événement de 8,2 ka, au moment où commence une anomalie de susceptibilité magnétique dans le bassin Ouest.



**Figure 40.** Figure synthèse comparant les résultats des différents secteurs entre eux et avec d'autres études, en fonction du temps. Les événements froids de 8,2, 9,3 et 10,3 ka y sont indiqués par les rectangles turquoise, de même que le refroidissement général de 8,6 ka en bleu pâle (rectangle bleu pâle ; Rohling & Pälike, 2005). Les événements de drainage final du LAO sont également indiqués (losanges bleus ; Gauthier et al., 2020 ; Brouard et al., 2021) de même que l'épisode de transgression marine du LAO (losange vert ; Gauthier et al., 2020) et l'évolution du pourcentage total de carbonates de la carotte MD99-2236, avec les pics de carbonates détritiques (DCP ; Jennings et al., 2015). Les barres colorées en dégradés représentent les séquences sédimentaires des cinq bassins, réparties selon les trois zones (vert = postglaciaire ; jaune = transition ; bleu = glaciomarin ; blanc = zone englacée). Les barres noires verticales indiquent la base de la carotte de chaque bassin, avec son numéro. Les petites courbes bleues et brunes représentent les pics de carbonates détritiques et d'IRDs, respectivement, tandis que le losange rouge représente le dépôt de la couche rouge. L'avancée de Cochrane et l'exposition de la moraine de Sebaskachu sont également indiquées (losanges orange) de même que l'IRD carbonaté de la carotte 13. Finalement, les barres grises et blanches représentent des épisodes de forte et faible productivité primaire, respectivement, causant des changements de propriétés magnétiques dans les carottes respectives.

## Limitations et perspectives

Le cœur de la thèse étant basé sur la chronologie des carottes sédimentaires, il est crucial de considérer l'importance de la calibration des âges  $^{14}\text{C}$  et en particulier, comme mentionné dans le chapitre 2, les potentielles variations temporelles de l'âge réservoir. En effet, celui-ci peut varier de plusieurs centaines d'années, et ce en peu de temps, du fait de variations d'influence des eaux de fontes appauvries en  $^{14}\text{C}$  ou de changements dans la stratification. De plus, les données présentées dans le chapitre 2 montrent la sensibilité de l'âge réservoir au matériel utilisé. En effet, en utilisant un même  $\Delta R$ , les coquilles de mollusques se trouvent à être 200 à 300 ans plus jeunes que les foraminifères contemporains, en particulier durant la période postglaciaire. De telles variations peuvent causer de mauvaises interprétations chronostratigraphiques, en particulier pour la série d'événements de déglaciation de la baie d'Hudson qui sont séparés de quelques siècles à peine. Ceci dit, l'identification des deux mêmes événements (couche rouge et DDCP) dans les carottes 20 et 24 avec un écart temporel différent d'une carotte à l'autre entre lesdits événements donne une opportunité d'évaluer les variations temporelles d'âge réservoir causées par des changements de conditions glaciomarines. Ainsi, des études visant à comparer les âges des mêmes événements de déglaciation dans différents secteurs peuvent permettre d'améliorer notre compréhension des changements spatiotemporels de l'âge réservoir.

D'autre part, la fin de la transition postglaciaire est suivie d'anomalies de susceptibilité magnétique dans les carottes des fjords Nachvak et Saglek et des bassins de la baie d'Hudson. Ces anomalies sont parfois assez prononcées et sont corrélées à des données paléomagnétiques de mauvaise qualité ( $\text{MAD} > 15^\circ$ , inclinaison loin de celle du GAD, etc.), ce qui complexifie les reconstitutions des variations du champ magnétique à l'Holocène (Stoner & St-Onge, 2007) et empêche d'utiliser cette méthode pour compléter les modèles d'âges en cas de manque de matériel directement datable. La dissolution des minéraux ferrimagnétiques semble être la cause de ces anomalies, comme proposé dans le chapitre 1. Un tel phénomène est connu pour se produire lors de la diagénèse précoce dans les milieux à haut taux de sédimentation, où les bactéries réduisent les oxydes de fer pour consommer la

matière organique présente en grandes quantités dans les sédiments postglaciaires (e.g., Liu et al., 2004; Roberts, 2015). Ceci dit, les anomalies de  $k_{LF}$  des carottes 14 et 28 semblent particulièrement prononcées à certaines profondeurs, comme indiqué par le  $Fe/k_{LF}$ . Il en va de même pour une autre carotte collectée dans le chenal Esquiman (entre le Québec et Terre-Neuve) durant la campagne MSM46 : cette carotte (MSM46-11-11-GC) présente même deux anomalies particulièrement prononcées. Ainsi, comme proposé dans le chapitre 1, il est possible que ces anomalies soient liées à d'importantes variations du flux de matière organique vers les fonds marins, probablement causées par des changements dans la productivité primaire et/ou dans les conditions océaniques. Il pourrait donc être intéressant d'investiguer ces anomalies dans les différents bassins de la marge continentale et de les interpréter en termes de changements environnementaux dans les différents secteurs. En outre, l'anomalie de  $k_{LF}$  de la carotte 20 est différente, car sa limite supérieure correspond au début de l'accélération du courant marin dans le bassin Ouest, qui débute donc vers 6,3 cal ka BP. Bien que la diminution locale du RSL puisse être la cause de cette accélération, ce changement pourrait être corrélé aux variations du courant ouest groenlandais et du courant du Labrador (Rashid et al., 2017; McCave et al., 2019; Weiser et al., 2021) ainsi qu'aux changements de productivité primaire dans les fjords Nachvak et Saglek marquant cette période.



## RÉFÉRENCES BIBLIOGRAPHIQUES

- Allan, E., de Vernal, A., Seidenkrantz, M., Briner, J.P., Hillaire-Marcel, C., Pearce, C., Meire, L., Røy, H., Mathiasen, A.M., Nielsen, M.T., Plesner, J.L., Perner, K., 2021. Insolation vs. meltwater control of productivity and sea surface conditions off SW Greenland during the Holocene. *Boreas* 50, 631–651. <https://doi.org/10.1111/bor.12514>
- Alley, R., Agustsdottir, A., 2005. The 8k event: cause and consequences of a major Holocene abrupt climate change. *Quaternary Science Reviews* 24, 1123–1149. <https://doi.org/10.1016/j.quascirev.2004.12.004>
- Alley, R.B., Mayewski, P.A., Sowers, T., Stuiver, M., Taylor, K.C., Clark, P.U., 1997. Holocene climatic instability: A prominent, widespread event 8200 yr ago. *Geology* 25, 483. [https://doi.org/10.1130/0091-7613\(1997\)025<0483:HCIAPW>2.3.CO;2](https://doi.org/10.1130/0091-7613(1997)025<0483:HCIAPW>2.3.CO;2)
- Andrews, J.T., MacLean, B., 2003. Hudson Strait ice streams: a review of stratigraphy, chronology and links with North Atlantic Heinrich events. *Boreas* 32, 4–17. <https://doi.org/10.1080/03009480310001010>
- Baldini, J.U.L., McDermott, F., Fairchild, I.J., 2002. Structure of the 8200-Year Cold Event Revealed by a Speleothem Trace Element Record. *Science* 296, 2203–2206. <https://doi.org/10.1126/science.1071776>
- Barber, D.C., Dyke, A., Hillaire-Marcel, C., Jennings, A.E., Andrews, J.T., Kerwin, M.W., Bilodeau, G., McNeely, R., Southon, J., Morehead, M.D., Gagnon, J.-M., 1999. Forcing of the cold event of 8,200 years ago by catastrophic drainage of Laurentide lakes. *Nature* 400, 344–348. <https://doi.org/10.1038/22504>
- Bastick, J., 2009. Evaluating marine ecological integrity monitoring measures for Nachvak and Saglek fiords, northern Labrador. M.Sc. thesis, 183 p., Royal Military College of Canada.
- Bell, T., Josenhans, H., 1997. The seismic record of glaciation in Nachvak Fjord, Northern Labrador. In: Davies, T. A., Bell, T., Cooper, A. K. et al. (eds) *Glaciated Continental Margins: An Atlas of Acoustic Images*. London: Chapman & Hall, pp. 190–193.

- Bellwald, B., Hjelstuen, B.O., Sejrup, H.P., Stokowy, T., Kuvås, J., 2019. Holocene mass movements in west and mid-Norwegian fjords and lakes. *Marine Geology* 407, 192–212. <https://doi.org/10.1016/j.margeo.2018.11.007>
- Bentley, S.J., Kahlmeyer, E., 2012. Patterns and mechanisms of fluvial sediment flux and accumulation in two subarctic fjords: Nachvak and Saglek Fjords, Nunatsiavut, Canada. *Can. J. Earth Sci.* 49, 1200–1215. <https://doi.org/10.1139/e2012-052>
- Blaauw, M., Christen, J.A., 2011. Flexible paleoclimate age-depth models using an autoregressive gamma process. *Bayesian Analysis* 6. <https://doi.org/10.1214/11-BA618>
- Blott, S.J., Pye, K., 2001. GRADISTAT: a grain size distribution and statistics package for the analysis of unconsolidated sediments. *Earth Surface Processes and Landforms* 26, 1237–1248. <https://doi.org/10.1002/esp.261>
- Broom, L.M., Campbell, D.C., Gosse, J.C., 2017. Investigation of a Holocene marine sedimentary record from Pond Inlet, northern Baffin Island, Nunavut 12. Summary of Activities, 93-104.
- Brouard, E., Roy, M., Godbout, P.-M., Veillette, J.J., 2021. A framework for the timing of the final meltwater outbursts from glacial Lake Agassiz-Ojibway. *Quaternary Science Reviews* 274, 107269. <https://doi.org/10.1016/j.quascirev.2021.107269>
- Brown, T., Reimer, K., Sheldon, Bell, T., Bentley, S., Pienitz, R., Gosselin, M., Blais, M., Carpenter, M., Estrada, E., Richerol, T., Kahlmeyer, E., Luque, S., Sjare, B., Fisk, A., Iverson, S., 2012. A first look at Nunatsiavut Kangidualuk (‘fjord’) ecosystems. In: Nunavik and Nunatsiavut: from science to policy. An Integrated Regional Impact Study (IRIS) of climate change and modernization. ArcticNet Inc., Quebec City, QC, 271-301. <https://doi.org/10.13140/2.1.4784.9924>
- Caron, M., Rochon, A., Montero-Serrano, J., St-Onge, G., 2019a. Evolution of sea-surface conditions on the northwestern Greenland margin during the Holocene. *J. Quaternary Science* 34, 569–580. <https://doi.org/10.1002/jqs.3146>
- Caron, M., St-Onge, G., Montero-Serrano, J.-C., Rochon, A., Georgiadis, E., Giraudeau, J., Massé, G., 2019b. Holocene chronostratigraphy of northeastern Baffin Bay based on radiocarbon and palaeomagnetic data. *Boreas* 48, 147–165. <https://doi.org/10.1111/bor.12346>
- Clark, P.U., 1988. Glacial geology of the Torngat Mountains, Labrador. *Canadian Journal of Earth Science* 25, 1184–1198. <https://doi.org/10.1139/e88-116>



- Clark, P.U., Brook, E.J., Raisbeck, G.M., Yiou, F., Clark, J., 2003. Cosmogenic <sup>10</sup>Be ages of the Saglek Moraines, Torngat Mountains, Labrador. *Geology* 31, 617. [https://doi.org/10.1130/0091-7613\(2003\)031<0617:CBAOTS>2.0.CO;2](https://doi.org/10.1130/0091-7613(2003)031<0617:CBAOTS>2.0.CO;2)
- Clark, P.U., Marshall, S.J., Clarke, G.K.C., Hostetler, S.W., Licciardi, J.M., Teller, J.T., 2001. Freshwater Forcing of Abrupt Climate Change During the Last Glaciation. *Science* 293, 283–287. <https://doi.org/10.1126/science.1062517>
- Couette, P.O., Ghienne, J. F., Lajeunesse, P., Van der Woerd, J., 2023. Climatic control on the retreat of the Laurentide Ice Sheet margin in easternmost Québec-Labrador (Canada) revealed by cosmogenic exposure dating. *Journal of Quaternary Science* 3525.
- Croudace, I.W., Rothwell, R.G. (Eds.), 2015. *Micro-XRF Studies of Sediment Cores: Applications of a non-destructive tool for the environmental sciences*, 1st ed. 2015. ed, *Developments in Paleoenvironmental Research*. Springer Netherlands : Imprint: Springer, Dordrecht. <https://doi.org/10.1007/978-94-017-9849-5>
- Dalton, A.S., Margold, M., Stokes, C.R., Tarasov, L., Dyke, A.S., Adams, R.S., Allard, S., Arends, H.E., Atkinson, N., Attig, J.W., Barnett, P.J., Barnett, R.L., Batterson, M., Bernatchez, P., Borns, H.W., Breckenridge, A., Briner, J.P., Brouard, E., Campbell, J.E., Carlson, A.E., Clague, J.J., Curry, B.B., Daigneault, R.-A., Dubé-Loubert, H., Easterbrook, D.J., Franzi, D.A., Friedrich, H.G., Funder, S., Gauthier, M.S., Gowan, A.S., Harris, K.L., Héту, B., Hooyer, T.S., Jennings, C.E., Johnson, M.D., Kehew, A.E., Kelley, S.E., Kerr, D., King, E.L., Kjeldsen, K.K., Knaeble, A.R., Lajeunesse, P., Lakeman, T.R., Lamothe, M., Larson, P., Lavoie, M., Loope, H.M., Lowell, T.V., Lusardi, B.A., Manz, L., McMartin, I., Nixon, F.C., Occhietti, S., Parkhill, M.A., Piper, D.J.W., Pronk, A.G., Richard, P.J.H., Ridge, J.C., Ross, M., Roy, M., Seaman, A., Shaw, J., Stea, R.R., Teller, J.T., Thompson, W.B., Thorleifson, L.H., Utting, D.J., Veillette, J.J., Ward, B.C., Weddle, T.K., Wright, H.E., 2020. An updated radiocarbon-based ice margin chronology for the last deglaciation of the North American Ice Sheet Complex. *Quaternary Science Reviews* 234, 106223. <https://doi.org/10.1016/j.quascirev.2020.106223>
- Day, R., Fuller, M., Schmidt, V.A., 1977. Hysteresis properties of titanomagnetites: Grain-size and compositional dependence. *Physics of the Earth and Planetary Interiors* 13, 260–267. [https://doi.org/10.1016/0031-9201\(77\)90108-X](https://doi.org/10.1016/0031-9201(77)90108-X)
- de Vernal, A., Guiot, J., Turon, J.-L., 2007. Late and Postglacial Paleoenvironments of the Gulf of St. Lawrence: Marine and Terrestrial Palynological Evidence. *Géographie physique et Quaternaire* 47, 167–180. <https://doi.org/10.7202/032946ar>

- Debret, M., Sebag, D., Desmet, M., Balsam, W., Copard, Y., Mourier, B., Susperrigui, A.-S., Arnaud, F., Bentaleb, I., Chapron, E., Lallier-Vergès, E., Winiarski, T., 2011. Spectrocolorimetric interpretation of sedimentary dynamics: The new “Q7/4 diagram.” *Earth-Science Reviews* 109, 1–19.  
<https://doi.org/10.1016/j.earscirev.2011.07.002>
- Deschamps, C., Montero-Serrano, J., St-Onge, G., 2018a. Sediment Provenance Changes in the Western Arctic Ocean in Response to Ice Rafting, Sea Level, and Oceanic Circulation Variations Since the Last Deglaciation. *Geochemistry, Geophysics, Geosystems* 19, 2147–2165. <https://doi.org/10.1029/2017GC007411>
- Deschamps, C., Montero-Serrano, J., St-Onge, G., Poirier, A., 2019. Holocene Changes in Deep Water Circulation Inferred From Authigenic Nd and Hf Isotopes in Sediment Records From the Chukchi-Alaskan and Canadian Beaufort Margins. *Paleoceanography and Paleoclimatology* 34, 1038–1056.  
<https://doi.org/10.1029/2018PA003485>
- Deschamps, C., St-Onge, G., Montero-Serrano, J., Polyak, L., 2018b. Chronostratigraphy and spatial distribution of magnetic sediments in the Chukchi and Beaufort seas since the last deglaciation. *Boreas* 47, 544–564.  
<https://doi.org/10.1111/bor.12296>
- Dietrich, P., Ghienne, J.-F., Normandeau, A., Lajeunesse, P., 2017. Reconstructing ice margin retreat using delta morphostratigraphy. *Scientific reports* 7, 16936.  
<https://doi.org/10.1038/s41598-017-16763-x>
- Drinkwater, K. F., 1986. Physical oceanography of Hudson strait and Ungava Bay. In *Elsevier oceanography series* 44, 237-264) [https://doi.org/10.1016/S0422-9894\(08\)70906-1](https://doi.org/10.1016/S0422-9894(08)70906-1)
- Drinkwater, K.F., 1988. On the mean and tidal currents in Hudson strait. *Atmosphere-Ocean* 26, 252–266. <https://doi.org/10.1080/07055900.1988.9649302>
- Duboc, Q., St-Onge, G., Lajeunesse, P., 2017. Sediment records of the influence of river damming on the dynamics of the Nelson and Churchill Rivers, western Hudson Bay, Canada, during the last centuries. *The Holocene* 27, 712–725.  
<https://doi.org/10.1177/0959683616670465>
- Duchesne, M.J., Pinet, N., Bolduc, A., Bédard, K., Lavoie, D., 2007. Seismic stratigraphy of the lower St. Lawrence River estuary (Quebec) Quaternary deposits and seismic signature of the underlying geological domains *Geological Survey of Canada Current Research* 2007-D2, 1-14. <https://doi.org/10.4095/224408>

- Dyke, A.S., 2004. An outline of North American deglaciation with emphasis on central and northern Canada, in: *Developments in Quaternary Sciences*. Elsevier, 373–424. [https://doi.org/10.1016/S1571-0866\(04\)80209-4](https://doi.org/10.1016/S1571-0866(04)80209-4)
- England, J., Dyke, A.S., Coulthard, R.D., Mcneely, R., Aitken, A., 2013. The exaggerated radiocarbon age of deposit-feeding molluscs in calcareous environments: Exaggerated radiocarbon ages of molluscs. *Boreas* 42, 362–373. <https://doi.org/10.1111/j.1502-3885.2012.00256.x>
- Engstrom, D.R., Hansen, B.C.S., 1985. Postglacial vegetational change and soil development in southeastern Labrador as inferred from pollen and chemical stratigraphy. *Can. J. Bot.* 63, 543–561. <https://doi.org/10.1139/b85-070>
- Fortin, D., Francus, P., Gebhardt, A.C., Hahn, A., Kliem, P., Lisé-Pronovost, A., Roychowdhury, R., Labrie, J., St-Onge, G., 2013. Destructive and non-destructive density determination: method comparison and evaluation from the Laguna Potrok Aike sedimentary record. *Quaternary Science Reviews* 71, 147–153. <https://doi.org/10.1016/j.quascirev.2012.08.024>
- Funk, J. A., Von Dobeneck, T., Reitz, A., 2004. Integrated rock magnetic and geochemical quantification of redoxomorphic iron mineral diagenesis in Late Quaternary sediments from the Equatorial Atlantic. In : *The South Atlantic in the Late Quaternary: Reconstruction of material budgets and current systems*. Berlin, Heidelberg : Springer Berlin Heidelberg, 2004. pp. 237-260.
- Gauthier, M.S., Kelley, S.E., Hodder, T.J., 2020. Lake Agassiz drainage bracketed Holocene Hudson Bay Ice Saddle collapse. *Earth and Planetary Science Letters* 544, 116372. <https://doi.org/10.1016/j.epsl.2020.116372>
- Godbout, P.-M., Roy, M., Veillette, J.J., 2020. A detailed lake-level reconstruction shows evidence for two abrupt lake drawdowns in the late-stage history of the eastern Lake Agassiz-Ojibway basin. *Quaternary Science Reviews* 238, 106327. <https://doi.org/10.1016/j.quascirev.2020.106327>
- Godbout, P.-M., Roy, M., Veillette, J.J., 2019. High-resolution varve sequences record one major late-glacial ice readvance and two drainage events in the eastern Lake Agassiz-Ojibway basin. *Quaternary Science Reviews* 223, 105942. <https://doi.org/10.1016/j.quascirev.2019.105942>
- Haberzettl, T., St-Onge, G., Lajeunesse, P., 2010. Multi-proxy records of environmental changes in Hudson Bay and Strait since the final outburst flood of Lake Agassiz-Ojibway. *Marine Geology* 271, 93–105. <https://doi.org/10.1016/j.margeo.2010.01.014>

- Hall, F.R., Andrews, J.T., Jennings, A., Vilks, G., Moran, K., 1999. Late Quaternary sediments and chronology of the northeast Labrador Shelf (Karlsefni Trough, Saglek Bank): Links to glacial history. *Geological Society of America Bulletin* 111, 1700–1713. [https://doi.org/10.1130/0016-7606\(1999\)111<1700:LQSAO>2.3.CO;2](https://doi.org/10.1130/0016-7606(1999)111<1700:LQSAO>2.3.CO;2)
- Heaton, T.J., Köhler, P., Butzin, M., Bard, E., Reimer, R.W., Austin, W.E.N., Bronk Ramsey, C., Grootes, P.M., Hughen, K.A., Kromer, B., Reimer, P.J., Adkins, J., Burke, A., Cook, M.S., Olsen, J., Skinner, L.C., 2020. Marine20—The Marine Radiocarbon Age Calibration Curve (0–55,000 cal BP). *Radiocarbon* 62, 779–820. <https://doi.org/10.1017/RDC.2020.68>
- Hill, D.F., Griffiths, S.D., Peltier, W.R., Horton, B.P., Törnqvist, T.E., 2011. High-resolution numerical modeling of tides in the western Atlantic, Gulf of Mexico, and Caribbean Sea during the Holocene. *Journal of Geophysical Research* 116, C10014. <https://doi.org/10.1029/2010JC006896>
- Hillaire-Marcel, C., 2005. La déglaciation et le relèvement isostatique sur la côte est de la baie d’Hudson. *Cahiers de géographie du Québec* 20, 185–220. <https://doi.org/10.7202/021319ar>
- Hillaire-Marcel, C., de Vernal, A., Piper, D.J.W., 2007. Lake Agassiz Final drainage event in the northwest North Atlantic. *Geophysical Research Letters* 34. <https://doi.org/10.1029/2007GL030396>
- Hjelstuen, B.O., Hafliðason, H., Sejrup, H.P., Lyså, A., 2009. Sedimentary processes and depositional environments in glaciated fjord systems — Evidence from Nordfjord, Norway. *Marine Geology* 258, 88–99. <https://doi.org/10.1016/j.margeo.2008.11.010>
- Hodell, D.A., Channell, J.E.T., Curtis, J.H., Romero, O.E., Röhl, U., 2008. Onset of “Hudson Strait” Heinrich events in the eastern North Atlantic at the end of the middle Pleistocene transition (~640 ka)? *Paleoceanography* 23, 1–16. <https://doi.org/10.1029/2008PA001591>
- Hoffmann, S.S., Dalsing, R.E., Murphy, S.C., 2019. Sortable silt records of intermediate-depth circulation and sedimentation in the Southwest Labrador Sea since the Last Glacial Maximum. *Quaternary Science Reviews* 206, 99–110. <https://doi.org/10.1016/j.quascirev.2018.12.028>
- Hofmann, D., Fabian, K., Schmieder, F., Donner, B., Bleil, U., 2005. A stratigraphic network across the Subtropical Front in the central South Atlantic: Multi-parameter correlation of magnetic susceptibility, density, X-ray fluorescence and  $\delta^{18}\text{O}$  records. *Earth and Planetary Science Letters* 240, 694–709. <https://doi.org/10.1016/j.epsl.2005.09.048>

- Hormes, A., Blaauw, M., Dahl, S.O., Nesje, A., Possnert, G., 2009. Radiocarbon wiggle-match dating of proglacial lake sediments – Implications for the 8.2ka event. *Quaternary Geochronology* 4, 267–277. <https://doi.org/10.1016/j.quageo.2008.12.004>
- Ives, J.D., 1976. The Saglek Moraines of Northern Labrador: A Commentary. *Arctic and Alpine Research* 8, 403. <https://doi.org/10.2307/1550444>
- Ives, J.D., 1957. Glaciation of the Torngat Mountains, Northern Labrador. *Arctic* 10, 66. <https://doi.org/10.14430/arctic3755>
- Jennings, A., Andrews, J., Pearce, C., Wilson, L., Ólfasdóttir, S., 2015. Detrital carbonate peaks on the Labrador shelf, a 13–7ka template for freshwater forcing from the Hudson Strait outlet of the Laurentide Ice Sheet into the subpolar gyre. *Quaternary Science Reviews* 107, 62–80. <https://doi.org/10.1016/j.quascirev.2014.10.022>
- Jennings, A.E., Manley, W.F., Maclean, B., Andrews, J.T., 1998. Marine evidence for the last glacial advance across eastern Hudson Strait, eastern Canadian Arctic. *Journal of Quaternary Science* 13, 501–514. [https://doi.org/10.1002/\(SICI\)1099-1417\(1998110\)13:6<501::AID-JQS391>3.0.CO;2-A](https://doi.org/10.1002/(SICI)1099-1417(1998110)13:6<501::AID-JQS391>3.0.CO;2-A)
- Josenhans, H.W., Zevenhuizen, J., Klassen, R.A., 1986. The Quaternary geology of the Labrador Shelf. *Canadian Journal of Earth Sciences* 23, 1190–1213. <https://doi.org/10.1139/e86-116>
- Kamula, C.M., Kuzyk, Z.Z.A., Lobb, D.A., Macdonald, R.W., 2017. Sources and accumulation of sediment and particulate organic carbon in a subarctic fjord estuary:  $^{210}\text{Pb}$ ,  $^{137}\text{Cs}$ , and  $\delta^{13}\text{C}$  records from Lake Melville, Labrador. *Canadian Journal of Earth Sciences* 54, 993–1006. <https://doi.org/10.1139/cjes-2016-0167>
- Kaufman, D. S., Miller, G. H., Stravers, J. A., Andrews, J. T., 1993. Abrupt early Holocene (9.9-9.6 ka) ice-stream advance at the mouth of Hudson Strait, Arctic Canada. *Geology*, 21(12), 1063-1066. [https://doi.org/10.1130/0091-7613\(1993\)021<1063:AEHKIS>2.3.CO;2](https://doi.org/10.1130/0091-7613(1993)021<1063:AEHKIS>2.3.CO;2)
- Kaufman, D., 2004. Holocene thermal maximum in the western Arctic (0–180°W). *Quaternary Science Reviews* 23, 529–560. <https://doi.org/10.1016/j.quascirev.2003.09.007>
- Kerwin, M.W., 1996. A Regional Stratigraphic Isochron (ca. 8000  $^{14}\text{C}$  yr B.P.) from Final Deglaciation of Hudson Strait. *Quaternary Research* 46, 89–98. <https://doi.org/10.1006/qres.1996.0049>

- King, G.A., 2007. A Standard Method for Evaluating Radiocarbon Dates of Local Deglaciation: Application to the Deglaciation History of Southern Labrador and Adjacent Québec. *Géographie physique et Quaternaire* 39, 163–182.  
<https://doi.org/10.7202/032600ar>
- Kirschvink, J., 1980. The least-squares line and plane and the analysis of palaeomagnetic data. *Geophysical Journal International*, 62(3), 699-718.
- Korff, L., von Dobeneck, T., Frederichs, T., Kasten, S., Kuhn, G., Gersonde, R., Diekmann, B., 2016. Cyclic magnetite dissolution in Pleistocene sediments of the abyssal northwest Pacific Ocean: Evidence for glacial oxygen depletion and carbon trapping: Magnetite Dissolution in the NW Pacific. *Paleoceanography* 31, 600–624.  
<https://doi.org/10.1002/2015PA002882>
- Kuzyk, Z.Z.A., Goñi, M.A., Stern, G.A., Macdonald, R.W., 2008. Sources, pathways and sinks of particulate organic matter in Hudson Bay: Evidence from lignin distributions. *Marine Chemistry* 112, 215–229.  
<https://doi.org/10.1016/j.marchem.2008.08.001>
- Kylander, M.E., Ampel, L., Wohlfarth, B., Veres, D., 2011. High-resolution X-ray fluorescence core scanning analysis of Les Echets (France) sedimentary sequence: new insights from chemical proxies. *Journal of Quaternary Science* 26, 109–117.  
<https://doi.org/10.1002/jqs.1438>
- Lajeunesse, P., St-Onge, G., 2008. The subglacial origin of the Lake Agassiz–Ojibway final outburst flood. *Nature Geoscience* 1, 184–188.  
<https://doi.org/10.1038/ngeo130>
- Lamb, A.L., Wilson, G.P., Leng, M.J., 2006. A review of coastal palaeoclimate and relative sea-level reconstructions using  $\delta^{13}\text{C}$  and C/N ratios in organic material. *Earth-Science Reviews* 75, 29–57. <https://doi.org/10.1016/j.earscirev.2005.10.003>
- Lambeck, K., Rouby, H., Purcell, A., Sun, Y., Sambridge, M., 2014. Sea level and global ice volumes from the Last Glacial Maximum to the Holocene. *Proceedings of the National Academy of Sciences* 111, 15296–15303.  
<https://doi.org/10.1073/pnas.1411762111>
- Lévesque, Y., St-Onge, G., Lajeunesse, P., Desiège, P., Brouard, E., 2020. Defining the maximum extent of the Laurentide Ice Sheet in Home Bay (eastern Arctic Canada) during the Last Glacial episode. *Boreas* 49, 52–70.  
<https://doi.org/10.1111/bor.12415>

- Lewis, C.F.M., Miller, A.A.L., Levac, E., Piper, D.J.W., Sonnichsen, G.V., 2012. Lake Agassiz outburst age and routing by Labrador Current and the 8.2 cal ka cold event. *Quaternary International* 260, 83–97.  
<https://doi.org/10.1016/j.quaint.2011.08.023>
- Lisé-Pronovost, A., St-Onge, G., Brachfeld, S., Barletta, F., Darby, D., 2009. Paleomagnetic constraints on the Holocene stratigraphy of the Arctic Alaskan margin. *Global and Planetary Change* 68, 85–99.  
<https://doi.org/10.1016/j.gloplacha.2009.03.015>
- Liu, Q., Roberts, A.P., Larrasoana, J.C., Banerjee, S.K., Guyodo, Y., Tauxe, L., Oldfield, F., 2012. Environmental magnetism: Principles and applications. *Reviews of Geophysics* 50, RG4002. <https://doi.org/10.1029/2012RG000393>
- Lochte, A.A., Repschläger, J., Kienast, M., Garbe-Schönberg, D., Andersen, N., Hamann, C., Schneider, R., 2019a. Labrador Sea freshening at 8.5 ka BP caused by Hudson Bay Ice Saddle collapse. *Nature Communication* 10, 586.  
<https://doi.org/10.1038/s41467-019-08408-6>
- Lochte, A.A., Repschläger, J., Seidenkrantz, M.-S., Kienast, M., Blanz, T., Schneider, R.R., 2019b. Holocene water mass changes in the Labrador Current. *The Holocene* 29, 676–690. <https://doi.org/10.1177/0959683618824752>
- Lutz, B., Wiles, G., Lowell, T., Michaels, J., 2007. The 8.2-ka abrupt climate change event in Brown's Lake, northeast Ohio. *Quaternary Research* 67, 292–296.  
<https://doi.org/10.1016/j.yqres.2006.08.007>
- MacLean, B. (ed.) 2001a. *Marine Geology of Hudson Strait and Ungava Bay, Eastern Arctic Canada: Late Quaternary Sediments, Depositional Environments, and Late Glacial–Deglacial History Derived from Marine and Terrestrial Studies*. Geological Survey of Canada Bulletin 566, 199 pp. Queen's Printer, Ottawa.
- MacLean, B., Vilks, G., Hardy, I., Deonarine, B., Jennings, A., Manley, W.F., 2001. Quaternary sediments in Hudson Strait and Ungava Bay. In MacLean, B. (ed.): *Marine Geology of Hudson Strait and Ungava Bay, Eastern Arctic Canada; Late Quaternary Sediments, Depositional Environments, and Late Glacial–Deglacial History Derived from Marine and Terrestrial Studies*, 71–126. Geological Survey of Canada Bulletin 566. Queen's Printer, Ottawa.
- Margold, M., Stokes, C.R., Clark, C.D., 2018. Reconciling records of ice streaming and ice margin retreat to produce a palaeogeographic reconstruction of the deglaciation of the Laurentide Ice Sheet. *Quaternary Science Reviews* 189, 1–30.  
<https://doi.org/10.1016/j.quascirev.2018.03.013>

- Margreth, A., Gosse, J.C., Dyke, A.S., 2017. Wisconsinan and early Holocene glacial dynamics of Cumberland Peninsula, Baffin Island, Arctic Canada. *Quaternary Science Reviews* 168, 79–100. <https://doi.org/10.1016/j.quascirev.2017.04.033>
- Matero, I.S.O., Gregoire, L.J., Ivanovic, R.F., Tindall, J.C., Haywood, A.M., 2017. The 8.2 ka cooling event caused by Laurentide ice saddle collapse. *Earth and Planetary Science Letters* 473, 205–214. <https://doi.org/10.1016/j.epsl.2017.06.011>
- Mazaud, A., 2005. User-friendly software for vector analysis of the magnetization of long sediment cores. *Geochemistry, Geophysics, Geosystems* 6, 1-5. <https://doi.org/10.1029/2005GC001036>
- McCave, I.N., Andrews, J.T., 2019. Distinguishing current effects in sediments delivered to the ocean by ice. II. Glacial to Holocene changes in high latitude North Atlantic upper ocean flows. *Quaternary Science Reviews* 223, 105902. <https://doi.org/10.1016/j.quascirev.2019.105902>
- McCave, I.N., Thornalley, D.J.R., Hall, I.R., 2017. Relation of sortable silt grain-size to deep-sea current speeds: Calibration of the ‘Mud Current Meter.’ *Deep Sea Research Part I: Oceanographic Research Papers* 127, 1–12. <https://doi.org/10.1016/j.dsr.2017.07.003>
- Mercier, D., 2007. Le paraglaciaire: évolution d'un concept. Du continent au bassin versant. *Théories et pratiques en géographie physique. Hommage au Professeur Alain Godard*, 592.
- Meyers, P.A., 1997. Organic geochemical proxies of paleoceanographic, paleolimnologic, and paleoclimatic processes. *Organic Geochemistry* 27, 213–250. [https://doi.org/10.1016/S0146-6380\(97\)00049-1](https://doi.org/10.1016/S0146-6380(97)00049-1)
- Moros, M., Emeis, K., Risebrobakken, B., Snowball, I., Kuijpers, A., McManus, J., Jansen, E., 2004. Sea surface temperatures and ice rafting in the Holocene North Atlantic: climate influences on northern Europe and Greenland. *Quaternary Science Reviews* 23, 2113–2126. <https://doi.org/10.1016/j.quascirev.2004.08.003>
- Mulder, T., E. Chapron, 2011. Flood deposits in continental and marine environments: Character and significance, in R. M. Slatt and C. Zavala, eds., *Sediment transfer from shelf to deep water—Revisiting the delivery system: AAPG Studies in Geology* 61, 1–30.
- Murton, J.B., Bateman, M.D., Dallimore, S.R., Teller, J.T., Yang, Z., 2010. Identification of Younger Dryas outburst flood path from Lake Agassiz to the Arctic Ocean. *Nature* 464, 740–743. <https://doi.org/10.1038/nature08954>



- Norris, S.L., Garcia-Castellanos, D., Jansen, J.D., Carling, P.A., Margold, M., Woywitka, R.J., Froese, D.G., 2021. Catastrophic Drainage From the Northwestern Outlet of Glacial Lake Agassiz During the Younger Dryas. *Geophysical Research Letters* 48. <https://doi.org/10.1029/2021GL093919>
- Occhietti, S., Parent, M., Lajeunesse, P., Robert, F., Govare, É., 2011. Late Pleistocene–Early Holocene Decay of the Laurentide Ice Sheet in Québec–Labrador, in: *Developments in Quaternary Sciences*. Elsevier, 601–630. <https://doi.org/10.1016/B978-0-444-53447-7.00047-7>
- Pieńkowski, A.J., Coulthard, R.D., Furze, M.F.A., 2023. Revised marine reservoir offset ( $\Delta R$ ) values for molluscs and marine mammals from Arctic North America. *Boreas* 52, 145–167. <https://doi.org/10.1111/bor.12606>
- Piva, A., Asioli, A., Schneider, R.R., Trincardi, F., Andersen, N., Colmenero-Hidalgo, E., Dennielou, B., Flores, J-A., Vigliotti, L., 2008. Climatic cycles as expressed in sediments of the PROMESS1 borehole PRAD1-2, central Adriatic, for the last 370 ka: 1. Integrated stratigraphy. *Geochemistry, Geophysics, Geosystems* 9, :Q01R01. <https://doi:10.1029/2007GC001713>
- Prinsenbergh, S. J., 1986. The circulation pattern and current structure of Hudson Bay. *Elsevier oceanography series*, 44, 187-204. [https://doi.org/10.1016/S0422-9894\(08\)70903-6](https://doi.org/10.1016/S0422-9894(08)70903-6)
- Poiré, A.G., Lajeunesse, P., Normandeau, A., Francus, P., St-Onge, G., Nzekwe, O.P., 2018. Late-Quaternary glacial to postglacial sedimentation in three adjacent fjord-lakes of the Québec North Shore (eastern Canadian Shield). *Quaternary Science Reviews* 186, 91–110. <https://doi.org/10.1016/j.quascirev.2018.02.013>
- Porinchu, D.F., MacDonald, G.M., Moser, K.A., Rolland, N., Kremenetski, K., Seppä, H., Rühland, K.M., 2019. Evidence of abrupt climate change at 9.3 ka and 8.2 ka in the central Canadian Arctic: Connection to the North Atlantic and Atlantic Meridional Overturning Circulation. *Quaternary Science Reviews* 219, 204–217. <https://doi.org/10.1016/j.quascirev.2019.07.024>
- Quillmann, U., Jennings, A., Andrews, J., 2010. Reconstructing Holocene palaeoclimate and palaeoceanography in Ísafjarðardjúp, northwest Iceland, from two fjord records overprinted by relative sea-level and local hydrographic changes. *Journal of Quaternary Science* 25, 1144–1159. <https://doi.org/10.1002/jqs.1395>
- Rashid, H., Piper, D.J.W., Lazar, K.B., McDonald, K., Saint-Ange, F., 2017. The Holocene Labrador Current: Changing linkages to atmospheric and oceanographic forcing factors: HOLOCENE LABRADOR CURRENT VIGOR. *Paleoceanography* 32, 498–510. <https://doi.org/10.1002/2016PA003051>

- Rémillard, A.M., St-Onge, G., Bernatchez, P., Héту, B., Buylaert, J.-P., Murray, A.S., Lajeunesse, P., 2017. Relative sea-level changes and glacio-isostatic adjustment on the Magdalen Islands archipelago (Atlantic Canada) from MIS 5 to the late Holocene. *Quaternary Science Reviews* 171, 216–233.  
<https://doi.org/10.1016/j.quascirev.2017.07.015>
- Rémillard, A.M., St-Onge, G., Bernatchez, P., Héту, B., Buylaert, J.-P., Murray, A.S., Vigneault, B., 2016. Chronology and stratigraphy of the Magdalen Islands archipelago from the last glaciation to the early Holocene: new insights into the glacial and sea-level history of eastern Canada. *Boreas* 45, 604–628.  
<https://doi.org/10.1111/bor.12179>
- Richerol, T., Fréchette, B., Rochon, A., Pienitz, R., 2016. Holocene climate history of the Nunatsiavut (northern Labrador, Canada) established from pollen and dinoflagellate cyst assemblages covering the past 7000 years. *The Holocene* 26, 44–60. <https://doi.org/10.1177/0959683615596823>
- Rignot, E., Velicogna, I., van den Broeke, M.R., Monaghan, A., Lenaerts, J.T.M., 2011. Acceleration of the contribution of the Greenland and Antarctic ice sheets to sea level rise. *Geophysics Research Letters*. 38, 1-5.  
<https://doi.org/10.1029/2011GL046583>
- Rinterknecht, V., Jomelli, V., Brunstein, D., Favier, V., Masson-Delmotte, V., Bourlès, D., Leanni, L., Schläppy, R., 2014. Unstable ice stream in Greenland during the Younger Dryas cold event. *Geology* 42, 759–762.  
<https://doi.org/10.1130/G35929.1>
- Roberts, A.P., 2015. Magnetic mineral diagenesis. *Earth-Science Reviews* 151, 1–47.  
<https://doi.org/10.1016/j.earscirev.2015.09.010>
- Roberts, A.P., Cui, Y., Verosub, K.L., 1995. Wasp-waisted hysteresis loops: Mineral magnetic characteristics and discrimination of components in mixed magnetic systems. *Journal of Geophysics Research: Solid Earth* 100, 17909–17924.  
<https://doi.org/10.1029/95JB00672>
- Roberts, A.P., Tauxe, L., Heslop, D., Zhao, X., Jiang, Z., 2018. A Critical Appraisal of the “Day” Diagram. *Journal of Geophysics Research: Solid Earth* 123, 2618–2644.  
<https://doi.org/10.1002/2017JB015247>
- Rohling, E.J., Pälike, H., 2005. Centennial-scale climate cooling with a sudden cold event around 8,200 years ago. *Nature* 434, 975–979.  
<https://doi.org/10.1038/nature03421>

- Ross, M., Utting, D.J., Lajeunesse, P., Kosar, K.G.A., 2012. Early Holocene deglaciation of northern Hudson Bay and Foxe Channel constrained by new radiocarbon ages and marine reservoir correction. *Quaternary Research* 78, 82–94. <https://doi.org/10.1016/j.yqres.2012.03.001>
- Roy, M., Dell'Oste, F., Veillette, J.J., de Vernal, A., Hélie, J.-F., Parent, M., 2011. Insights on the events surrounding the final drainage of Lake Ojibway based on James Bay stratigraphic sequences. *Quaternary Science Reviews* 30, 682–692. <https://doi.org/10.1016/j.quascirev.2010.12.008>
- Saucier, F.J., Senneville, S., Prinsenber, S., Roy, F., Smith, G., Gachon, P., Caya, D., Laprise, R., 2004. Modelling the sea ice-ocean seasonal cycle in Hudson Bay, Foxe Basin and Hudson Strait, Canada. *Climate Dynamics* 23, 303–326. <https://doi.org/10.1007/s00382-004-0445-6>
- Shaw, J., Piper, D.J.W., Fader, G.B.J., King, E.L., Todd, B.J., Bell, T., Batterson, M.J., Liverman, D.G.E., 2006. A conceptual model of the deglaciation of Atlantic Canada. *Quaternary Science Reviews* 25, 2059–2081. <https://doi.org/10.1016/j.quascirev.2006.03.002>
- Shaw, J., Todd, B.J., Li, M.Z., Mosher, D.C., Kostylev, V.E., 2014. Chapter 2 Continental shelves of Atlantic Canada. In: Chiocci & Chivas (eds) *Continental Shelves of the World*. *Memoirs* 41, 7–19. <https://doi.org/10.1144/M41.2>
- Shilts, W.W., 1980. Flow patterns in the central North American ice sheet. *Nature* 286, 213–218. <https://doi.org/10.1038/286213a0>
- Stewart, D. B., Lockhart, W. L., 2005. An overview of the Hudson Bay Marine Ecosystem. *Canadian Technical Report of Fisheries and Aquatic Sciences* no. 2586.
- Stewart, D. B., Howland, K. L., 2009. An ecological and oceanographical assessment of the alternate ballast water exchange zone in the Hudson Strait Region. Fisheries and Oceans Canada. *Canadian Science Advisory Secretariat. Research Document* 2009/008.
- Stoker, M.S., Wilson, C.R., Howe, J.A., Bradwell, T., Long, D., 2010. Paraglacial slope instability in Scottish fjords: examples from Little Loch Broom, NW Scotland. *Geological Society, London, Special Publications*, 344, 225–242. <https://doi.org/10.1144/SP344.16>
- Stokes, Ch.R., 2017. Deglaciation of the Laurentide Ice Sheet from the Last Glacial Maximum. *CIG* 43, 377–428. <https://doi.org/10.18172/cig.3237>

- Stoner, J.S., St-Onge, G., 2007. Chapter Three Magnetic Stratigraphy in Paleooceanography: Reversals, Excursions, Paleointensity, and Secular Variation, in: *Developments in Marine Geology*. Elsevier, 99–138. [https://doi.org/10.1016/S1572-5480\(07\)01008-1](https://doi.org/10.1016/S1572-5480(07)01008-1)
- St-Onge, G., Chapron, E., Mulsow, S., Salas, M., Viel, M., Debret, M., Foucher, A., Mulder, T., Winiarski, T., Desmet, M., Costa, P.J.M., Ghaleb, B., Jaouen, A., Locat, J., 2012. Comparison of earthquake-triggered turbidites from the Saguenay (Eastern Canada) and Reloncavi (Chilean margin) Fjords: Implications for paleoseismicity and sedimentology. *Sedimentary Geology* 243–244, 89–107. <https://doi.org/10.1016/j.sedgeo.2011.11.003>
- St-Onge, G., Hillaire-Marcel, C., 2001. Isotopic constraints of sedimentary inputs and organic carbon burial rates in the Saguenay Fjord, Quebec. *Marine Geology* 176, 1–22. [https://doi.org/10.1016/S0025-3227\(01\)00150-5](https://doi.org/10.1016/S0025-3227(01)00150-5)
- St-Onge, G., Lajeunesse, P., 2007. Flood-Induced Turbidites From Northern Hudson Bay And Western Hudson Strait: A Two-Pulse Record Of Lake Agassiz Final Outburst Flood?, in: Lykousis, V., Sakellariou, D., Locat, J. (Eds.), *Submarine Mass Movements and Their Consequences*. Springer Netherlands, Dordrecht, pp. 129–137. [https://doi.org/10.1007/978-1-4020-6512-5\\_14](https://doi.org/10.1007/978-1-4020-6512-5_14)
- St-Onge, G., Lajeunesse, P., Duchesne, M.J., Gagné, H., 2008. Identification and dating of a key Late Pleistocene stratigraphic unit in the St. Lawrence Estuary and Gulf (Eastern Canada). *Quaternary Science Reviews* 27, 2390–2400. <https://doi.org/10.1016/j.quascirev.2008.08.023>
- St-Onge, G., Mulder, T., Francus, P., Long, B., 2007. Chapter Two Continuous Physical Properties of Cored Marine Sediments, in: *Developments in Marine Geology*. Elsevier, 63–98. [https://doi.org/10.1016/S1572-5480\(07\)01007-X](https://doi.org/10.1016/S1572-5480(07)01007-X)
- St-Onge, G., Mulder, T., Piper, D.J.W., Hillaire-Marcel, C., Stoner, J.S., 2004. Earthquake and flood-induced turbidites in the Saguenay Fjord (Québec): a Holocene paleoseismicity record. *Quaternary Science Reviews* 23, 283–294. <https://doi.org/10.1016/j.quascirev.2003.03.001>
- Straneo, F., Saucier, F., 2008a. The outflow from Hudson Strait and its contribution to the Labrador Current. *Deep Sea Research Part I: Oceanographic Research Papers* 55, 926–946. <https://doi.org/10.1016/j.dsr.2008.03.012>
- Straneo, F., Saucier, F.J., 2008b. The Arctic–Subarctic Exchange Through Hudson Strait, in: Dickson, R.R., Meincke, J., Rhines, P. (Eds.), *Arctic–Subarctic Ocean Fluxes*. Springer Netherlands, Dordrecht, pp. 249–261. [https://doi.org/10.1007/978-1-4020-6774-7\\_11](https://doi.org/10.1007/978-1-4020-6774-7_11)

- Syvitski, J., Andrews, J.T., Schafer, C.T., Stravers, J.A., 2022. Sediment fill of Baffin Island fjords: Architecture and rates. *Quaternary Science Reviews* 284, 107474. <https://doi.org/10.1016/j.quascirev.2022.107474>
- Syvitski, J.P.M., 1991. Towards an understanding of sediment deposition on glaciated continental shelves. *Continental Shelf Research* 11, 897–937. [https://doi.org/10.1016/0278-4343\(91\)90085-K](https://doi.org/10.1016/0278-4343(91)90085-K)
- Syvitski, J.P.M., Lee, H.J., 1997. Postglacial sequence stratigraphy of Lake Melville, Labrador. *Marine Geology* 143, 55–79. [https://doi.org/10.1016/S0025-3227\(97\)00090-X](https://doi.org/10.1016/S0025-3227(97)00090-X)
- Syvitski, J.P.M., Praeg, D.B., 1989. Quaternary Sedimentation in the St. Lawrence Estuary and Adjoining Areas, Eastern Canada: An Overview Based on High-Resolution Seismo-Stratigraphy. *Géographie physique et Quaternaire* 43, 291–310. <https://doi.org/10.7202/032784ar>
- Tarasov, L., Dyke, A.S., Neal, R.M., Peltier, W.R., 2012. A data-calibrated distribution of deglacial chronologies for the North American ice complex from glaciological modeling. *Earth and Planetary Science Letters* 315–316, 30–40. <https://doi.org/10.1016/j.epsl.2011.09.010>
- Tauxe, L., 1993. Sedimentary records of relative paleointensity of the geomagnetic field: theory and practice. *Reviews of geophysics*, 31(3), 319-354.
- Tauxe, L., Mullender, T.A.T., Pick, T., 1996. Potbellies, wasp-waists, and superparamagnetism in magnetic hysteresis. *Journal of Geophysical Research* 101, No. B1, 571-583.
- Thomas, E.R., Wolff, E.W., Mulvaney, R., Steffensen, J.P., Johnsen, S.J., Arrowsmith, C., White, J.W.C., Vaughn, B., Popp, T., 2007. The 8.2ka event from Greenland ice cores. *Quaternary Science Reviews* 26, 70–81. <https://doi.org/10.1016/j.quascirev.2006.07.017>
- Ullman, D.J., Carlson, A.E., Hostetler, S.W., Clark, P.U., Cuzzone, J., Milne, G.A., Winsor, K., Caffee, M., 2016. Final Laurentide ice-sheet deglaciation and Holocene climate-sea level change. *Quaternary Science Reviews* 152, 49–59. <https://doi.org/10.1016/j.quascirev.2016.09.014>
- Vacchi, M., Engelhart, S.E., Nikitina, D., Ashe, E.L., Peltier, W.R., Roy, K., Kopp, R.E., Horton, B.P., 2018. Postglacial relative sea-level histories along the eastern Canadian coastline. *Quaternary Science Reviews* 201, 124–146. <https://doi.org/10.1016/j.quascirev.2018.09.043>

- Vickers, K.J., Ward, B.C., Utting, D.J., Telka, A.M., 2010. Deglacial reservoir age and implications, Foxe Peninsula, Baffin Island. *Journal of Quaternary Science* 25, 1338–1346. <https://doi.org/10.1002/jqs.1419>
- Vilks, G., Deonarine, B., Winters, G., 1987. Late Quaternary marine geology of Lake Melville, Labrador. Geological Survey of Canada, paper No. 87, 1-50. <https://doi.org/10.4095/122409>
- Vilks, G., Mudie, P.J., 1983. Evidence for Postglacial Paleoceanographic and Paleoclimatic Changes in Lake Melville, Labrador, Canada. *Arctic and Alpine Research* 15, 307. <https://doi.org/10.2307/1550827>
- von Grafenstein, U., Erlenkeuser, H., Müller, J., Jouzel, J., Johnsen, S., 1998. The cold event 8200 years ago documented in oxygen isotope records of precipitation in Europe and Greenland. *Climate Dynamics* 14, 73–81. <https://doi.org/10.1007/s003820050210>
- Weiser, J., Titschack, J., Kienast, M., McCave, I.N., Lochte, A.A., Saini, J., Stein, R., Hebbeln, D., 2021. Atlantic water inflow to Labrador Sea and its interaction with ice sheet dynamics during the Holocene. *Quaternary Science Reviews* 256, 106833. <https://doi.org/10.1016/j.quascirev.2021.106833>
- Weninger, B., Alram-Stern, E., Bauer, E., Clare, L., Danzeglocke, U., Jöris, O., Kubatzki, C., Rollefson, G., Todorova, H., van Andel, T., 2006. Climate Forcing Due to the 8200 Cal yr BP Event Observed at Early Neolithic Sites in the Eastern Mediterranean. *Quaternary Research* 66, 401–420. <https://doi.org/10.1016/j.yqres.2006.06.009>
- Young, N.E., Briner, J.P., Miller, G.H., Lesnek, A.J., Crump, S.E., Thomas, E.K., Pendleton, S.L., Cuzzone, J., Lamp, J., Zimmerman, S., Caffee, M., Schaefer, J.M., 2020. Deglaciation of the Greenland and Laurentide ice sheets interrupted by glacier advance during abrupt coolings. *Quaternary Science Reviews* 229, 106091. <https://doi.org/10.1016/j.quascirev.2019.106091>
- Zemp, M., Huss, M., Thibert, E., Eckert, N., McNabb, R., Huber, J., Barandun, M., Machguth, H., Nussbaumer, S.U., Gärtner-Roer, I., Thomson, L., Paul, F., Maussion, F., Kutuzov, S., Cogley, J.G., 2019. Global glacier mass changes and their contributions to sea-level rise from 1961 to 2016. *Nature* 568, 382–386. <https://doi.org/10.1038/s41586-019-1071-0>









